AFIT/GCS/ENG/96D-06

ARTIFICIAL COCHLEA DESIGN USING
MICRO-ELECTRO-MECHANICAL
SYSTEMS

THESIS
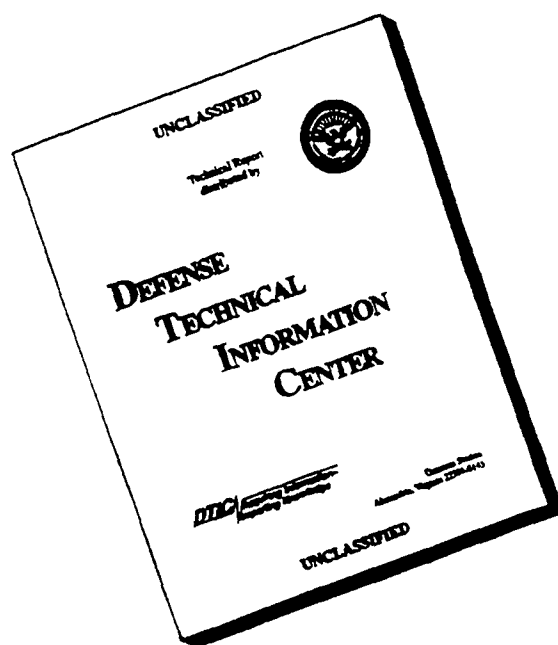
George C. Dalton II, BS EET
Captain, USAF

AFIT/GCS/ENG/96D-06

The views expressed in this thesis are those of the
author and do not reflect official policy or position
of the Department of Defense or the U.S. government.

Approved for public release; distribution unlimited.

19970218 094

DISCLAIMER NOTICE

THIS DOCUMENT IS BEST
QUALITY AVAILABLE. THE
COPY FURNISHED TO DTIC
CONTAINED A SIGNIFICANT
NUMBER OF PAGES WHICH DO
NOT REPRODUCE LEGIBLY.

Artificial Cochlea Design Using

Micro-Electro-Mechanical Systems

Thesis

Presented to the Faculty of the Graduate School of Engineering

of the Air Force Institute of Technology

Air University (AU)

Air Education and Training Command (AETC)

In Partial Fulfillment of the

Requirements for the Degree of

Master of Science in Computer Engineering

George C. Dalton II, BS EET

Captain, USAF

December 17, 1996

AFIT/GCS/ENG/96D-06

Abstract

The use of Micro-Electro-Mechanical Systems (MEMS) in the design of an artificial cochlea is investigated in depth. Interdigitated finger (comb), cantilever, bridge, and mirror resonators are presented as possible devices used to implement the artificial cochlea. These resonators are demonstrated to be extremely high Q devices, capable of being tuned with a simple DC bias. This suggests a possible change to existing cochlea models that claim highly complex AC feedback as being responsible for changes in the damping of the basilar membrane. The new cochlea model presented here, using MEMS to approximate the tuning of the basilar membrane, may be closer to the workings of the actual cochlea, as we understand it today.

Acknowledgments

Over the past eighteen months, my family, friends, colleagues, and professors have provided the support, without which, this effort could not have succeeded. With their encouragement, and the help of God, I was able to overcome many moments of self doubt and anxiety, and complete the work you have before you.

First I want to thank my family for understanding my long hours away from them, and all the missed weekends. My wife, Chong Hui, helped take much of the load off me by handling most of the household chores, and shuttling our 5 children to and from their extracurricular activities. I know my children missed not having me around as much. About half way through the program, my eldest daughter, Mia, said "Daddy, we don't do anything together anymore." I know she understands now, and I want her, and all of my children, to know the success of this thesis is owed greatly to them. Now that it is complete we can make up for the time not spent together. I also want to thank my parents, George and Mary, and my sisters,

Deborah, Irene, and Noreen. Their continuous words of encouragement and praise helped me through the tough times.

To Dr. Victor Bright, my thesis advisor, who's advice and constant prodding enabled me to achieve success, I thank you. A special thanks also to fellow Brooklynite and member of my thesis committee Dr. Matt Kabrisky, who's vast knowledge, insight, and keen sense of humor kept me going even when things looked grim. His quote, "All the easy stuff's been done," has been flashing across my marquee screen-saver for some time, propelling me to achieve. I also want to thank the other members of my committee, Dr. Steve Rogers and Dr. Marty DeSimeo. Their guidance and suggestions have aided me immeasurably. I would also like to thank my sponsor, Capt Adrian Michalicek, at Phillips Lab for supporting me in this endeavor.

To the rest of the MEMS group, thanks for answering my ceaseless questions, and interrupting your work so that I could finish mine. To Capt Rob Reid, who never met a differential equation he couldn't solve, and soon to be Dr. Reid, thanks for teaching me the basics. To Maj. Bill Cowan, thank you for giving up your interferometer so I could spend countless hours getting devices to resonate, and for use of your mirrors. To Maj.

Dave Burns, thanks for managing not to blind me with your lasers, and for all your help and advice. And thanks to Capt Jeff Butler, for helping me put things in perspective.

I am also grateful for all the help supplied by Mr. Bob Conkle, who can build anything and lays a mean tile, and Mr. Charlie Powers, who fought many battles to ensure I had the supplies and manuals I needed. Also, thanks to Gary Mauersberger, for the excellent computer support he provided me, and his aid in fighting the MS Word monster.

More thanks go to the VLSI lunch bunch, who through your insane conversations, helped me to keep my sanity. Capt Javier Marti, Capt James Savage, and 2Lt George Roelke, thanks for your help and friendship.

Lastly I like to thank Capt Marshall Messamore, for our many conversations on many diversified topics, which served as a diversion during the "all-nighters" and sometimes helped me look at problems from a different perspective. His occasional "boos" while hiding in the dark halls outside the VLSI lab helped to keep me on my toes.

Table of Contents

List of Figures

List of Tables

Artificial Cochlea Design Using Micro-Electro-Mechanical Systems

Chapter 1

1. Introduction

Man, in his efforts to overcome his environment, has continually attempted to uncover and copy Mother Nature's secrets. Sometimes these efforts are successful, as in the case of flight. Other times, we are not as successful. Presently, people suffering from hearing loss are fitted with devices that amplify sound, but don't begin to perform the complex processing that takes place in the human auditory system. As anyone familiar with these devices can attest, their performance is mediocre at best. If the secrets of the mammalian auditory system can be unlocked and reproduced, genuine hearing loss correction, like flight, could be a reality.

1.1 Purpose

Currently, no device exists that accurately reproduces the function of the human cochlea. Such a device will be highly complex since it has to be time, frequency, and phase discriminating, and will have to operate at high

speeds. While cochlear research has been ongoing for over a century, the first attempts at building such a device took place only a short time ago.

One of the first attempts at building an analog cochlea took place in the early 1960's by John L. Stewart of Armstrong Laboratories at Wright-Patterson AFB [1]. In 1988 Lyon and Mead documented the first Very Large Scale Integration (VLSI) of an Analog Cochlea [2]. Even though this is a relatively short time ago, advances in electronic devices are outpacing our ability to apply them, and many new devices have been designed since the first analog cochlea. One such category of devices, Micro-Electro-Mechanical Systems (MEMS), has been referred to as another "solution in search of a problem" [3], meaning there are many fields where these devices can be applied that have not been thus far attempted. The advantages of these devices are their very small size, measured in microns, and their high Q, the quality factor. An analog cochlea designed with MEMS devices is a major advance in cochlear modeling.

The purpose of this thesis is to lay the groundwork for an artificial cochlea designed using MEMS. This new innovation in artificial cochlea design is different from all previous designs, in that it uses electro-mechanical transducers to mimic the innerworkings of the living cochlea.

Since these devices operate in a manner much closer to that of actual cochlear filtering sections than the previously used electronic devices, a more accurate model is obtained. The use of MEMS in cochlear mechanics may soon unlock the secrets of the living cochlea.

1.2 Problem Statement.

Speech recognition promises a myriad of technological advances. For instance, the use of speech recognition interfaces might reduce our reliance on keyboards and monitors, thus saving millions of dollars each year for the Department of Defense, and the country as a whole, by reducing medical problems such as carpal tunnel syndrome and radiation exposure. As another example, the use of speech recognition and hearing prosthetic devices may someday remediate deafness.

In the words of Plato, "Necessity ... is the mother of invention." The need for a more accurate sound processor is apparent in fields of speech recognition, sound localization, deafness correction, and many others. The devices created in these areas to date have been rather clumsy [2,4-5]. By building an analog of the human/mammalian cochlea, a better understanding of this natural device can be obtained and modeled. The

more accurate this model is, the better the applications using this model will be. The cochlea itself is an electromechanical device, so modeling it using MEMS is a natural choice.

1.3 Scope

The scope of this research is limited to improving the current understanding of the cochlea by further refining its model. Only the electromechanical aspects of cochlea design are discussed. No devices (such as speech recognizers, hearing prosthetics, etc.) are implemented. The subject of neural transmission of signals generated by the cochlea is not addressed.

The overall scope of this thesis is to address the use of MEMS in artificial cochlea design to improve several key components of existing models. Specifically, a new focus on the Q of cochlear sections (which controls the sharpness of tuning) affecting the overall tuning of the cochlea, and control over these sections is presented. The intent is to broaden the field of cochlear mechanics by introducing these new devices, and presenting a new theory of cochlear tuning.

1.4 Approach

The approach taken for this thesis is to consider design criterion of a new type of artificial cochlea. Not only are the MEMS devices themselves considered, but the design of the overall system representing the cochlea is examined in detail. The effects of the new design on current cochlea models are contemplated and carefully discussed.

1.4.1 Cochlea Design With MEMS

The first stages of the human auditory system constitute a complex control system. Sound enters the ear and is first processed by the outer ear. The main function of the outer ear is to channel the incoming sound into the inner ear, while controlling, to some extent, the intensity of the sound and emphasizes specific frequency components. Next, the sound is processed by the inner ear, whose primary component is the cochlea. The cochlea analyzes the incoming sound into discrete frequencies, at varying amplitudes, which it then reports to the brain. Since this process occurs in real time, other information, such as phase changes, are also detected. The brain, in turn, sends signals back to the cochlea. These signals enable the cochlea to change the way it processes the incoming sound.

This system is modeled in Chapter 5 using a computer as a controller to act as the brain. There must also be a device that acts as the cochlea. For the artificial cochlea presented here, this device is a series of MEMS devices, each with a unique resonance frequency in the auditory range, ideally spanning the entire range. Each device can be tuned about its resonance by the controller. Interface between the controller and artificial cochlea is accomplished via the system buses, using a preassembled personal computer (PC) prototype circuit card.

1.4.1.1 *Overall Design Description*

To facilitate understandability, reusability, and maintainability, a top-down modular approach is used. The highest level is a computer circuit card. This card contains all the circuitry associated with the artificial cochlea, where possible. The exception is the placement of the MEMS devices themselves. Initially, the MEMS devices must be placed in a vacuum chamber to realize their high Q performance. After prototyping, these devices can be placed in multi-chip modules, along with their associated drive and sense circuitry, and hermetically packed in a vacuum.

The intent is to implement only the essential components in hardware, and to use software to control them. Where possible, Commercial Off The Shelf (COTS) components are used. The circuit card design discussed later is computer architecture dependent, designed for the x86 architecture, but is portable to any other architecture.

1.4.1.2 Computer Circuit Card Description

The artificial cochlea overall design block diagram is shown in Figure 1-1. The control program interfaces with the circuit card via the system buses. The computer interface and control logic circuits contain all of address and decode circuits, enabling the all aspects of the circuit card to be supervised by the control program. The control program enables the source of the input signal, then polls the individual MEMS devices for their values. Signals sensed on these devices are converted to digital, and returned to the control program. The control program can emulate various conditions on the artificial cochlea, similar to the control the brain has over an actual cochlea. For instance, it can listen to a single frequency, or over a wide range of harmonically related, or inharmonic frequencies. The control program can also apply feedback to any individual MEMS device to zero in

on a single frequency among many others.
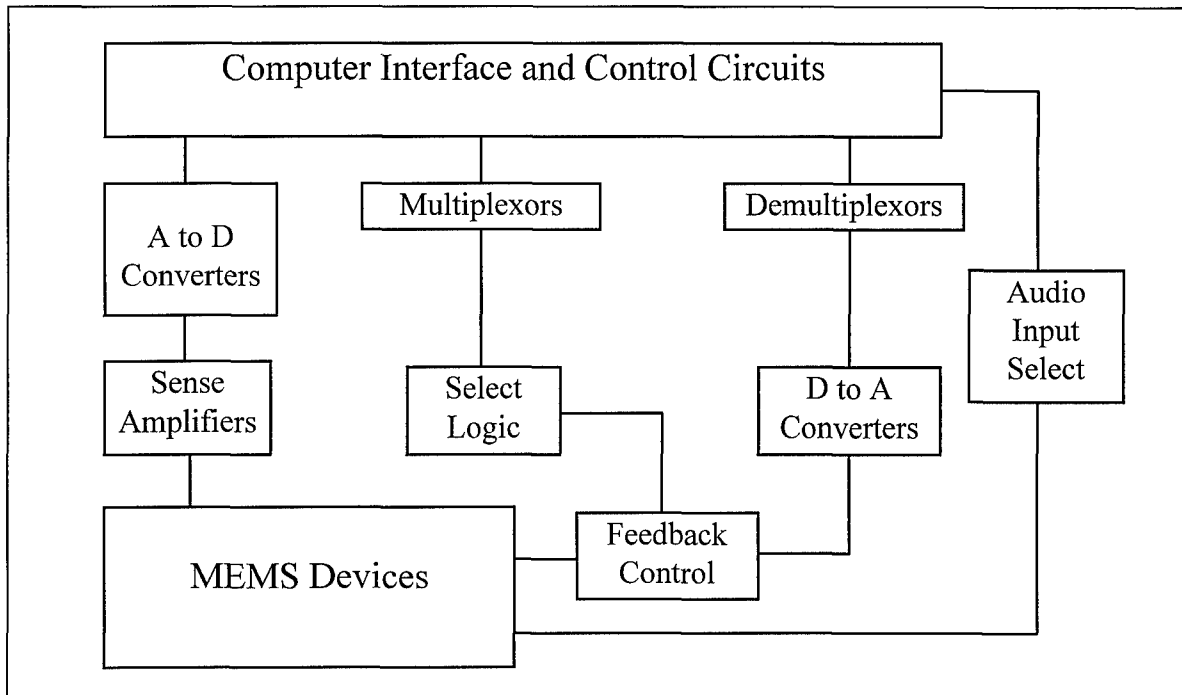
Figure 1-1 - Artificial cochlea overall block diagram. The design of the artificial cochlea implemented using MEMS and controlled by a microprocessor is depicted. The MEMS devices are auditory range tunable resonators. They are driven and sensed under supervision of a control program residing in the processor's main memory.

1.4.1.3 MEMS Control Circuitry

The MEMS control circuitry consists of the select logic, sense amplifiers, and feedback control. SmartMUMPs [6], which combines MEMS with the appropriate drive and sense circuitry, is being considered, since the signal coming from the MEMS chip will already be conditioned.

This allows the use of discrete components on the computer circuit card. However, the SmartMUMPs chip, as delivered, is not vacuum packed, and must be operated from within a vacuum chamber. Another option considered, is a vacuum packed multi-chip module, with MEMS and VLSI die combined. This has the advantage of providing a large number of resonators along with the associated drive/sense logic on a single chip that can be placed on an ordinary circuit card.

The purpose of the MEMS control circuit is to control the individual MEMS devices. Each MEMS device requires a separate sense amplifier and feedback control circuit. Figure 1-2 shows the overall block diagram for this circuit. The cantilever is driven by the Feedback Control Circuit. At resonance, the cantilever has maximum deflection, and the signal sensed is also at its maximum level. This sensed signal is amplified and sent off the chip to an analog to digital converter, and to the processor. The select logic enables one sense/feedback pair at a time under the direction of the control program.

The control program decides when to apply the feedback signal. The audio signal is applied to all cantilevers simultaneously. When the control

program requires, feedback is used to dampen the oscillations of the

individual cantilevers. This can be accomplished by applying the sensed
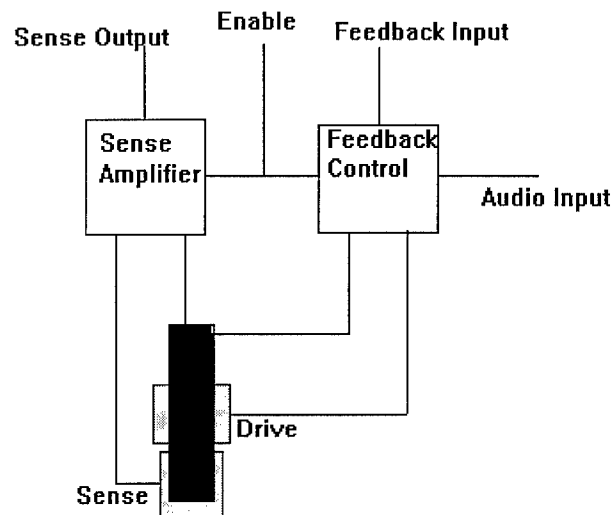
Figure 1-2 - Sense Amplifier and Feedback Control block diagram. Top view of cantilever being driven by the feedback control block, with output being sensed by the sense amplifier.

signal back into the drive 180° out of phase (inverted), effectively nullifying

the original drive signal. The sense signal can also be fed back in phase,

increasing the drive on the cantilevers.

A simpler, more efficient way to do this, is to instead apply and vary

a DC bias. By changing the DC drive, both the amplitude and resonant

center frequency of the MEMS can be varied. This, in effect, simulates

what is believed to be the function of the outer hair cells of the cochlea.

The control program, by applying a DC drive across the MEMS devices, simulates a stiffening of the cochlea's basilar membrane. This is due to the changes in the spring constant, k, used in the frequency equation due to added tension in the MEMS devices caused by the DC drive component, thus changing the MEMS resonant frequency.

1.4.1.4 MEMS Description

Cantilever, bridge, interdigitated finger (comb), and mirror type resonators are considered for the MEMS devices. As stated earlier, SmartMUMPs, one of the processes used to implement the MEMS devices, enables the output of the MEMS to be sensed and amplified on chip [6]. This reduces the signal loss, enabling small changes in capacitance to be sensed. The SmartMUMPs process is discussed in detail in the next Chapter.

1.4.1.5 Software Design Description

The control program acts as the master controller for the artificial cochlea, in an attempt to simulate the way we currently believe the human brain controls the cochlea. This software, as described, plots the audio signal along with the data from the individual MEMS, so that real time

comparisons with preprogrammed physiological data can be made.

1.5 Plan of Development

This thesis is broken down into six chapters. The first was a general overview of the problem, and an approach to the solution to the problem. Chapter 2 begins with a discussion of the cochlea, and how the cochlea functions within the auditory system, with an emphasis on cochlea modeling. It then describes MEMS design and fabrication details. Chapter 3 presents the theory behind designing an artificial cochlea using MEMS devices. Furthermore, it explains how a desktop computer can be used to act as the controller for the artificial cochlea, much in the same way the brain controls the living cochlea. Chapter 4 describes the setup and testing of the individual MEMS devices, as well as the overall artificial cochlea. Chapter 5 contains the results of the tests detailed in Chapter 4. Lastly, the conclusions and recommendations for future work are presented in Chapter 6.

Chapter 2

2. Literature Review

This Chapter is an overview of pertinent research previously accomplished. First, a presentation of cochlear mechanics and models is provided, followed by a discussion of the design and fabrication of MEMS.

2.1 The Cochlea

The way that the cochlea interfaces the outside world with our brain, enabling us to hear, has been studied since the turn of the century. To understand how something as complex as the cochlea functions, it must be first transformed into something easier to understand. To that end, many models have been attempted.

2.1.1 Background

The cochlea is an integral part of the mammalian auditory system. Located in the inner ear, this spiral shaped component, similar in shape to a snail (Figure 2-1), plays a major role in converting sound into electrical signals the brain can understand. It does this through a complex system of

hair cells that connect to neurons linking the brain with the auditory system.

These hair cells number over 25,000 with each transmitting and receiving
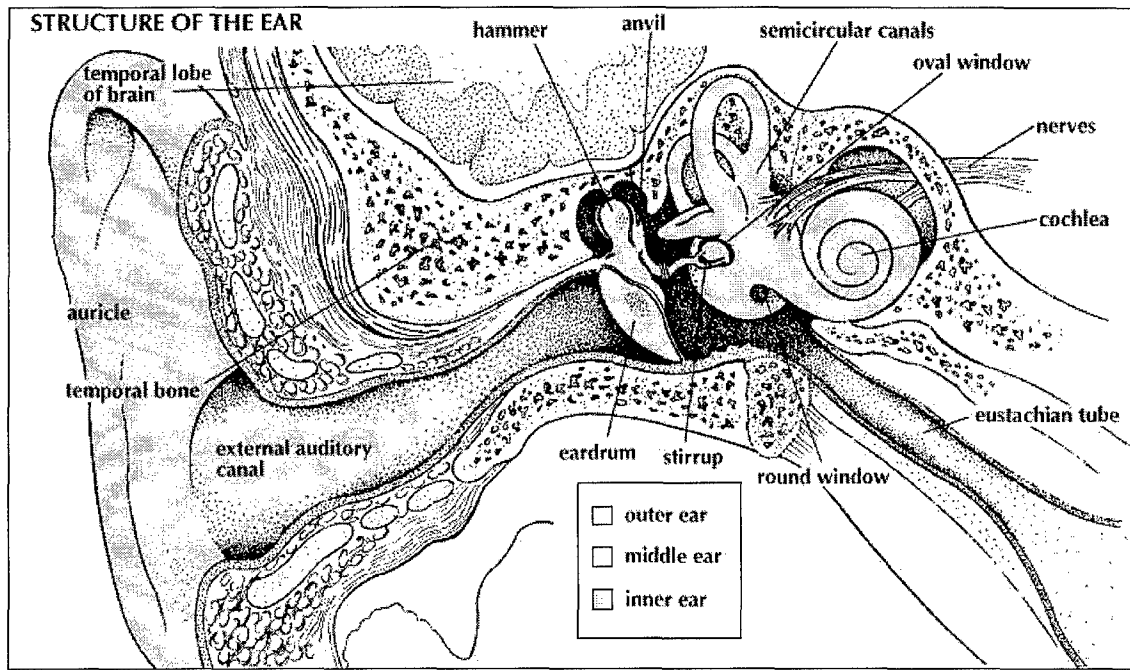
Figure 2-1 - The human auditory system. The location and physical description of the cochlea inside the auditory system [7].

electrical signals to and from the brain. The bundled hair cells are sensitive

to motion of the basilar membrane (BM) caused by the incoming sound

source (Figure 2-2). When in motion, the hair cells generate electrical

signals. The signals sent to the brain are the converted pressure waves

caused by sound. Signals are also received from the brain to control the hair

cells [8]. This, effectively, is a highly complex control system.

Physically, the cochlea is a fluid-filled device divided into three

partitions as shown in Figure 2-3: the scala vestibuli, the scala tympani, and

the scala media [9-11]. The basilar membrane is located between the

Negative displacement   Resting position   Positive displacement
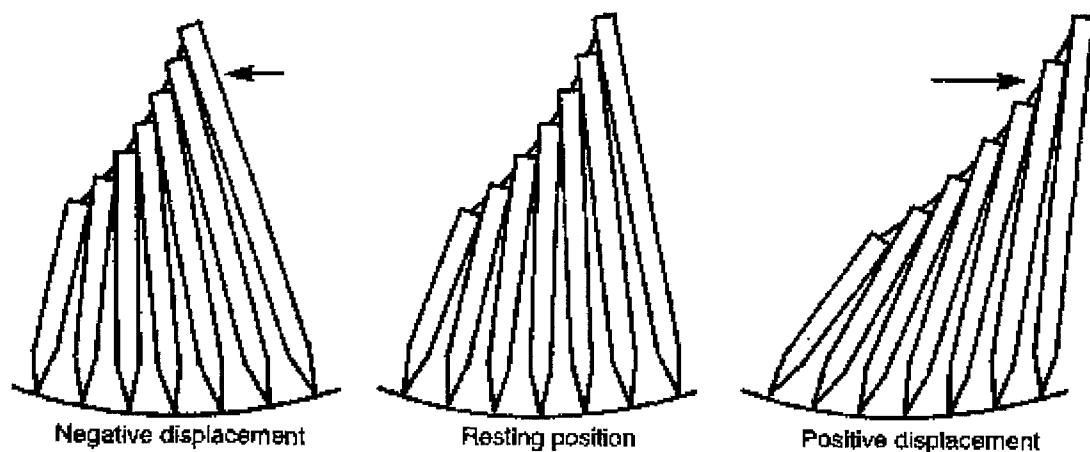
Figure 2-2 - Movement of hair cells. Sound traveling on the basilar membrane (BM) causes hair cells to be displaced. Outer hair cells, controlled by electrical stimulus from the brain, alter the effect that the sound has on the BM [8].

scala media and scala tympani. The inner and outer hair cells lie above the

basilar membrane. There are approximately three times as many outer hair

cells as there are inner hair cells. The hair cells are connected to nerve

fibers that transmit signals to and from the brain. Hair cells are columnar or

flasked shape, as shown in Figure 2-4, and produce electrical signals when

moved.
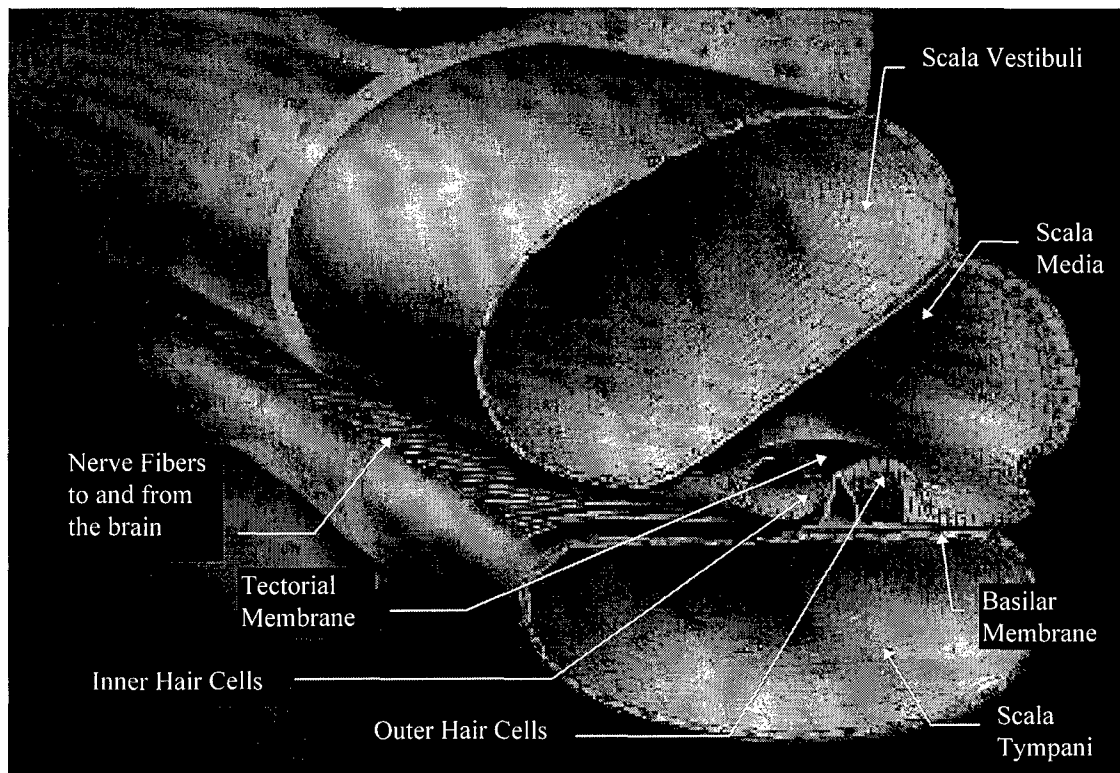
Figure 2-3 - The human cochlea. Cross-sectional view of the human cochlea showing the major components [7].
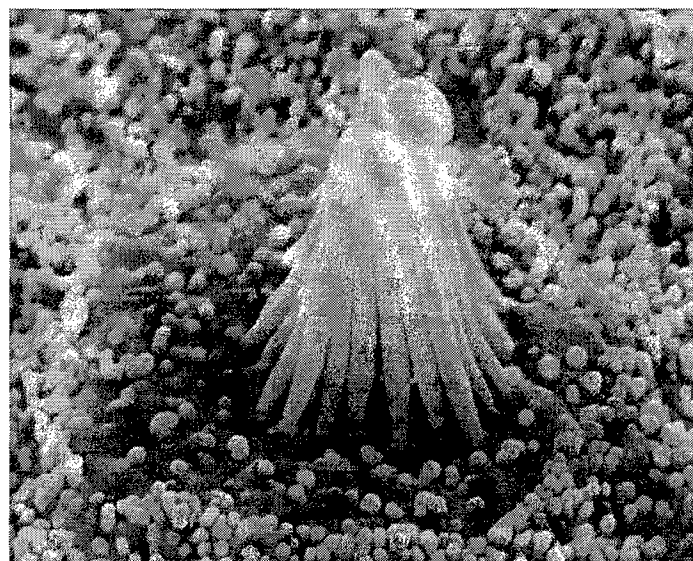
Figure 2-4 - Hair cell from a frog's sacculus. Movement of the bundle towards the tall edge excites the cell [8].

The three cochlea partitions work in conjunction with the rest of the auditory system to enable a human to hear frequencies from approximately 20 Hz to about 20,000 Hz with such acuity that, at some frequencies, a 1 Hz change can be distinguished [10]. The partitions also provide automatic gain control, that is, controlling the volume of the input sound [9-12]. That is why we can hear a pin drop when it is quiet, and conversely, are not deafened when a train passes.
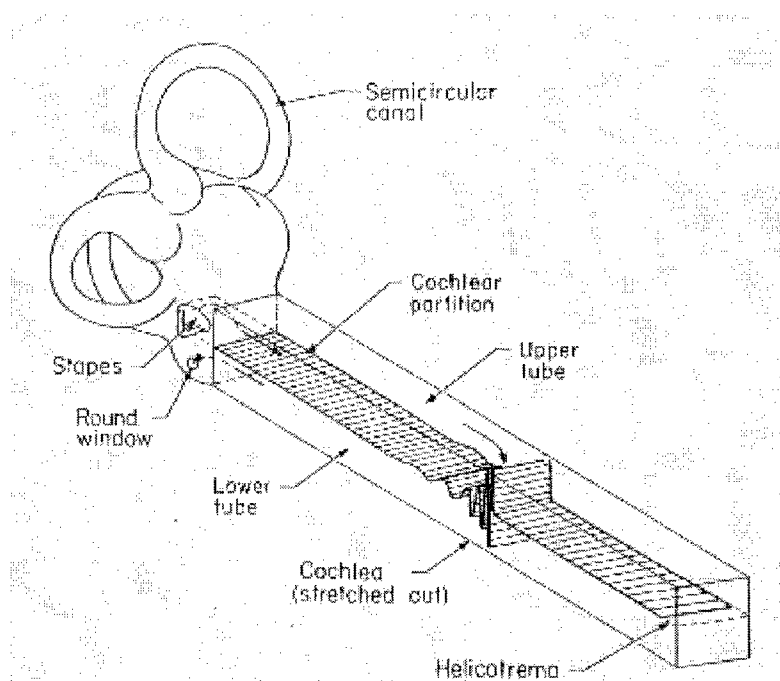
Figure 2-5 - Simplified cochlear model. Traveling wave on the basilar membrane [10].

Before the cochlea receives the sound to be processed, it is first preprocessed by the outer ear. This begins when sound enters the ear,

causing the eardrum to vibrate. The eardrum is connected to a series of tiny bones that transfer the sound to the base of the cochlea. Sound enters the cochlea through a small opening called the oval window. It travels down the scalar vestibuli and afterward out through the scalar tympani. Between these lies the basilar membrane. Sound causes the BM to vibrate, with maximum displacement at points along the membrane that are sensitive to specific frequencies present in the incoming sound. These points of maximum displacement correspond to the resonance frequency of the particular section of the BM. This is shown in the simplified model of the cochlea in Figure 2-5. Each point on the BM has an associated frequency that causes maximum displacement.

Figure 2-6 shows the innerworkings of the cochlea. Each inner hair cell senses the motion of the BM and reports the motion for its particular location to the brain via afferent synapses. Synapses, connections between the nerve fibers and the hair cells, when excited release a chemical neurotransmitter generating electrical signals that travel to the brain by way of nerve fibers [8]. The brain, can control the movement of the BM section by sending signals to the outer hair cells via the efferent nerve fibers.
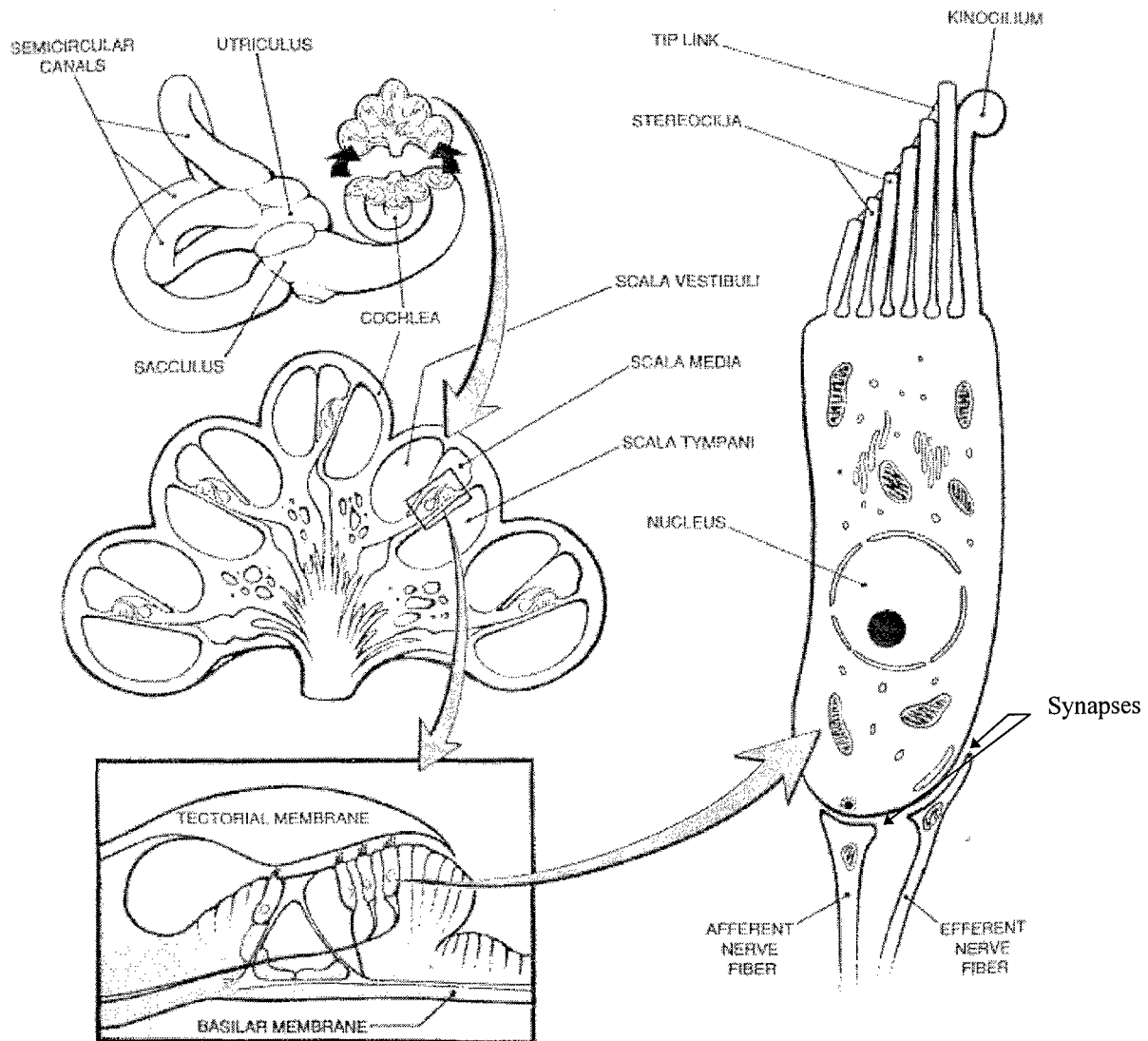
Figure 2-6 - Detailed illustration of the innerworkings of the cochlea [8].

2.1.2 Cochlear Modeling

Essentially the cochlea can be modeled as a transmission line, or a

dynamic series-parallel resonant circuit as shown in Figure 2-7. Each

cochlear section acts analogous to a resonant circuit. The system, however

is non-linear, and difficult to model exactly. As stated earlier, research in

this area has a relatively short history. Mathematical models can be dated

back to the 1930's. Since the 1950's, many analog models were devised.

The first VLSI implementation of an analog cochlea model, by Lyon and

Mead, occurred in 1988 [2].

Since then, several improved versions have been synthesized. The

first, by Watts, Kerns, and Lyon used the experience gained with the
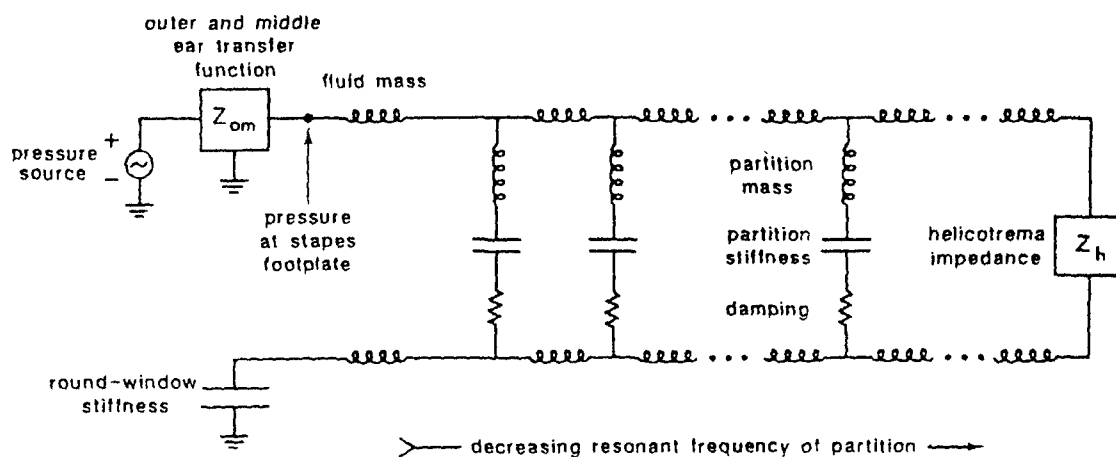
Figure 2-7 - Cochlear equivalent electrical circuit. The cochlea can be modeled as a series of tuned RLC tank circuits. Between each subsequent stage is an inductor representing the fluid mass. Each stage represents a specific point on the basilar membrane with its unique resonance frequency [10].

original silicon cochlea to further address dynamic range, stability, device

mismatch, and compactness issues [13]. The VLSI analog cochlea model

was used by others to address diverse issues, such as binaural hearing [5],

speech representation [4], and speaker recognition [9]. The latest design uses switched-capacitors to implement the analog cochlea, thus decreasing the size while at the same time increasing the frequency response and dynamic range [14].

2.1.2.1 Early Artificial Cochlea Design

Models of the cochlea have been conceptualized for almost a century. Georg Von Békésy, known for his experiments on the cochleae of cadavers in the early 1930's and later receiving a Noble Prize in Physiology and Medicine in 1961 for this work, created the first cochlear model. He constructed a hydraulic working model of the cochlea using the data from his experiments [15]. The data he obtained, however, were inaccurate. We know now that cochlea is an active device, controlled by the brain. Since the brain of all his subjects had ceased to function, so had the ability of the cochleae to respond appropriately to the stimulus he provided.

Implementing models and comparing them to nature is a time honored practice of learning and maintaining forward progress. Early cochlear models, while now obsolete, provided others with a window into the problems associated with copying Nature.

Von Békésy's experiments and observations, while fundamentally flawed, were a giant step in the field of auditory research. Stewart's analog cochlea [1] was one of the first in a series of implemented models that helped to further the thinking on the subject. Many other attempts at unlocking the secrets of the auditory system have brought us to where we are today, and it will probably take many more attempts to realize the goal.

2.1.2.2 *Mathematical Models of the Cochlea*

As knowledge in the field has increased, many other models have been proposed [17-27].

In one such model, "Mathematical Models of the Cochlea" [20], Neeley describes the macromechanics and micromechanics of the cochlea. Cochlea macromechanics is chiefly concerned with the inertial properties of the cochlear fluid, and the pressure distribution thereof. Cochlear micromechanics looks at the cross-section of the BM, defining it in terms of lumped mass, stiffness, and damping at selected positions along the partition.

Early cochlear macromechanics reduced to finding the pressure differences in a rectangular box [20]. This is possible due to several

assumptions: The cochlear fluid is incompressible, the spiral shape is not significant, and the upper and lower channels are geometrically symmetric.

In discussing cochlear micromechanics, Neely observes the distinction between the postmortem and living cochlear mechanics, citing the term "cochlear amplifier," which he attributes to Davis [27]. The "cochlear amplifier" refers to the fact that BM displacements are sharply tuned, and respond roughly as depicted in Figure 2-11, the tuning curve of a cat [20].

The results of the model are depicted in Figure 2-8. In the model M_1, R_1, and K_1 are the lumped mass, damping, and stiffness of the BM, respectively. The interesting point of this model is the use of the term γ in the outer hair cell (OHC) filter section. He describes this dimensionless parameter as "the necessary transduction to and from the electrochemical domain ...."

The following year, Neely refined his model, spending more time comparing his model to actual experimental evidence [23]. This comparison included physiologic data compiled for squirrel monkeys and

fluid
force +

BM filter

$$\frac{1}{K_1 + R_1 i\omega + M_1 (i\omega)^2}$$

BM
displacement

IHC

OHC
force

OHC filter

$$\frac{\gamma K_3}{K_2 + R_2 i\omega + M_2 (i\omega)^2}$$

cochlear fluid
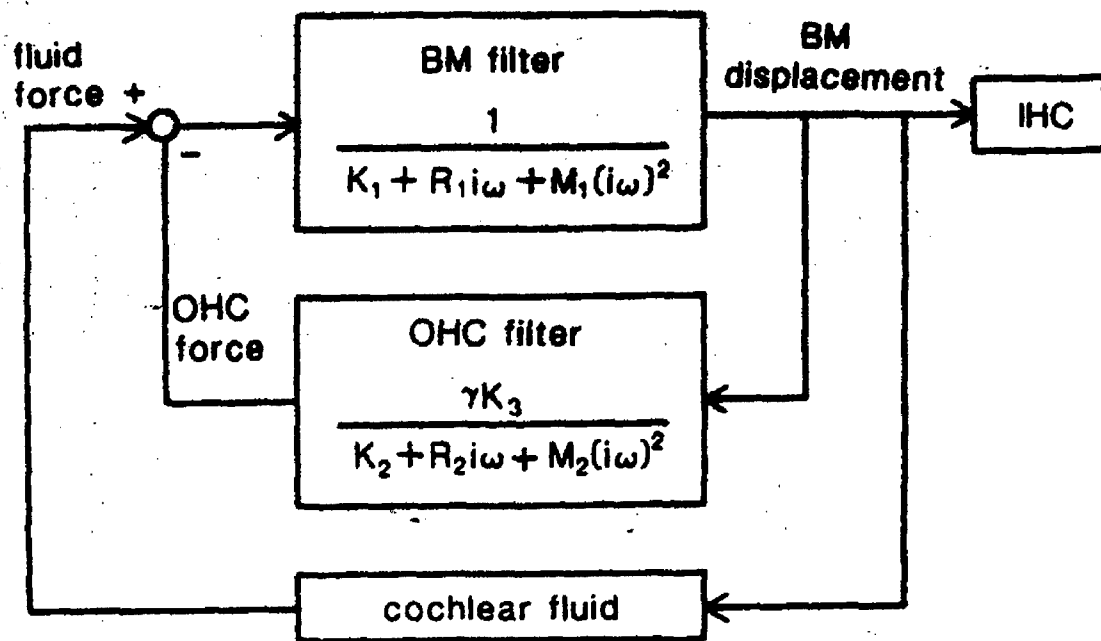
Figure 2-8 - Neely model of the cochlea. Complex feedback from the outer hair cells is applied back to the basilar membrane to tune the cochlea [20].

guinea pigs using Mössbauer techniques. The Mössbauer technique uses Doppler-shifted gamma rays to detect movement of a small radiation source mounted on the cochlear partition [2]. Using this technique, a progressive decline in the sensitivity and sharpness of tuning as the condition of the animal deteriorated was shown [23]. Also discussed is the generation of spontaneous octoacoustic emissions (sounds emanating from the ear), which is attributed to excessive gain in the cochlea amplifier.

2.1.2.3 Time Domain Digital Cochlear Model

One of the most recent, and most comprehensive models, is Kates's "Time Domain Digital Cochlear Model" [25-26]. He uses a Modified Transmission Line (MTL) approach, shown in Figure 2-9, to model the individual sections of the BM. Similar to the Analog Cochlea proposed by Lyon and Mead [2], Kates focuses on adjusting the Q of each cochlear section by changing the damping of the particular section. This is accomplished by applying complex feedback to the filter sections.
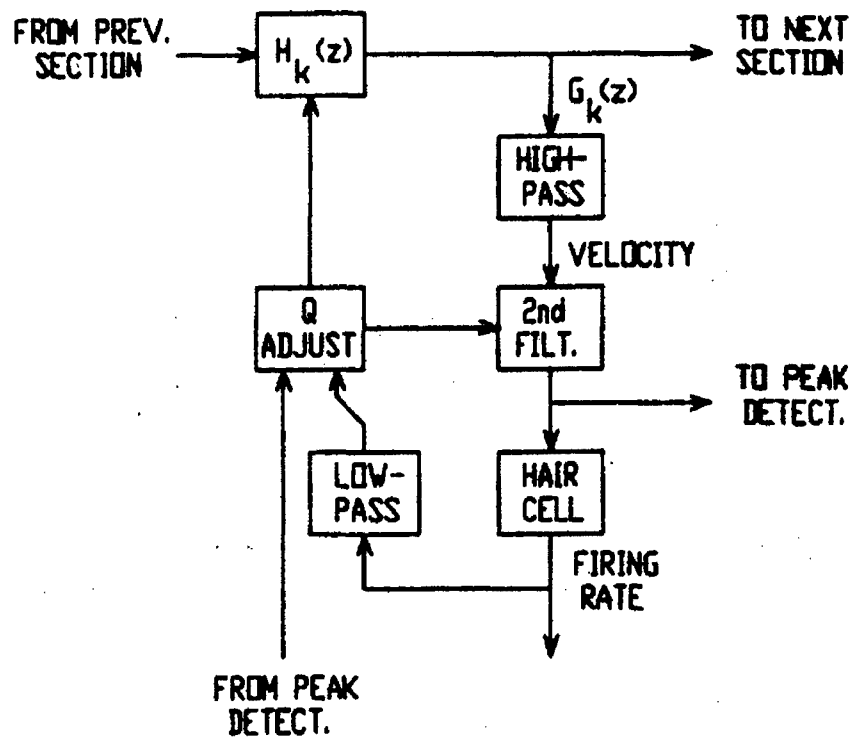
Figure 2-9 - Block diagram of the Kate's model. A section of the BM is described as two filter sections, each with variable Q, controlled by complex feedback [26].

Figure 2-10 shows a set of frequency response curves for the Kate's

MTL model. The magnitude response curves are inverted compared to

physiological data. For example,

Figure 2-11 shows a sampling of tuning curves from a cat's cochlea [28].

These curves, similar to tuning curves of other animals, are described by

Kates as having a narrow but rounded peak at the characteristic frequency, a

very steep high-frequency slope, a response zero about one octave below

the peak, and a flat tail extending to the low-frequency cutoff [26].

Magnitude
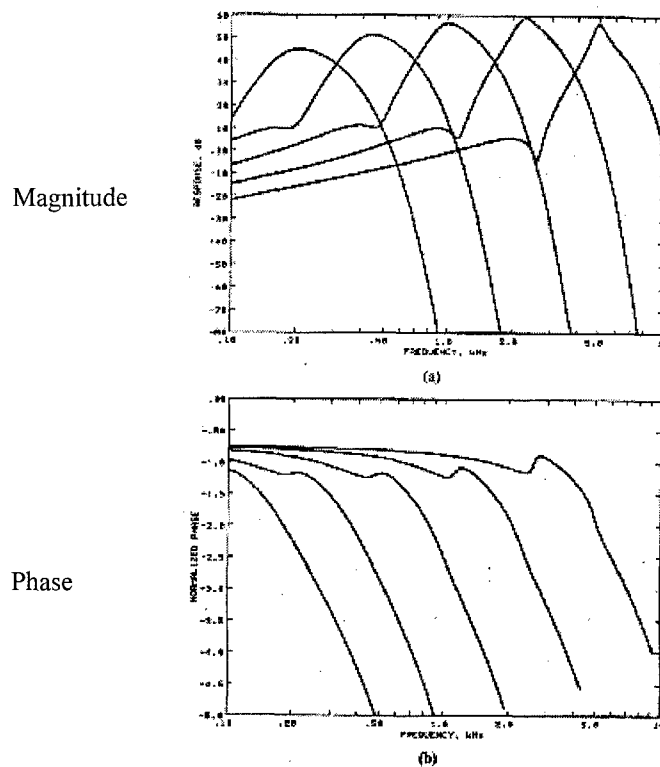
Phase

Figure 2-10 -- Cochlear tuning curves for Kates model (a) Gain vs. frequency (b) Phase vs. frequency [26].

It is difficult to find live human cochlea donors to experiment on, but according to Kates, a human cochlear tuning curve can be approximated by dividing the frequencies by three based on the mechanical properties of human and feline cochleae [26]. The normal cat auditory range is approximately 96 Hz to 60 KHz. Dividing by three yields 32 Hz to 20 KHz.
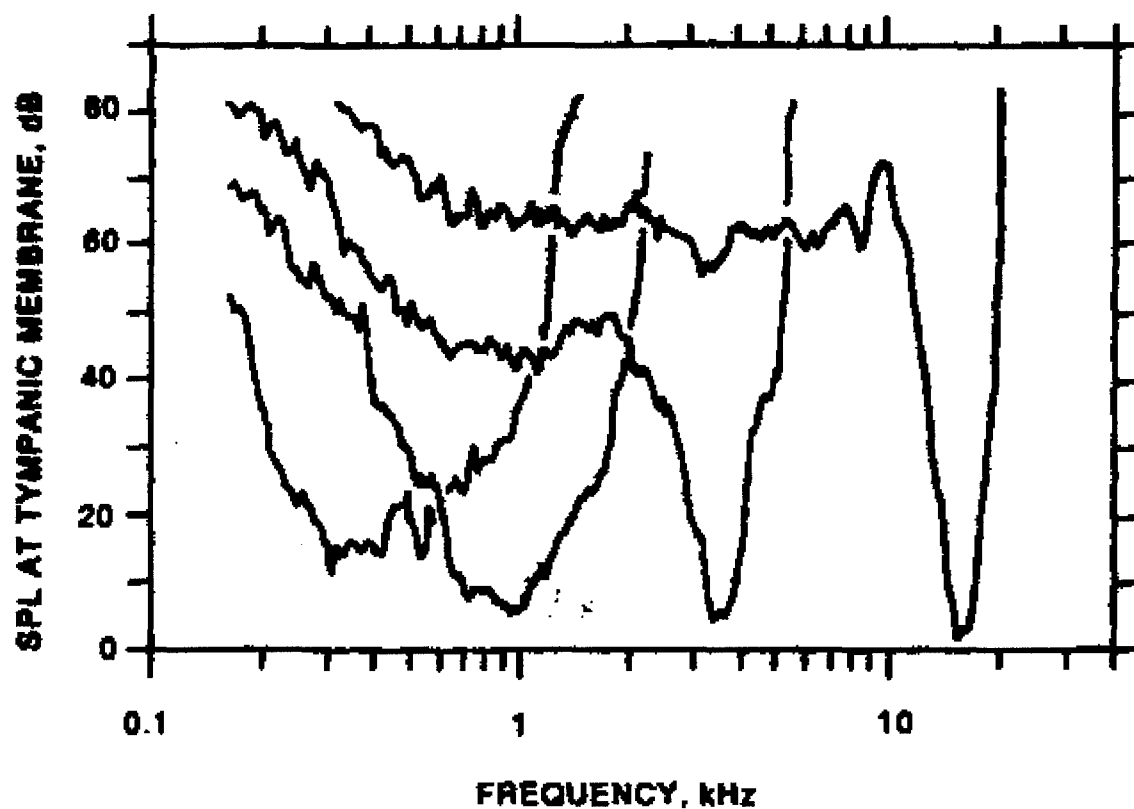
Figure 2-11 - Tuning curve of a cat's cochlea [28].

A frequency to place mapping is performed assuming a normalized cochlear distance, from apex to base, $0 \leq x \leq 1$, using [25]:

$$f(x) = 160 \cdot (10^{2.1x} - 0.8) \qquad (2\text{-}1)$$

Knowing that the higher frequencies cause vibrations on the BM closest to the stapes [20], this equation shows the highest frequency, 20 KHz, is sensed on the BM at the entry to the cochlea, such that when x = 1, f(x) = 20000 Hz. The greater the distance traveled along the BM away from the stapes/oval window, toward the helicotrema, the lower the frequency sensed.

2.1.2.4 VLSI Implementations of the Artificial Cochlea

Lyon and Mead developed the first VLSI implementation of an analog electric cochlea in 1988 [2]. They intended to incorporate as much of the current knowledge and function into the device, while at the same time keeping the device simple. By this time, it was clear that the cochlea was an active device. They refer to experiments performed on chinchillas where spontaneous acoustic emission could be heard for several meters. These emissions are caused by physical oscillations on the BM not induced by incoming sound. Tinnitus, or ringing in the ears, is caused by the same non-induced oscillation. The explanation of these oscillations is that the

Automatic Gain Control (AGC) is out of alignment. More positive feedback is applied than actually required thus causing oscillation. Lyon and Mead go on to suggest that the outer hair cells are muscles that pump mechanical energy into the BM, reducing the damping, thereby changing the Q of the cochlea.

To implement the "silicon cochlea", Lyon and Mead used cascaded stages of transconductance amplifiers (TZA) [2]. Each stage representing a tap along the BM, and a first order system of wave propagation. Each TZA implemented a low-pass filter section. A delay element was also added to approximate the second order system of fluid mass and membrane stiffness. This second order system controls the quality factor (Q) and delay (τ) of each stage. In all, 480 stages were used, each stage was set to be slower than its predecessor.

Four years later the original model was improved to capture more of the finer detail of an actual living cochlea [13]. To increase the dynamic range of the transconductance amplifiers, source degradation was inserted with the addition of diodes. Large-signal instability was eliminated by changing the types of amplifiers used in the second order section. Also,
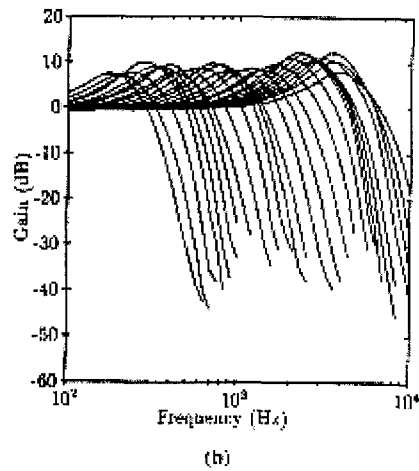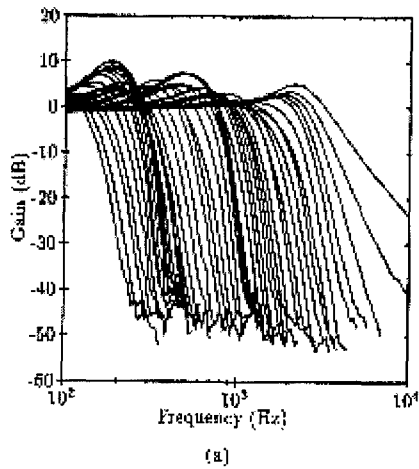
Figure 2-12 - Frequency response curves of the VLSI implementations of the analog cochlea. (a) Original Lyon-Mead cochlea (b) Improved cochlea [13].

small change on the Q control circuitry enabled better Q control. Figure 2-

12 and Figure 2-13 show comparisons of the frequency response and Q

factor profiles of the silicon cochlea before and after the changes.
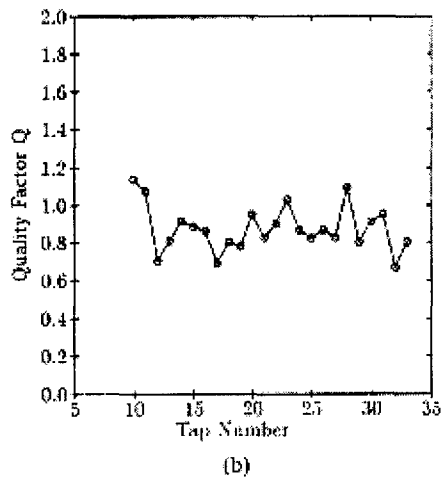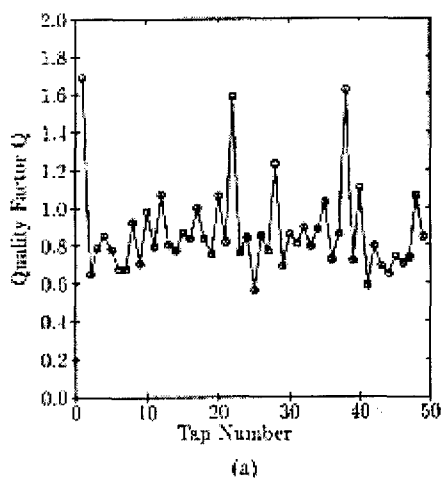
Figure 2-13 - Quality factor profiles of the VLSI implementations of the analog cochlea. (a) Original Lyon-Mead cochlea (b) Improved cochlea [13].

2.1.2.5 Switched Capacitor Artificial Cochlea

A recently proposed model by Bor and Wu [14] is based upon

Zwislocki's 1950 transmission line model [29]. By using switched

(a)
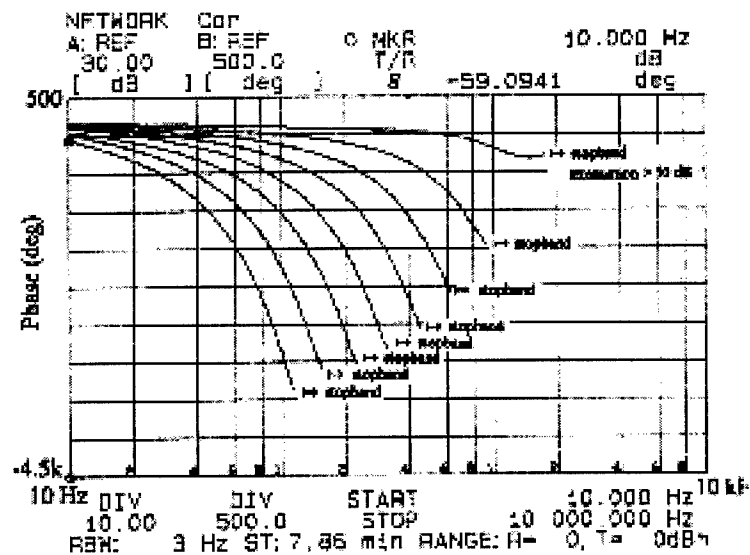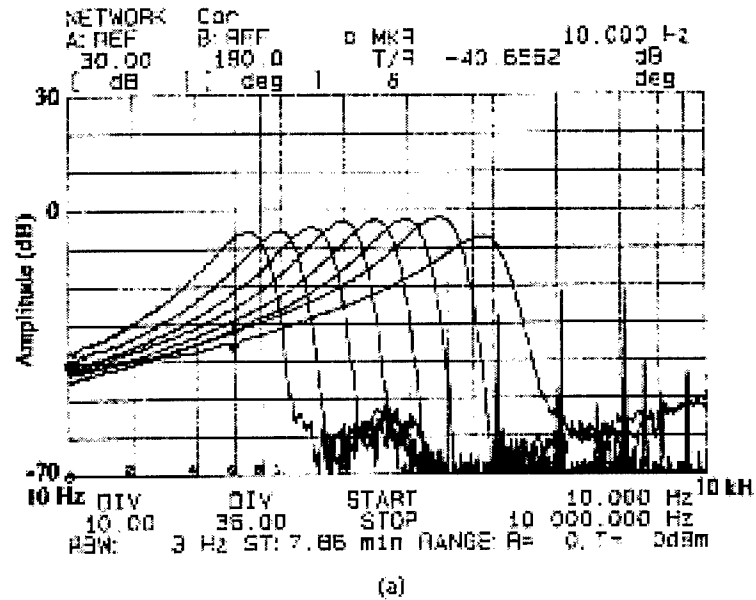
Figure 2-14 - Frequency response of the Switched Capacitor Cochlea [14].

capacitors, the required number of low-order filter stages is decreased. The trade off however, is the increased complexity of controlling multiple clocks, and the losses associated with clocking in general. The resultant waveforms (Figure 2-14) are similar to that of the Lyon-Mead cochlea.

2.1.3 Cochlea Model Summary

The models presented are representative of the current state of cochlear modeling. There are many other models, each with its own slant, but for the scope of this thesis the presented models are sufficient. Each of the models has the same general approach. Break the cochlea into sections, model each section, and put the sections together in a system. The modern implementations all use electronic components, some using large scale integration, to implement the individual sections and overall system.

Two major problems exist in the previously discussed models. First, none of the models, theoretical or implemented, can detect a 1 Hz change in frequency. This is because all the tuning curves presented are fairly broad, even though they are referred to as "high Q." The other problem is the complexity of the feedback required to tune the various sections. The suggested dampening of the BM by complex AC signals is difficult to

implement, and possibly an inaccurate representation of the actual workings of the cochlea.

To achieve truly "high Q" resonators, a different technology must be used. The next section reviews a new technology that is perfect for the job, Micro-Electro-Mechanical Systems (MEMS).

2.2 MEMS Design
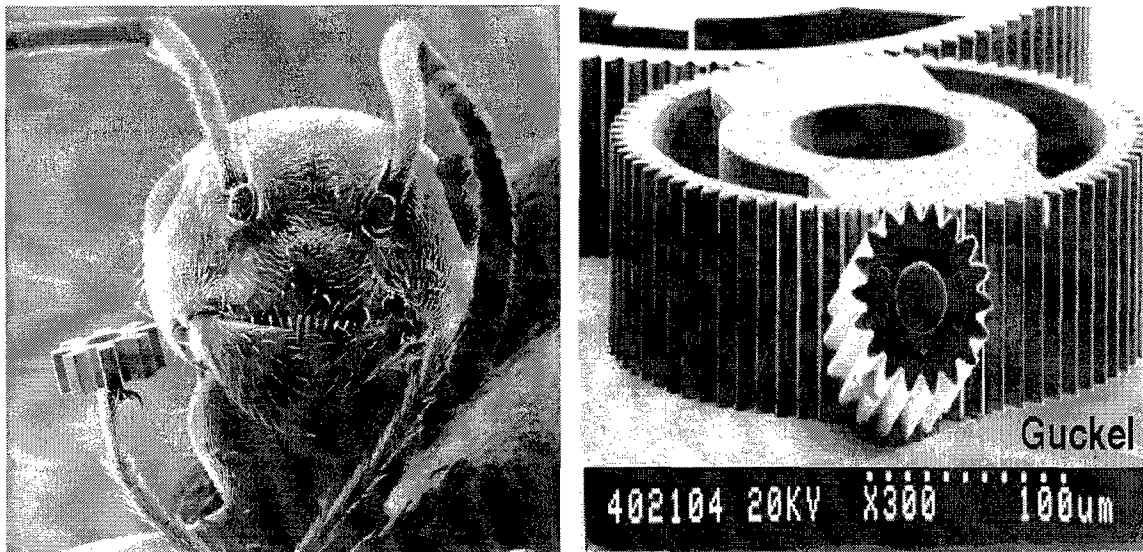
Figure 2-15 - Size of MEMS devices. Left - A size comparison of a real ant holding a miniature gear. Right - More miniature gears [30].

2.2.1 Introduction to MEMS

Miniaturization is the wave of the future. The semiconductor industry, and their customers, have been chanting "Smaller, faster, cheaper" for the past three decades. Now, the technology exists to design and

construct microscopic mechanical devices using similar technologies.

Micro-Electro-Mechanical Systems (MEMS), are miniature electro-mechanical devices, that are typically actuated by electrostatic or current means. MEMS can be used to construct simple mechanical structures, like the gears in Figure 2-15, or more complex electromechanical devices. Of these electromechanical devices, cantilevers and bridges are the most likely candidates for the numerous controlled resonance circuits required to emulate a complex wave on the BM. Similar in function to sections of the BM, these structures vibrate when signals are applied. Design of these structures implemented in MEMS has been studied in-depth [3, 32-47]. Microphones can also be implemented using MEMS, and their use has also been the subject of much research [40,48-52]. Other devices that may be used to act as resonators, or assist in the development of an artificial cochlea, include mirrors [3], thermal devices [53-59], voltage referencing devices [59], and microswitches [60].

2.2.2 MEMS Overview
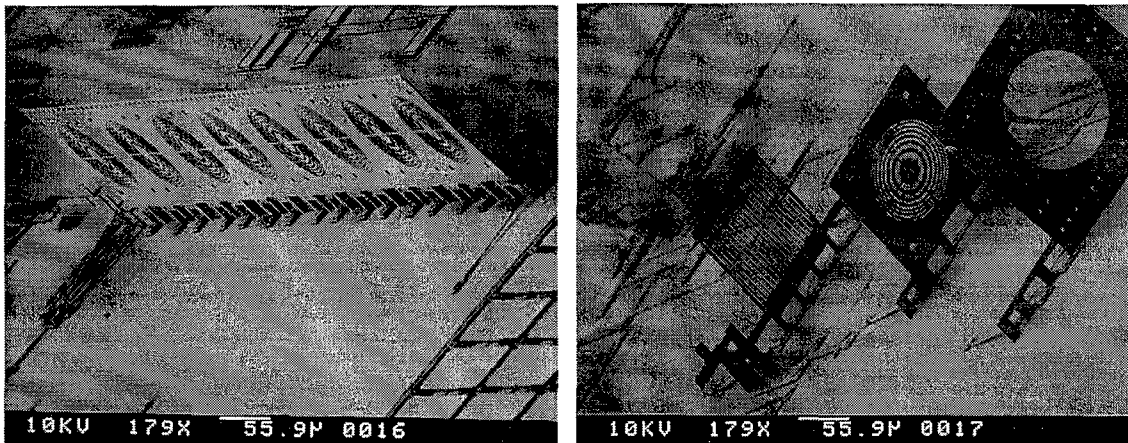
Figure 2-16 - Examples of MEMS Devices: Pop-up Fresnel lenses are just one example of the utility of MEMS [3].

MEMS can be used to implement a variety of miniature mechanical and electromechanical devices at the microscopic level. Actuators, lenses, resonators, steerable mirrors, and many other devices can be implemented. Figures 2-16 and 2-17 illustrate the utility of MEMS.
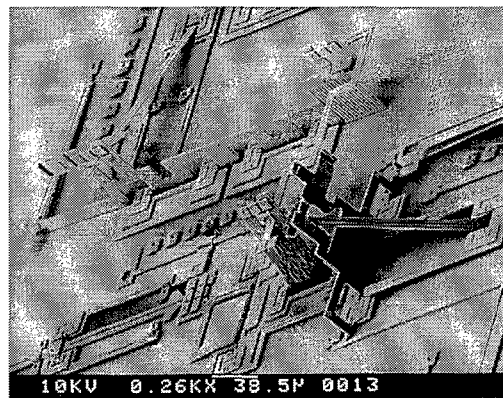
Figure 2-17 - Locking pop-up hinged structures allow operation of devices perpendicular to a die [3].

MEMS design can be implemented in MAGIC, Cadence (Figure 2-18), and many other Computer Aided Design tools. The output from these tools is a CalTech Intermediate File (CIF), which is sent to the fabrication facility.

Figure 2-18 - Design of MEMS using Cadence [3].

2.2.3 MEMS Fabrication

This section presents the options available for implementing MEMS devices. The capabilities and limitations of the two leading general purpose MEMS foundries are discussed, followed by a presentation of the process used for the devices implemented for this thesis.

2.2.3.1 MEMS Fabrication Overview
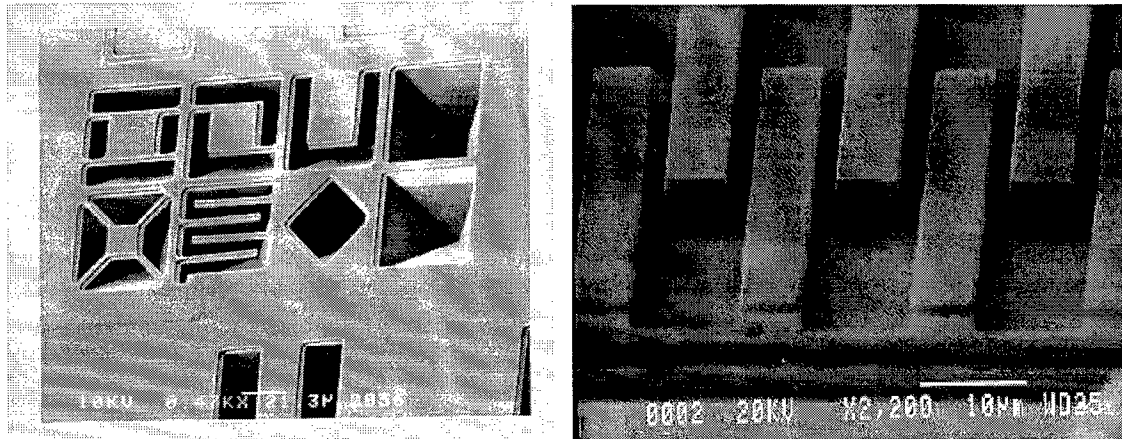
Figure 2-19 - Cantilevers and other MEMS devices. The devices on the left were fabricated using the MOSIS process. The devices on the right were fabricated using the MUMPs process [61].

Two of the commercial foundry alternatives for MEMS implementation are the Multi-User MEMS Processes (MUMPs) [6,62] and the Metal Oxide Semiconductor Implementation Service (MOSIS) [41,63-64]. Using the MUMPs process enables the designer to create highly complex mechanical structures, but this process is not adequate for on-chip electronic circuit design. On the other hand, MOSIS is excellent for circuit design, but limited in MEMS design. Figure 2-19 shows products of these two processes. SmartMUMPs is a new process that combines features of both [6].

2.2.3.2 Introduction to SmartMUMPs

The MCNC Multi-User MEMS Processes (MUMPs), supported by the Advanced Research Projects Agency (ARPA), is a low cost fabrication program for use by industry, government, and academia. MUMPs is excellent for the construction of MEMS devices, but is very limited in circuit design. MCNC's SmartMUMPs [6] is a new process, which combines MEMS with the electronics to drive and sense these devices.

Another alternative for the production of MEMS is the MOSIS process. While MOSIS is an excellent facility for producing CMOS VLSI designs, it is lacking in MEMS design.

Figure 2-20 shows examples of MEMS devices fabricated using MOSIS. Notice the curling of the beams. This is caused by residual stress in the released layers. Also, since there are only two polysilicon layers, three dimensional design is limited. MUMPs, however, with three polysilicon layers, allows for three dimensional design. It is however, not suited for CMOS design. The major reasons for this are:

- Highly doped substrate, making it conductive

- Uniformly doped substrate (no n or p-wells)

- Polysilicon, as deposited, has high residual stress, and must be annealed at temperatures greater than 1000°C after deposition. This is incompatible with CMOS, which requires temperatures less than 400°C.
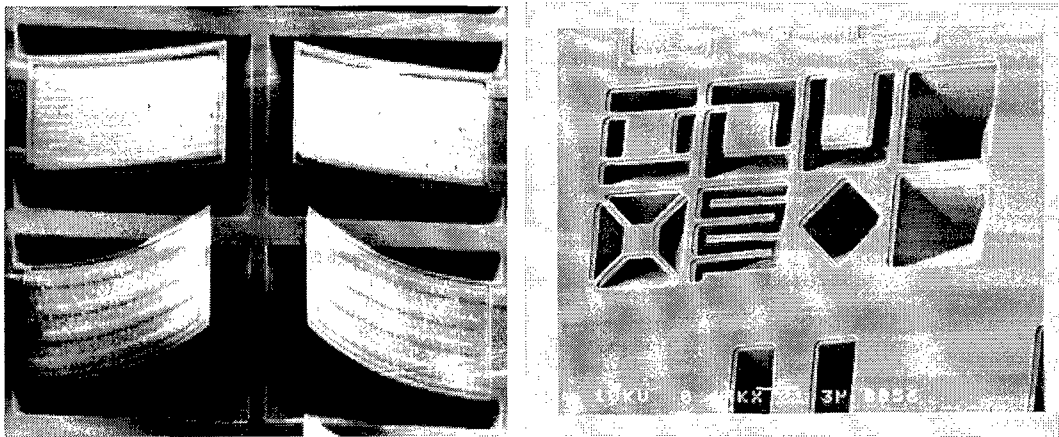
Figure 2-20 - MEMS designs using the MOSIS process. The beams (left) show the effects of residual stress in the polysilicon [6].

Since these processes are limited, designers were forced to use both. MUMPs for the MEMS devices, and MOSIS for the associated sense circuits. To help alleviate this, MCNC has introduced SmartMUMPs, which combines MEMS designs with a standard set of CMOS devices to drive and sense the MEMS. Since SmartMUMPs is an addition to MUMPs, the MUMPs process will be introduced first.

2.2.3.3 The MUMPs Process

The MUMPs process is a three-layer polysilicon surface micromachining process that has a total of seven layers over a substrate (Figure 2-21) [6]. The substrate is an n-type (100) silicon wafer heavily doped with phosphorous to reduce/prevent feed-through from electrostatic devices on the surface.

First a thin nitride layer is deposited over the substrate to provide electrical isolation. Then the first polysilicon layer, Poly0, is deposited and patterned. A phosphosilicate glass (PSG) is then deposited. This is called the "first oxide," and is one of the sacrificial layers that can be etched away. On top of this oxide, the next layer of polysilicon, Poly1, is deposited. Another layer of PSG follows, the "second oxide", along with one more layer of polysilicon, Poly2. The last layer deposited is the metal, usually gold. Table 2-1 shows the nominal thickness of each layer, and the associated masks.

After the last two layers of polysilicon are deposited, but before metal is deposited, the wafer is annealed at temperatures exceeding 1000°C for
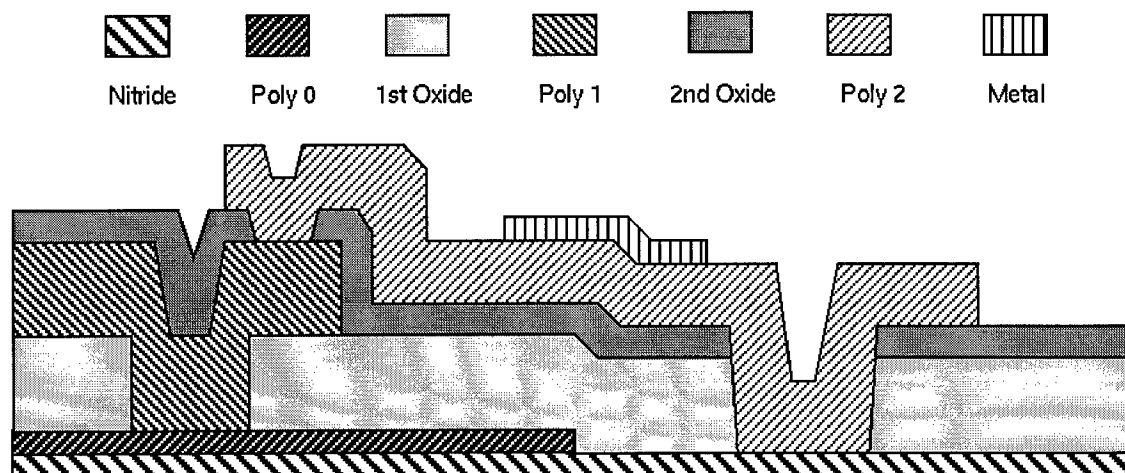
Figure 2-21 - Cross-sectional view of the seven layers of the MUMPs process. Various electro-mechanical devices can be implemented by patterning these seven layers [6]. (Drawing not to scale)

Table 2-1 - Layers of the MUMPs Process [6].

Material Layer	Thickness (microns)	Lithography Level Name
Nitride	**0.6**	**N/A**
Poly 0	**0.5**	**POLY0 (HOLE0)**
First Oxide	**2.0**	**ANCHOR1**
Poly 1	**2.0**	**POLY1 (HOLE1)**
Second Oxide	**0.75**	**POLY1_POLY2_VIA ANCHOR2**
Poly 2	**1.5**	**POLY2 (HOLE2)**
Metal	**0.5**	**METAL (HOLEM)**

one hour. This effectively dopes the polysilicon from surrounding PSG, and reduces residual stress.

After the metal layer is deposited, a coating of photoresist is applied

to protect the die during dicing and shipment. The die is released by

immersing it in a 49% by weight hydrofluoric acid (HF) solution. Normally

this is done by the participants in their own facilities, but can also be done

by MCNC for a fee.

2.2.3.3.1 Flip Chip Technology

The idea behind SmartMUMPs is to combine the MEMS devices with

some ability to sense and drive them. The VLSI chip, known as the Ecosys

chip, is soldered directly onto the MEMS chip using a fluxless soldering

technique called Plasma Assisted Dry Soldering (PADS). The MEMS chip
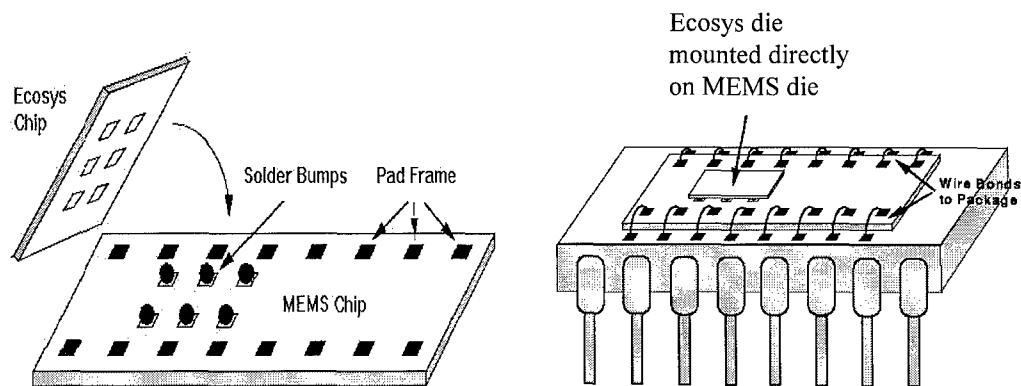
Figure 2-22 - SmartMUMPs packaging. The VLSI electronics chip (Ecosys chip) is soldered directly onto the MEMS chip, which is then wire bonded to a standard package [6].

is then wire bonded to a standard package. This process, illustrated in

Figure 2-22, minimizes the capacitive and inductive losses between the

MEMS and electronic devices. Thus, the performance of the combined

chips is greatly enhanced, and the size of the overall system reduced.
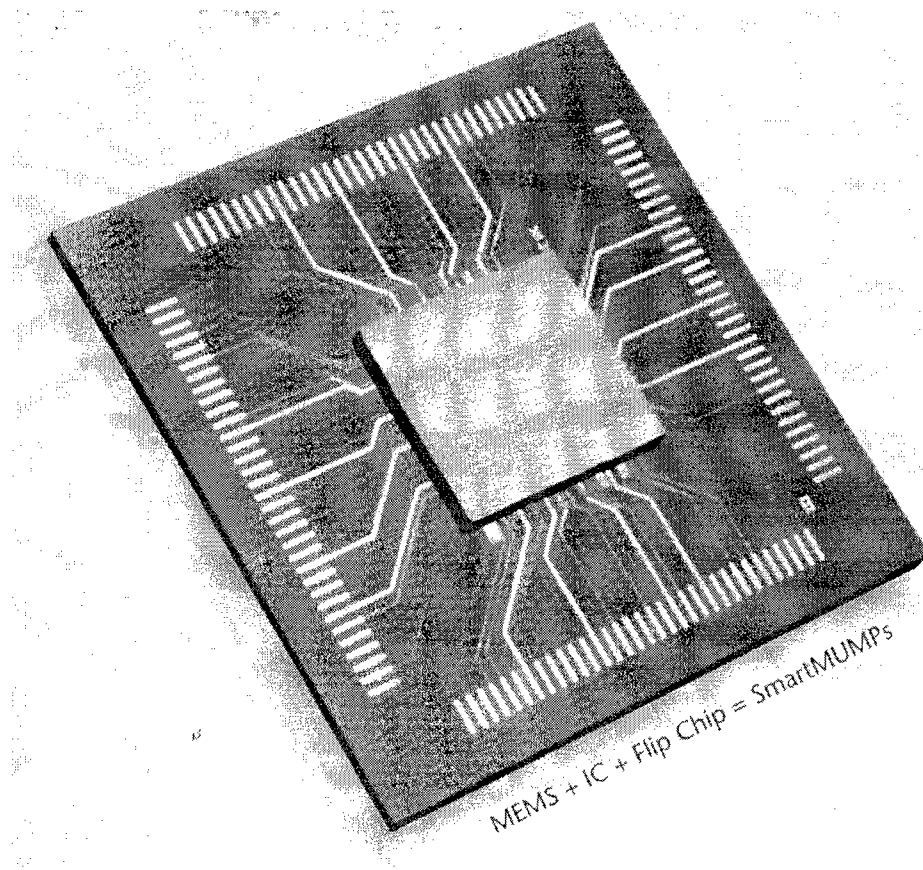
Figure 2-23 - Photograph of combined MEMS and ECOSYS chip before wire bonding to a standard package [6]. The ECOSYS chip is centered on the MEMS chip. The area of the MEMS chip underneath the Ecosys chip is available to place MEMS devices, but these devices can not be probed. There is typically a 60 μm gap between chips, which is enough clearance for most pop up devices, but any pop-up devices placed here would require activation outside the perimeter of the Ecosys chip.

Figure 2-23 depicts the actual combined chip before wire bonding. Notice that a large amount of space is "wasted" on the MEMS with wiring from the Ecosys chip to the outside pad frame.

2.2.3.3.2 The Electromechanical Control System ASIC (Ecosys)

The Ecosys chip puts the Smart into SmartMUMPs. It consists of seven distinct circuits determined by the MEMS community to be of primary importance. They are:

- **Buffer Amplifier with Driven Shield (BAWDS)** is a sensor that avoids the potentially overwhelming effects of capacitance to substrate by measuring the response of a capacitive divider to a voltage pulse, unity buffering the output of the divider and driving a shield (see Figure 2-24).

- **Transimpedance Amplifier (TZA)** Measures displacement current by exciting the circuit under test with a sinusoidal signal. The resultant output is Amplitude Modulated and sent off chip. The user must demodulate the signal. Can be used to measure capacitive changes in the femto Farad range (see Figure 2-25).
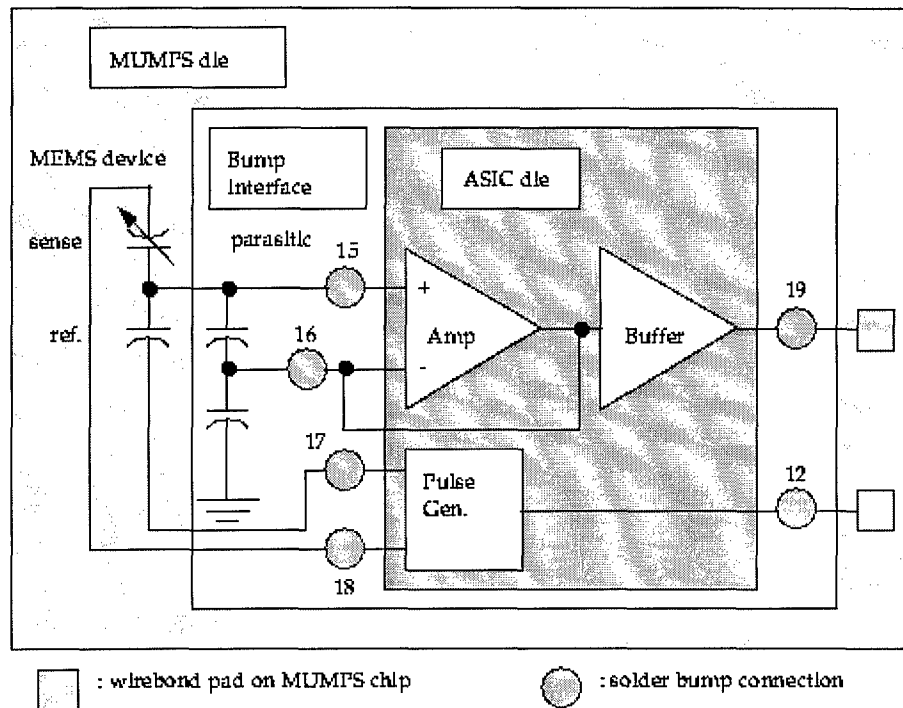
Figure 2-24 - Buffer Amplifier with Driven Shield (BAWDS) [6].
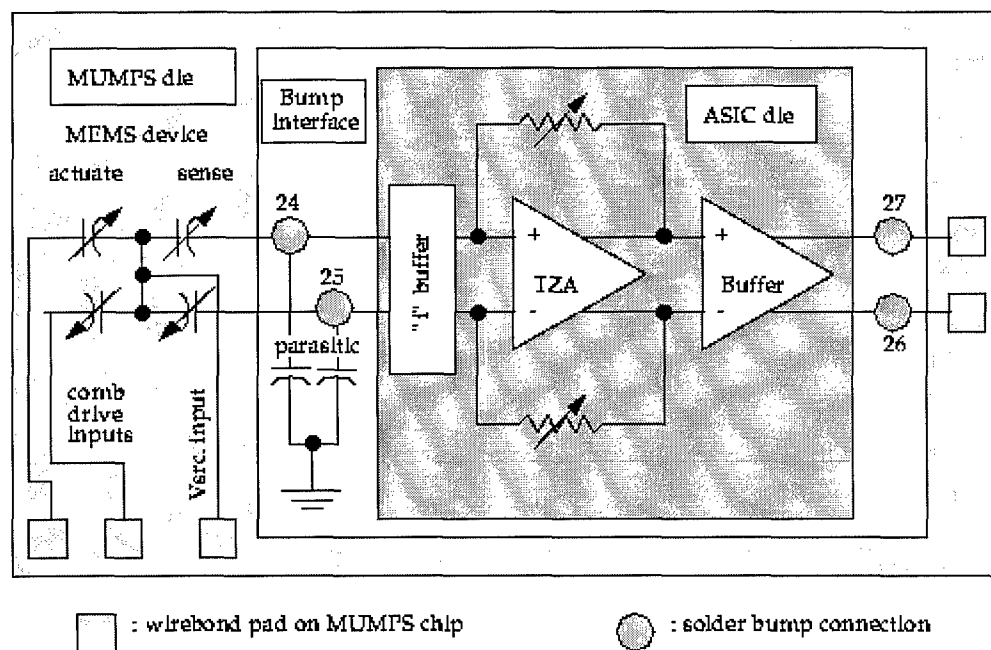
Figure 2-25 - Transimpedance Amplifier (TZA) [6].
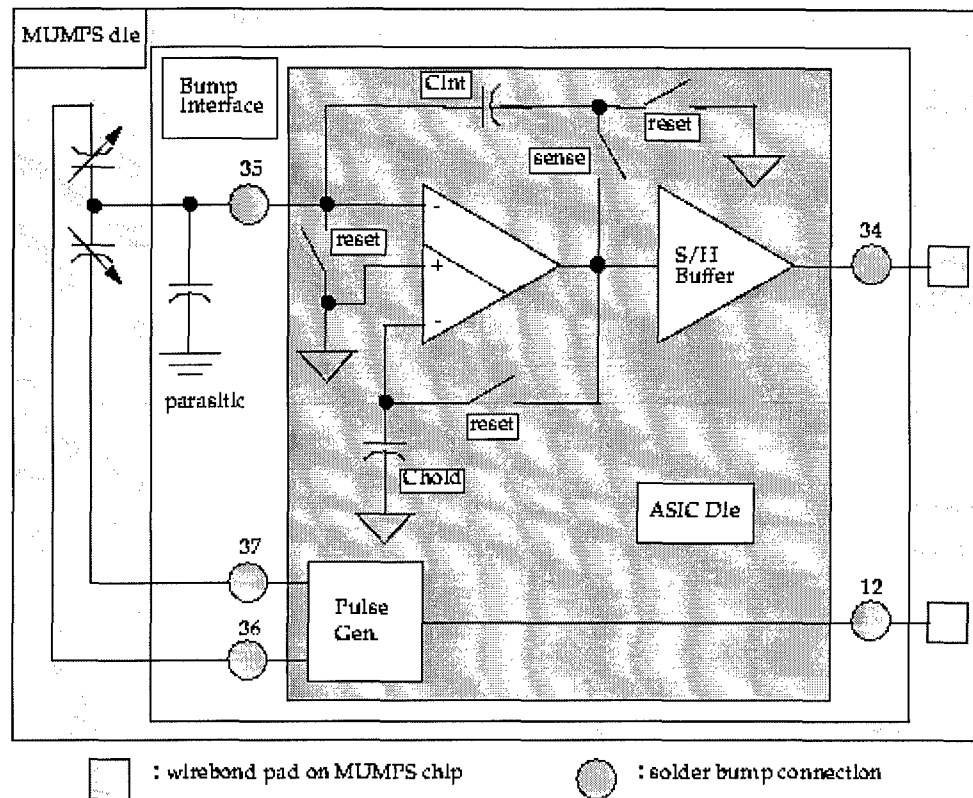
Figure 2-26 - Correlated Double-Sampling Integrator (CDSInt) [6].

- **Correlated Double-Sampling Integrator (CDSInt)** A capacitive sense

circuit that employs a sample and hold to cancel the offset voltage during

the sense phase of the circuit. Can be used to sense capacitances in the

range 0.25pF to 0.75pF (see Figure 2-26).

- **Differential Correlated Double-Sampling Integrator (DCDSInt)**

Performs the same sensing function as the CDSInt, but has differential

input and output, further reducing the susceptibility to noise and stray

capacitances (see Figure 2-27).
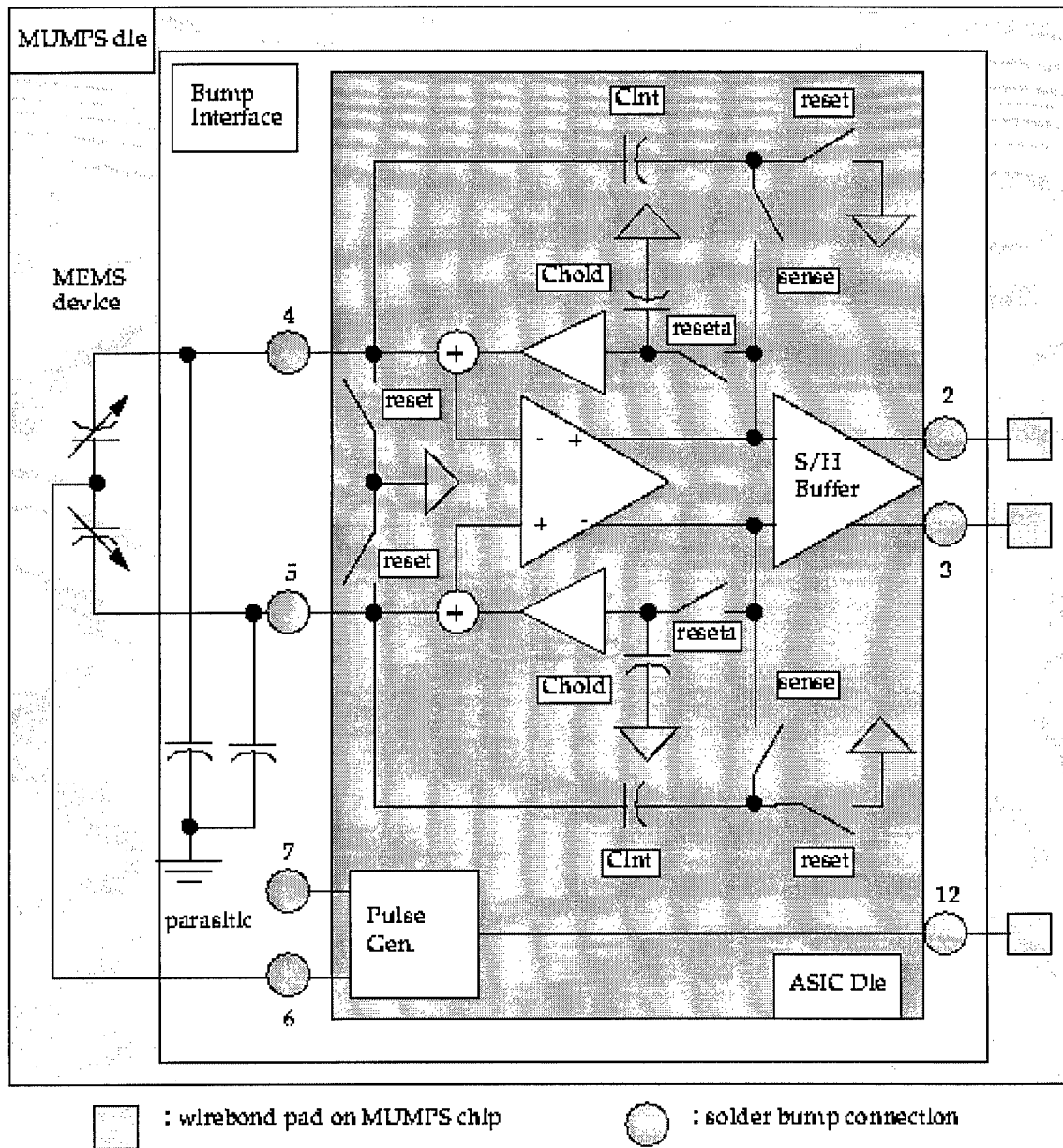
Figure 2-27 - Differential Correlated Double-Sampling Integrator (DCDSInt) [6].

- **Current Reference (IRef)** Used to mirror external currents to the other circuit.

- **Clock Generator (ClockGen)** Uses an external clock, *extclk*, to derive clocks for the CDS integrators, pulse generators, and Sample and Hold circuits.

- **Pulse Generator (PGen)** Creates +/- pulses from a digital clock provided by the Clock Generator. The high level voltage is set by the *vrefpulse* input. The amplitude is set by the *ibiaspulse* input.

These circuits are connected to the Ecosys pins shown in Table 2-2. The pin locations are predetermined and must be routed to the outer padframe by the designer.

2.2.3.3.3 SmartMUMPs Summary

The SmartMUMPs process is designed for prototyping and testing MEMS. It has the advantages of reducing noise and loss in a design, eliminating the need to wire bond the sense circuits, and using tested sense and drive circuits. Its usefulness is limited though, by the number of I/O

Table 2-2 - Pin Out of the SmartMUMPs Chip [6].

Pin #	Name	ASIC Connection	Description
1	exrdcds	external input	external differential CDS bias resistor
2	dcdsout1	external output	DCDSInt output 1
3	dcdsout2	external output	DCDSInt output 2
4	csense2	input from MEMS	Diff. capacitor 2 to DCDSInt
5	csense1	input from MEMS	Diff. capacitor 1 to DCDSInt
6	vpulse1	output to MEMS	MEMS stimulus pulse #1
7	vpulse1b	output to MEMS	MEMS stimulus pulse bar #1
8	exrsnh	external input	external sample and hold bias resistor
9	vdd	external power	digital (noisy) supply (+5V)
10	gnd	external power	digital (noisy) ground
11	vdda	external power	analog (quiet) supply (+5V)
12	extclk	external input	external clock input
13	TBD	external	potential ASIC connection
14	exrbawds	external input	external BAWDS bias resistor
15	bawdsin	input from MEMS	buffer amplifier with driven shield input
16	shield	output to MEMS	shield driver output
17	vpulse3	output to MEMS	MEMS stimulus pulse #3
18	vpulse3b	output to MEMS	MEMS stimulus pulse bar #3
19	bawdsout	external output	buffer amplifier with driven shield output
20	vrefnsnh	external input	voltage input reference for single sided CDS S/H
21	gnda	external power	analog (quiet) ground
22	vbias	external input	multi-use voltage bias
23	exrtza	external input	external TZA bias resistor
24	tzain1	input from MEMS	TZA displacement current sense input1
25	tzain2	input from MEMS	TZA displacement current sense input2
26	tzaout2	external output	TZA displacement current sense output2
27	tzaout1	external output	TZA displacement current sense output1
28	rfbias	external input	TZA feedback resistor (FED) bias Voltage
29	ibiaspulse	external input	pulse Gens. bias current
30	exrcds	external input	external single sided CDS bias resistor
31	vdda	external power	analog (quiet) supply (+5V)
32	vrefpulse	external input	voltage reference for pulse Gens.
33	cdsout2	external output	single sided CDS output signal 2 (diff. out)
34	cdsout1	external output	single sided CDS output signal 1 (diff.out)
35	csense	input from MEMS	sense capacitor to single sided CDS
36	vpulse2b	output to MEMS	MEMS stimulus pulse bar #2
37	vpulse2	output to MEMS	MEMS stimulus pulse #3
38	vrefsnh	external input	sample and hold voltage reference
39	vrefcds	external input	single sided CDS voltage reference
40	gnda	external power	analog (quiet) ground

pins. Since there are only five actual sense/drive circuits, only a few MEMS devices can be connected.

2.2.4 MEMS Summary

MEMS could well be the next technology breakthrough. Their utility is just beginning to be realized. The MUMPs process currently being used, including the VLSI augmentation SmartMUMPs provides, will be further refined to increase the utility of these tiny devices.

Devices of this new technology are ideally suited for use in artificial cochlea design. One of the major limiting factors of previously implemented cochlear models is the electronic devices they used. These electronic devices were unable to achieve the high Q required to accurately model the cochlea. MEMS resonators, as described in the next chapter, are extremely high Q devices. This enables them to be precisely tuned with large gain at the specific frequency they are designed for.

Chapter 3

3. Theoretical Development

This Chapter develops in detail the mathematical basis behind all design decisions in the following chapters. The equations developed here will be compared later with the actual values of the experimental data, shown in Chapter 4.

3.1 Cantilever and Bridge Design

For the purposes of this thesis, we will need a series of devices that will resonate at specific frequencies within the perceptual frequency range of the human auditory system (approximately 20 Hz to 20 KHz). Cantilever

Cantilever   **Bridge**

Drive Electrode   Sense Electrode
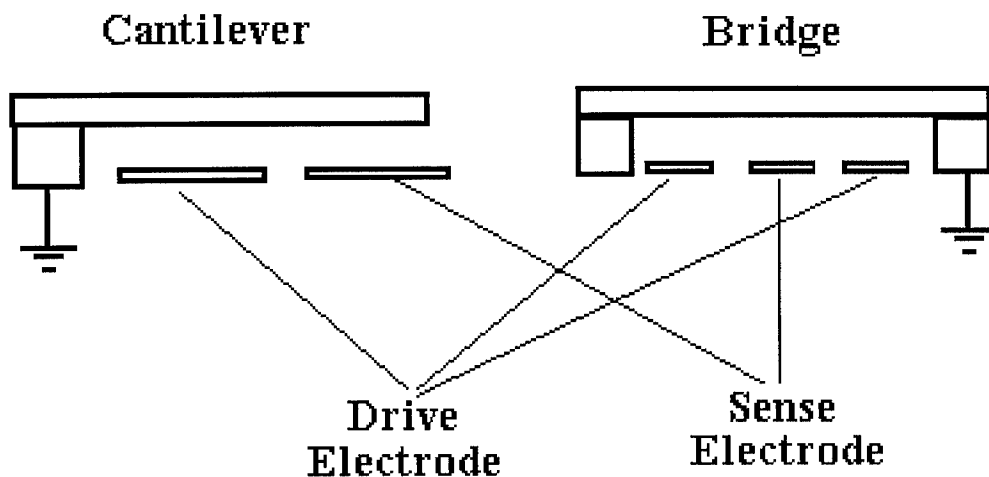
Figure 3-1 - Cantilever and Bridge. The cantilever (left) has a free arm, while the bridge(right) is clamped on both ends.

and bridge like structures (Figure 3-1), at first, appear to be the natural choice for these devices. Simple to construct, and easy to understand, these devices resonate at predetermined frequencies with predictable quality factor Q.

3.1.1 Calculating Cantilever/Bridge Resonance

Kuhns [42] and Read [25] spend a considerable effort discussing the derivation of the formula's for determining resonance of beams. Resonance of mechanical springs is determined using:

$$f = \frac{1}{2 \cdot \pi} \cdot \sqrt{\frac{k}{M}}$$ (3-1)

where k is the spring constant, and M is the suspended mass.

For simple cantilevers and bridges implemented in MEMS, the resonant frequency can be determined using [38,40]:

$$f = \frac{\lambda_i^2 \cdot t}{4 \cdot \pi \cdot l^2} \cdot \sqrt{\frac{E}{3 \cdot \rho}} \text{ Hz}$$ (3-2)

where E, ρ, l, t are Young's modulus, density, length, and thickness of the beam, respectively. λ_i is the eigenvalue, where i is the integer

representing the resonance node number [38]. For cantilevers $\lambda_1 =$

1.875104 [65], and for bridges $\lambda_1 = 4.730041$ [65].

For the polysilicon in the MUMPs process, E is approximately 162 GPa

[44,66] and $\rho_{polysilicon} = 2.33 \times 10^3$ kg/m^3 [67].

3.1.2 Calculating Cantilever/Bridge Q

The quality factor, or Q, is a measure of bandwidth. The higher the Q

factor the greater the gain at a particular
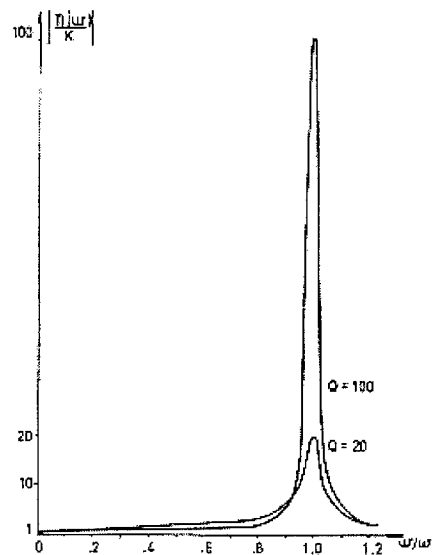
Figure 3-2 - Comparison of Different Q's. Measured from the half-power points (0.707 x peak), the Q of a circuit is a measure of bandwidth. Here, the amplitude of response is much greater for the higher Q circuit compared with the lower Q circuit [10].

frequency, but also the smaller the bandwidth (Figure 3-2). Measured from

the half power points of a frequency plot, the formula for Q is

$$Q = \frac{f_0}{\Delta f_0} \qquad (3\text{-}3)$$

For the simple beams, the formula is [38]:

$$Q = \frac{\sqrt{E \cdot \rho} \cdot b}{24 \cdot \mu} \cdot \frac{t}{l} \qquad (3\text{-}4)$$

where b is the width of the beam, μ is the surrounding medium viscosity

$(1.8 \times 10^{-5} \text{ N s/m}^2$ in air), ρ is the density, t is the thickness, and l is the

length of the cantilever.

Notice that the width of the cantilever, b, is only a factor in

determining Q, not the resonant frequency. So to increase the quality factor

of a cantilever, while maintaining the same resonance frequency, increase

the width of the beam.

3.1.3 Calculating Capacitance

Increasing the width of the beam also increases the capacitance

between the plates. This is useful for a capacitive sense circuit.

The capacitance can be determined from basic physics as:

$$C = K \cdot \frac{A}{4 \cdot \pi \cdot k \cdot d} \text{ Farads} \qquad\qquad (3\text{-}5)$$

where the constant $k = 9 \times 10^9$;

the dielectric constant K=1 in a vacuum (1.0006 in air);

d is the separation between plates;

and A is the area of the plates.

MEMS devices generally must be operated in a vacuum due to the damping caused by air. As vacuum is increased the viscosity of the medium approaches zero (perfect vacuum), and the Q approaches infinity. Only frictional losses in the material limit the Q in a perfect vacuum.

3.1.4 Shifting Q and Resonant Frequency

By applying a DC bias to a resonating MEMS device it is possible to shift its Q and resonant frequency. This is a result of the increased stress induced on the device. However, when the amplitude of the resonance becomes large enough, the higher order terms become appreciable, and the resonator exhibits a non-linear response. This is mainly due to the addition of the third-order spring constant, which becomes significant when the resonating amplitude becomes sufficiently large [68].

The force relationship becomes [68]:

$$F = kx \pm |\gamma| \cdot x^3 \qquad (3\text{-}6)$$

Where k is the second order spring constant, and γ is the third order spring constant.

The response equation of the resonant system then becomes [68]

$$m\ddot{x} + \zeta\dot{x} + kx \pm \gamma x^3 = b \cdot \cos(\omega t) \qquad (3\text{-}7)$$
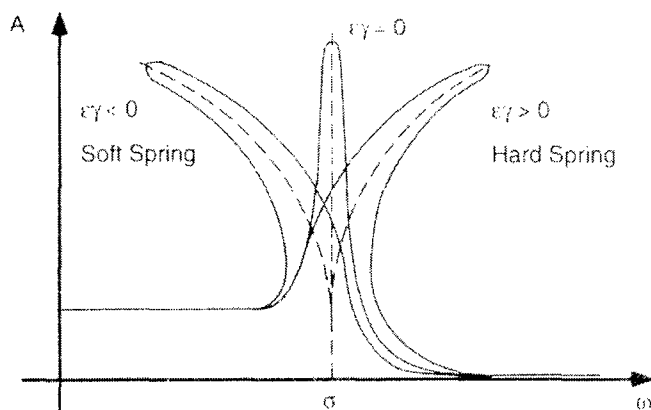
Figure 3-3 - Nonlinearity of devices defined by the Duffing equation. The natural resonance (σ) occurs when third order spring constant (γ) is negligible. When the resonating amplitude of a device becomes large enough that γ becomes appreciable the resonator exhibits a non-linear response. The device will then demonstrate a hysteresis response to input signals [68].

where:

$\ddot{x}$ is the second derivative of displacement, x, with respect to time;

$\dot{x}$ is the first derivative of displacement, x, with respect to time;

m is the resonating mass;

ζ is the damping coefficient;

b is the amplitude of the applied resonant force.

This is known as the Duffing equation [68]. The effect is illustrated in

Figure 3-3 and Figure 3-4.
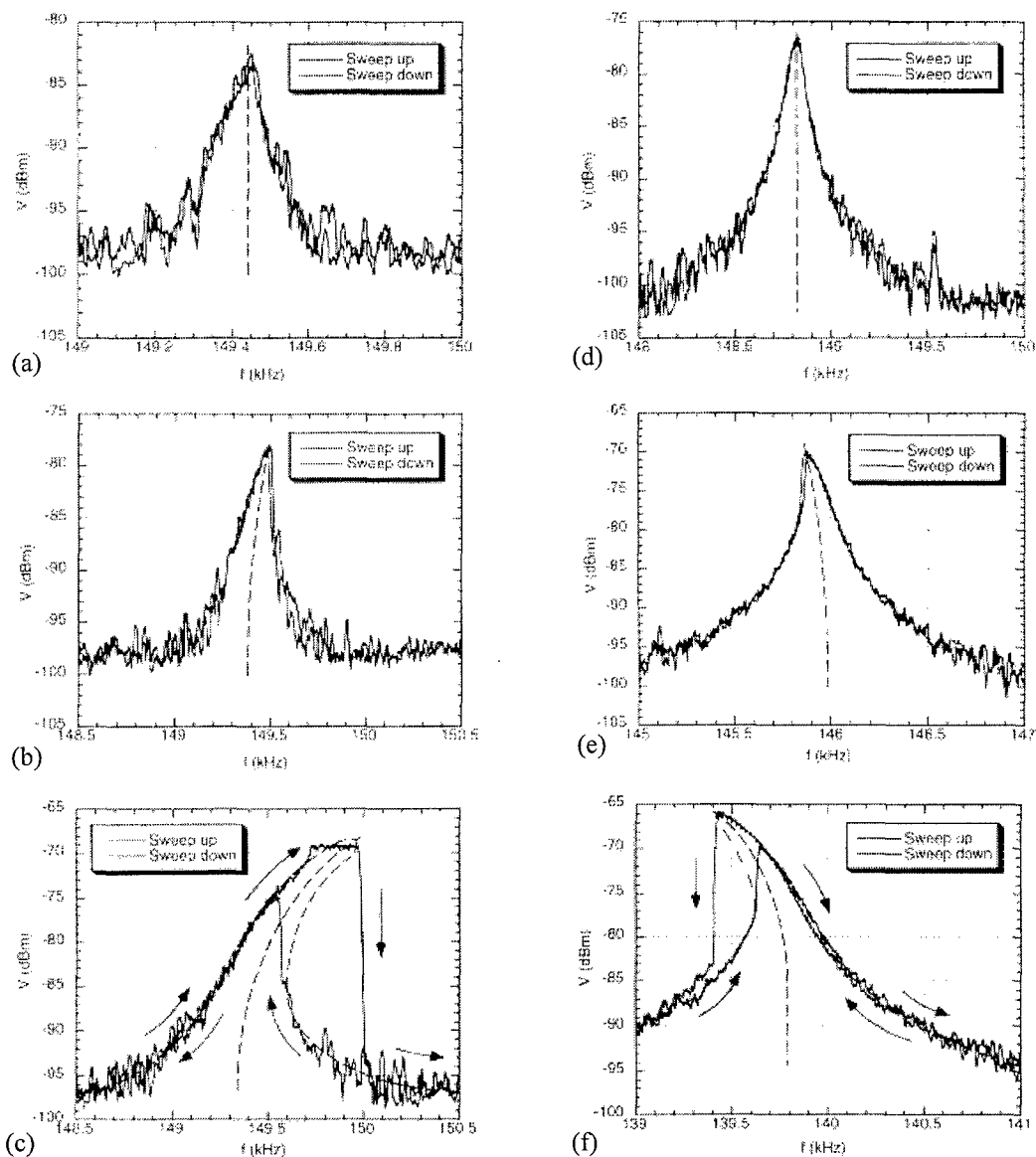
Figure 3-4 - Effect of DC voltage on resonant waveforms. Left, device under test is a tunable Single Crystal Silicon (SCS) resonator with DC tuning voltage fixed at 5V, and the sinusoidal excitation voltage varying from (a) 1.5V (b) 2.0V (c) 3.0V peak to peak. Right, tunable resonator with a sinusoidal input voltage fixed at 1.5V peak to peak, and DC tuning voltage varying from (d) 10V (e) 20 V (f) 30V DC [68].

3.1.5 Driving and Sensing Cantilevers

While cantilevers and bridges are easy to design, they are difficult to operate. Since the electrostatic force is nonlinear the drive voltage must be kept small. For vibrational amplitudes greater than 1/3 of the gap the device will "slam down" [66]. That is, once a suspended beam has touched the layer it was suspended above, van der Waals forces keep it down. This is called "stickage."

To determine drive voltage versus deflection for cantilevers use [44]

$$V = (z_0 - d_f)\sqrt{\frac{8kd_f^3}{27\varepsilon_0 Lb}} \qquad (3\text{-}8)$$

where:

ε_0 is the free space dielectric constant (8.854×10^{-12});

z_0 is the resting position of the beam (distance above the substrate);

d_f is the beam deflection;

L, b, k are the length, width, and spring constant of the beam.

3.2 Interdigitated Finger (Comb) Resonator Design
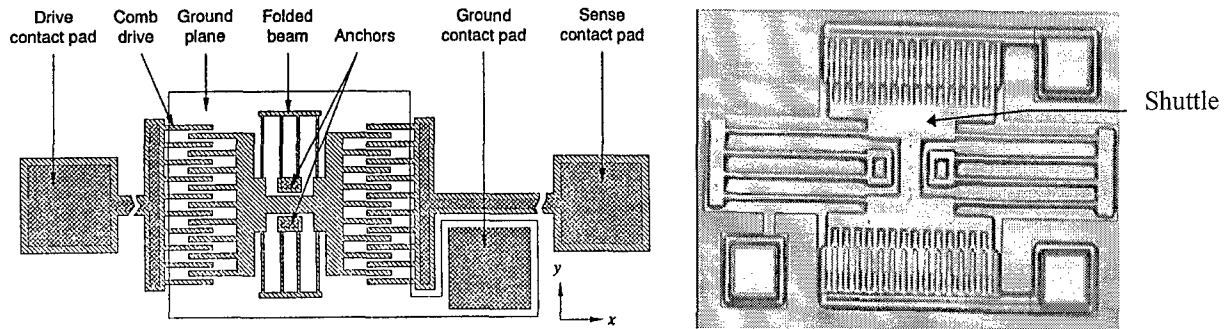
Figure 3-5 - Comb drive layout. The schematic diagram of a comb (left) illustrates the layout of a comb [69]. Symmetric in design, the drive and sense pads can be reversed without affecting operation. The center structure, or shuttle, is suspended above the substrate by two folded beam springs anchored at two points. When driven at the resonance frequency, the shuttle will swing back and forth in the x direction. Resonance can be detected by comparing the drive and sense signals, noting a change in phase and amplitude at the resonance frequency. Actual picture of a comb (right), shows gold pads and shadows under suspended springs. This device is stuck down, which can be observed by noting the area where the fingers overlap, and recognizing the difference in depth. The stationary sense and drive fingers should be at the same level as the fingers on the shuttle.

Comb resonator designs, as shown in Figure 3-5, are different from cantilever and bridge designs in that combs are actuated parallel to the substrate plane. This has certain advantages over orthogonal actuation. First of all, the gap between the fingers is held relatively constant, with less chance of the device being stuck. A DC bias can also aid in keeping the device from sticking down to the substrate by minimizing the vertical oscillations. The 1/3 distance rule therefore does not apply, and the devices

can be operated with greater drive. This, in turn, provides a larger sense signal, making these devices easier to sense and drive. Another major advantage has to do with damping. In the presence of air, vertically actuated devices such as cantilevers, bridges, and mirrors, are limited by squeeze-film damping [69]. That is, air is sandwiched between the structure and substrate, applying a force opposite to the actuating force. This is the reason these devices are operated in a vacuum. However, with horizontally actuated devices, squeeze-film damping is not a concern. Air below the device acts as a cushion that the structure glides over. There is still friction in the form of drag, but is much less inhibiting. This underlying air flow is termed Couette flow [69]. Since these devices have much less damping, they can operate in air. However, the Q is greatly reduced, on the order of 100 depending on beam length. On the other hand, Qs of 50,000 have been achieved in good vacuum [69].

The downside of combs is the size and complexity of their design. These devices are usually much larger than beam, bridge, and mirror structures. Calculating their resonance is also more involved.

3.2.1 Calculating Comb Resonance

The dissertation by Tang [69] explored in detail the mathematical basis for resonance in a comb. This section is a summary of his work.

As with other mechanical spring devices, to calculate the resonance it is first necessary to determine the spring constant, k, and the mass, M of the device. To move the shuttle some distance, X_0, a force in the x direction, F_x, must be applied. As shown in Figure 3-6, each of the beams supporting the shuttle has length L, width w, and thickness h. Assuming the outer truss is rigid, justified by its wider design, the slopes of both ends of the beams are set to zero as part of the boundary conditions. The force acts on each beam equally, such that the force on each beam is $F_x/4$. The deflection equation for the segment AB can be given as [69]:

$$x(y) = \frac{F_x}{4(12EI_z)}(3Ly^2 - 2y^3) \qquad \text{for } 0 \le y \le L \qquad (3\text{-}9)$$

where E is Young's modulus, and I_z is the cross sectional moment of inertia for the beam with respect to the z axis (perpendicular to the substrate). Since the segment has a zero slope on either end it cannot be treated as a
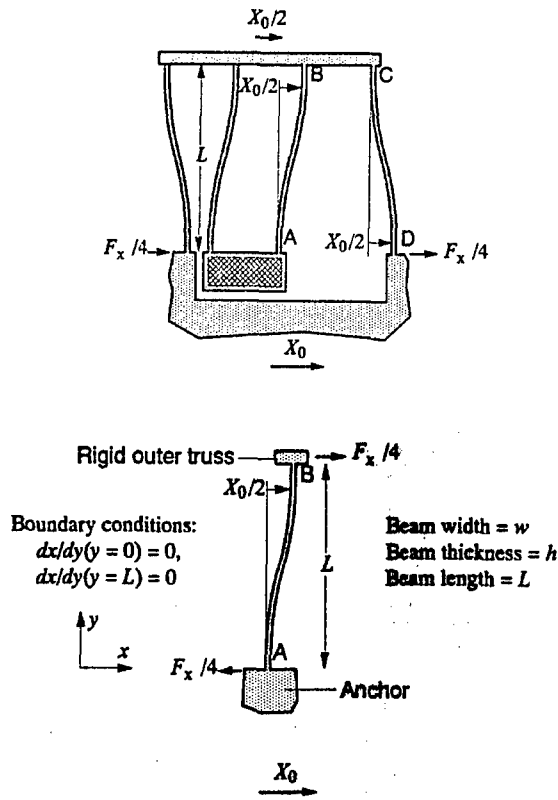
Figure 3-6 - Mode shape of folded beam support and segment. Diagram illustrates the mode shape (bending) of the folded beam springs that support the shuttle when it is displaced a distance X_0 under a force F_x [69].

simple cantilever beam, but since it is know that it is deflected by $X_0/2$ at

point B, a boundary condition of $x(L) = X_0/2$ can be used so that:

$$\frac{X_0}{2} = \frac{F_x}{4(12EI_z)}(3Ly^2 - 2y^3),$$

which leads to $X_0 = \dfrac{F_x L^3}{24EI_z}$ (3-10)

The spring constant in the x direction for a single beam is then:

$$k_x = \frac{F_x}{X_0} = \frac{24EI_z}{L^3}$$

(3-11)

In the same way, the spring constant for a single beam in the z direction is derived as:

$$k_z = \frac{F_z}{X_0} = \frac{24EI_x}{L^3}$$

(3-12)

The moments of inertia for each beam in the x and z directions are calculated by:

$$I_x = \frac{h^3 w}{12} \text{ and } I_z = \frac{h w^3}{12}$$

(3-13)

Motion in the y direction can generally be ignored since:

$$k_y = \frac{AE}{L}$$

(3-14)

where A is the beam's cross-sectional area

and the ratio of the spring constants in the y and x direction yields:

$$\frac{8k_y}{k_x} = \frac{8AE/L}{24EI_x/L^3} = \frac{4whL^2}{w^3 h} = \frac{4L^2}{w^2}$$

(3-15)

With a typical beam length of 200 microns and width of 2 microns, this ratio is 40,000, so movement in this direction can be ignored.

Tang also showed that by adding sections of folded beams, the spring constant could be reduced by k/n, where n is the number of 4 parallel beams.

To calculate mass Tang used Rayleigh's energy method, where the maximum kinetic energy is equal to the maximum potential energy. He calculated the total effective mass for a 2 truss 8 beam folded spring comb to be:

$$M = M_p + \frac{1}{4} M_t + \frac{12}{35} M_b \qquad (3\text{-}16)$$

where M_p, M_t, and M_b are the mass of the plate, trusses, and beams respectively.

Using the spring constant in the x direction, and the effective mass, the resonant frequency can be calculated as:

$$f = \frac{1}{2\pi} \sqrt{\frac{k_x}{M}} = \frac{1}{2\pi} \sqrt{\frac{24 E I_z}{(M_p + \frac{1}{4} M_t + \frac{12}{35} M_b) L^3}} \; \text{Hz} \qquad (3\text{-}17)$$

There will also be a resonant frequency in the vertical direction, which is generally unwanted. In air its amplitude is relatively small due to squeeze-film damping, but in a vacuum it could be significant. To minimize this resonance, a DC bias is placed across the drive and ground pads.

3.2.2 Calculating Comb Q

When in air, energy dissipation through Couette flow dominates the energy lost through drag on the top surface [69]. Considering Couette flow only will give an upper bound on the Q estimated by [69]:

$$Q = \frac{d}{\mu A_p} \sqrt{Mk_x} \qquad (3\text{-}18)$$

where μ is the viscosity of air, Ap is the area of the plate, and d is the distance above the substrate.

In a vacuum, most of the energy is lost through the anchors or in the structure itself. Therefore the Q will be very high.

3.2.3 Driving and Sensing Comb Resonators

The easiest way to test these devices is to apply a signal source to the

drive pad, and a DC source across the drive and ground pads, sweep the frequency of the source in the vicinity of the expected resonance, and observe through a microscope for movement. This is how MCNC determines the resonance of the comb test devices it places on each run [70]. They use 50 V DC bias and 16 V peak to peak signal sources for visual observation in air. This setup was derived from Tang [69]. In his dissertation he calls for DC biases up to 40 V and drive of 10 V peak for visual observation in air of the comb devices he designed.

Electrical sensing of resonance is much more accurate than visual observation. Tang also discusses electrical detection using the test setups in Figure 3-7. Without DC bias, the AC drive signal will go positive and negative with respect to ground. The comb reacts to both peaks, thereby a frequency doubling effect is observed. The drive signal frequency must be half of the comb resonance frequency to drive the comb.
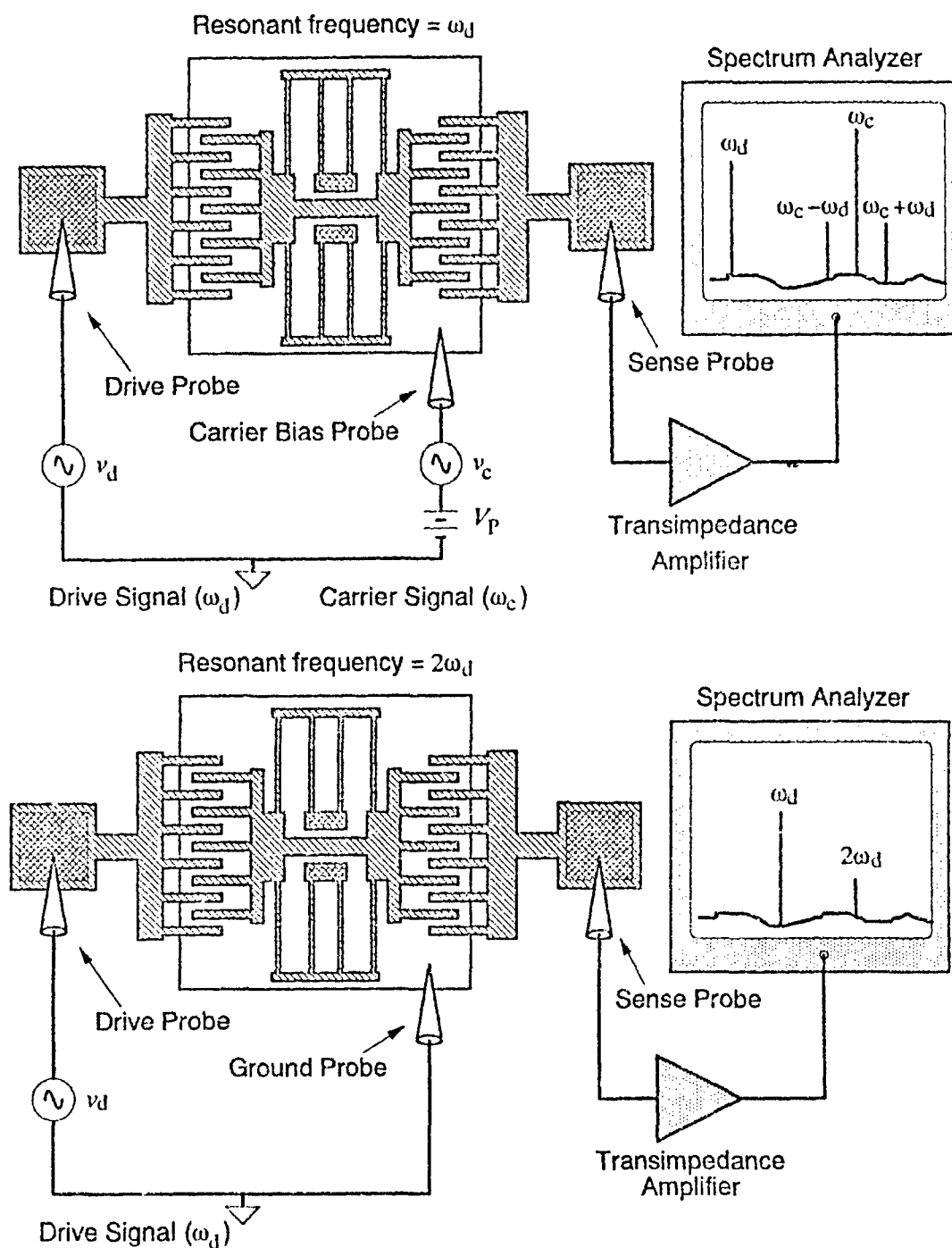
Figure 3-7 - Comb resonance test setups. The top setup uses a carrier, modulated by the time-varying sense capacitance to drive the comb. The bottom setup applies the drive signal directly to the drive pad, without DC bias. In this case the drive signal frequency is half of the resonant frequency due to the frequency doubling effect [69].

3.3 Mirror/Actuator Resonator Designs
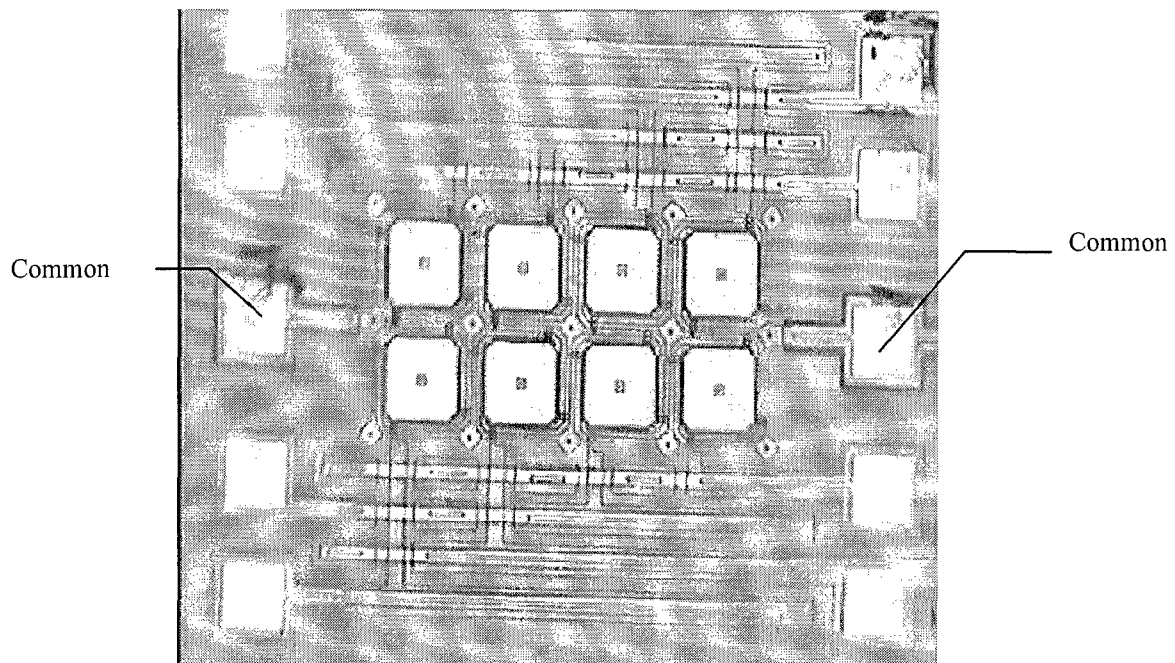
Figure 3-8 - Photograph of an addressable mirror array. The mirrors are operated by placing one probe on the common, and selecting the individual mirrors by placing the other probe on any one of the mirror drive pads. Each mirror has a Poly0 bottom plate and an 80 by 80 micron Poly2 top plate supported by four 130 by 2 micron flexures. Note the damage on some of the pads caused by probe placement.

Mirrors and vertical actuators can also serve as resonators. A mirror is a preferably flat structure suspended by two or more beams, called flexures, and has a reflective surface. A vertical actuator has the same definition, with the exception that its surface need not be reflective. Both are basically mass held above the substrate with springs. These devices are normally used in arrays of like devices, as shown in Figure 3-8.

3.3.1 Calculating Mirror Resonance

As in the case of the devices previously discussed, determining the resonance frequency is an exercise in determining the spring constant and mass of the device. The spring constant has three components [71]:

$$k_{cs} = \frac{Ewt^3}{L^3} \qquad k_t = \frac{KE}{2(L_1 + L_2)L_2^2(1+v)\sin(\theta)} \qquad k_s = \frac{\sigma(1-v)wt}{2L}$$

$$k = N(k_{cs} + k_t + k_s) \tag{3-19}$$

where

k_{cs} is the cross-sectional spring constant, k_t is the torsional spring constant, and k_s is an added stress term;

KE is the kinetic energy of the spring (when in motion, equal to ½mv²);

E is Young's modulus, σ is the stress of the material, v is the Poisson ratio, N is the number of flexures;

w, t, L are the width, thickness, and length of the flexures respectively;

L_1 and L_2 are the primary and secondary lengths of the flexure (in the case of bent flexures).

If the flexures are straight, then the k_t can be ignored. The mass, M, is a simple volume times density calculation. Using the k and M, the resonant frequency is calculated using Equation 3-1.

3.3.2 Driving Mirrors

The mirrors, like cantilevers and bridges, are simple two port devices. A source on one port and a return on the other is required to operate the device. To calculate the voltage required to drive the device use [71]:

$$V = (z_0 - d_f) \sqrt{\frac{2kd_f}{\varepsilon_0 A}} \tag{3-20}$$

where:

ε_0 is the free space dielectric constant (8.854×10^{-12});

z_0 is the resting position of the mirror (distance above the substrate);

d_f is the mirror deflection;

A is the surface area of the mirror.

To calculate the maximum voltage the device can operate set $d_f = z_0/3$. Deflections greater than 1/3 of the gap cause instabilities in the system [66].

Chapter 4

4. Experimental Setups, Procedures, and Design Descriptions

This Chapter describes the experimental setups required to process and validate the designs used to implement selected MEMS devices. Step by step procedures are described to ensure that future researchers can reproduce the results described in Chapter 5, and subsequent advancements can be realized. Each of the MEMS designs, and the overall system design, are discussed in detail.

4.1 Experimental Setups

Approximately two months after submitting a design to MCNC, the dice are returned to the designer. For each MUMPs die site, about 15 die are produced. Before the die can be tested they must be post-processed to remove the protective layer of photoresist, and to release the structures. After post-processing, the devices on the die can be tested. The following sections describe the setups required for post-processing and testing of the individual die.

4.1.1 Die Post-processing

When dice are received they must first be post-processed. This entails removing the protective photoresist, and subsequently releasing the device structures. Recall, the MUMPs process utilizes three patterned polysilicon layers, with an added metal layer deposited last. Between the polysilicon layers lie oxide layers. Any exposed oxide layers are etched away during post-processing, leaving the patterned three dimensional polysilicon design. To release these structures, hydrofluoric (HF) acid is used. This is one of the most hazardous chemicals known to man. Using
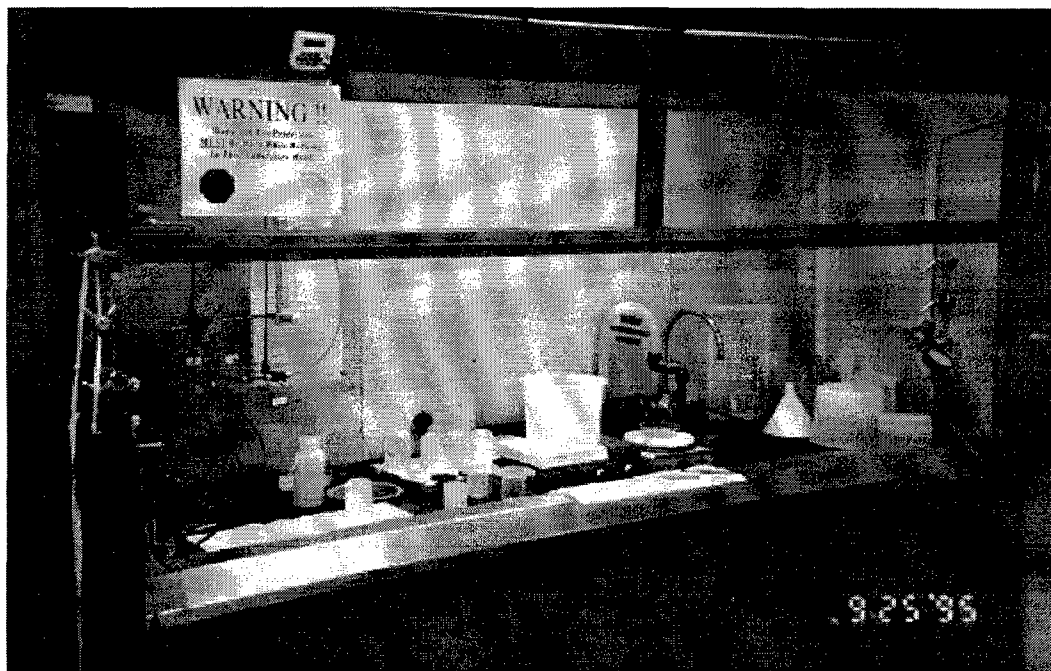
Figure 4-1 - Facility used to release MEMS devices [3].

this chemical mandates certain precautions. Rubber gloves must be worn to prevent the liquid chemical from soaking through the skin and reacting with the calcium in the bones. Eye protection must always be in place in the form of goggles or a face shield. Since HF vaporizes readily, all work must proceed under a chemical vapor hood with the appropriate negative pressure. Figure 4-1 shows the hood in place in the AFIT MEMS laboratory. Care must be also taken in disposal of all chemicals after use. Additional containers are available to recapture used chemicals. The MEMS release procedures are discussed later in this chapter.

4.1.2 Scanning Electron Microscope

After releasing the individual die, it is inspected to ensure proper fabrication and release. In some cases, this can be done using a standard microscope. For most MEMS devices, however, the need for a three dimensional view requires using the Scanning Electron Microscope (SEM). Shown in Figure 4-2, the SEM is capable of magnifications on the order of 1000 times, and can rotate the die in three dimensions. The SEM has a built-in Polaroid camera, enabling high quality pictures of micron sized objects.
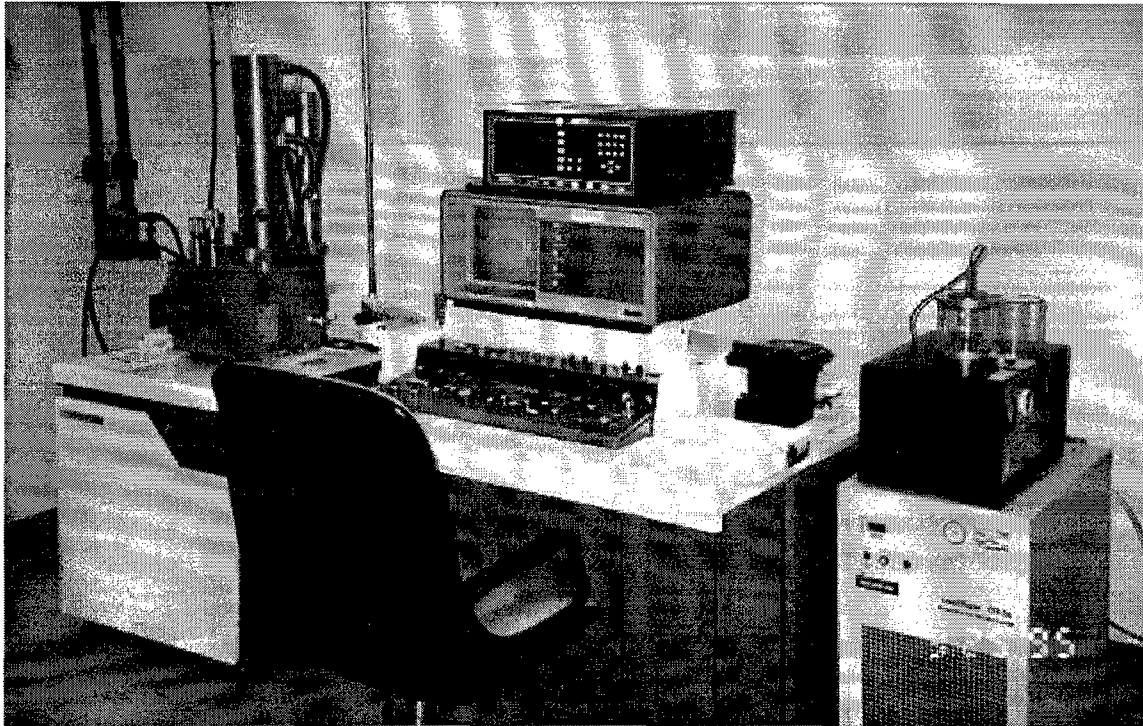
Figure 4-2 - Scanning Electron Microscope setup [3].

4.1.3 Test Equipment Description

The following test equipment was used in the testing of the MEMS

devices:

Network/Spectrum Analyzer - Hewlett-Packard, Model HP 4195A

This analyzer, shown in Figure 4-3, measures changes in the

frequency spectrum in the range of 10 Hz to 500 MHz. It can measure the

transmission coefficients, phase and amplitude changes, over this entire

range, and with an add-on directional bridge, it measures the reflection

coefficients for frequencies greater than 100 KHz.
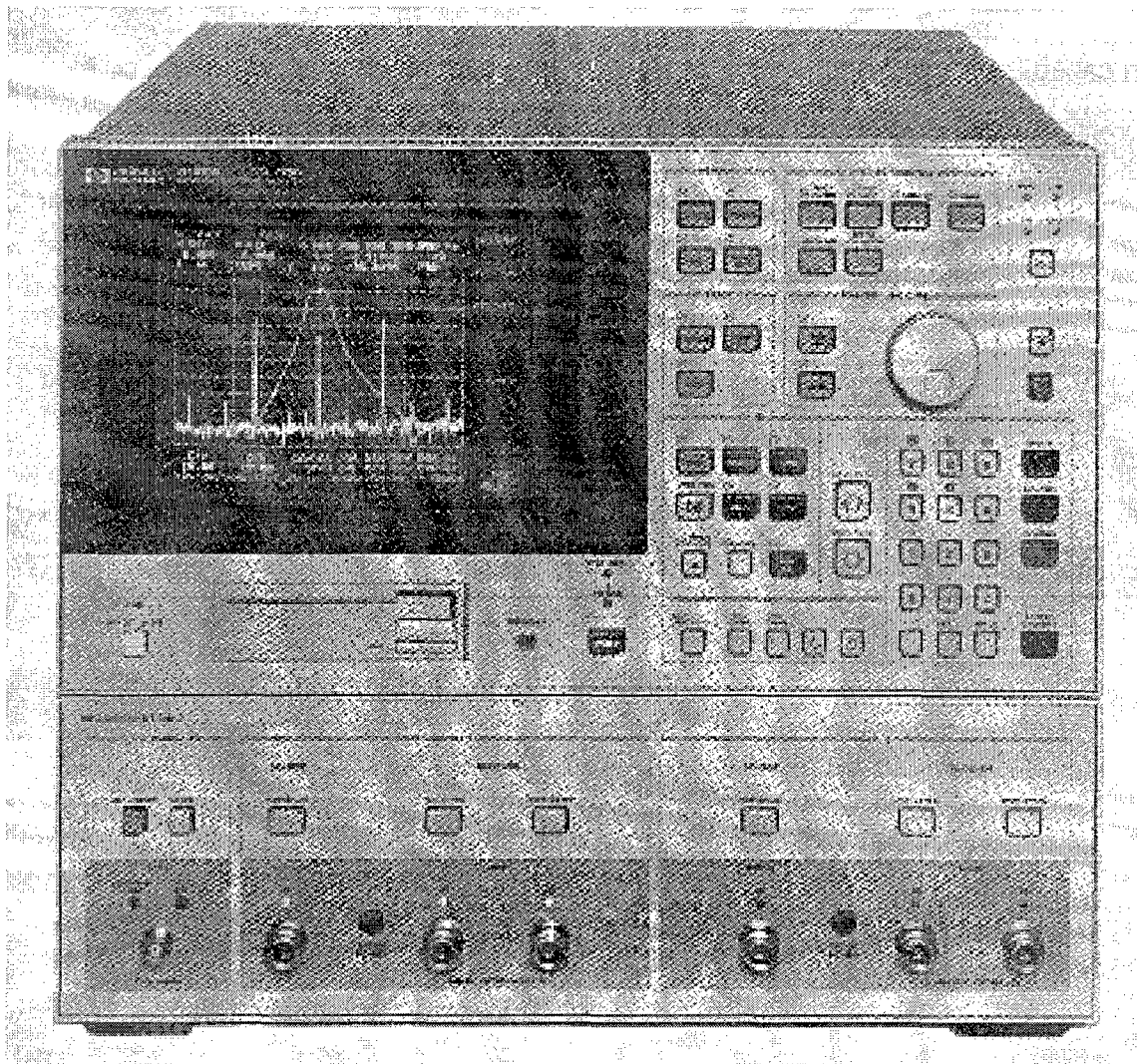
Figure 4-3 - Photograph of the 4195A Network/Spectrum analyzer.

<u>*Micro-manipulator table*</u> - The micromanipulator Company, Model #6200

The micromanipulator is a microscope station that allows for the probing of die. The die, as well as the base of each of the probes, are held in place by a vacuum. The die can be moved in the three dimensions, but

can not be tilted to view the raised structures created in MEMS. The station

itself sits on an air table that is floated by a compressor or a nitrogen tank.

This isolates the microscope from vibrations that exist in any building. This

probe station is useful for inspecting die, but can not be used to test the

devices described in this thesis due to the absence of a vacuum chamber.

Dual Power Supply - Powertec, Model #6C3000

This is an analog power supply that provides two independent voltage

or current sources. Each source is capable of supplying 0 to 36 VDC at 1 A.

The two supplies can be tied in series to form a 0 to 72 VDC supply.

Digital Multimeter - Fluke, Model #8600A

The multimeter measures currents, voltages, and resistances and

displays the values in a decimal readout. The meter can read voltages up to

1000 VDC or 750 VAC, and currents up to 10 A. Resistances up to 32 MΩ

can also be measured.

Function Generators - 1.Wavetek, Model #148, 2.Hewlett Packard, Model

#3314A

The Wavetek is a 20 MHz AM/FM/PM generator with one 50 Ω and

one 75 Ω output. It supplies up to 15 V peak-to-peak sinusoids, and can

superimpose up to 7.5 VDC bias. The HP 3314A is a programmable source,

able to supply square, sinusoidal, or sawtooth waveforms in the range of 10

Hz to 20 MHz. It has an output voltage range of 0.1 to 10 V peak to peak,

with up to 10 VDC bias. The device will automatically sweep through

specified frequency ranges. This is useful for optically determining

resonance of comb actuators.

Ball Bonder - Kulicke and Soffa Industries, Inc., Model #4124

This ultrasonic bonder is used to wire bond dice to packages. It uses

temperature, pressure, and high frequency vibration to bond 25 µm diameter

gold wire to die and package bond pads, enabling the designed devices to be

placed in circuit cards.

Scanning Electron Microscope - International Scientific Instruments, Model

WB-6

This high performance microscope has an approximate 4 nm

resolution, and is used to characterize released die. A built-in Polaroid

camera enables high quality pictures of micron sized devices.

Thermal Testing Station - MMR Technologies, Inc., Model K20P4-4

The Low Temperature Micro Probe (LTMP) is used to measure temperature sensitive devices. For the purposes of this thesis, only the vacuum chamber and probes were used. None of the thermal capabilities were exercised. A die is inserted into the chamber on a cold finger, which is held in place with three screws. The cold finger has a ten pin connector providing electrical connectivity outside the vacuum. Additionally, the LTMP has four probe manipulators that connect the probe tips inside the vacuum with external Sub Miniature Adapter (SMA) connectors, allowing four temporary connections with the die. Test equipment can then be connected to the devices via the SMA connectors with cables. Each probe can be precisely moved in three directions, X, Y, and Z over a 1.0 x 1.0 x 0.25 inch volume by using three external knobs. Figure 4-4 depicts the probing of the die. A microscope is mounted above the chamber, and optical access is made possible through a sapphire window. A vacuum pump, capable of achieving less than 20 mTorr vacuum, is connected to the chamber via a gas manifold shown in Figure 4-5. Additionally, nitrogen backfill and pressure sensing are performed by the manifold.
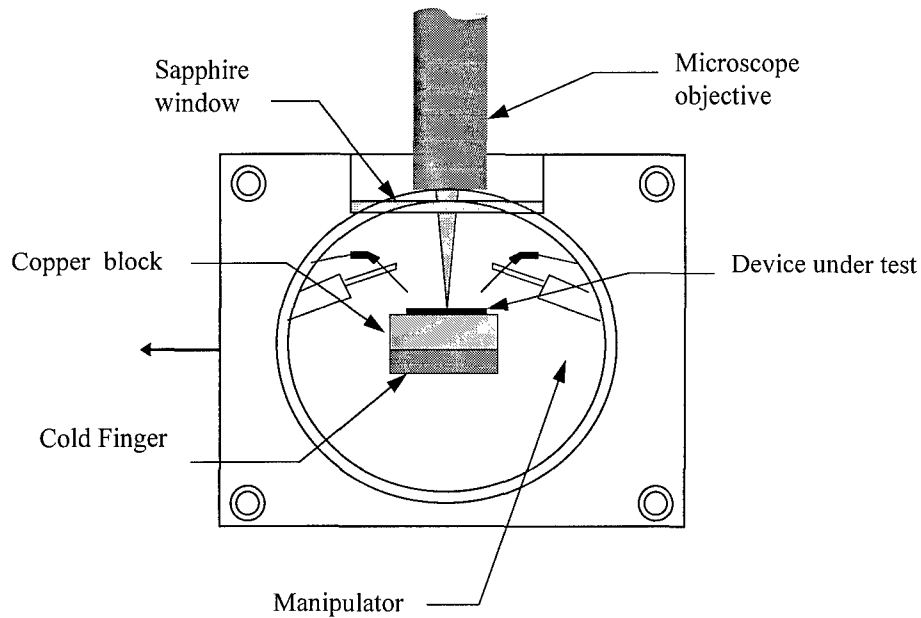
Figure 4-4 - Cut-away view of the vacuum chamber [3]. Access into the vacuum chamber is admitted by four micromanipulator probes. The device under test is viewed under the microscope, probed, and subsequently operated by external test equipment.
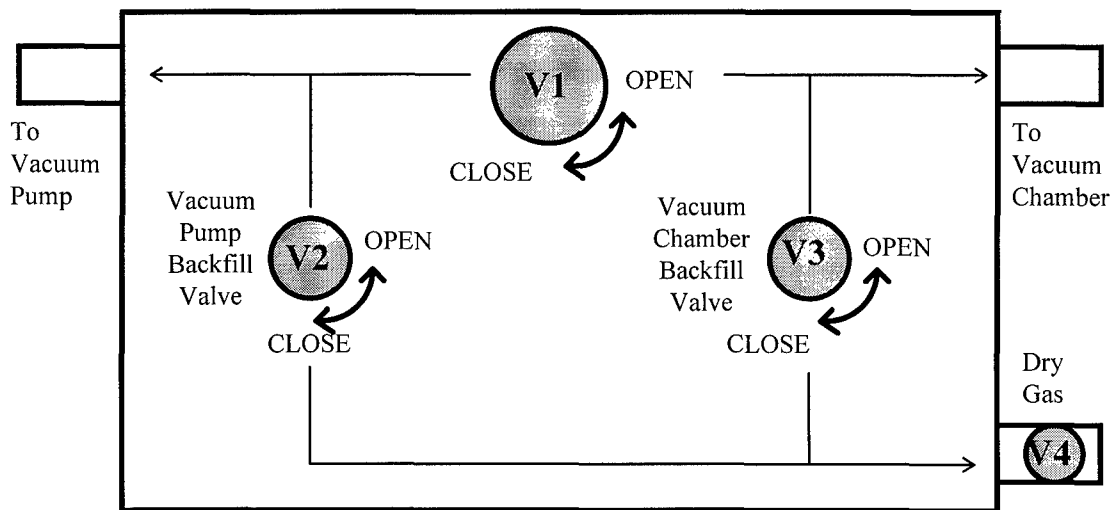
Figure 4-5 - Vacuum Manifold Layout.

Programmable Stepping Motor Controller with Translation Stages -

Klinger Scientific, Model CC1.2

Used, in conjunction with the vacuum chamber, to position the area

of interest of the die under test under the sapphire window. A remote

control allows users to keep their eyes on the die while positioning.

4.1.4 Device Test Setup

Pictured in Figure 4-6, the device test setup includes the vacuum

chamber and test equipment rack. The vacuum chamber rests on top of the

depicted air table to minimize vibrational noise. Access into the vacuum

chamber is enabled via four internal probes. These probes are connected to

the appropriate test equipment through external connectors. Access to the

chamber can also be obtained though the external connector on the cold

finger. This connector has ten pins that extend into the chamber, and are

normally connected to the cold finger for refrigeration purposes. However,

they can be disconnected from the cold finger and used as I/O signals to and

from the device under test (DUT). A broken cold finger was refurbished for

this purpose. So, a total of 14 connections, 4 probed and ten wire-wrapped,

to the DUT are possible.
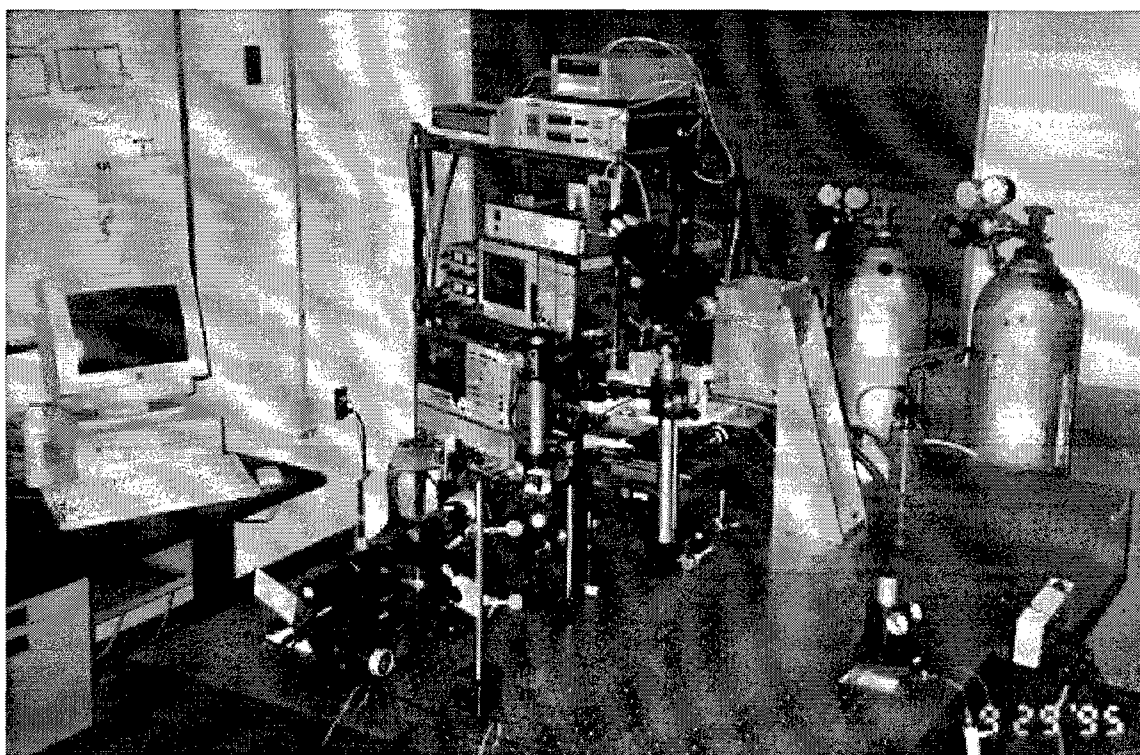
Figure 4-6 - MEMS lab vacuum chamber experimental setup [3].

4.2 Procedures

The following procedures were used to post-process and test the

MEMS devices.

4.2.1 Die Post Processing

Releasing the MUMPs die entails removing the protective

photoresist, etching the sacrificial oxide layers, rinsing, and drying. The

procedure, illustrated in Table 4-1, is somewhat excessive on the times, but

ordinarily results in a good clean release. All beakers must first be rinsed out with deionized water (DIW) and then blown dry with nitrogen to remove contaminants. It is important to remember that a piece of dust is a boulder relative to the micron size devices being released. Keeping the

Table 4-1 - Release Procedure for MUMPs Die [6,72].

Step	Solution	Time	Notes
1	Acetone	15 min.	Removes Protective Photoresist
2	Methanol	5 min.	Rinse off acetone
3	Deionized water (DIW)	5 min.	Rinse off acetone/methanol
4	HF (49%)	2.5 min.	Etch sacrificial layers
5	DIW	5 min.	Rinse off etchant
6	Clean DIW	10 min.	Ensure etchant rinsed off
7	2-Propanol	5 min.	Removes water
8	Methanol	10 min.	Ensure water is removed
9	Hot Plate at ~60 °C	~30 sec.	Evaporate 2-Propanol/ methanol

work area and containers clean is essential for a good release.

Except for the HF bath, the time in a solution does not have to be exact. Some devices will require a longer HF bath, but all the devices constructed for this thesis released properly following the stated procedure

with times listed. Increasing the rinse times can improve, although very slightly, the overall process. Two alcohol rinses at the end are not essential, but the second rinse serves to further minimize the amount of dust and debris on the released die. The rinses also ensure that all water is removed. Failure to remove the water can lead to device stickage to substrate due to van der Waals forces.

It is important to follow all safety rules while working in the laboratory. Wear of protective clothing, gloves, and eyeware is imperative. The risk of exposure to dangerous chemicals is real, and the consequences severe. Also ensure that the chemical vapor hood is working properly, and the chemicals used are properly disposed.

Table 4-2 - Vacuum Chamber Pump Down Procedure [3].

Step	Operation
1	Ensure all valves are in the closed position (turned clockwise)
2	Turn on the vacuum pump. If the pump does not transition from initial noisy to subsequent quiet operation, turn pump off and check all vacuum line connections to ensure they are tight.
3	Turn on power to Convectron vacuum gauge. Check power light on front panel (red). Observe that the pressure indicated is 760 Torr or greater.
4	Open vacuum isolation valve (V_1). Chamber pressure can now be monitored from the vacuum gauge.
5	When vacuum gauge reads 100 mTorr or less, proceed to device testing.

4.2.2 Vacuum Chamber Setup and Use

The procedures described in Table 4-2 are used to pump down the

vacuum chamber to levels that alleviate the damping caused by air on the

Table 4-3 - Vacuum Chamber Backfill Procedure [3].

Step	Operation
1	Allow the vacuum chamber pressure to increase above 5 mTorr when operation of the MMR refrigerator has terminated and has warmed the refrigerator to room temperature (300 K).
2	Close the vacuum isolation valve (V_1).
3	Regulate the pressure from the nitrogen backfill tank to 15 psi or less. The pressure gauge is attached to regulator that is screwed into the nitrogen bottle.
4	Open backfill isolation valve (V_4). If gas pressure exceeds atmospheric pressure by more than 1 psi, the pressure relief valve (V_R) will open, allowing some of the backfill gas to escape. Gas hissing may therefore be evident.
5	Open the vacuum chamber valve (V_3). The flow restrictor will limit gas flow so that the pressure will increase to atmospheric slowly. When the vacuum gauge (VG) indicates atmospheric pressure, proceed to step 6.
6	Close vacuum chamber backfill valve (V_3).
7	Turn off the vacuum pump.
8	Open the pump line backfill valve (V_2). Wait until the pressure relief valve starts venting. Will hear gas hissing.
9	The cold finger can now be removed, and the device under test removed/replaced. When complete, securely screw the cold finger back into place.
10	Close the pump line backfill valve (V_2).
11	Close the backfill gas isolation valve (V_4).
12	Close the main valve on the nitrogen backfill tank.

MEMS devices. The valves referenced are shown in Figure 4-5. When placing a new device in the chamber, the chamber must first be depressurized. The air we breath is too dirty to allow into the chamber. Microbes and dust particles would contaminate the chamber, so a back pressure is supplied to the chamber before removing the cold finger. Table 4-3 lists the steps necessary to depressurize the chamber, and remove the die without contaminating the chamber.

4.2.3 MEMS Testing

Detecting the small changes that occur when a MEMS device enters resonance is no easy task. Equally as challenging, is determining the frequency and drive for each device type. A flexible setup is extremely important for testing devices of different sizes and structures. Many variations of test setups were investigated before a valid test setup was devised for both the horizontally and vertically actuated devices. Figure 4-7 is the test setup used to detect comb resonance. Following the procedures in Table 4-4 device resonance is observed and can be varied.
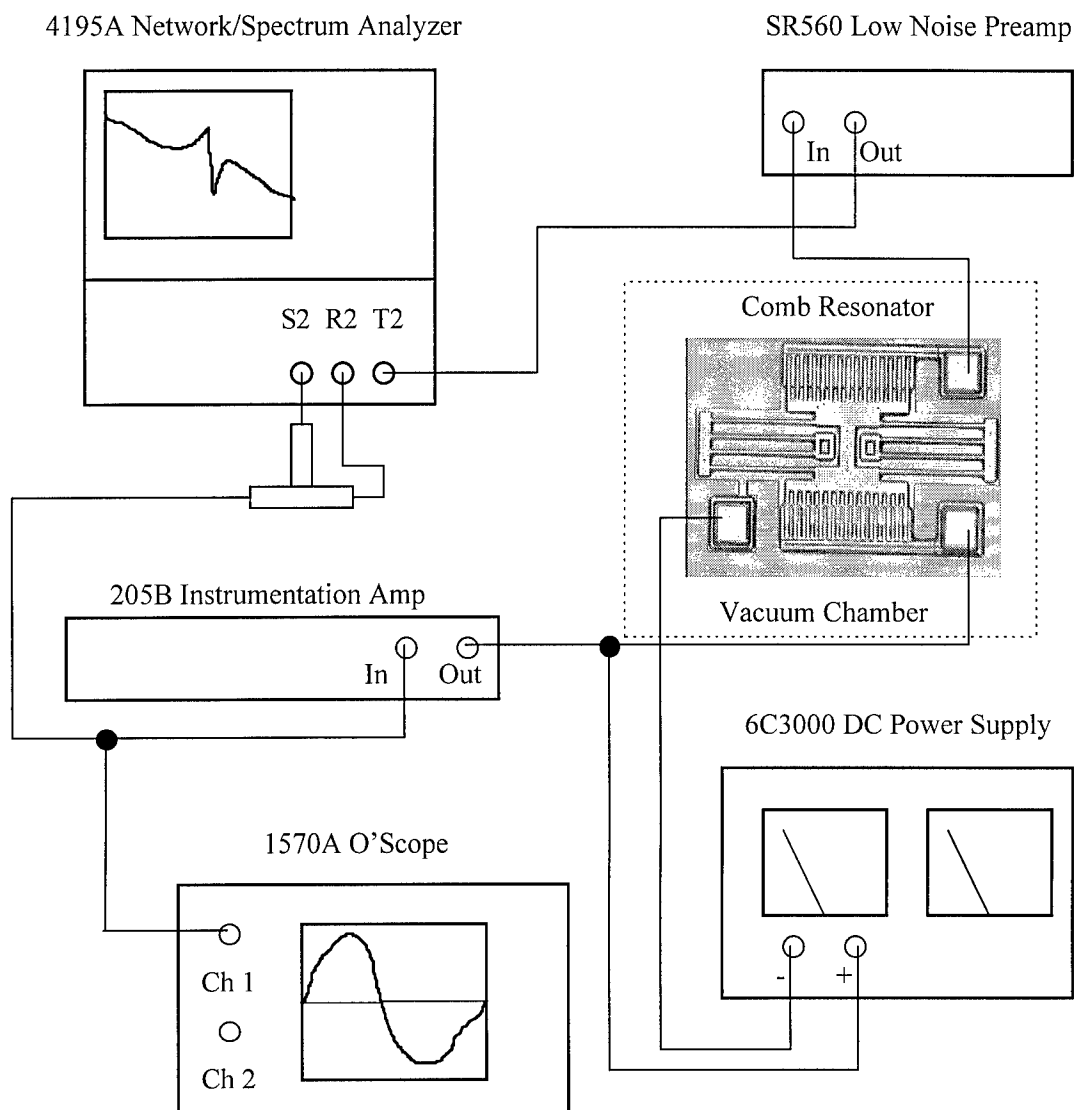
Figure 4-7 - Comb resonator test setup. This setup was used to test comb devices. The DC bias is applied across the ground plate and drive. The resonance observed on the network analyzer is half of the actual resonance when the DC voltage is zero. When sufficient DC bias is applied, the actual resonance of the comb is observed on the network analyzer. Varying the DC bias from that point permits tuning of the resonant frequency of the device under test. The connections from the vacuum chamber are made with SMA to coaxial cables. All other connections are made with standard coaxial cables. T-connectors are used at the cable junctions.

Table 4-4 - Comb Test Procedure.

Step	Operation
1	Insert test die in vacuum chamber and initiate vacuum following procedures in Table 4-2 and Table 4-3.
2	Turn on test equipment
3	Select ports on 4195A using the procedures described in the operation manual. Either combination of S1, R1, T1 or S2, R2, T2 can be used.
4	Set S1 or S2 to low setting (-40 dBm)
5	Connect equipment as shown in Figure 4-7.
6	Set DC bias to 20 V
7	Set Preamp to a gain of 20. Frequency range (band limit) can also be set.
8	Set instrumentation amp to a gain of 10
9	Probe the die as illustrated in Figure 4-7.
10	Adjust S1 or S2 to approximately -11.5 dBm, R1 or R2 to 10 dB, and T1 or T2 to 20 dB. Ensure waveform output from the 4195A after amplification by the instrumentation amplifier is approximately 2.25 V peak to peak using the oscilloscope.
11	Set start and stop frequencies in the approximate range of the expected resonance. Use the span and center frequency adjustments to zoom in on resonance.
12	Record changes of resonant waveform under changing signal and DC source values.

For one port devices, such as cantilevers and mirrors, the setup is slightly different. The source waveform is superimposed on a DC bias, as shown in Figure 4-8. The procedures for testing these devices, shown in Table 4-5, vary from the comb test procedures only in the amount of applied drive.

Table 4-5 - Cantilever and Mirror Test Procedure.

Step	Operation
1	Insert test die in vacuum chamber and initiate vacuum following procedures in Table 4-2 and Table 4-3.
2	Turn on test equipment
3	Select ports on 4195A using the procedures described in the operation manual. Either combination of S1, R1, T1 or S2, R2, T2 can be used.
4	Set S1 or S2 to low setting (-40 dBm)
5	Connect equipment as shown in Figure 4-8.
6	Set DC bias to 5 V or less
7	Set Preamp to a gain of 100. Frequency range (band limit) can also be set.
8	Set instrumentation amp to a gain of 5
9	Probe the die as illustrated in Figure 4-8.
10	Adjust S1 or S2 slowly up to approximately -9.9 dBm, R1 or R2 to 10 dB, and T1 or T2 to 30 dB. Ensure waveform output from the 4195A after amplification by the instrumentation amplifier is approximately 1.3 V peak to peak using the oscilloscope. It is important not to overdrive these devices or damage will result. Start at a low drive and slowly increase until resonance is noted.
11	Set start and stop frequencies in the approximate range of the expected resonance. Use the span and center frequency adjustments to zoom in on resonance.
12	Record changes of resonant waveform under changing signal and DC source values.

Figure 4-8 - Cantilever and mirror test setup. This setup was used to test one port devices. The DC bias is applied in series with the AC source. The resonance observed on the network analyzer is half of the actual resonance, since the DC is not applied across the device. Varying DC bias changed the resonant frequency of the device under test. The connections from the vacuum chamber are made with SMA to coaxial cables. All other connections are made with standard coaxial cables. T-connectors are used at the cable junctions.

4.3 MEMS Design Descriptions

This section describes the designs submitted to MCNC for

fabrication. In all, five fabrication runs were met, MUMPs 11 through

MUMPs 15, with the last two runs including SmartMUMPs designs. Since

cantilevers were considered the device of choice for most of the design

period, they represent the majority of the initial designs. The last two runs also focused on many different mirror and comb designs.

4.3.1 MUMPs 11

The intent of the designs on the MUMPs 11 AFIT 2 die, shown in Figure 4-9, was to implement a series of cantilevers that could be used to characterize the device as a resonator, and to determine the drive voltages. The designs used groups of five cantilevers of the same length, with widths of 10, 20, 30, 40, and 50 microns. Groups of cantilevers in lengths of 50, 100, 150, 200, 250 and 300 microns were constructed as shown in Figure 4-10. Three types of layer combinations were used to implement the cantilevers while keeping the dimensional designs the same. Poly1, Poly2, and Poly12 implementations were constructed. Poly1 and Poly12 cantilevers have a 2 micron gap between the device and the underlying Poly0 sense/drive layer. The Poly2 cantilevers have a 4.75 micron gap, so they can be driven harder. This large gap is caused by etching away the Poly1 (2.0 microns), First Oxide (2.0 microns), and Second Oxide (0.75) layers, leaving the Poly2 beam free-standing. The Poly12 cantilevers are the thickest, measuring 4.25 microns, since they a 2 micron Poly1 layer, a

0.75 micron oxide layer, and a 1.5 micron Poly2 layer sandwiched together.

Therefore the Poly12 cantilevers are the stiffest, and will resonate at higher

frequencies.
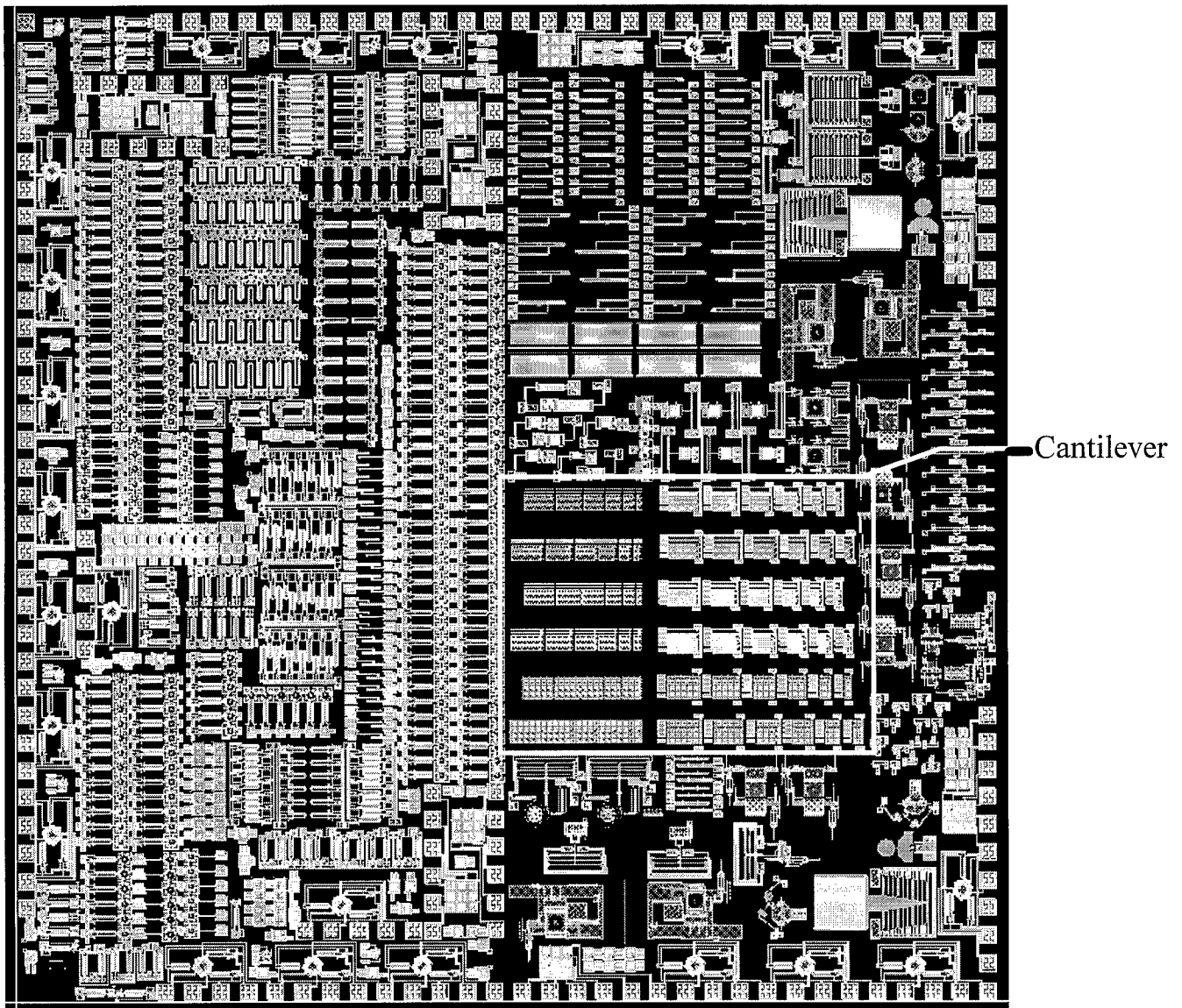
Cantilever

Figure 4-9 - Cadence layout of MUMPs 11 AFIT2 die.
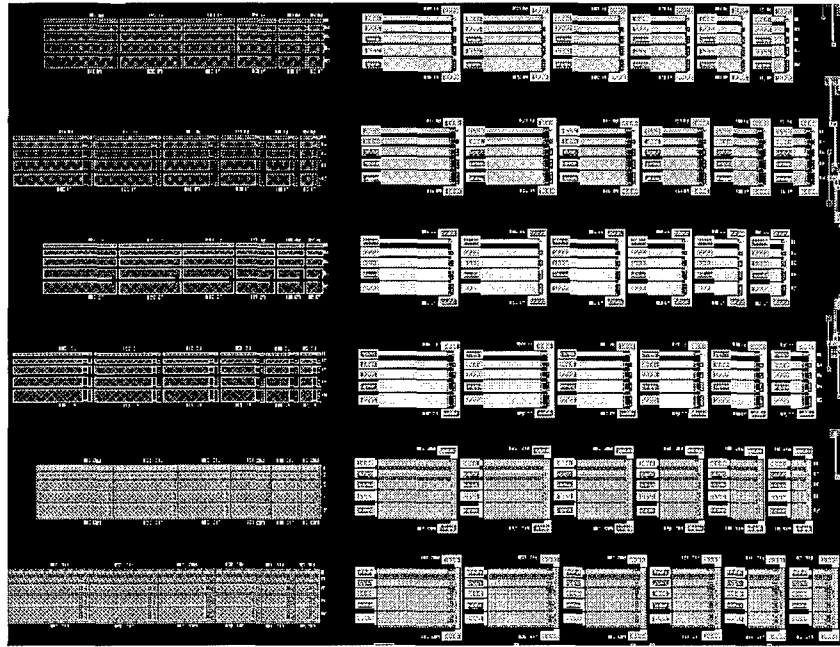
Figure 4-10 Close-up of cantilevers on MUMPs 11 AFIT2 die.

Each group
of cantilevers
has a label to
identify
materials. P1
100 means
beam is made
of poly 1, and
is 100 µm
long *.

Cantilever
stuck down

Probe Pads
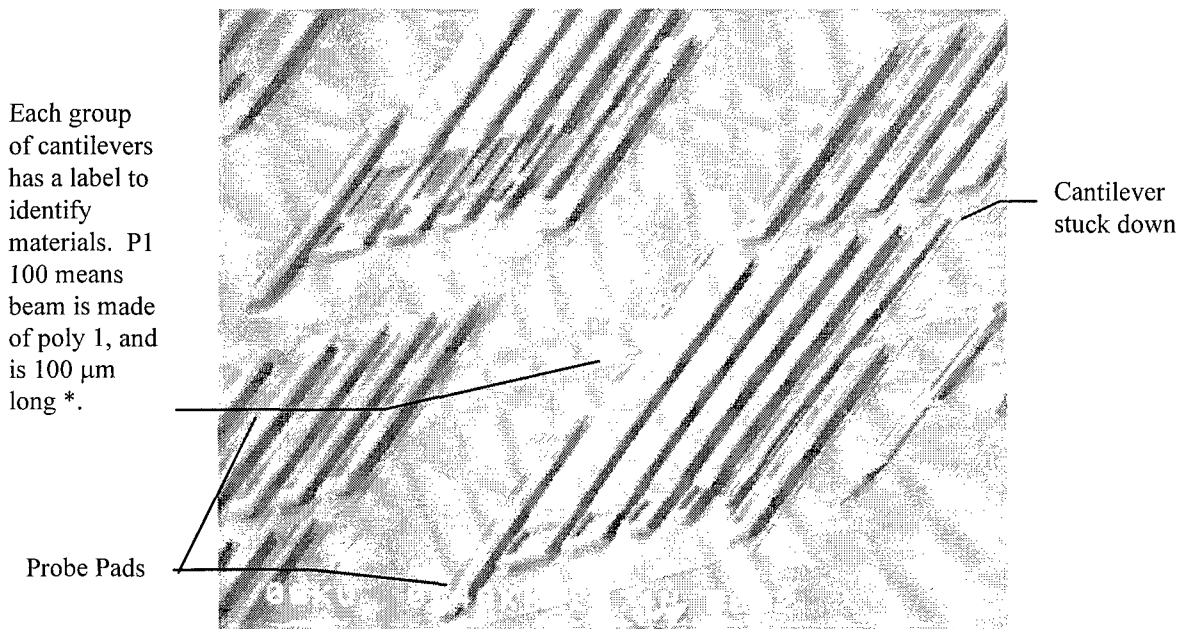
* Some of the devices on MUMPs 12 were labeled incorrectly. The beam length is actually 25 µm longer
than labeled. These devices can be identified by an elongated connection at the common end as
described in Figure 4-12.

*Figure 4-11 - SEM of MUMPs 11 cantilevers. Cantilevers designed in
groups of five, each cantilever in the group having equal length, varying in
width. Probe pads allow testing of the devices with the micromanipulator.*

Figure 4-11 is a micrograph of a group of Poly1 cantilevers using the

Scanning Electron Microscope (SEM). The same design, as it appears in

the Cadence CAD tool, is shown in Figure 4-12.
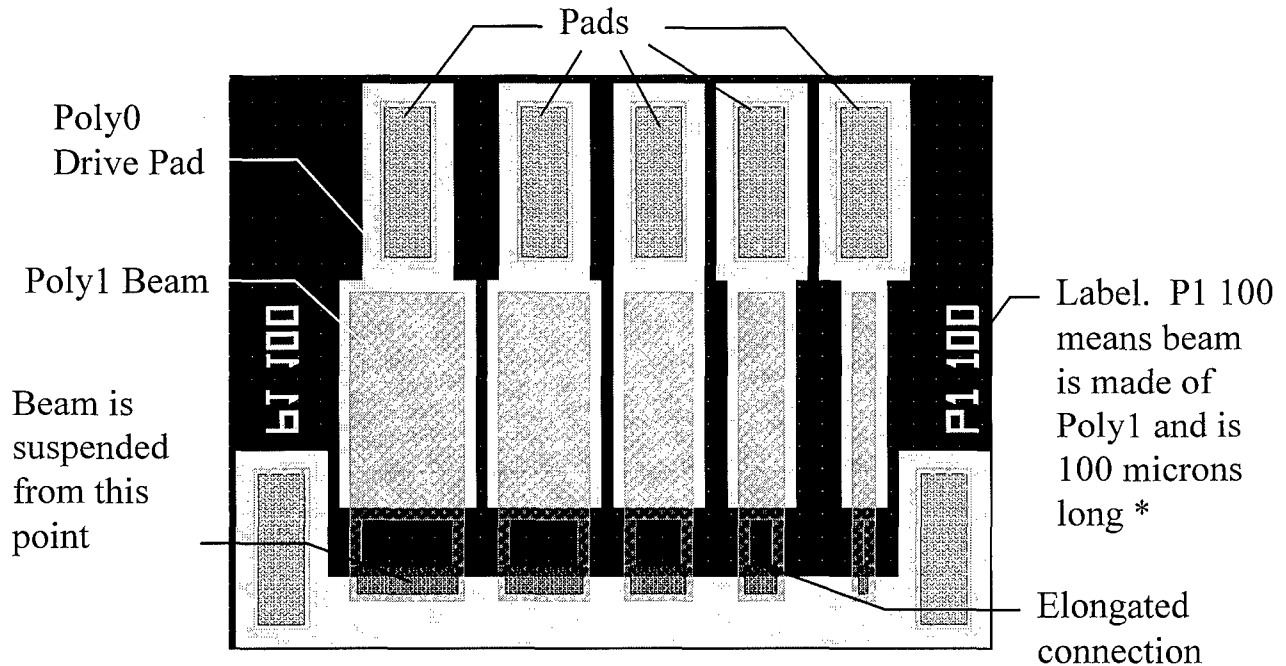
* The gap between the common spine and the solid part of each beam is 25 μm in the design shown. This must be added to the labeled beam length, which is 100 μm, for a total of 125 μm. Half of the cantilevers implemented have this elongated connection, and are therefore labeled incorrectly.

Figure 4-12 - Cadence layout of cantilevers shown in Figure 4-11. The widths are varied from 50 microns (left) to 10 microns (right) in 10 micron intervals.

4.3.2 MUMPs 12

Only a few devices were placed on the MUMPs 12 AFIT3 die.

Figure 4-13 shows these devices. The intention of the design was to

experiment with separate drive and sense pads. All the cantilevers were

designed using Poly2.
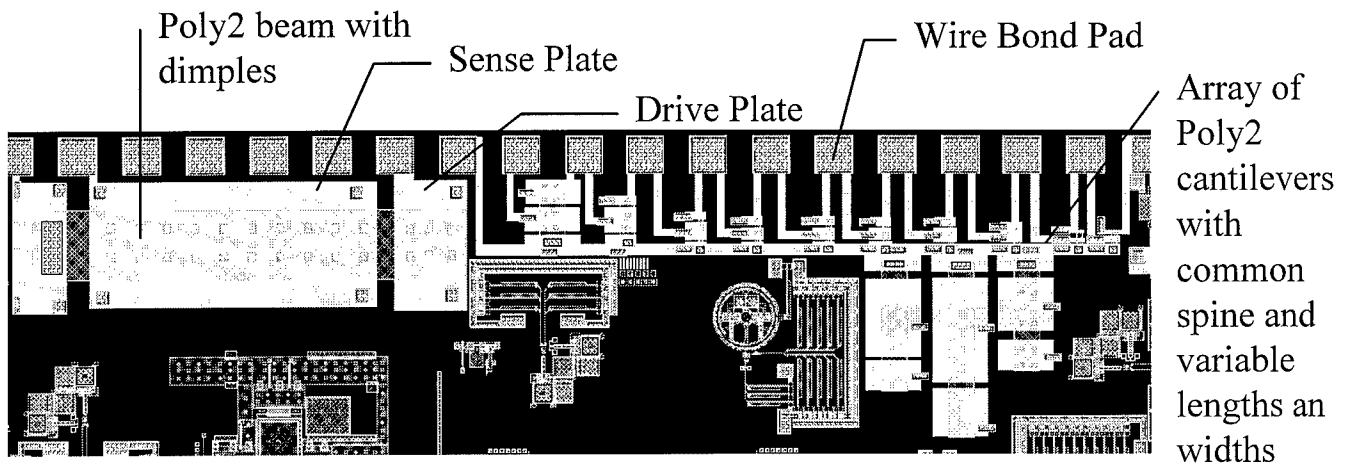
Figure 4-13 - Close-up of cantilevers on MUMPs 12 AFIT3 die.

Another die submitted for this run by Maj. Bill Cowan, MUMPs 12 AFIT 2, included mirror actuators. These devices can also act as resonators, as described in Chapter 3. Figure 4-14 shows the devices laid out in three columns of different lengths. Actuators are arranged in groups of five as shown in Figure 4-15. The first pad of each group is common to all actuators in the group. Individual actuators are selected by placing drive across the common pad, and the pad connected to the bottom plate of the chosen device. The first column is actuators of 88 micron length with two flexures. The center and right columns are four flexure actuators with lengths of 147 and 86 microns, respectively. The top row of each column is a sampling of five different flexure widths. Each of these widths is subsequently repeated on their own row. The widths are 1.0, 1.25, 1.5, 1.75,

and 2.0 microns. The implemented flexure array is shown in Figure 4-16.

Each of the individual actuators, as shown in Figure 4-17, is made of a

Poly0 drive plate below a Poly1 top plate. Added to the top plate is a Poly2,

oxide, and gold sandwich to give it additional mass. Figure 4-18 is a close-

up Cadence design of the actuators describing the key features.
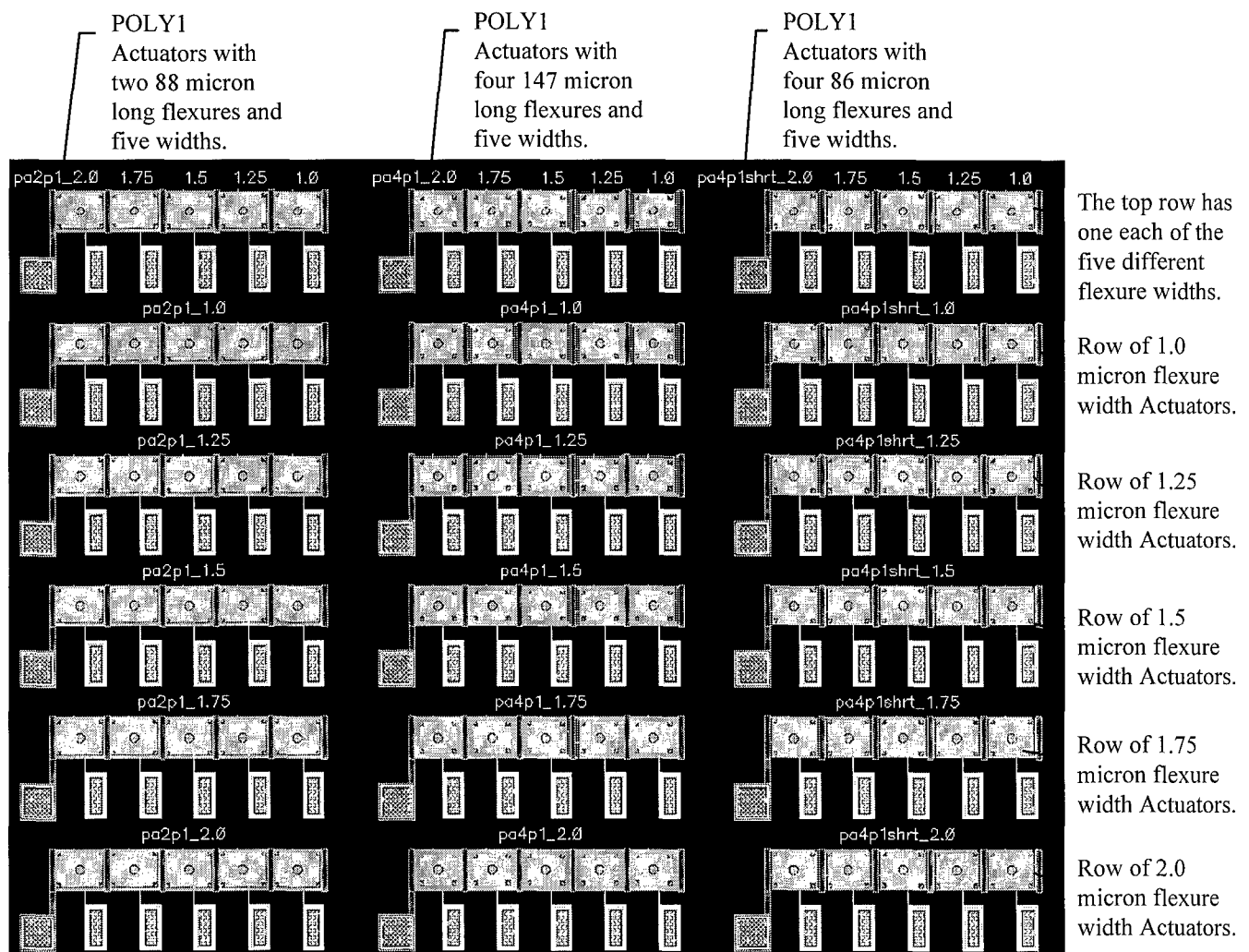
Figure 4-14 - Cadence layout of MUMPs 12 AFIT 2 Actuators.
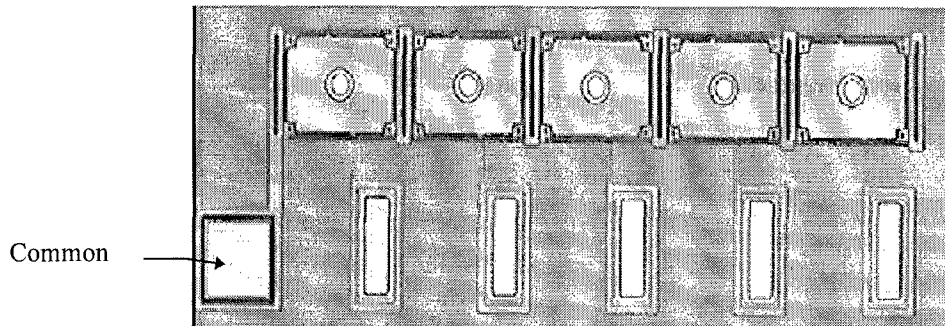
Common

Figure 4-15 - Snapshot of a group of implemented actuators on MUMPs 12. The square pad (left) is common to all actuators. The individual actuators are driven by placing a drive signal across the common pad and the pad that corresponds to the actuator. The devices were implemented in three flexure lengths (86, 88, and 147 micron). The 86 and 147 micron length flexure actuators have four Poly1 flexures suspending the Poly1 top plate above a Poly0 bottom plate. The 88 micron length flexure actuators have two flexures and uses the same materials as the four flexure actuators. The width of the flexures was varied from 1.0 to 2.0 micron in 0.25 micron increments.

POLY1
Actuators with
two 88 micron
long flexures and
five widths.

POLY1
Actuators with
four 147 micron
long flexures and
five widths.

POLY1
Actuators with
four 86 micron
long flexures and
five widths.

The top row has one each
of the five different
flexure widths.

Row of 1.0 micron flexure
width Actuators.

Row of 1.25 micron flexure
width Actuators.

Row of 1.5 micron flexure
width Actuators.

Row of 1.75 micron
flexure width Actuators.

Row of 2.0 micron flexure
width Actuators.

Figure 4-16 - Snapshot of MUMPs 12 Actuators. Video snapshot of actuators implemented from the Cadence design described in Figure 4-14. The size of the top plates of the three actuator types in microns is 86x66, 70x58, and 78x66 for the three columns, left to right respectively.

Flexure
(88 by 1.25 microns)

Poly2/Gold
added mass

Poly1 Top Plate
(86 by 66 microns)

Poly0 Wire
connecting Poly0
Bottom Plate to
external pad (not
shown)

Flexure
(147 by 1.25 microns)

Poly2/Gold
added mass

Poly1 Top Plate
(70 by 58 microns)

Poly0 Wire
connecting Poly0
Bottom Plate to
an external pad
(not shown)
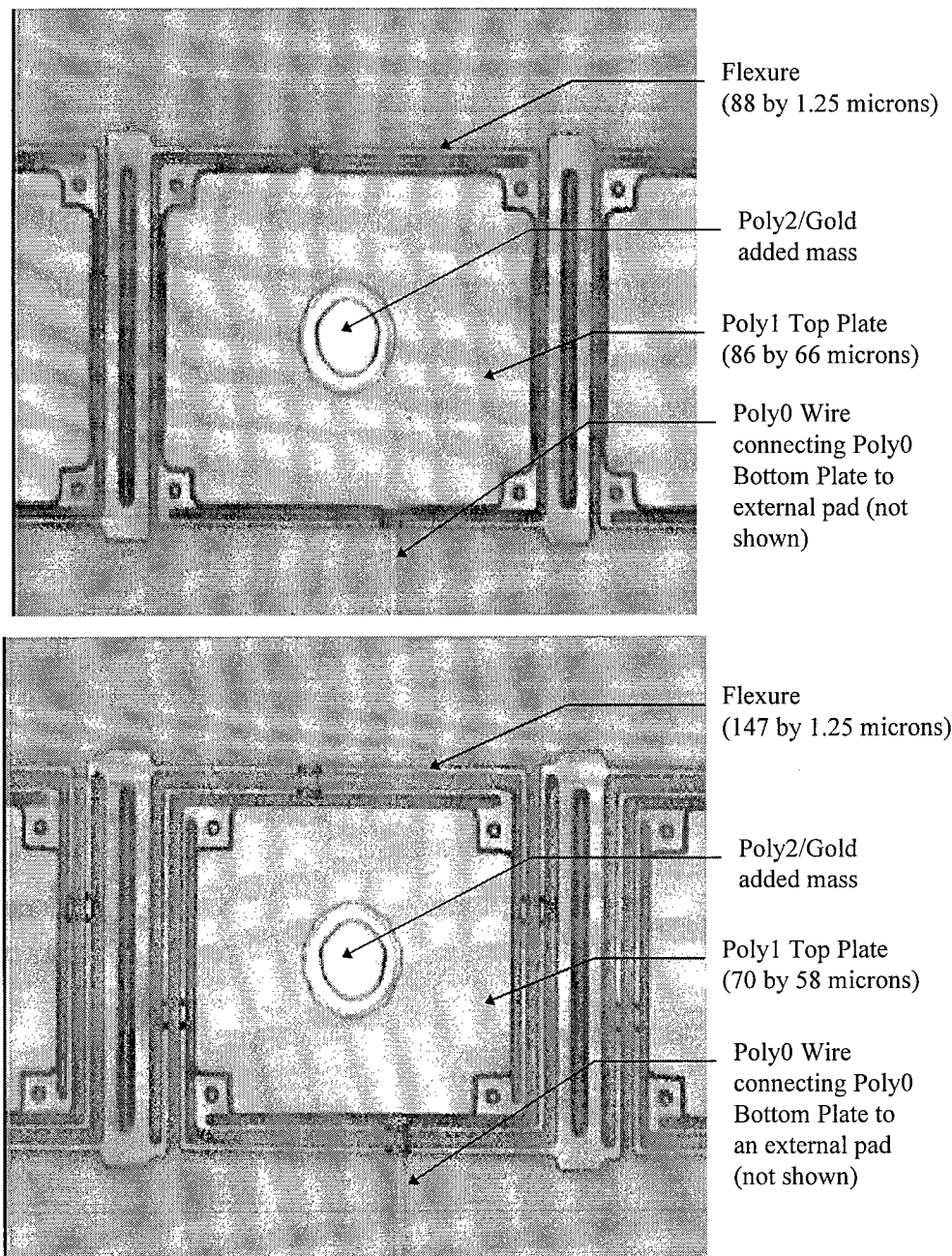
Figure 4-17 - Snapshot of two and four flexure actuators. Close-up video snapshot of implemented two and four flexure actuators on MUMPs 12. The two flexure actuator (top) has a flexure length of 88 microns. The four flexure actuator (bottom) has a flexure length of 147 microns. The flexure widths of both mirrors is 1.25 microns. The Poly0 bottom plate is directly below the Poly1 top plate, and cannot be seen in the snapshot.
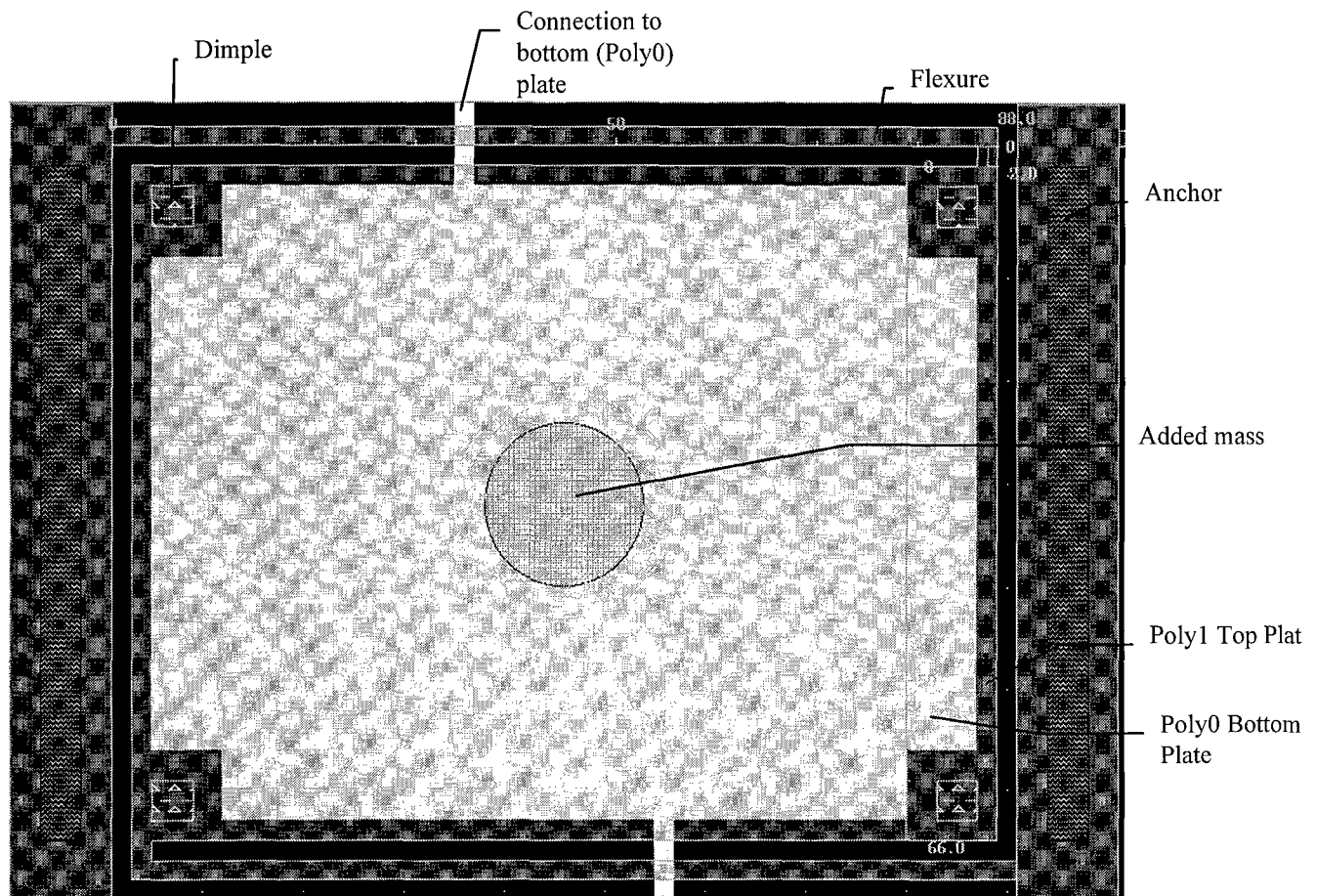
Figure 4-18 - Close-up of a two flexure actuator. The top plate, made of POLY1, is suspended above a plate of POLY0 by two 88 micron flexures. The flexures extend to structures on both sides that are anchored to the substrate. The circular structure in the center is made of POLY2, oxide, and gold and is added to increase the mass of the plate. The gold also acts as a reflective surface, making the structure a mirror. Dimples are added in the four corners of the 86 by 66 micron top plate to help keep it from sticking if it is slammed down onto the POLY0 plate.

4.3.3 MUMPs 13

Figure 4-19 shows the Cadence layout of the MUMPs 13 AFIT3 die. The purpose of this design was to build an array of cantilevers, with a single drive, and separate senses. The cantilevers designed, were a hybrid of those designed in the two previous runs. Groups of cantilevers were connected to
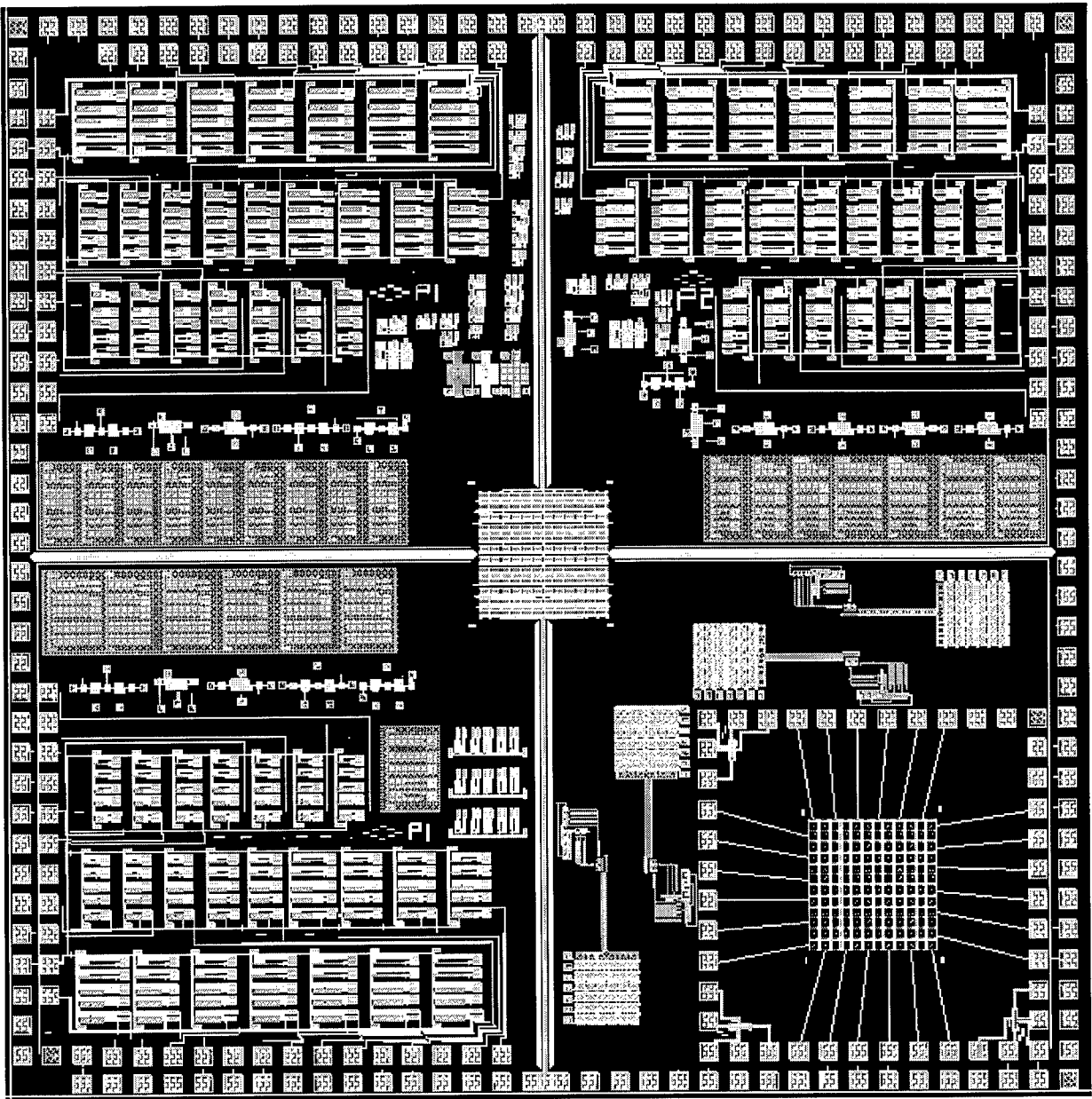
Figure 4-19 - Cadence layout of MUMPs 13 AFIT 3 die.

form the array, as in Figure 4-20, and each cantilever in the group has a

separate drive and sense pad. Two arrays were constructed, one with Poly1

cantilevers, and the other with Poly2. A group of Poly12 cantilevers was added for testing, but not connected in an array.

Figure 4-20 - Close-up of an array of cantilevers on MUMPs 13 AFIT3 die.

4.3.4 MUMPs 14 (SmartMUMPs)

This was the first generally available SmartMUMPs run. As discussed in Chapter 2, the Ecosys die is place on top of the MUMPs die with a predetermined pin layout. MCNC provides a ready-made padframe, shown in Figure 4-21, to place the user defined devices. While the center of the chip, within the inner padframe, can be used to place devices, those
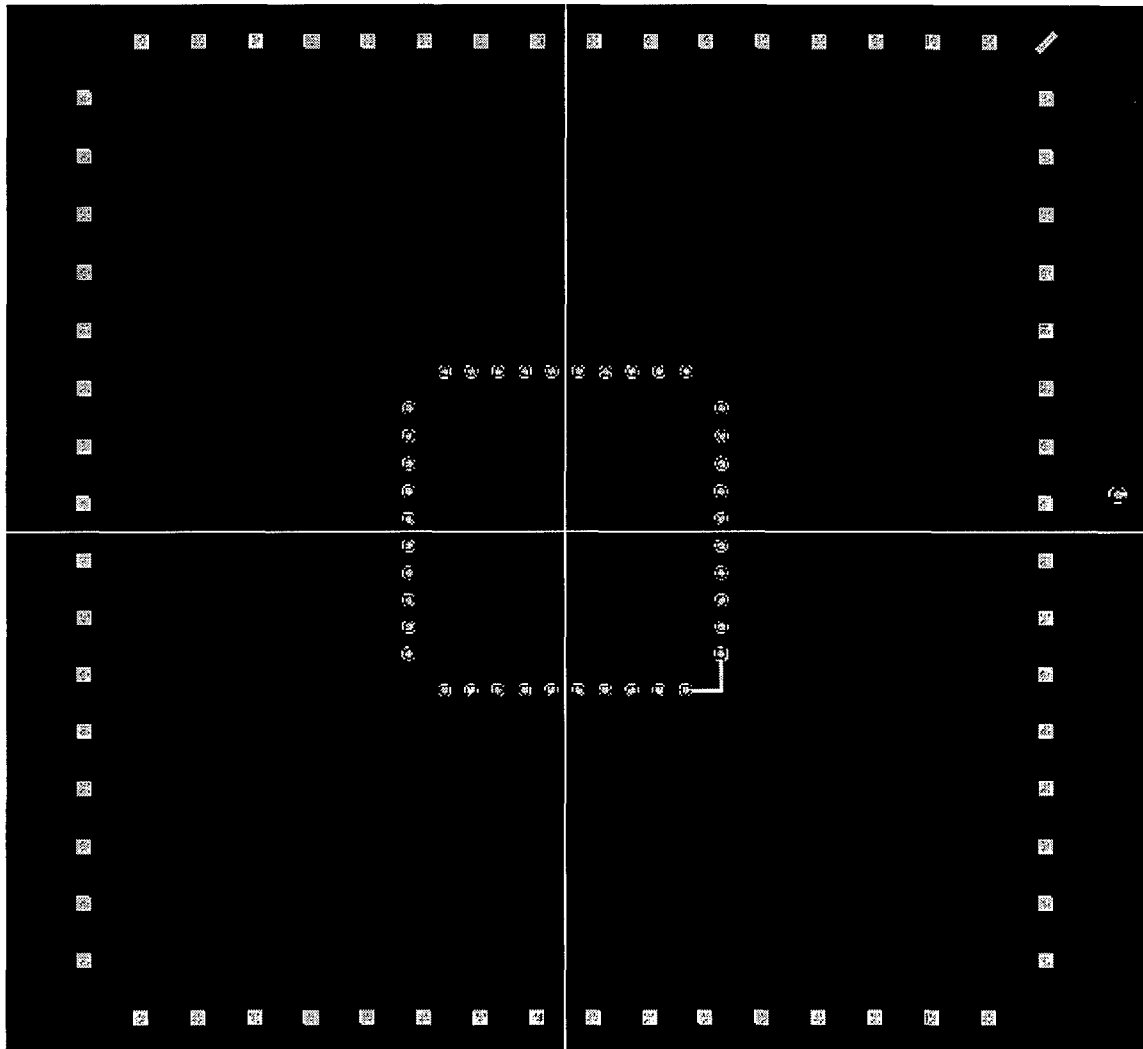
Figure 4-21 - SmartMUMPs Pad Frame supplied by MCNC [6]. The Ecosys die is soldered directly to the inner padframe. The outer padframe is wire bonded to a standard package.

devices will be covered by the Ecosys die. The Ecosys die is soldered

directly to the inner padframe. The outside padframe is wire bonded to a

standard package. As with standard MUMPs run, approximately 15 of the

die are returned. With SmartMUMPs, however, it is not necessary to
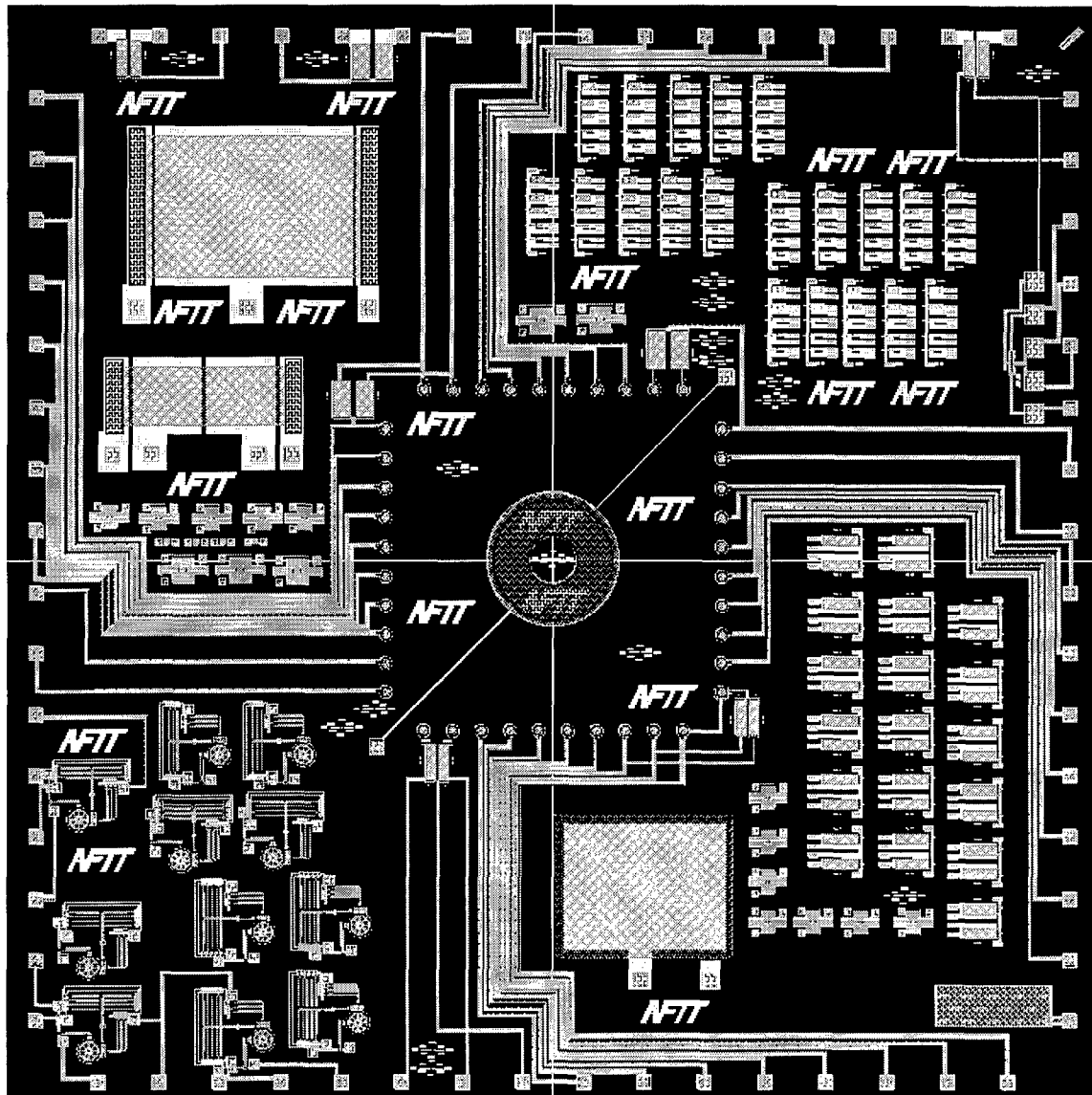
Figure 4-22 - Cadence layout of MUMPs 14 (SmartMUMPs). Four cantilever devices are connected to the Ecosys circuits. Most of the inner padframe required for the Ecosys chip are routed to the outer padframe. The bottom right pad of the outer padframe is connected to the substrate by breaching the nitride layer. This will be used to ground the substrate.

post-process the die. SmartMUMPs die are returned completely released

and packaged.

One of the disadvantages of using SmartMUMPs is the large amount

of wiring required to the center of the chip. Figure 4-22 is the Cadence

layout for the MUMPs 14 SmartMUMPs die. Only four devices can be
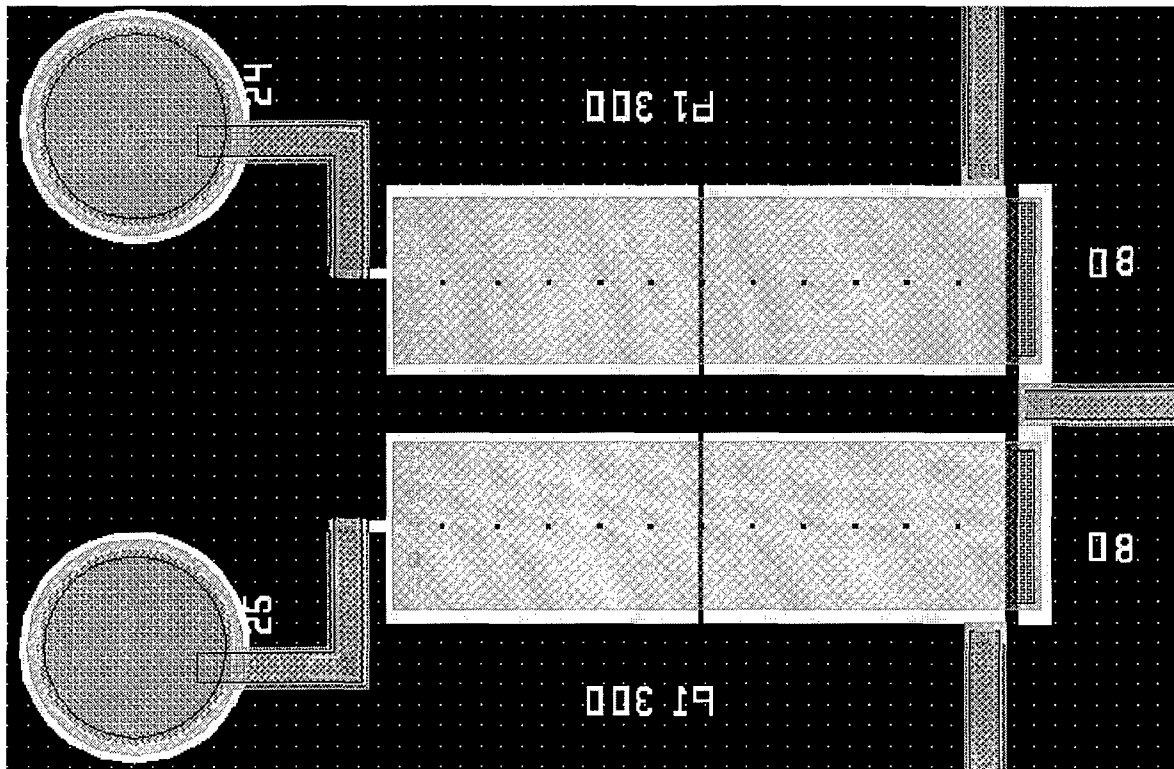
Figure 4-23 - Close-up of Cadence layout of test device connected to TZA circuit.

connected to the Ecosys chip. The wiring is used for input, output, and

control voltages required to run the Ecosys chip. The wiring itself is

designed to be low capacitance, by stacking Poly1, Poly2, and metal, which

is stapled to the substrate approximately every 100 microns.

Different configurations of cantilever devices were connected to each

of the four major Ecosys circuits. Each circuit was connected with guidance

from the SmartMUMPs user's manual [6], as described in Chapter 2.

Figures 4-23 through 4-26 show the cantilever devices connected to the four

Ecosys circuits. The purpose of the dual cantilever design is to use the extra

cantilever as a reference.
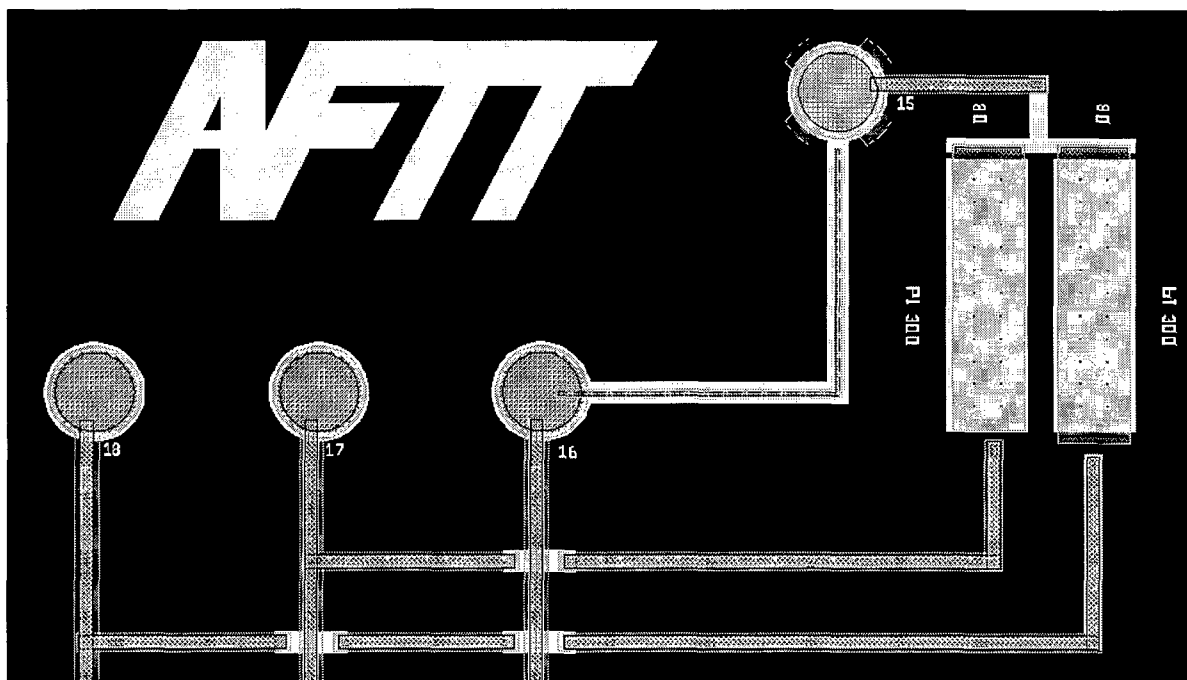
Figure 4-24 - Close-up of Cadence layout of test device connected to BAWDS Circuit.
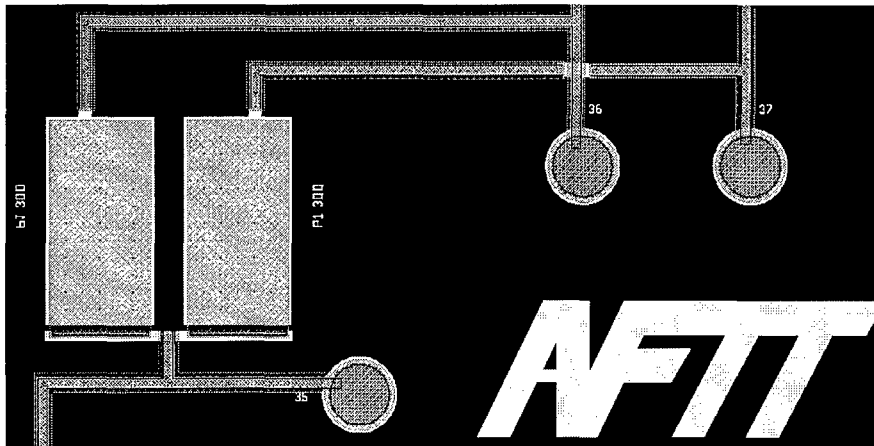
Figure 4-25 - Close-up of Cadence layout of test device connected to CDSInt circuit.
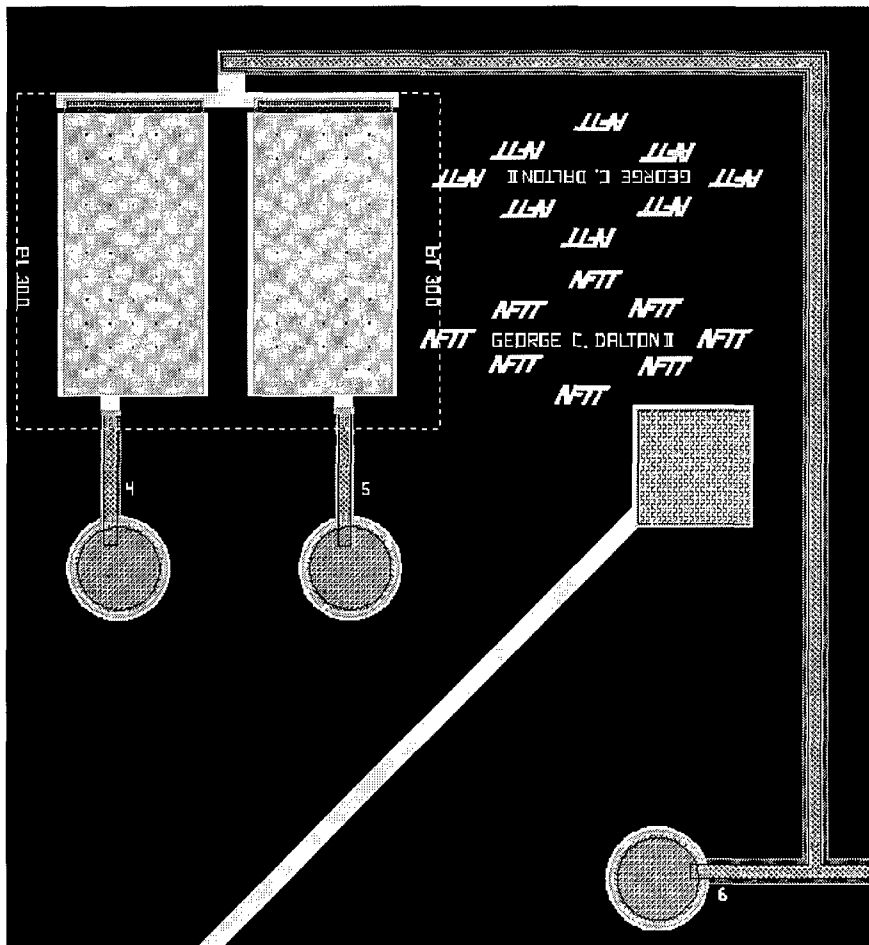
Figure 4-26 - Close-up of Cadence layout of test device connected to DCDSInt circuit.

4.3.5 MUMPs 15

At the time of this design, only one type of comb resonator was available, the MCNC test device. It was clear that comb drives were excellent resonators, and should be further characterized. Resonance had been observed close to predicted values, and the ability to tune these devices with a DC bias was evident. Accordingly, MUMPs 15 focused on these devices. Devices were placed on two separate die. One is a standard MUMPs die, shown in Figure 4-27, and the other is a SmartMUMPs die, shown in Figure 4-28.
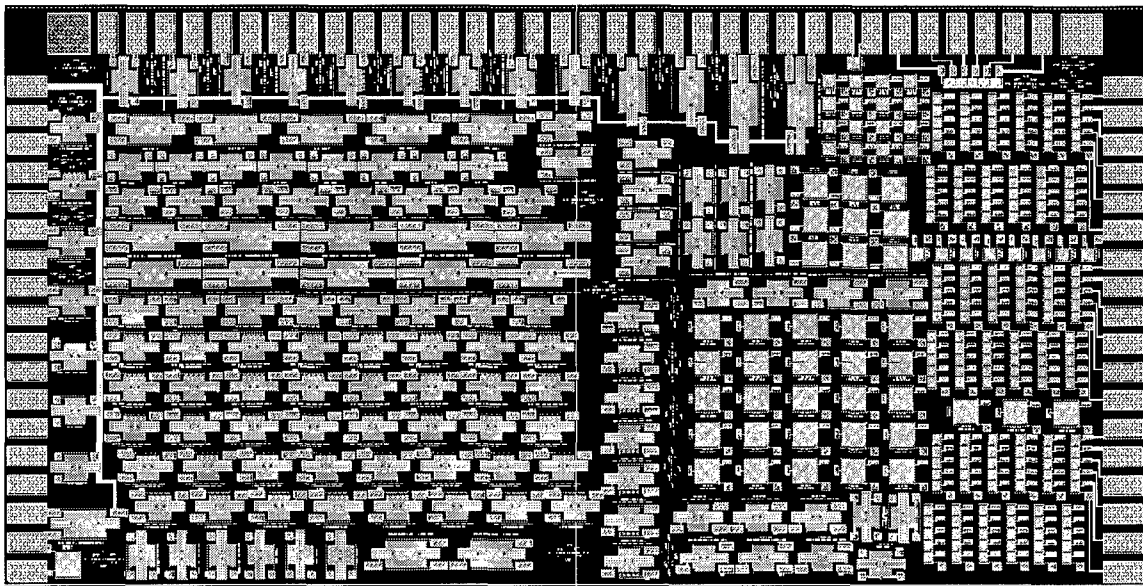
Figure 4-27 - Cadence layout of MUMPs 15 AFIT4. Combs, mirrors, and actuators fill the top half of this die. These will be used to further characterize their properties as resonators.

The left quadrant of AFIT4 is completely devoted to combs as is most

of AFIT8. The right quadrant contains assorted mirrors and actuators that
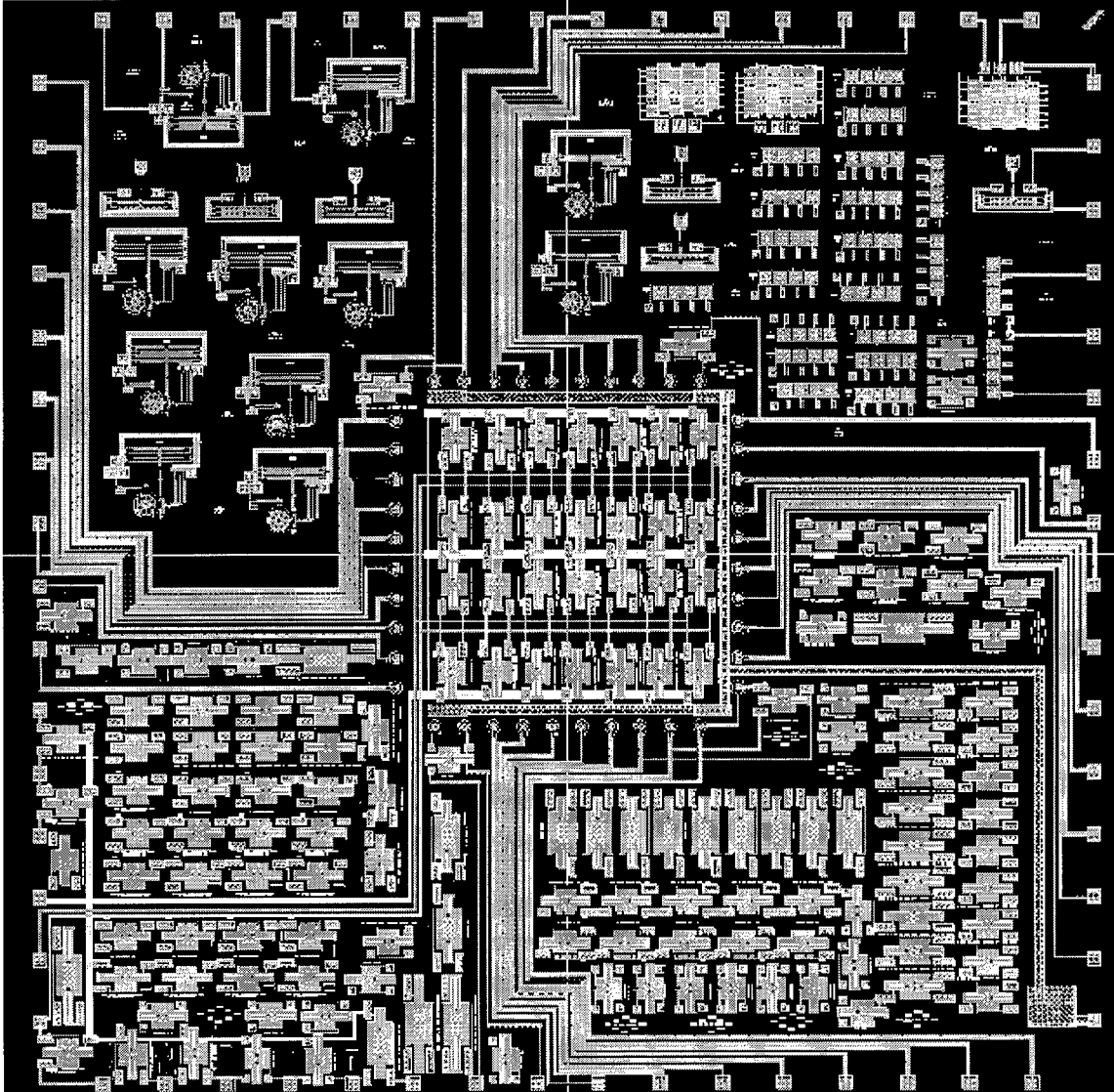
Figure 4-28 - MUMPs 15 AFIT8 (SmartMUMPs). Four comb devices are attached to the Ecosys circuits. Many comb devices, of varying widths, spring lengths, and number of fingers were placed on this die. Note the ground pin is now connected to five nitride breaches, one by the ground pin itself, and the other four adjacent to the devices connected to the Ecosys die. This was done after an ominous warning from MCNC suggesting substrate grounds be placed close to devices connected to the Ecosys die.

can be used to further refine the characterizing setup describe previously, and get a better understanding of how these devices can be used as resonators.

4.4 Circuit Card Design Description

The Artificial Cochlea is to be implemented, in part, on a PC compatible prototype card. These cards are available for under $100 and provide all the required decode logic. They also provide signal isolation of the address and data lines, protecting both the PC and the circuit being prototyped. Using the prototype card simplifies the task at hand, and avoids "reinventing the wheel."

The JDR Microdevices© PDS-601/611, PC Bus Breadboard with I/O Decode Logic, was purchased to implement the artificial cochlea. This prototype board features a large breadboard area, reconfigurable address decoding, clearly labeled test and tie points, and complete isolation from the PC system buses. Bus isolation is provided by 75LS541, gated octal buffers, which also re-drive the signals ensuring proper levels. Another feature is the 74LS245, bi-directional octal transceivers, which gate data to and from the data bus. The Intel 8255, programmable parallel peripheral

interface, is included to simplify the creation of complex multi-port devices, which is exactly what is needed for the artificial cochlea. An Intel 8253, programmable interval timer is also included, enabling the generation of accurate timing delays under software control.

4.4.1 PC Interface

The prototype card interfaces with the PC using the system buses. Predetermined addresses are available to access the various ports on the card. The addresses are selectable by use of a dip switch.

4.4.2 MEMS Interface

The MEMS devices interface with the PC using A/D and D/A converters via the PC Interface. Data registers are used to keep the state for both reads and writes. For instance, to apply a constant DC voltage to a particular device, it is first selected by the software, then its data register is loaded with a value. The value in the register is then converted to a DC voltage by its D/A converter. The applied voltage will not change until the data in the register is updated. Similarly, values read from the device are converted to digital by the A/D converter, and then latched into the data

registers when the device is selected. This data can then be used by the control program to make decisions, or be plotted.

4.5 Software Design Description

While the software to control the artificial cochlea will have to wait until the actual implementation, preliminary design can begin after considering the requirements. The software should be implemented with a

```
                    ┌─────────────────┐
                    │  Main Program   │
                    └─────────────────┘
              ┌───────────┴───────────┐
    ┌──────────────────┐      ┌──────────────────┐
    │  Circuit Card    │      │ Waveform Display │
    │  Control         │      │                  │
    └──────────────────┘      └──────────────────┘
    ┌──────┬──────┬──────┐
 ┌──────┐ ┌──────┐ ┌──────┐
 │ Read │ │Drive │ │Select│
 │Device│ │Device│ │Device│
 └──────┘ └──────┘ └──────┘
```
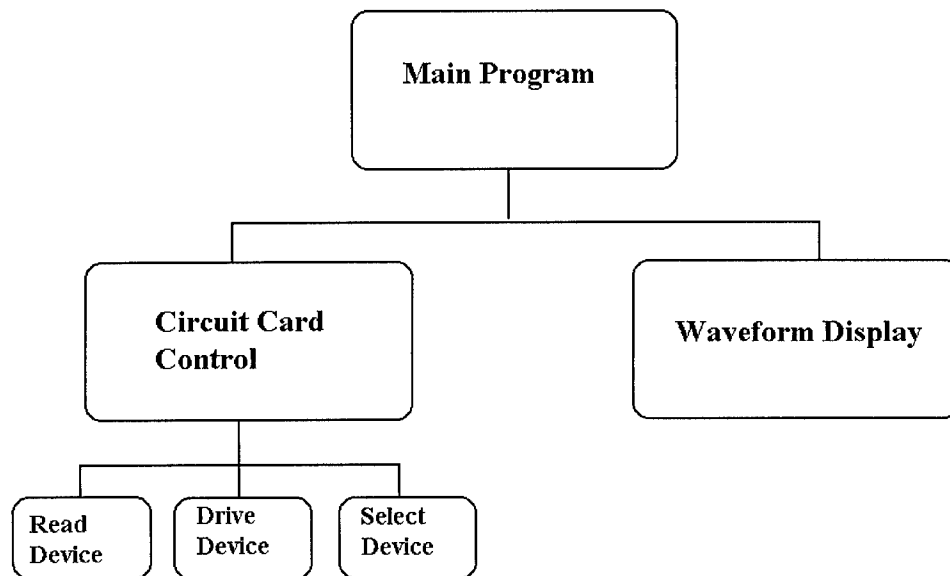
Figure 4-29 - Overall block diagram of control program.

Graphical User Interface (GUI), giving the user full control over the program and the circuit card being controlled. Figure 4-29 is an overall block diagram of the software.

4.5.1 Main Program

The purpose of the Main Program is to interface the user with the Circuit Card, giving the user full control over the MEMS devices.

4.5.2 Circuit Card Control Module

The Circuit Card Control Module contains all of the software to interface with the Circuit Card. It allows devices to be selected, driven, and polled.

4.5.3 Waveform Display Module

The Waveform Display Module allows the data obtained by the Circuit Card Control Module to be displayed. The data can be plotted graphically, or in tables. Both input and output data can be displayed simultaneously.

Chapter 5

5. Results and Discussion

This Chapter describes the individual and overall results of the thesis research. Three general classes of resonators were designed and tested: cantilevers, mirror/actuators, and combs. Resonance is observed for all three classes, and the effects of DC bias is explored. Also, the nonlinear operation of the devices and the Q variance is presented. Observations of how these natural resonators work leads to a new look at the mechanics of the cochlea.

5.1 Results

All of the MEMS devices constructed and tested worked as expected. Two new test setups, described in Chapter 4, were developed empirically until dependable and flexible setups were found. There are so many variables when testing these devices (i.e.: devices that are not fully released, stuck down, etc.) that absolute trust in the set-up is essential. Even so, testing these devices can be tedious. The devices must be placed in the vacuum chamber, probed, driven, and measured. Probing sometimes

damages the device under test. If it was the last device of its kind, then another die must be released, and the process restarted.

Once the developed test set-up proved itself reliable, the results were obtained. The test results of the individual devices are revealed in the following sections. Calculations for the theoretical values are found in Appendix A.

5.1.1 Resonator Design Results

In all, three different classes of resonators were designed and tested: cantilevers, mirror/actuators, and combs. Each of these devices was made to resonate, and measured. Experimentation with varying the Q and the resonant center frequency was conducted, and yielded surprising results. This section describes the results of the experiments.

5.1.1.1 RLC Test Circuit Design

The RLC circuit used to verify the test setup worked exactly as expected. A 100 μH inductor was placed in parallel with a 0.22 μF capacitor and a 100 KΩ resistor (component values are nominal). Since the RLC circuit does not require a vacuum, a slightly modified test set-up based

on Figure 4-7 was used. The RLC circuit was connected to the test set-up

using coaxial to 2-wire cables. The ground wires were tied together, and the

RLC circuit was connected between the two pins that correspond to the

center pins of the coaxial cable. The amplifiers were set to unity gain, and

no DC was applied. The resonant frequency results are shown in Table 5-1

and Figure 5-1.

Table 5-1 - RLC Test Circuit Results.

Calculated Resonant	33932 Hz
Observed Resonant	35625 Hz
% error	5 %
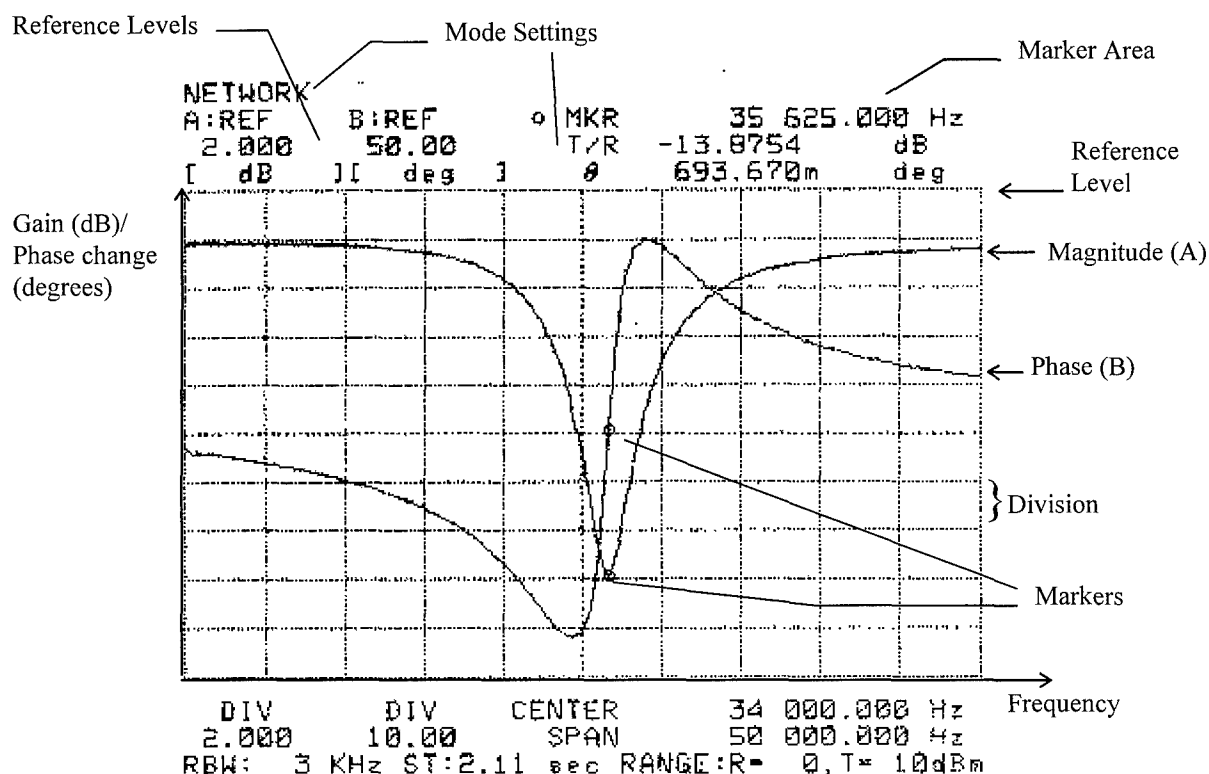
Figure 5-1 - Measured resonance of RLC test device. The 4195A displays all pertinent

information of a plot in the window, which can then be printed. At top left, the mode setting shows the analyzer is in the network analyzer transmission mode (T/R). The x axis is in the frequency domain (in Hertz). In the lower right corner the center frequency and the span of the current window are specified. To determine the frequency per division, divide the span by 10 (the number of divisions across the screen). In this case, the frequency per division is 5 KHz. The range of the frequencies displayed is therefore 9 KHz to 59 KHz. The y axis shows the gain (loss) of the magnitude, trace (A), in dB, and the change in phase, trace (B), in degrees. The reference settings (upper right) indicate the reference value for the vertical divisions at the very top of the display. At lower left, the units per division for the A and B traces are displayed. The leftmost value is the dB/division for the magnitude trace, currently set to 2 dB/division. To the right of that, the degrees/division for the phase trace is displayed, currently showing 10 degrees/division. To find the value of the bottom peak of the magnitude curve, count the divisions from the top (~7.9), multiply by the dB/division (2), and subtract from the reference level (2). This gives -13.8 dB. A better way to do this is to simply place the marker at the peak and read the value from the marker section (top right). The marker section also displays the frequency, in this case the resonant frequency of the RLC circuit, and the phase change from the reference.

The small error can be attributed to the precision of the RLC circuit components used (10 % commercial tolerance), the capacitance and inductance in the test leads, and possibly calibration errors in the test equipment. A five percent error is a good indication that the test setup is measuring what is intended.

5.1.1.2 Cantilever Design

Cantilevers of the three material types, Poly1, Poly2, Poly12, were tested using the setup of Figure 4-8 described in the previous chapter. All of the cantilevers tested are from MUMPs 11. The preamp was adjusted to a gain of 100, while the instrumentation amplifier was set to a gain of 5.

The 4195A source was varied from -9.7 dBm to -11.9 dBm depending on the length of the cantilever. The longer the cantilever, the smaller the drive signal that was required. Also, Poly1 cantilevers had to be driven even less, since the gap between the device and the substrate is less than for the Poly2, 2 vs. 4.75 microns, and it is not as stiff as the Poly12 cantilevers. The drive signal after amplification was less than 1.25 V_{p-p} for all cantilevers tested.

Care must be taken not to overdrive the cantilevers or the devices will be damaged. Along these lines, an interesting case of van der Waals forces in action was noted during testing. If a relatively long cantilever was slammed down with sufficient force, the van der Waals forces continued to pull it down along its length in a whipping motion, evidenced by the resultant damage, that was powerful enough to snap the beam off the layer it was suspended from.

5.1.1.2.1 Observing Cantilever Resonance

The cantilevers were tested using the setup shown in Figure 4-8. Resonance was observed near expected values as shown in Figure 5-2. Both cantilevers are being driven with the same drive signal, 1.25 V peak to peak, with no DC bias. Since the Poly12 cantilever is much more rigid than

the Poly1 cantilever, it has less swing during resonance under the same

drive. Therefore, its return signal is also smaller. With the given drive the
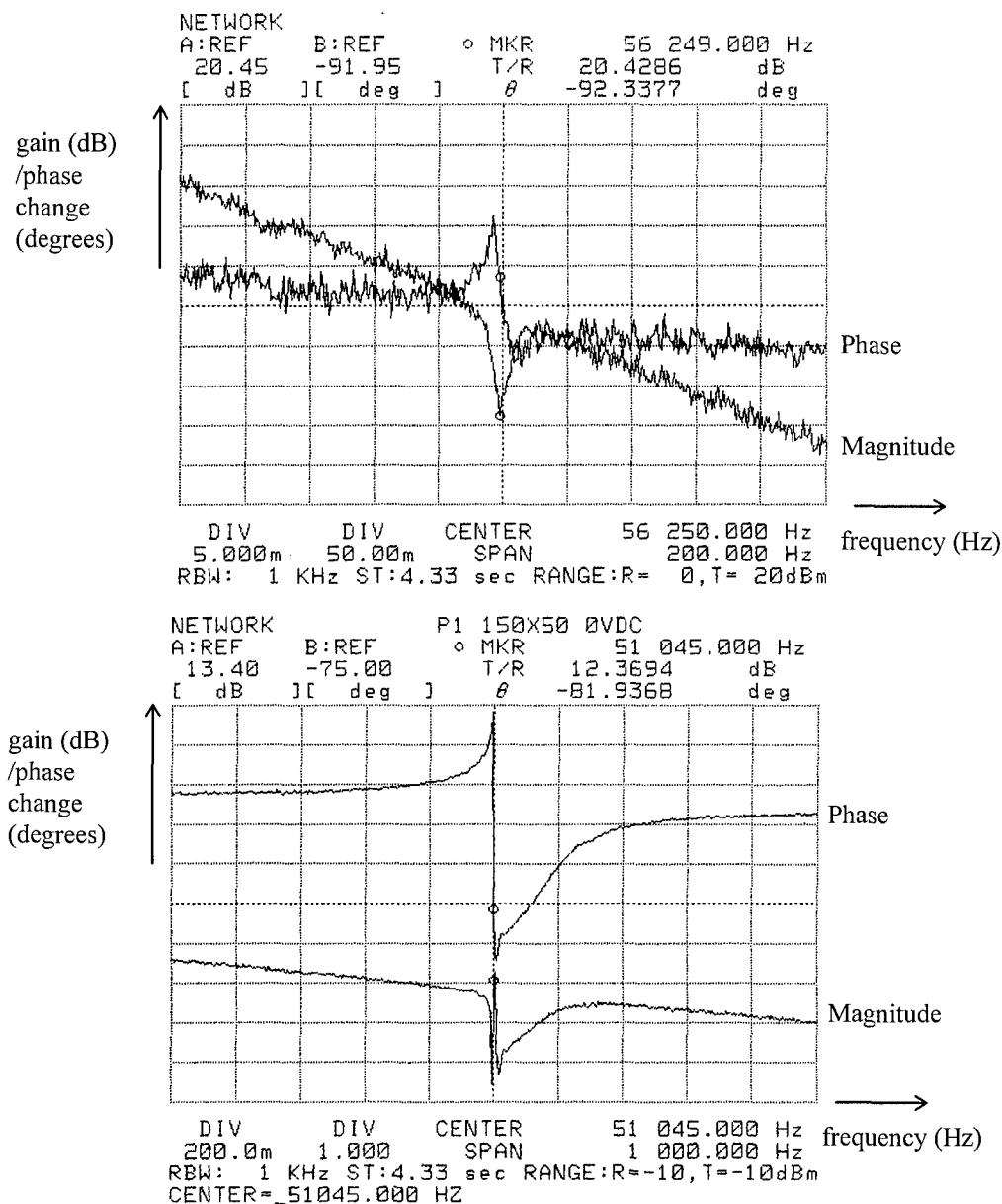
Figure 5-2 - Observed resonance of two cantilevers. Top: A Poly12 cantilever, 200 microns long by 50 microns wide, has an observed resonance of 56.249 KHz. Bottom: A Poly 1 cantilever, 150 microns long by 50 microns wide, has an observed resonance of 51.045 KHz. Both cantilevers are being driven with the same drive signal, 1.25 V peak to peak, with no DC bias and a 20 mTorr vacuum. The actual resonance of both beams is actually twice the value observed when taking into account the frequency doubling effect.

Poly12 cantilever's observed resonance in very noisy. This can be

remedied by applying more drive. The same drive value, however, is

sufficient to drive the Poly1 cantilever out of the noise region.

Poly1 cantilever resonances were observed close to expected values

as shown in Figure 5-3 and Table 5-2. Similarly, Poly2 cantilevers are

shown in Figure 5-4 and Table 5-3. The dominant parameter in the

cantilever resonant frequency calculation is the beam length, since it is a

cubic factor in determining the spring constant in the resonance equation

(Equation 3-1). This is reflected in the theoretical calculations, as well as

observed resonances.
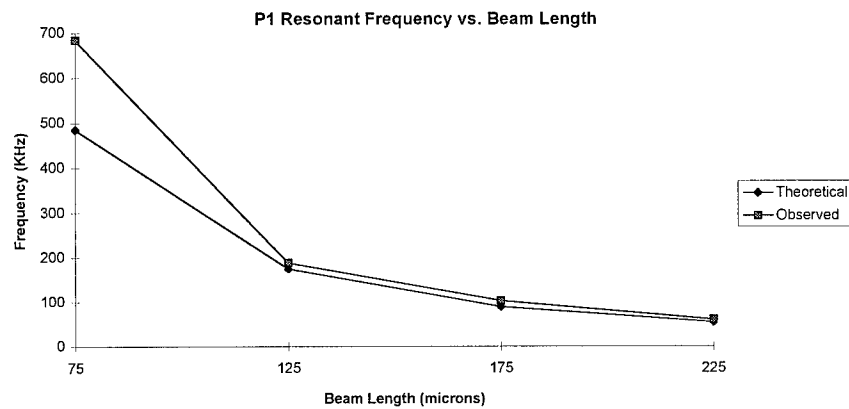
Figure 5-3 - Effect of beam length on Poly1 cantilever resonance. As the length of the cantilever is increased, the resonant frequency decreases as expected from Equation 3-2. The results are for a MUMPs 11 Poly1 cantilever with a 50 micron width (shown in Figure 4-11) with a constant 1.0 V peak to peak drive signal, no DC bias, and a 20 mTorr vacuum. The resonance detected on the 4195A Network Analyzer is half of the actual resonating frequency of the beam as verified with a laser interferometer.

Table 5-2 - Poly1 Cantilever Beam Length vs. Resonant Frequency.

Beam Length	Theoretical Resonance (KHz)	Observed Resonance (KHz)†	% Error (Theo-Obs)/Theo * 100
75	485.1	683.38	40.87
125	174.6	187.83	7.58
175	89.1	102.09	14.58
225	53.9	59.50	10.39

† The frequencies in this column are the observed multiplied by 2 to account for the frequency doubling effect.
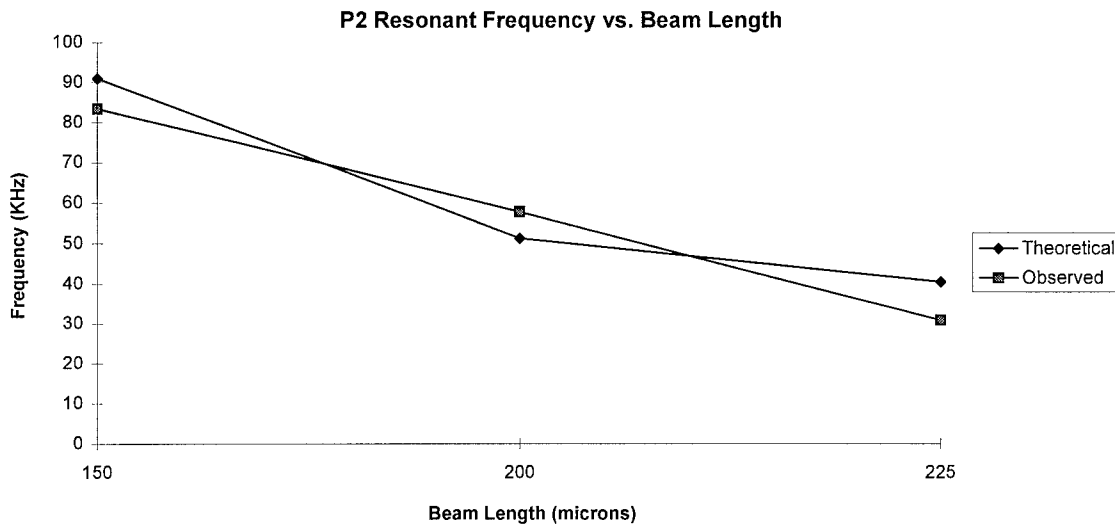
Figure 5-4 - Effect of beam length on Poly2 cantilever resonance. As the length of the cantilever is increased, the resonant frequency decreases as expected from Equation 3-2. The results are for a MUMPs 11 Poly2 cantilever with a 50 micron width with a 1.25 V peak to peak drive signal, no DC bias, and a 20 mTorr vacuum.. The resonance detected on the 4195A Network Analyzer is half of the actual resonating frequency of the beam as verified with a laser interferometer.

Table 5-3 - Poly2 Cantilever Beam Length vs. Resonant Frequency.

Beam Length	Theoretical Resonance (KHz)	Observed Resonance (KHz) †	% Error (Theo-Obs)/Theo * 100
150	91.0	83.45	8.30
200	51.2	57.73	12.75
225	40.4	30.72	23.96

† The frequencies in this column are the observed multiplied by 2 to account for the frequency doubling effect.

Several factors can be cited for the error between theoretical and observed resonance. Placement of probes on the test pads has a significant effect on the resonance. Where and how the probes are place can change the resonance observed on the network analyzer up to 10%. This is most likely caused by the stress placed on the materials at different points, and the capacitance of the probes. Likewise, capacitive loading of the device by external connections and test equipment may also be a factor in the disagreement, since the capacitance of the devices being measured is very small, measured in femto Farads, and the capacitances of the external connections are orders of magnitude greater.

5.1.1.2.2 Varying Cantilever Resonance

As discussed in Chapter 3, the width of the cantilever, b, is only a factor in determining Q, not the resonant frequency. This suggests that the width of the beam has no effect on resonance. However, experimentally this was shown not to be completely accurate. Changing the width varies

P2 Resonant Frequency vs. Beam Width

P12 Resonant Frequency vs. Beam Width
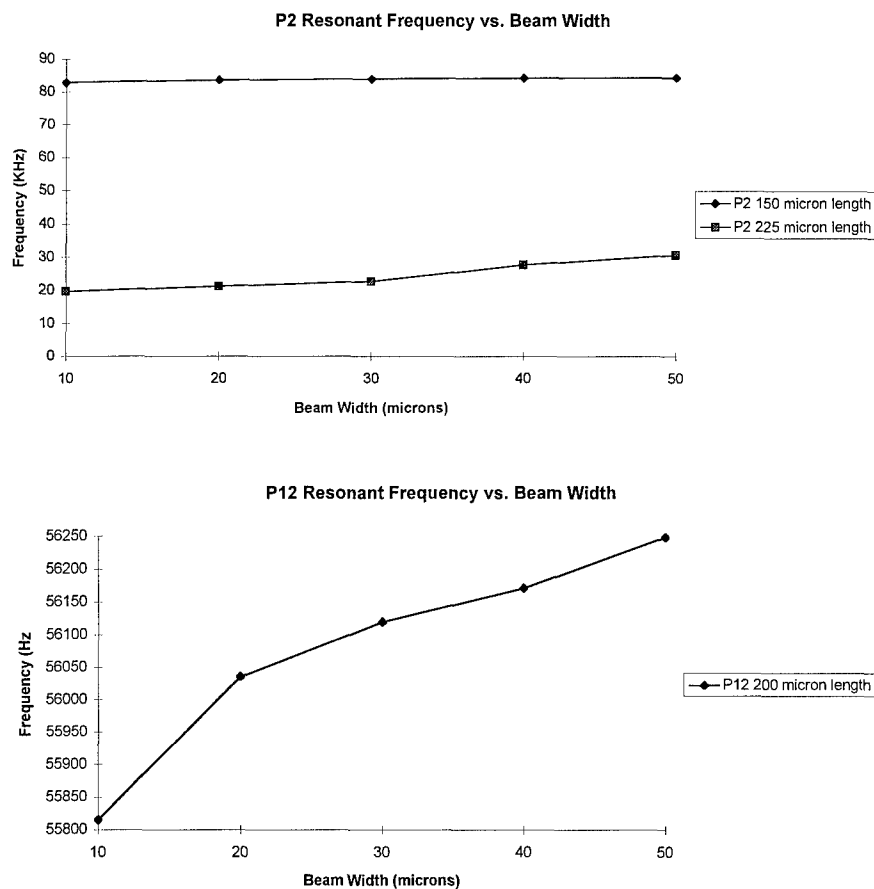
Figure 5-5 - Effect of beam width on cantilever resonance. As the width of the beam increases, the resonance frequency increases. This is not modeled in the resonant frequency equation (Equation 3-2) for cantilevers, and appears to have greater affect on longer beams. All cantilevers are from the MUMPs 11 die. All devices were driven with a 0.8 V peak to peak drive signal, with no DC bias, in a 20 mTorr vacuum.

the resonance slightly. Figure 5-5 shows the effect of varying the width of the cantilever. The effect is small relative to the actual resonance of the beam, but should be taken into consideration. Interestingly, varying beam width seems to affect longer beam more than shorter ones. This can be explained in terms of added stiffness. Since the shorter beams are already more rigid than longer beams, adding more width only increases the stiffness of the shorter beams slightly. Conversely, the longer beams are relatively more flexible, and increasing the beam width increases their rigidity more significantly. Since the resonant frequency is directly proportional to the beam stiffness, the more rigid a beam is, the higher its resonance.

The more interesting result is the effect of DC bias on resonant frequency. As demonstrated in Figure 5-6, the resonance of a cantilever can be tuned significantly by superimposing a DC bias on the drive source. The cantilever can be tuned through a span of over 16 KHz with a 23 volt bias. At 24 volts, however, the cantilever is slammed down. Operating close to this region is not recommended. Transients, like those generated when the air table compressor turns on, will cause the device to slam down if operating near the region of instability.

The reason for this effective tunability can be found in the equation for capacitance (Equation 3-5). As the DC bias value is increased, the distance between the plates decreases. Since the capacitance is inversely proportional to this distance, the capacitance increases. However, the resonant frequency is inversely proportional to the capacitance, therefore the resonant frequency decreases. After a certain point, the force down on the beam caused by the DC bias and drive signal is greater than the upward force of the springs, and the beam slams down.

P12 Cantilever Resonant Frequency vs. DC Bias
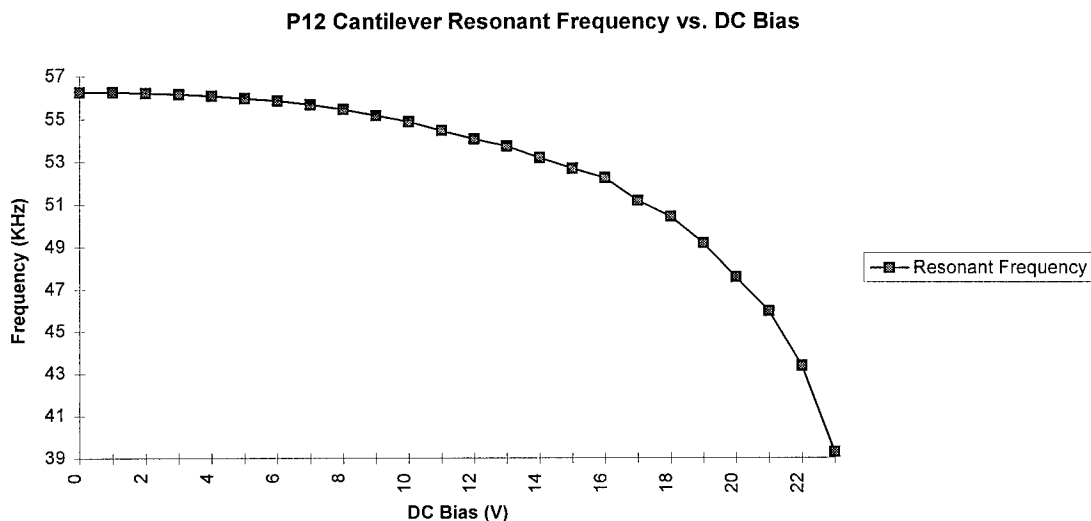
Figure 5-6 - Effect of DC bias on cantilever resonance. As the DC bias superimposed on the drive signal is increased, the resonant frequency of the cantilever decreases exponentially. The device is a Poly12 cantilever, 200 microns long by 50 microns wide driven with a constant 1.25 V peak to peak drive signal in a 20 mTorr vacuum. Voltages greater than 23 volts cause the cantilever to contact the substrate.

5.1.1.3 Mirror/Actuator Design

Similar to cantilevers, mirrors and actuators can be resonated perpendicular to the substrate. When used as resonators, there is no difference between an actuator and a mirror. Both are simply masses suspended by springs. Resonance was observed on over 75 individual actuators using the set-up shown in Figure 4-8. The observed resonances were very close to the predicted values, validating both the equations used to determine the resonance and the process used to implement the devices. Additionally, over 30 resonance measurements on three devices were conducted as the DC bias was varied using the same set-up.

Three types of actuators were tested. One is a two flexure actuator with flexure lengths of 88 microns. The other two are four flexure actuators with 86 and 147 micron lengths. Each type has five different flexure widths: 1.0, 1.25, 1.5, 1.75, and 2.0 microns. The actuators are labeled PA, for piston actuator, followed by the number of flexures, the material of the top plate, and the width of the actuator. For example, PA2P1_1.0 is a 2 flexure piston actuator with a top plate made of Poly1, and a flexure width of 1.0 microns. For the four flexure actuators, the 86

micron length flexure length actuators have an additional element in the label, "shrt", to distinguish them from the 147 micron length actuators (i.e.: PA4P1_1.0_shrt). All of the actuators tested are MUMPs 12 AFIT2 die designed by Major Bill Cowan.

5.1.1.3.1 Observing Actuator Resonance

Resonance of actuators was observed in the frequency range of 44 KHz to 127 KHz. Figure 5-7 shows the resonant waveform of two actuators using the setup described in Figure 4-8. Notice that the waveform of the two flexure actuator (labeled PA2P1_1.0) has two resonances. The reason for this is that the two flexures have slightly different lengths as implemented. Some of the actuators tested showed even greater frequency variations between the resonant peaks of different flexures. This can be accounted for by slight differences in the way the flexures were drawn in Cadence. When measuring resonance of the actuators with multiple resonances, the most predominant resonance was used. In the case of multiple resonances of comparable size, then the first resonance was used.

NETWORK   PA2P1_1.0
A:REF   B:REF   o MKR   59 825.000 Hz
-8.000   -40.00   T/R   -10.8466   dB
[dB   ][deg]   θ   -86.3889   deg

gain (dB)
/phase
change
(degrees)

2 Flexure Piston Actuator
86 x 66 micron top plate
88 x 1.0 micron flexures
Poly1

Phase

Magnitude

DIV   DIV   CENTER   58 775.000 Hz   frequency (Hz)
1.000   5.000   SPAN   20 000.000 Hz
RBW: 1 KHz ST:4.33 sec RANGE:R=   0,T= 10dBm

NETWORK   PA4P1_1.5
A:REF   B:REF   o MKR   51 250.000 Hz
-1.000   -48.00   T/R   -4.87716   dB
[dB   ][deg]   θ   -67.7627   deg

gain (dB)
/phase
change
(degrees)

4 Flexure Piston Actuator
70 x 58 micron top plate
86 x 1.5 micron flexures
Poly1

Phase

Magnitude

DIV   DIV   CENTER   52 900.000 Hz   frequency (Hz)
1.000   2.000   SPAN   10 000.000 Hz
RBW: 1 KHz ST:4.33 sec RANGE:R=   0,T= 0dBm

Figure 5-7 - Observed actuator resonance. The resonance of two and four flexure actuators is observed on the 4195A network analyzer. The source voltage was set to 0.8 V peak to peak, with no DC bias voltage applied, inside a 20 mTorr vacuum. The 2 flexure actuator (top) demonstrates the effect of slight differences in the flexures.

5.1.1.3.2 Varying Mirror/Actuator Resonance

Excellent results were obtained working with actuators. Figure 5-8 and Table 5-4 shows the actual verses theoretical change in resonance when the flexure width of a PA2P1 actuator was varied. The error averaged about 10%, which is very good considering the variables involved. The chief contributor to this error is most likely that the flexures were modeled as straight beams, when in fact they include bends. The theoretical length was calculated on the straight portion of the beams, ignoring a small portion of the beam after the bend. The actuators are from MUMPs 12, and were driven with a 0.3 V peak to peak signal with no DC bias applied. Surprisingly, the 1.0 and 1.25 micron width flexures had resonances further apart than expected. The values should be closer together, since AFIT students have shown that there is little to no difference in the implemented size of these widths. The MUMPs design rules state that the minimum width of these flexures should not be less than 2.0 microns. However, in the time honored Air Force custom dating back to the days of Chuck Yeager, pushing the limits of the design rules proved them to be conservative. The error for the 1.25 width flexures then is actually greater than recorded. As

with cantilevers, probe placement is one possible explanation for the

disparity.

PA2P1 Resonant Frequency vs. Flexure Width
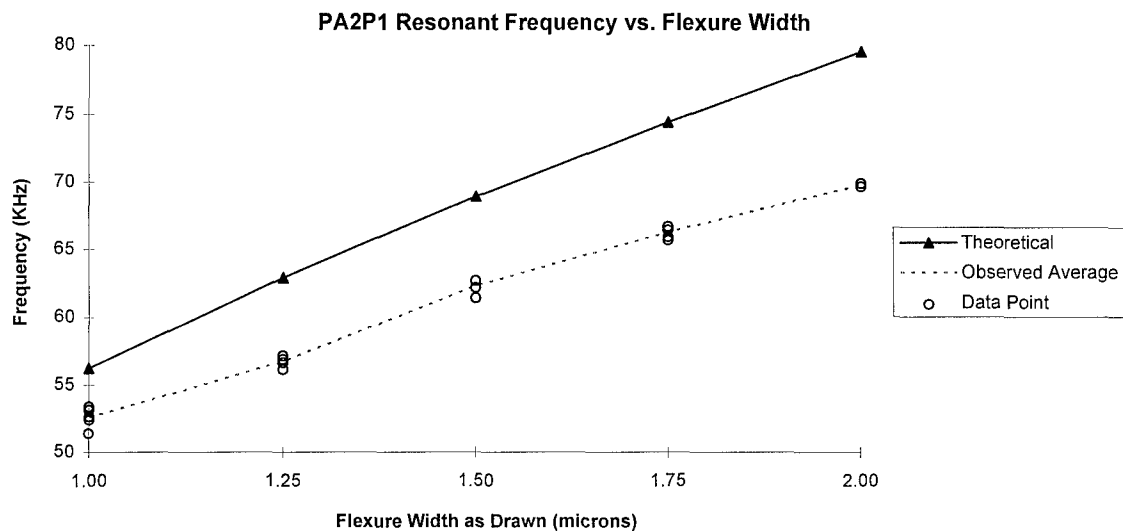
Figure 5-8 - Effect of flexure width on two flexure actuator resonance. The resonance of the two flexure actuators with 88 micron length flexures is measured for five flexure widths, ranging from 1.0 to 2.0 microns. The source voltage was set to 0.8 V peak to peak, with no DC bias voltage applied, inside a 20 mTorr vacuum.

Table 5-4 - PA2P1 Flexure Width vs. Resonant Frequency.

Thickness (microns)	Theo Res (KHz)	Actuator1	Actuator2	Actuator3	Actuator4	Actuator5	Observed Ave (KHz)	% Error
1.00	56.25	51.4	52.4	53.15	53.4	52.65	52.60	6.488889
1.25	62.89	56.15	57.15	56.9	56.9	56.65	56.75	9.763078
1.50	68.89	62.15	62.65	61.4	62.65	62.65	62.30	9.565975
1.75	74.41	66.65	66.65	65.65	66.4	65.9	66.25	10.96627
2.00	79.55	69.9	69.9	69.65	69.9	69.65	69.80	12.25644

The results for the four flexure actuators, shown in Figure 5-9 and

Tables 5-5 and 5-6, on the other hand, reflect the 1.0 - 1.25 flexure width
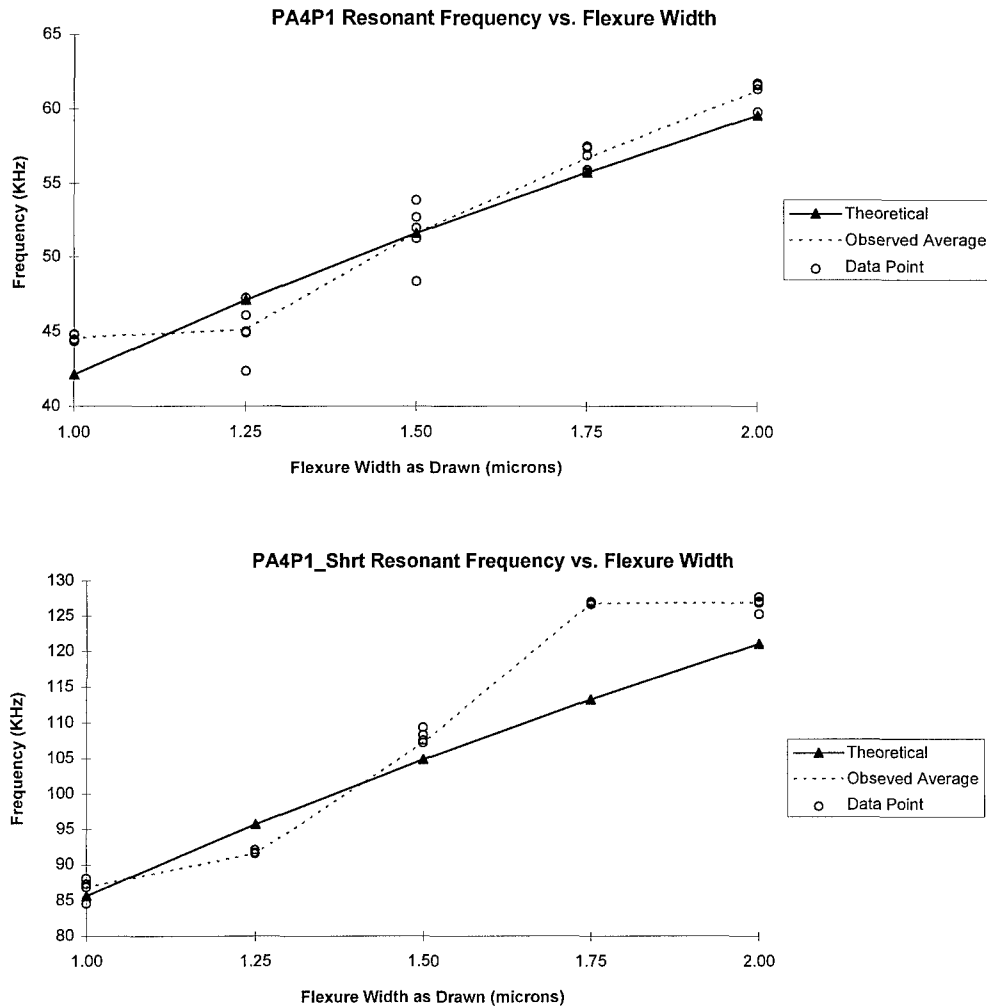
Figure 5-9 - Effect of flexure width on four flexure actuator resonance. The resonance of the four flexure actuators with 147 micron (top) and 86 micron (bottom) length flexures is measured for five flexure widths, ranging from 1.0 to 2.0 microns

Table 5-5 - PA4P1_SHRT Flexure Width vs. Resonant Frequency.

Flexure Width	Theo Res (KHz)	Actuator1	Actuator2	Actuator3	Actuator4	Actuator5	Obs Ave Res (Khz	% Error
1.00	85.63	86.325	84.575	87.325	88.075	88.075	86.88	1.45393
1.25	95.74	90.65	92.125	91.75	91.675	91.6	91.56	4.365991
1.50	104.9	102.9	109.375	108.3	107.9	107.55	107.21	2.197331
1.75	113.3	126.45	127.025	127.075		126.65	126.80	11.91527
2.00	121.1	126.8	127.75	127.125	127.45	125.325	126.89	4.781173

Table 5-6 - PA4P1 Flexure Width vs. Resonant Frequency.

Flexure Width	Theo Res (KHz)	Actuator1	Actuator2	Actuator3	Actuator4	Actuator5	bs Ave Res (KH	% Error
1.00	42.14	44.795	44.815	44.485	44.48	44.36	44.59	5.806834
1.25	47.11	45	42.35	44.9	46.075	47.25	45.12	4.23477
1.50	51.61	48.35	51.25	52.7	51.975	53.85	51.63	0.029064
1.75	55.75	57.537	55.937	57.4	56.9	55.775	56.71	1.721614
2.00	59.6	61.375	61.625	61.75	61.7	59.825	61.26	2.776846

anomaly. It is, in fact, very pronounced for the PA2P1 actuators. Even so,

the error for all these actuators, was very low. The only exception is the

PA4P1_SHRT_1.75 actuators. While the data for the five actuators is very

close, it is 12% off the theoretical value. Again, this is most likely caused

by probe placement.
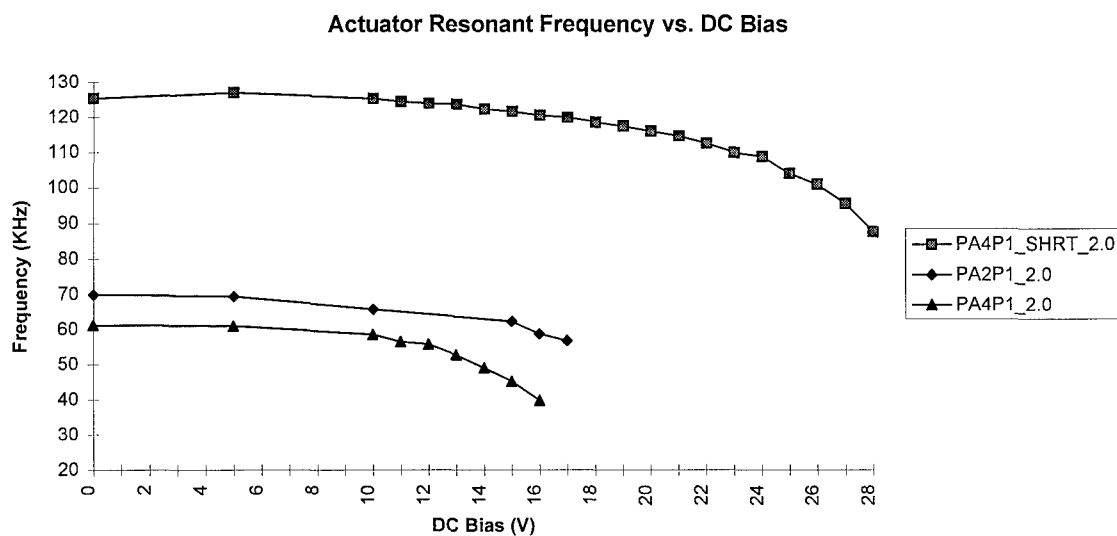
Figure 5-10 - Effect of DC bias on actuator resonance. Similar to the effect on cantilever resonance, a DC bias superimposed on a constant 0.3 V peak to peak drive signal causes the resonance frequency to drop as the DC voltage is increased.

The effect DC bias has on resonance, demonstrated with cantilevers, is also apparent in actuators. Figure 5-10 and Table 5-7 depict the changes in resonance as DC bias is increased. This follows the capacitance argument presented in the cantilever section.

Table 5-7 - DC Bias vs. Resonant Frequency.

	PA4P1_shrt_2.0	PA2P1_2.0	PA4P1_2.0
DC	Frequency	Frequency	Frequency
Volts	KHz	KHz	KHz
0	125.375	69.9	61.25
5	126.9	69.4	61
10	125.25	65.75	58.5
11	124.3		56.5
12	123.8		55.7
13	123.6		52.75
14	122.2		49
15	121.5	62.25	45.25
16	120.45	58.75	39.75
17	119.75	56.75	
18	118.45		
19	117.35		
20	115.9		
21	114.55		
22	112.45		
23	109.8		
24	108.7		

5.1.1.4 Comb Design

Much success was attained using comb resonators. They were the first devices successfully operated and measured. Since the drive signal can be much higher than the other devices tested, so is the sensed output. These devices were used to develop the implemented test setups.

5.1.1.4.1 Observing Comb Resonance

Resonance was observed with a MUMPs 13 comb fairly close to the

theoretical expectation. The theoretical resonance was calculated to be

approximately 25 KHz. The observed, shown measured with the network
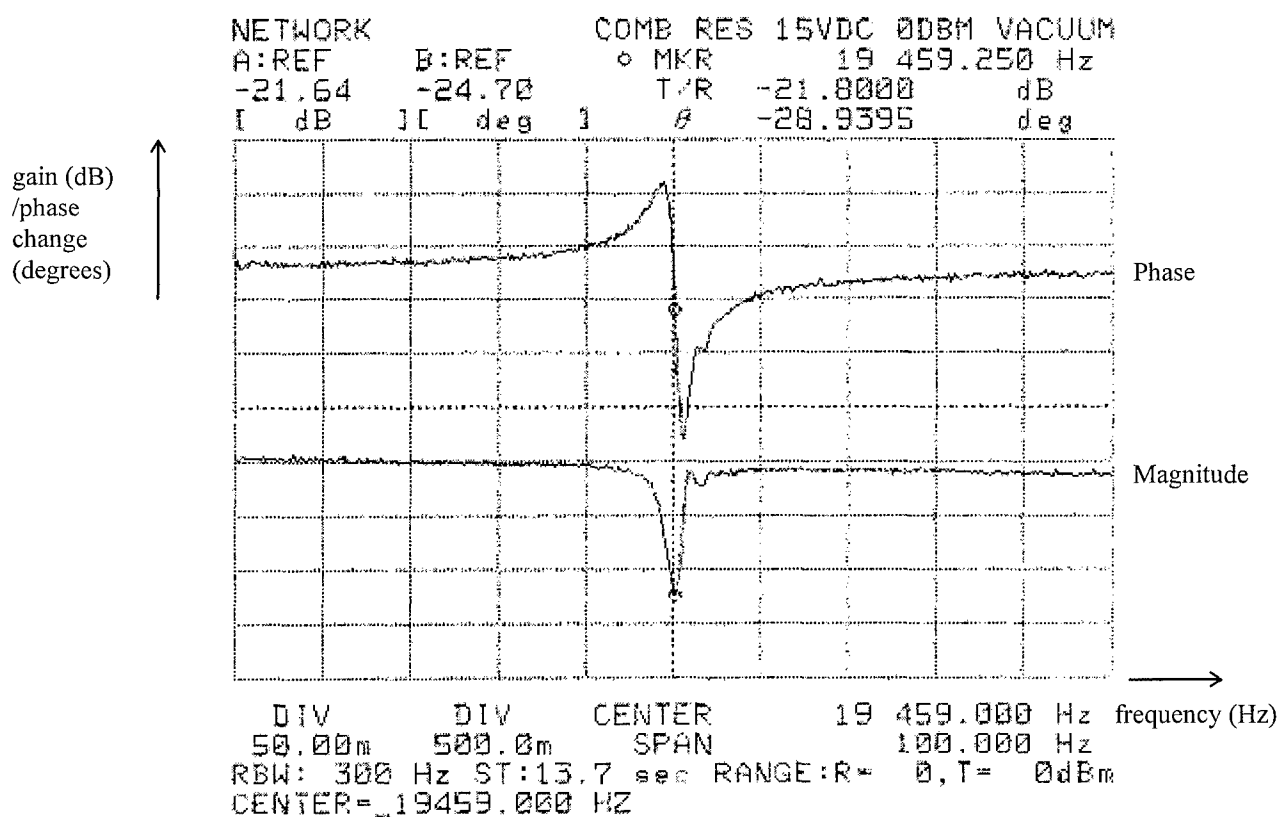
Figure 5-11 - Observed resonance of comb. A MUMPs 13 comb with resonance
observed at 19.46 KHz. The drive voltage was set to 2.25 V peak to peak, with a bias of
15 VDC in 20 mTorr vacuum.

analyzer in Figure 5-11, is approximately 19.5 KHz. The percent error is

computed to be 22 %. There are several reasons this error is somewhat

large. First, when calculating the theoretical value, the effects of vertical

oscillations were ignored. Also, the mass and spring constant were

determined from the design as drawn. The large amount of perimeter area

(e.g.: the comb fingers) is much more susceptible to over-etching compared

to cantilevers and mirrors. Also, there was only one design type for combs

on the runs received to date, so it's difficult to arrive at any conclusion on

the limited data. Tests on MUMPs 15 will yield more results when the die

arrives.

5.1.1.4.2 Varying Comb Resonance

The DC voltage, applied across the drive and ground, was varied and

the resonance measured using procedures of Table 4-4. The results are

plotted in Figure 5-12 using the same device whose resonance was shown in

Figure 5-11. The source was kept constant at 2.25 V peak to peak, and the

DC bias was adjusted until the operation of the device became nonlinear, as

shown in Figure 5-14.

By changing the DC bias applied across the drive and ground pads,

the center frequency was shifted down several Hertz. This is small

compared to the shift realized with cantilevers and actuators, but may also

Comb Resonant Frequency vs. DC Bias
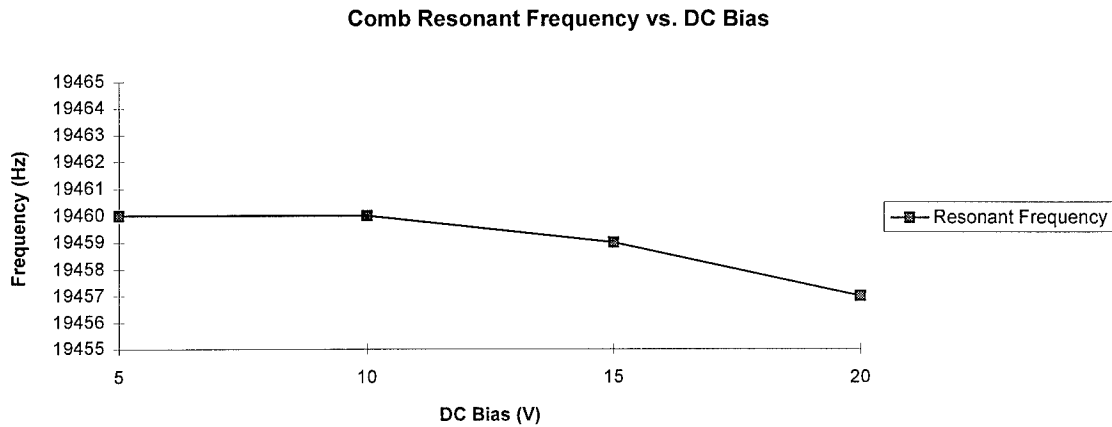
Figure 5-12 - Effect of DC bias on MUMPs 13 comb resonance. As DC bias is increased from 5 to 20 V, while keeping the signal source constant at 2.25 V peak to peak, the resonant frequency of the comb is shifted down approximately 4 Hz. Measurements conducted in a 20 mTorr vacuum.

Table 5-8 - Observed Resonance of MUMPs 13 Comb.

DC Bias (VDC)	Observed Resonance (KHz)
5	19.460
10	19.460
15	19.459
20	19.457

prove useful if only small changes are required. The reason this change is much smaller than observed with the other devices is due to the comb being a horizontal, not vertical, actuator. Since the capacitance of the device is a

function of the overlap of the fingers, not in the distance between parallel plates, pulling the top plate down slightly only affects the finger overlap slightly, and therefore only has a small effect on the resonance.

5.1.2 Varying the Q of the MEMS devices

As discussed in Chapter 3, the width of the cantilever, b, is a factor in determining Q. Yet, since the amount of width change was relatively small, from 10 microns to 50 microns, no observable change of Q was detected using this method.

The most significant parameter in determining Q is the vacuum level. It was observed that as the vacuum was decreased, a rapid widening of the resonance curve took place. Since rapidly changing the vacuum is not feasible in a functioning system, this avenue was not explored further.

The Q of the overall system using these extremely high Q devices can be made anything the designer wants. By placing these devices spectrally close together, and driving them independently, virtually any kind of tuning curve can be imitated.

5.1.3 Non-Linear Operation of MEMS Devices

All of the devices displayed usual linear behavior with low drive

source and bias, but when overdriven the devices demonstrated a non-linear

characteristic, as shown in Figure 5-13. This non-linear operation had a

hysteresis

```
NETWORK
A:REF       B:REF        o MKR       56 037.000 Hz
  20.30      -91.50        T/R     20.2936       dB
[   dB   ][   deg   ]     θ      -91.9533      deg
```

gain (dB) /phase change (degrees) ↑

Magnitude

Phase

```
    DIV        DIV      CENTER       56 037.000 Hz      ⟶
  5.000m     100.0m     SPAN                200.000 Hz      frequency (Hz)
RBW:   1 KHz  ST:4.33 sec  RANGE:R=  0,T= 20dBm
SPAN=_200.000 HZ
```
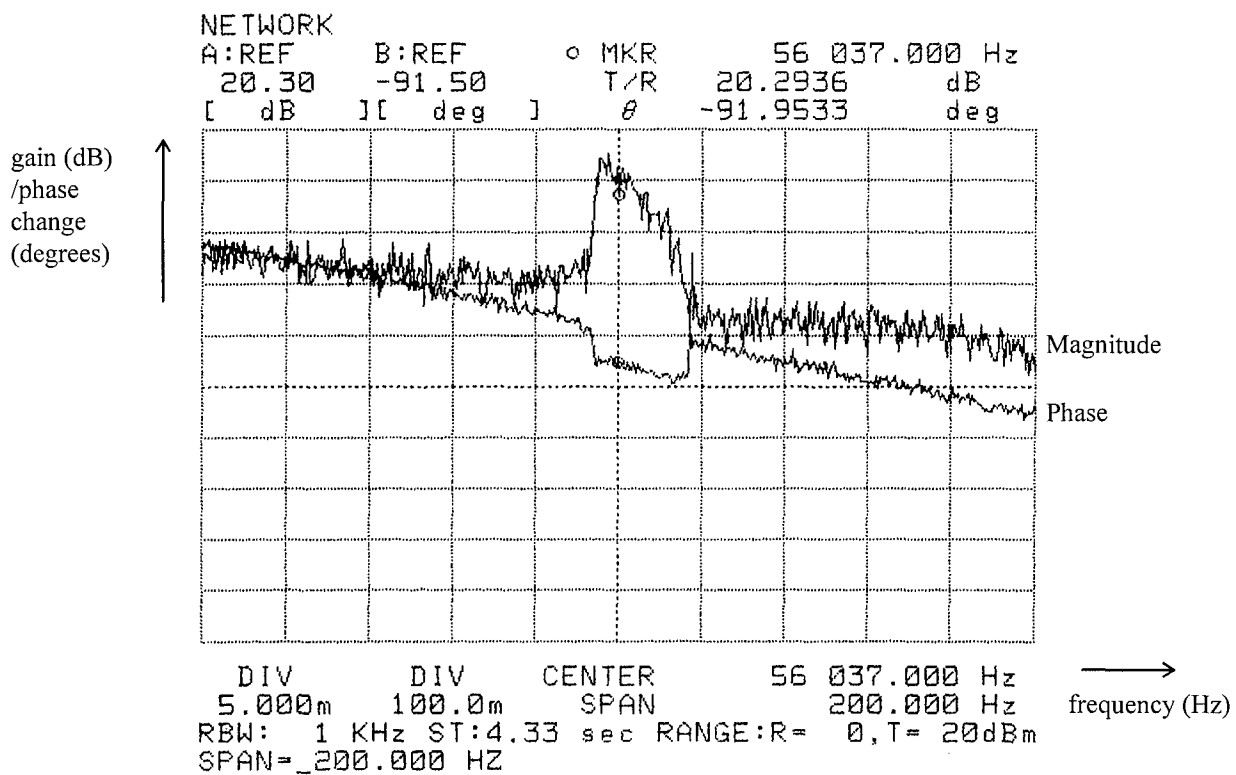
Figure 5-13 - Nonlinear operation of a MUMPs 11 Poly12 cantilever. A Poly12 beam of 200 micron length and 20 micron width is driven into nonlinear operation by a 1.25 V peak to peak signal. No DC bias is applied.

associated with it, which was explained by the Duffing Equation (Equation

3-7).
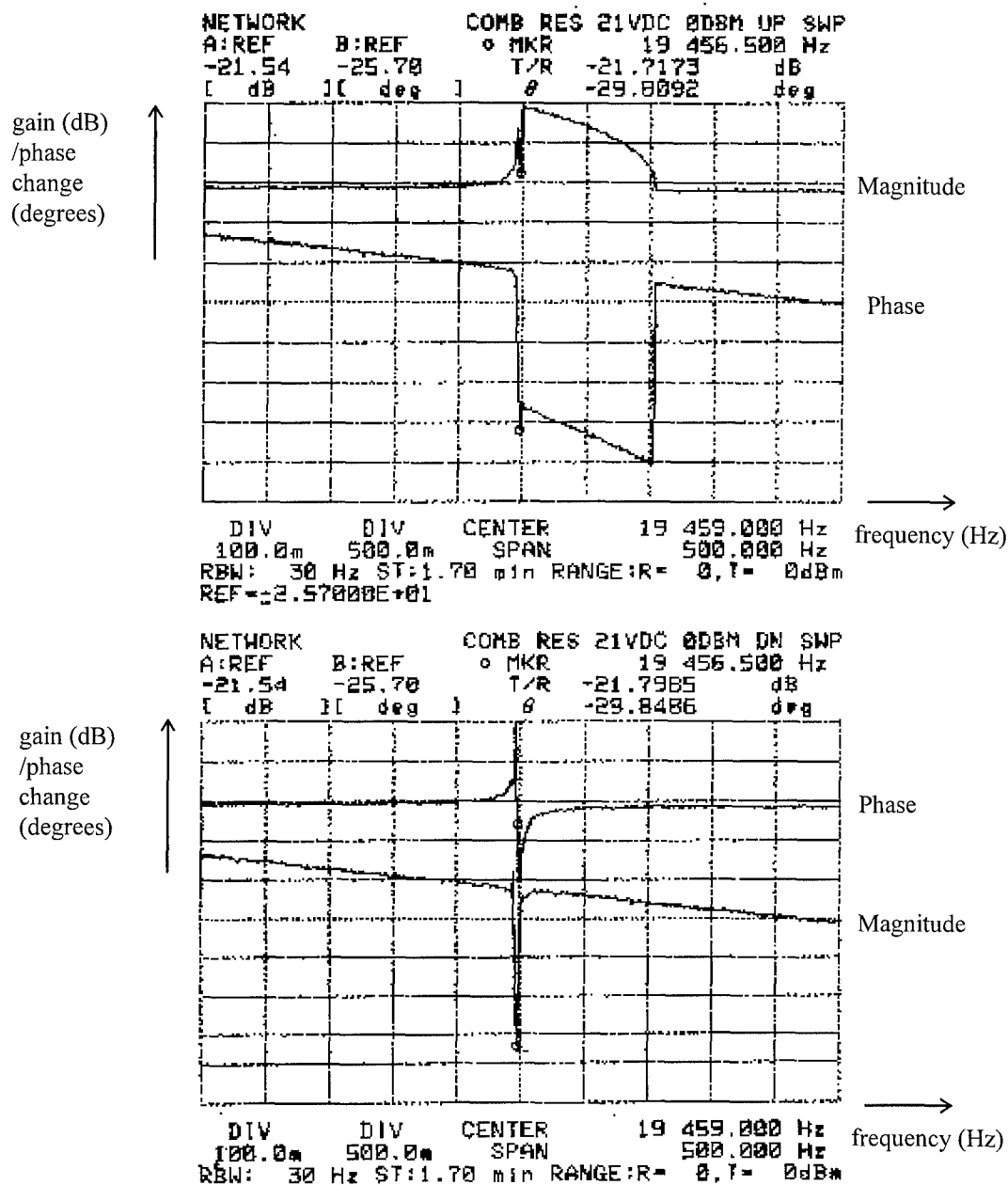
Figure 5-14 - *Nonlinear operation of MUMPs 13 comb. The comb is overdriven, with a 2.25 V peak to peak signal and 21 VDC in a 20 mTorr vacuum, giving a squared off response curve as seen above (top). When the sweep is reversed, and the signal drive voltage and DC bias remaining constant, only the center frequency is displayed (bottom). This is due to the hysteresis of the device when operated nonlinearly.*

Figure 5-14 depicts the nonlinear operation observed while

overdriving a MUMPs 13 comb. As the device is overdriven, the peak

bends. When the drive signal sweep is changed to a downsweep, the

expected resonance waveform is displayed.

5.1.4 SmartMUMPs Testing

A series of equipment problems, some due to severe hurricane

weather on the east coast where the MCNC foundry is located, delayed

delivery of the SmartMUMPs chips on time for inclusion into this thesis.

These delays have also pushed back the delivery date of MUMPs 15.

Follow-up research should include the results of the devices on the

SmartMUMPs and MUMPs 15 runs.

5.1.5 Cochlear Model Results

Previous cochlear models have been limited by the low Q of

contemporary electronic devices. With the addition of driven MEMS

devices much has changed. These devices, high Q in nature, with the ability

to be tuned with a simple DC bias, could change the way the cochlea is

presently modeled.

The new model, shown in Figure 5-15, is a series of sections

composed of MEMS devices and drive/sense electronics, each section with a presumed one to one correspondence with the basilar sections. Each MEMS device is designed to a unique resonant frequency in the auditory range. Each is initially biased midway of its linear operating region for maximum frequency swing on either side of the spectrum. A voltage limiting device, not shown in the figure, may be required to keep the devices from being damaged. This device would be placed between the incoming sound source and the individual MEMS devices, one per device. This would also be representative of the function of the cochlear fluid. Before the sound signal is introduced, the microprocessor polls all the devices, developing a baseline that it uses for all subsequent decisions.

When the microprocessor has completed the baseline, the sound signal is applied to all of the sections simultaneously. The microprocessor polls the devices to determine the resonances of the applied sound signal. It then makes decisions regarding which, if any, frequencies it wants to focus on. DC bias is then altered to the devices neighboring the frequencies of interest, effectively retuning the adjacent sections.

Since all the data to and from the Analog to Digital and Digital to

Analog converters are latched, the state of the cochlea can be modified and sampled for any instance of time.
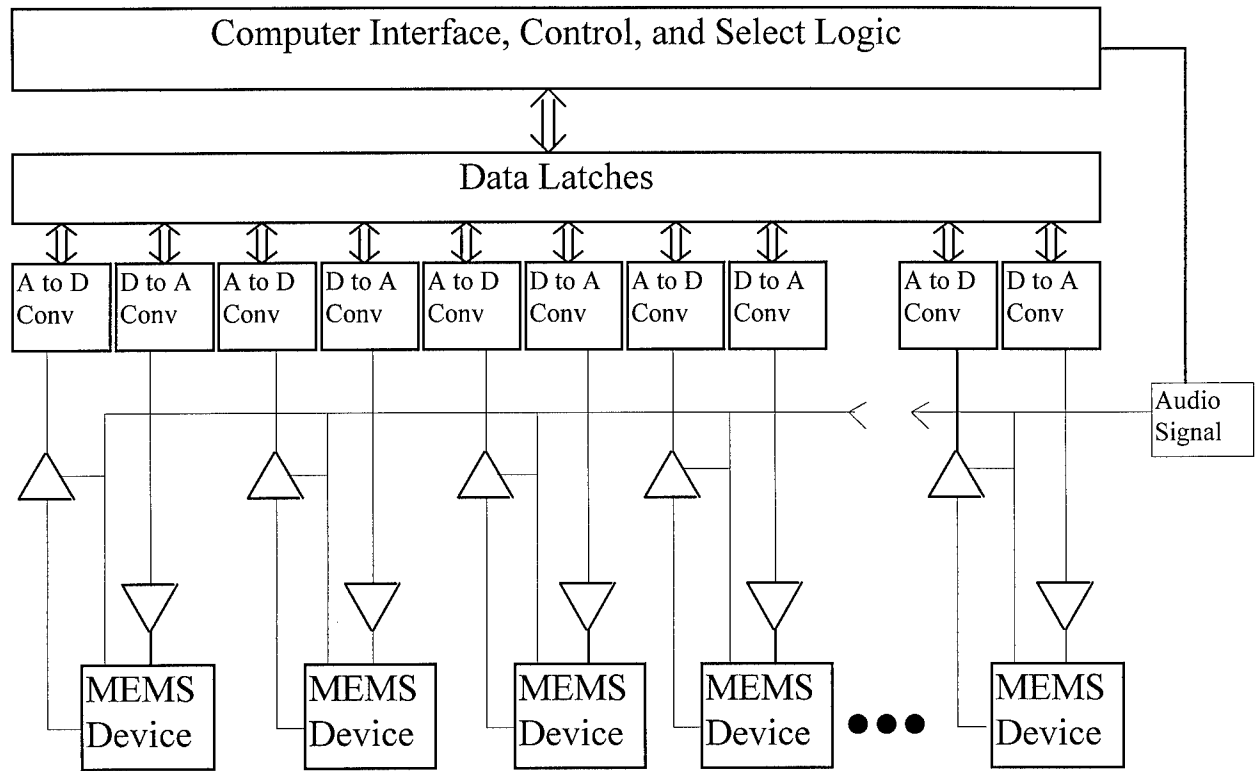
Figure 5-15 - Artificial Cochlea Designed with MEMS. A series of MEMS devices is used to model the micromechanics of the basilar membrane. Ideally, the MEMS devices are on a one to one basis with the sections of the basilar membrane. Sound is applied to all the sections under the control of the microprocessor program. Each section is then polled to determine if it is in resonance. The microprocessor, acting as the brain, can then tune the sections not in resonance via a DC tuning voltage, to assist the resonant sections.

5.2 Discussion

5.2.1 Designing a Better Resonator

The Poly2 cantilever and comb resonators were resonant in the upper auditory range. However, none of the resonators as designed operated in the lower auditory range. The problem is one of increasing the mass of the device, while lowering its spring constant. To build a cantilever that resonates at 500 Hz using the highest density materials, a Poly2/gold sandwich, with the largest possible gap to keep the structure from touching the substrate, would require the length to be over 1200 microns. It was determined experimentally that structures over 300 microns stick down without being driven. Making the beam wider allows them to be longer also, but only slightly. Another possible solution would be to make the cantilevers tapered. That is, start with a wide beam at the base and gradually decrease the width until it comes to a point (triangular shaped). Still another possible solution, is to design a cantilever that operates close to the lower auditory range, and use DC bias to further tune the device as demonstrated earlier.

To resonate at 500 Hz, a hex mirror would have to have 500 micron sides, and 300 micron flexures. This structure, given the current process, would be stuck down by its own weight. Other mirror designs that resonate at this frequency range may be possible.

It is theoretically possible to have a comb drive resonate at these low frequencies. A comb, twice as long as the one tested, made of Poly1, Poly2, oxide, and topped with gold, with 1 micron by 300 micron supports would have a detectable resonance close to 500 Hz. The actual resonance would be twice the detected resonance. A multitude of comb designs were submitted in MUMPs 15, but have not yet been fabricated. Besides the ability to resonate at low frequencies combs have other advantages.

The most difficult task in working with resonators at the micron scale is in electrically detecting when the device is in resonance. Combs offer two very significant advantages over the other designs considered in this respect. The first advantage is that resonance can be observed visually. This is important in that the designer of the detection circuit has immediate and clear feedback as to the operation of the sensing circuit. The second, and equally important advantage, is that the comb resonator can be driven

much more than the other devices considered, and therefore has a much larger sensed signal. It is difficult to slam a comb down, compared to the ease of doing so with cantilevers.

The major disadvantage of comb resonators is their size. Compared to a cantilever, a comb is massive. Also, they do not have the tunability demonstrated by cantilevers with small changes in DC voltage.

5.2.2 Updating the Cochlear Model

As described earlier, the theory that the Q of basilar membrane varies dependent on the input is commonly accepted. Von Bekesy described very low Q resonance basilar membrane characteristics in his experiments with cadavers. Conversely, experiments with live primates using Mössbauer methods have shown very high Q basilar membrane behavior. One way to explain this would be to cite for cadavers the absence of some metabolically based neuronal function controlling the cochlea with complex AC control signals acting as a positive feedback system [2,26]. A simpler, and possibly more accurate hypothesis, would be the loss of a DC polarization voltage upon death.

A new approach to describing what may actually be occurring is to
consider the basilar membrane as a series of tunable resonators with
constant Q. The resonators are tuned with simple DC bias changes, versus
complex AC waveform positive feedback. By using local recruitment, a
sharpened tuning curve, similar to that observed in the living cochlea, can
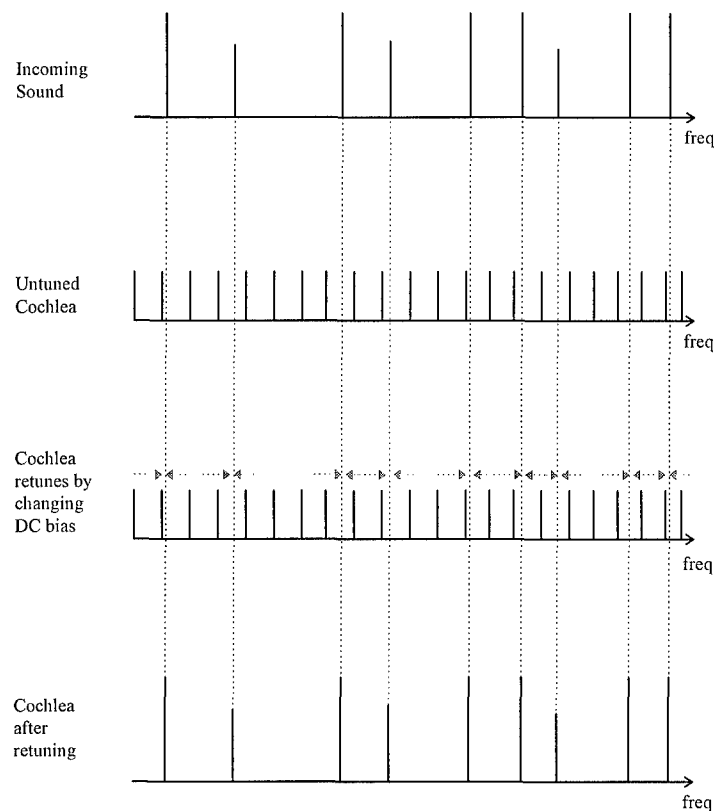
Figure 5-16 - Revised model of the cochlea.

be produced. Figure 5-16 illustrates the new tuning model. The cochlea is untuned until sound presents itself. Then, cochlear sections closest to the specific frequencies of the incoming sound retune to match the sound. The retuning results from simple bias adjustments, rather than complex AC feedback. For someone looking at the overall effect, it would appear that the Qs of the sections are changing dependent on incoming sound waveform, but upon closer inspection, local recruitment and retuning are responsible. This could be interpreted as the observed section varying Q if retuning was not considered.

Chapter 6

6. Conclusions and Recommendations

This chapter summarizes the conclusions of the research conducted for this thesis. Suggested follow-on work and applicability of the research conducted into other fields is also presented.

6.1 Conclusions

Two main research efforts were conducted. The first was a search for MEMS devices that were suitable to act as resonators. Three such devices were designed, implemented and characterized: cantilevers, combs, and mirror/actuators. To facilitate testing, two new setups were devised. These test setups proved to be accurate and reliable. Using these test set-ups, all three devices were shown to resonate close to their designed values. The resonant frequencies of these devices were also shown to vary with an applied DC bias. This enables them to serve as tunable resonators. There are many applications for these tunable resonators, especially since they are extremely high Q. These devices were also demonstrated to act nonlinearly

when the applied drive was too large. The nonlinearity was shown to have a hysteresis, described by the Duffing Equation.

The second research area was the human auditory system, particularly the cochlea. The objective was to perform the necessary preliminary design to build an artificial cochlea, so that future efforts can realize the goal of building a working artificial cochlea that accurately reproduces the natural cochlea's response to sound. Using the knowledge gained from observing working micro-mechanical resonators, a new cochlear mechanics model was suggested. The observation that retuning local basilar sections would appear the same to an outside observer as changing the damping of the basilar membrane. The damping theory is what current models rely on, but the retuning method is much more elegant and natural. The new model relies on simple bias changes and local recruitment to tune the cochlea, as opposed to the complex signal feedback expressed in current models. The addition of a computer controller is also a major advance, since it directly models the presumed active control of the brain..

An artificial cochlea designed with MEMS appears feasible. While it is too early to judge, the results of this work may affect the field of auditory

research and various other fields that rely upon it. It is exciting to think that cochlear modeling has just taken a giant leap with the introduction of these tiny electro-mechanical devices, called MEMS. Their characteristic high Q, and their ability to be tuned with a simple DC voltage, may model some crucial aspects of the live cochlea. The fact that they are mechanical devices and, if properly placed and biased, can react to movements of neighboring devices supports the theory of local recruitment.

The results of this thesis are only a building block for future work. It was shown that an artificial cochlea designed with MEMS has significant advantages over contemporary designs. The ability to dynamically retune the cochlea may give a new explanation to an old problem.

6.2 Recommendations for Future Work

The logical follow on to the work presented here is to build a working model of the cochlea utilizing the MEMS devices described. This device can then used to further the knowledge of the workings of the auditory system, and may one day lead to a myriad of technological advances. Further steps required toward that end include further improving the resonators used, and implementing a vacuum packed multi-chip module

with MEMS resonators and the associated drive and sense circuits. The testing of the MEMS devices can be further enhanced by programming the 4195A to automatically seek out the resonance of the device under test, and by building/procuring a vacuum chamber specifically suited for wire-boned MEMS chips.

The MEMS devices described in this thesis can be used to implement many other devices. They can be substituted for electronic resonators in a multitude of electronic systems, wherever high Q is a concern. For instance, they could be used to implement a spectrum analyzer on a chip, radio and television tuners, sensors, etc. In the area of electronic transmission, where an overcrowded spectrum requires better frequency management, tunable high Q MEMS resonators could be used to implement high quality transmitters and receivers, possibly enabling a tighter use of the frequency spectrum.

Potential military applications of MEMS resonators in the area of electronic communication supporting IFF, TACAN, GPS, targeting, etc. are innumerable. Likewise, sound related applications of an implemented artificial cochlea will lead us into the 21st century.

Appendix A - Theoretical Calculations Using MathCad

Poly12 Cantilevers

$E := 169 \cdot 10^9 \cdot Pa$ Young's Modulus

$tp := 4.25 \cdot 10^{-6} \cdot m$ Thickness of Poly12

$\lambda := 1.875104$ Eigenvalue for simple beam

$pp := 2.3 \cdot 10^3 \cdot \dfrac{kg}{m^3}$ Density of Polysilicon

Function to calculate the % Error
T is the theoretical value
O is the observed value

$$Error(T, O) := \left| \frac{T - O}{T} \right|$$

The two methods for calculating the resonant frequency:
f1 uses Equation 3-XX, and ignores the width of the beam.
f2 uses Equation 3-XX, and also takes into account the width of the beam
(however, this has no effect since w is a term in both k and M, and is therefore
factored out).

$$f1(l) := \frac{\lambda^2 \cdot tp}{4 \cdot \pi \cdot l^2} \cdot \sqrt{\frac{E}{3 \cdot pp}}$$

$$f2(l, w) := \left| \begin{array}{l} k \leftarrow \dfrac{E \cdot w \cdot (tp)^3}{l^3} \\[2mm] M \leftarrow w \cdot l \cdot tp \cdot pp \\[2mm] \dfrac{1}{2 \cdot \pi} \cdot \sqrt{\dfrac{k}{M}} \end{array} \right.$$

225 x 50 μ   Half of the cantilevers label P12 200 have actual lengths (as drawn) of 225
         microns

$l := 225 \cdot 10^{-6} \cdot m$ $w := 50 \cdot 10^{-6} \cdot m$

$f1(l) = 1.162 \cdot 10^5 \cdot sec^{-1}$ $f2(l, w) = 1.145 \cdot 10^5 \cdot sec^{-1}$

225 x 40 μ

$l := 225 \cdot 10^{-6} \cdot m$ $w := 40 \cdot 10^{-6} \cdot m$

$f1(l) = 1.162 \cdot 10^5 \cdot sec^{-1}$ $f2(l, w) = 1.145 \cdot 10^5 \cdot sec^{-1}$

225 x 30 μ

$l := 225 \cdot 10^{-6} \cdot m$ $w := 30 \cdot 10^{-6} \cdot m$

$f1(l) = 1.162 \cdot 10^5 \cdot sec^{-1}$ $f2(l, w) = 1.145 \cdot 10^5 \cdot sec^{-1}$

Note that the width has no effect on the calculated value of resonance, but does effect real
cantilevers

225 x 20 μ

$l := 225 \cdot 10^{-6} \cdot m$ $w := 40 \cdot 10^{-6} \cdot m$

$f1(l) = 1.162 \cdot 10^{5} \cdot sec^{-1}$ $f2(l, w) = 1.145 \cdot 10^{5} \cdot sec^{-1}$

225 x 10 μ

$l := 225 \cdot 10^{-6} \cdot m$ $w := 30 \cdot 10^{-6} \cdot m$

$f1(l) = 1.162 \cdot 10^{5} \cdot sec^{-1}$ $f2(l, w) = 1.145 \cdot 10^{5} \cdot sec^{-1}$

set up range and granularity

$$r1 := 10 \cdot 10^{-6} \cdot m \qquad r2 := 350 \cdot 10^{-6} \cdot m \qquad n := 1 \qquad l := r1, r1 + \frac{r1}{n} .. r2$$

P12 Cantilever Resonance vs. Length

Y-axis: Resonant Frequency (Hz), with $\frac{f1(l)}{}$ and $f2\left(l, 50 \cdot 10^{-6} \cdot m\right)$

X-axis: Length (m), ranging from $5 \cdot 10^{-5}$ to 0.00035
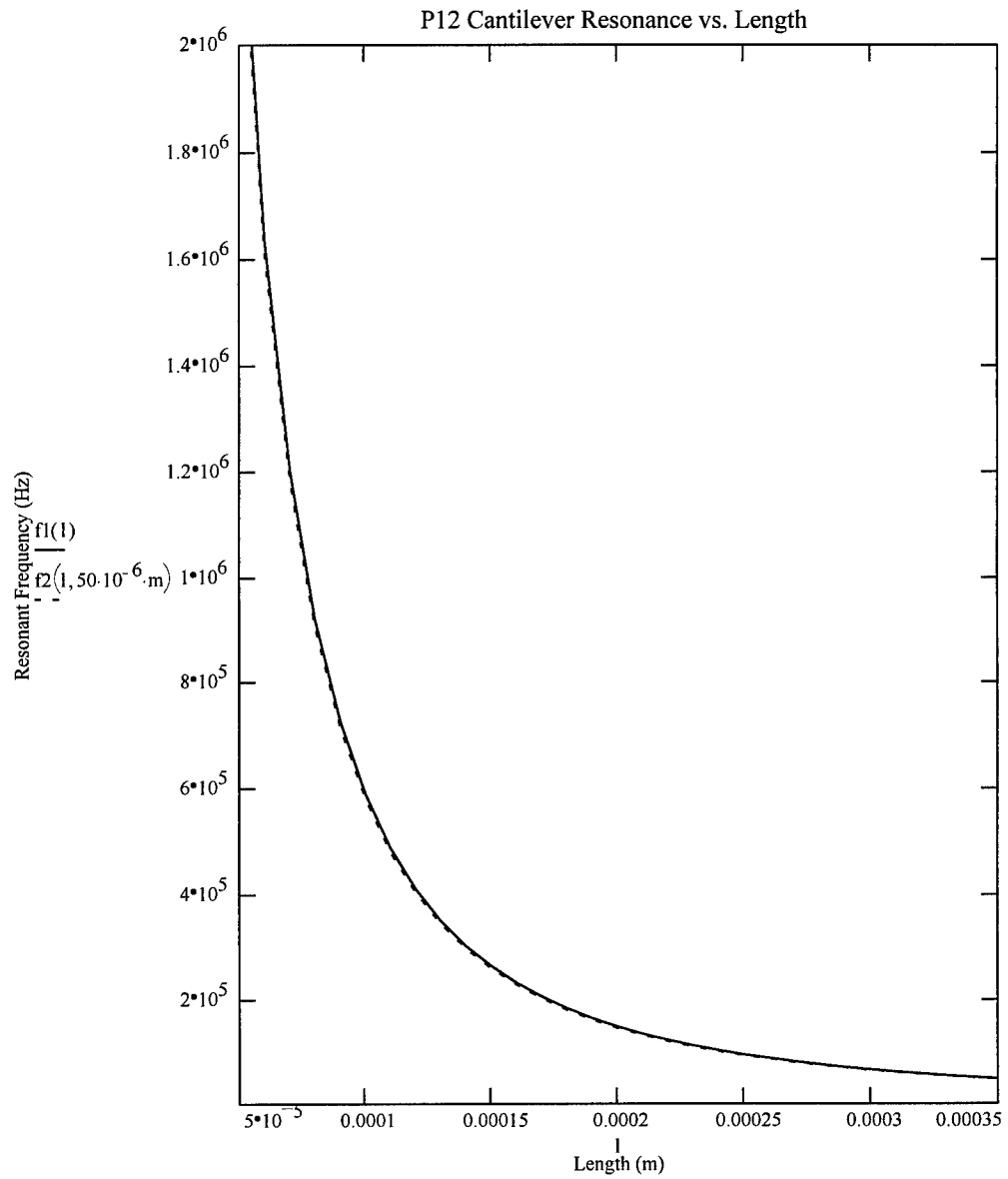
l	$f1(l)$	$f2(l, 50 \cdot 10^{-6} \cdot m)$
$1 \cdot 10^{-5} \cdot m$	$5.885 \cdot 10^{7} \cdot sec^{-1}$	$5.798 \cdot 10^{7} \cdot sec^{-1}$
$2 \cdot 10^{-5} \cdot m$	$1.471 \cdot 10^{7} \cdot sec^{-1}$	$1.45 \cdot 10^{7} \cdot sec^{-1}$
$3 \cdot 10^{-5} \cdot m$	$6.539 \cdot 10^{6} \cdot sec^{-1}$	$6.442 \cdot 10^{6} \cdot sec^{-1}$
$4 \cdot 10^{-5} \cdot m$	$3.678 \cdot 10^{6} \cdot sec^{-1}$	$3.624 \cdot 10^{6} \cdot sec^{-1}$
$5 \cdot 10^{-5} \cdot m$	$2.354 \cdot 10^{6} \cdot sec^{-1}$	$2.319 \cdot 10^{6} \cdot sec^{-1}$
$6 \cdot 10^{-5} \cdot m$	$1.635 \cdot 10^{6} \cdot sec^{-1}$	$1.611 \cdot 10^{6} \cdot sec^{-1}$
$7 \cdot 10^{-5} \cdot m$	$1.201 \cdot 10^{6} \cdot sec^{-1}$	$1.183 \cdot 10^{6} \cdot sec^{-1}$
$8 \cdot 10^{-5} \cdot m$	$9.195 \cdot 10^{5} \cdot sec^{-1}$	$9.06 \cdot 10^{5} \cdot sec^{-1}$
$9 \cdot 10^{-5} \cdot m$	$7.265 \cdot 10^{5} \cdot sec^{-1}$	$7.158 \cdot 10^{5} \cdot sec^{-1}$
$1 \cdot 10^{-4} \cdot m$	$5.885 \cdot 10^{5} \cdot sec^{-1}$	$5.798 \cdot 10^{5} \cdot sec^{-1}$
$1.1 \cdot 10^{-4} \cdot m$	$4.864 \cdot 10^{5} \cdot sec^{-1}$	$4.792 \cdot 10^{5} \cdot sec^{-1}$
$1.2 \cdot 10^{-4} \cdot m$	$4.087 \cdot 10^{5} \cdot sec^{-1}$	$4.026 \cdot 10^{5} \cdot sec^{-1}$
$1.3 \cdot 10^{-4} \cdot m$	$3.482 \cdot 10^{5} \cdot sec^{-1}$	$3.431 \cdot 10^{5} \cdot sec^{-1}$
$1.4 \cdot 10^{-4} \cdot m$	$3.003 \cdot 10^{5} \cdot sec^{-1}$	$2.958 \cdot 10^{5} \cdot sec^{-1}$
$1.5 \cdot 10^{-4} \cdot m$	$2.616 \cdot 10^{5} \cdot sec^{-1}$	$2.577 \cdot 10^{5} \cdot sec^{-1}$
$1.6 \cdot 10^{-4} \cdot m$	$2.299 \cdot 10^{5} \cdot sec^{-1}$	$2.265 \cdot 10^{5} \cdot sec^{-1}$
$1.7 \cdot 10^{-4} \cdot m$	$2.036 \cdot 10^{5} \cdot sec^{-1}$	$2.006 \cdot 10^{5} \cdot sec^{-1}$
$1.8 \cdot 10^{-4} \cdot m$	$1.816 \cdot 10^{5} \cdot sec^{-1}$	$1.79 \cdot 10^{5} \cdot sec^{-1}$
$1.9 \cdot 10^{-4} \cdot m$	$1.63 \cdot 10^{5} \cdot sec^{-1}$	$1.606 \cdot 10^{5} \cdot sec^{-1}$
$2 \cdot 10^{-4} \cdot m$	$1.471 \cdot 10^{5} \cdot sec^{-1}$	$1.45 \cdot 10^{5} \cdot sec^{-1}$
$2.1 \cdot 10^{-4} \cdot m$	$1.334 \cdot 10^{5} \cdot sec^{-1}$	$1.315 \cdot 10^{5} \cdot sec^{-1}$
$2.2 \cdot 10^{-4} \cdot m$	$1.216 \cdot 10^{5} \cdot sec^{-1}$	$1.198 \cdot 10^{5} \cdot sec^{-1}$
$2.3 \cdot 10^{-4} \cdot m$	$1.112 \cdot 10^{5} \cdot sec^{-1}$	$1.096 \cdot 10^{5} \cdot sec^{-1}$
$2.4 \cdot 10^{-4} \cdot m$	$1.022 \cdot 10^{5} \cdot sec^{-1}$	$1.007 \cdot 10^{5} \cdot sec^{-1}$
$2.5 \cdot 10^{-4} \cdot m$	$9.416 \cdot 10^{4} \cdot sec^{-1}$	$9.277 \cdot 10^{4} \cdot sec^{-1}$
$2.6 \cdot 10^{-4} \cdot m$	$8.706 \cdot 10^{4} \cdot sec^{-1}$	$8.577 \cdot 10^{4} \cdot sec^{-1}$
$2.7 \cdot 10^{-4} \cdot m$	$8.073 \cdot 10^{4} \cdot sec^{-1}$	$7.954 \cdot 10^{4} \cdot sec^{-1}$
$2.8 \cdot 10^{-4} \cdot m$	$7.506 \cdot 10^{4} \cdot sec^{-1}$	$7.396 \cdot 10^{4} \cdot sec^{-1}$
$2.9 \cdot 10^{-4} \cdot m$	$6.998 \cdot 10^{4} \cdot sec^{-1}$	$6.894 \cdot 10^{4} \cdot sec^{-1}$
$3 \cdot 10^{-4} \cdot m$	$6.539 \cdot 10^{4} \cdot sec^{-1}$	$6.442 \cdot 10^{4} \cdot sec^{-1}$
$3.1 \cdot 10^{-4} \cdot m$	$6.124 \cdot 10^{4} \cdot sec^{-1}$	$6.033 \cdot 10^{4} \cdot sec^{-1}$
$3.2 \cdot 10^{-4} \cdot m$	$5.747 \cdot 10^{4} \cdot sec^{-1}$	$5.662 \cdot 10^{4} \cdot sec^{-1}$
$3.3 \cdot 10^{-4} \cdot m$	$5.404 \cdot 10^{4} \cdot sec^{-1}$	$5.324 \cdot 10^{4} \cdot sec^{-1}$
$3.4 \cdot 10^{-4} \cdot m$	$5.091 \cdot 10^{4} \cdot sec^{-1}$	$5.016 \cdot 10^{4} \cdot sec^{-1}$
$3.5 \cdot 10^{-4} \cdot m$	$4.804 \cdot 10^{4} \cdot sec^{-1}$	$4.733 \cdot 10^{4} \cdot sec^{-1}$

Poly1 Cantilevers

$E := 169 \cdot 10^9 \cdot Pa$ — Young's Modulus

$tp := 2.0 \cdot 10^{-6} \cdot m$ — Thickness of Poly1

$\lambda := 1.875104$ — Eigenvalue for simple beam

$\rho p := 2.3 \cdot 10^3 \cdot \dfrac{kg}{m^3}$ — Density of Polysilicon

Function to calculate the % Error

T is the theoretical value

O is the observed value

$$Error(T, O) := \left| \frac{T - O}{T} \right|$$

The two methods for calculating the resonant frequency:

f1 uses Equation 3-XX, and ignores the width of the beam.

f2 uses Equation 3-XX, and also takes into account the width of the beam (however, this has no effect since w is a term in both k and M, and is therefore factored out).

$$f1(l) := \frac{\lambda^2 \cdot tp}{4 \cdot \pi \cdot l^2} \cdot \sqrt{\frac{E}{3 \cdot \rho p}}$$

$$f2(l, w) := \begin{vmatrix} k \leftarrow \dfrac{E \cdot w \cdot (tp)^3}{l^3} \\ M \leftarrow w \cdot l \cdot tp \cdot \rho p \\ \dfrac{1}{2 \cdot \pi} \cdot \sqrt{\dfrac{k}{M}} \end{vmatrix}$$

225 x 50 μ — Half of the cantilevers label P12 200 have actual lengths (as drawn) of 225 microns

$l := 225 \cdot 10^{-6} \cdot m$ $w := 50 \cdot 10^{-6} \cdot m$

$f1(l) = 5.47 \cdot 10^4 \cdot sec^{-1}$ $f2(l, w) = 5.39 \cdot 10^4 \cdot sec^{-1}$

225 x 40 μ

$l := 225 \cdot 10^{-6} \cdot m$ $w := 40 \cdot 10^{-6} \cdot m$

$f1(l) = 5.47 \cdot 10^4 \cdot sec^{-1}$ $f2(l, w) = 5.39 \cdot 10^4 \cdot sec^{-1}$

225 x 30 μ

$l := 225 \cdot 10^{-6} \cdot m$ $w := 30 \cdot 10^{-6} \cdot m$

$f1(l) = 5.47 \cdot 10^4 \cdot sec^{-1}$ $f2(l, w) = 5.39 \cdot 10^4 \cdot sec^{-1}$

Note that the width has no effect on the calculated value of resonance, but does effect real cantilevers

225 x 20 μ

$l := 225 \cdot 10^{-6} \cdot m$ $w := 40 \cdot 10^{-6} \cdot m$

$f1(l) = 5.47 \cdot 10^4 \cdot sec^{-1}$ $f2(l, w) = 5.39 \cdot 10^4 \cdot sec^{-1}$

225 x 10 μ

$l := 225 \cdot 10^{-6} \cdot m$ $w := 30 \cdot 10^{-6} \cdot m$

$f1(l) = 5.47 \cdot 10^4 \cdot sec^{-1}$ $f2(l, w) = 5.39 \cdot 10^4 \cdot sec^{-1}$

200 x 50 μ

$l := 200 \cdot 10^{-6} \cdot m$ $w := 50 \cdot 10^{-6} \cdot m$

$f1(l) = 6.924 \cdot 10^4 \cdot sec^{-1}$ $f2(l, w) = 6.821 \cdot 10^4 \cdot sec^{-1}$

175 x 50 μ

$l := 175 \cdot 10^{-6} \cdot m$ $w := 50 \cdot 10^{-6} \cdot m$

$f1(l) = 9.043 \cdot 10^4 \cdot sec^{-1}$ $f2(l, w) = 8.91 \cdot 10^4 \cdot sec^{-1}$

150 x 50 μ

$l := 150 \cdot 10^{-6} \cdot m$ $w := 50 \cdot 10^{-6} \cdot m$

$f1(l) = 1.231 \cdot 10^5 \cdot sec^{-1}$ $f2(l, w) = 1.213 \cdot 10^5 \cdot sec^{-1}$

125 x 50 μ

$l := 125 \cdot 10^{-6} \cdot m$ $w := 50 \cdot 10^{-6} \cdot m$

$f1(l) = 1.772 \cdot 10^{5} \cdot sec^{-1}$ $f2(l, w) = 1.746 \cdot 10^{5} \cdot sec^{-1}$

100 x 50 μ

$l := 100 \cdot 10^{-6} \cdot m$ $w := 50 \cdot 10^{-6} \cdot m$

$f1(l) = 2.769 \cdot 10^{5} \cdot sec^{-1}$ $f2(l, w) = 2.729 \cdot 10^{5} \cdot sec^{-1}$

75 x 50 μ

$l := 75 \cdot 10^{-6} \cdot m$ $w := 50 \cdot 10^{-6} \cdot m$

$f1(l) = 4.923 \cdot 10^{5} \cdot sec^{-1}$ $f2(l, w) = 4.851 \cdot 10^{5} \cdot sec^{-1}$

50 x 50 μ

$l := 50 \cdot 10^{-6} \cdot m$ $w := 50 \cdot 10^{-6} \cdot m$

$f1(l) = 1.108 \cdot 10^{6} \cdot sec^{-1}$ $f2(l, w) = 1.091 \cdot 10^{6} \cdot sec^{-1}$

set up range and granularity

$$r1 := 10 \cdot 10^{-6} \cdot m \qquad r2 := 350 \cdot 10^{-6} \cdot m \qquad n := 1 \qquad l := r1, r1 + \frac{r1}{n} .. r2$$

P1 Cantilever Resonance vs. Length

Resonant Frequency (Hz) — $\frac{f1(l)}{f2(l, 50 \cdot 10^{-6} \cdot m)}$

Length (m)
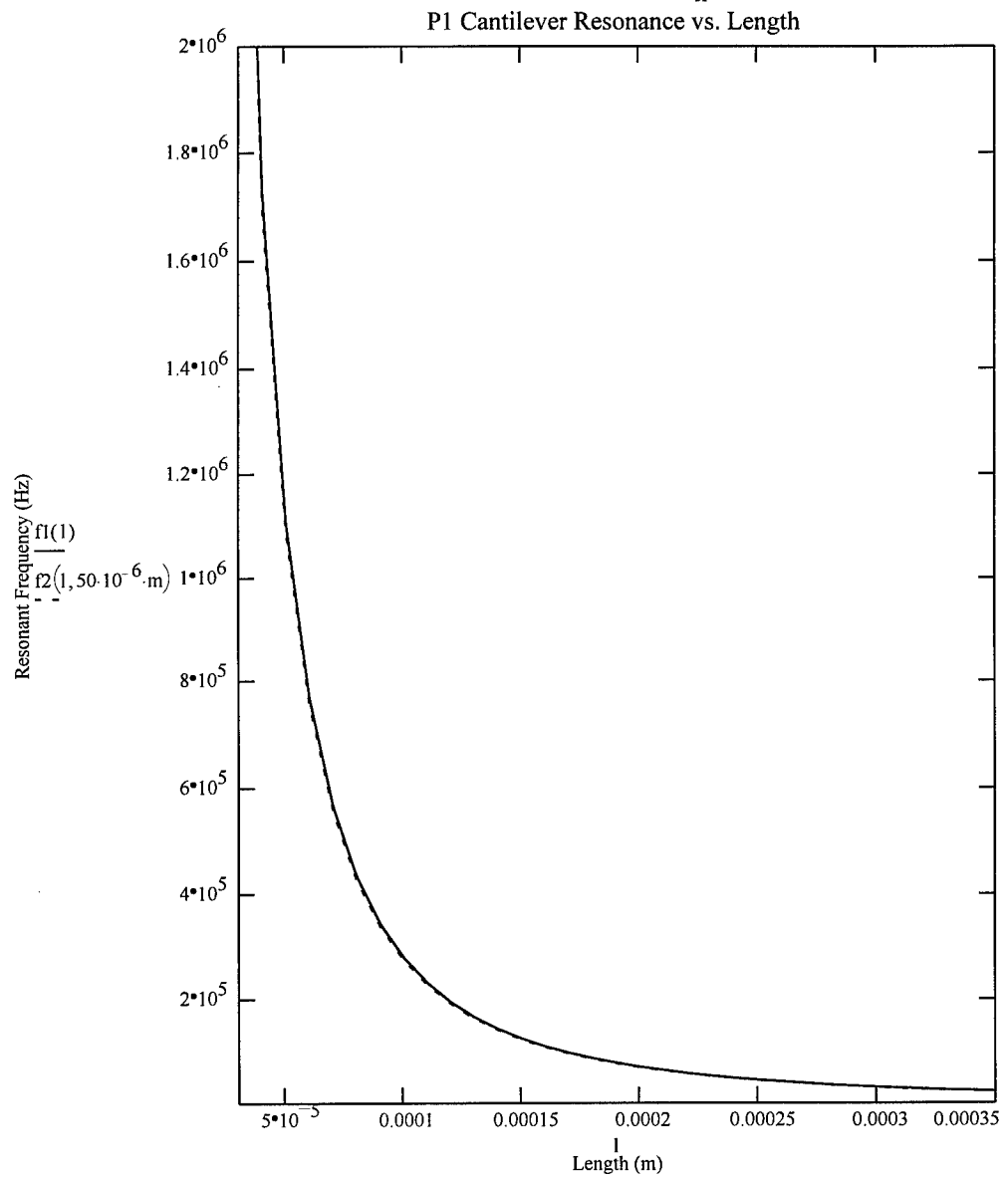
l	$f1(l)$	$f2(1, 50 \cdot 10^{-6} \cdot m)$
$1 \cdot 10^{-5} \cdot m$	$2.769 \cdot 10^7 \cdot sec^{-1}$	$2.729 \cdot 10^7 \cdot sec^{-1}$
$2 \cdot 10^{-5} \cdot m$	$6.924 \cdot 10^6 \cdot sec^{-1}$	$6.821 \cdot 10^6 \cdot sec^{-1}$
$3 \cdot 10^{-5} \cdot m$	$3.077 \cdot 10^6 \cdot sec^{-1}$	$3.032 \cdot 10^6 \cdot sec^{-1}$
$4 \cdot 10^{-5} \cdot m$	$1.731 \cdot 10^6 \cdot sec^{-1}$	$1.705 \cdot 10^6 \cdot sec^{-1}$
$5 \cdot 10^{-5} \cdot m$	$1.108 \cdot 10^6 \cdot sec^{-1}$	$1.091 \cdot 10^6 \cdot sec^{-1}$
$6 \cdot 10^{-5} \cdot m$	$7.693 \cdot 10^5 \cdot sec^{-1}$	$7.579 \cdot 10^5 \cdot sec^{-1}$
$7 \cdot 10^{-5} \cdot m$	$5.652 \cdot 10^5 \cdot sec^{-1}$	$5.568 \cdot 10^5 \cdot sec^{-1}$
$8 \cdot 10^{-5} \cdot m$	$4.327 \cdot 10^5 \cdot sec^{-1}$	$4.263 \cdot 10^5 \cdot sec^{-1}$
$9 \cdot 10^{-5} \cdot m$	$3.419 \cdot 10^5 \cdot sec^{-1}$	$3.369 \cdot 10^5 \cdot sec^{-1}$
$1 \cdot 10^{-4} \cdot m$	$2.769 \cdot 10^5 \cdot sec^{-1}$	$2.729 \cdot 10^5 \cdot sec^{-1}$
$1.1 \cdot 10^{-4} \cdot m$	$2.289 \cdot 10^5 \cdot sec^{-1}$	$2.255 \cdot 10^5 \cdot sec^{-1}$
$1.2 \cdot 10^{-4} \cdot m$	$1.923 \cdot 10^5 \cdot sec^{-1}$	$1.895 \cdot 10^5 \cdot sec^{-1}$
$1.3 \cdot 10^{-4} \cdot m$	$1.639 \cdot 10^5 \cdot sec^{-1}$	$1.615 \cdot 10^5 \cdot sec^{-1}$
$1.4 \cdot 10^{-4} \cdot m$	$1.413 \cdot 10^5 \cdot sec^{-1}$	$1.392 \cdot 10^5 \cdot sec^{-1}$
$1.5 \cdot 10^{-4} \cdot m$	$1.231 \cdot 10^5 \cdot sec^{-1}$	$1.213 \cdot 10^5 \cdot sec^{-1}$
$1.6 \cdot 10^{-4} \cdot m$	$1.082 \cdot 10^5 \cdot sec^{-1}$	$1.066 \cdot 10^5 \cdot sec^{-1}$
$1.7 \cdot 10^{-4} \cdot m$	$9.583 \cdot 10^4 \cdot sec^{-1}$	$9.441 \cdot 10^4 \cdot sec^{-1}$
$1.8 \cdot 10^{-4} \cdot m$	$8.548 \cdot 10^4 \cdot sec^{-1}$	$8.421 \cdot 10^4 \cdot sec^{-1}$
$1.9 \cdot 10^{-4} \cdot m$	$7.672 \cdot 10^4 \cdot sec^{-1}$	$7.558 \cdot 10^4 \cdot sec^{-1}$
$2 \cdot 10^{-4} \cdot m$	$6.924 \cdot 10^4 \cdot sec^{-1}$	$6.821 \cdot 10^4 \cdot sec^{-1}$
$2.1 \cdot 10^{-4} \cdot m$	$6.28 \cdot 10^4 \cdot sec^{-1}$	$6.187 \cdot 10^4 \cdot sec^{-1}$
$2.2 \cdot 10^{-4} \cdot m$	$5.722 \cdot 10^4 \cdot sec^{-1}$	$5.637 \cdot 10^4 \cdot sec^{-1}$
$2.3 \cdot 10^{-4} \cdot m$	$5.235 \cdot 10^4 \cdot sec^{-1}$	$5.158 \cdot 10^4 \cdot sec^{-1}$
$2.4 \cdot 10^{-4} \cdot m$	$4.808 \cdot 10^4 \cdot sec^{-1}$	$4.737 \cdot 10^4 \cdot sec^{-1}$
$2.5 \cdot 10^{-4} \cdot m$	$4.431 \cdot 10^4 \cdot sec^{-1}$	$4.366 \cdot 10^4 \cdot sec^{-1}$
$2.6 \cdot 10^{-4} \cdot m$	$4.097 \cdot 10^4 \cdot sec^{-1}$	$4.036 \cdot 10^4 \cdot sec^{-1}$
$2.7 \cdot 10^{-4} \cdot m$	$3.799 \cdot 10^4 \cdot sec^{-1}$	$3.743 \cdot 10^4 \cdot sec^{-1}$
$2.8 \cdot 10^{-4} \cdot m$	$3.532 \cdot 10^4 \cdot sec^{-1}$	$3.48 \cdot 10^4 \cdot sec^{-1}$
$2.9 \cdot 10^{-4} \cdot m$	$3.293 \cdot 10^4 \cdot sec^{-1}$	$3.244 \cdot 10^4 \cdot sec^{-1}$
$3 \cdot 10^{-4} \cdot m$	$3.077 \cdot 10^4 \cdot sec^{-1}$	$3.032 \cdot 10^4 \cdot sec^{-1}$
$3.1 \cdot 10^{-4} \cdot m$	$2.882 \cdot 10^4 \cdot sec^{-1}$	$2.839 \cdot 10^4 \cdot sec^{-1}$
$3.2 \cdot 10^{-4} \cdot m$	$2.705 \cdot 10^4 \cdot sec^{-1}$	$2.665 \cdot 10^4 \cdot sec^{-1}$
$3.3 \cdot 10^{-4} \cdot m$	$2.543 \cdot 10^4 \cdot sec^{-1}$	$2.506 \cdot 10^4 \cdot sec^{-1}$
$3.4 \cdot 10^{-4} \cdot m$	$2.396 \cdot 10^4 \cdot sec^{-1}$	$2.36 \cdot 10^4 \cdot sec^{-1}$
$3.5 \cdot 10^{-4} \cdot m$	$2.261 \cdot 10^4 \cdot sec^{-1}$	$2.227 \cdot 10^4 \cdot sec^{-1}$

Poly2 Cantilevers

$E := 169 \cdot 10^9 \cdot Pa$ Young's Modulus

$tp := 1.5 \cdot 10^{-6} \cdot m$ Thickness of Poly2

$\lambda := 1.875104$ Eigenvalue for simple beam

$\rho p := 2.3 \cdot 10^3 \cdot \dfrac{kg}{m^3}$ Density of Polysilicon

Function to calculate the % Error
T is the theoretical value
O is the observed value

$Error(T, O) := \left| \dfrac{T - O}{T} \right|$

The two methods for calculating the resonant frequency:
f1 uses Equation 3-XX, and ignores the width of the beam.
f2 uses Equation 3-XX, and also takes into account the width of the beam
(however, this has no effect since w is a term in both k and M, and is therefore
factored out).

$f1(l) := \dfrac{\lambda^2 \cdot tp}{4 \cdot \pi \cdot l^2} \cdot \sqrt{\dfrac{E}{3 \cdot \rho p}}$

$f2(l, w) := \begin{vmatrix} k \leftarrow \dfrac{E \cdot w \cdot (tp)^3}{l^3} \\ M \leftarrow w \cdot l \cdot tp \cdot \rho p \\ \dfrac{1}{2 \cdot \pi} \cdot \sqrt{\dfrac{k}{M}} \end{vmatrix}$

225 x 50 μ   Half of the cantilevers label P12 200 have actual lengths (as drawn) of 225 microns

$l := 225 \cdot 10^{-6} \cdot m$ $w := 50 \cdot 10^{-6} \cdot m$

$f1(l) = 4.103 \cdot 10^4 \cdot sec^{-1}$ $f2(l, w) = 4.042 \cdot 10^4 \cdot sec^{-1}$

225 x 40 μ

$l := 225 \cdot 10^{-6} \cdot m$ $w := 40 \cdot 10^{-6} \cdot m$

$f1(l) = 4.103 \cdot 10^4 \cdot sec^{-1}$ $f2(l, w) = 4.042 \cdot 10^4 \cdot sec^{-1}$

225 x 30 μ

$l := 225 \cdot 10^{-6} \cdot m$ $w := 30 \cdot 10^{-6} \cdot m$

$f1(l) = 4.103 \cdot 10^4 \cdot sec^{-1}$ $f2(l, w) = 4.042 \cdot 10^4 \cdot sec^{-1}$

Note that the width has no effect on the calculated value of resonance, but does effect real cantilevers

cantilevers

225 x 20 μ

$l := 225 \cdot 10^{-6} \cdot m$

$w := 40 \cdot 10^{-6} \cdot m$

$f1(l) = 4.103 \cdot 10^4 \cdot sec^{-1}$

$f2(l, w) = 4.042 \cdot 10^4 \cdot sec^{-1}$

225 x 10 μ

$l := 225 \cdot 10^{-6} \cdot m$

$w := 30 \cdot 10^{-6} \cdot m$

$f1(l) = 4.103 \cdot 10^4 \cdot sec^{-1}$

$f2(l, w) = 4.042 \cdot 10^4 \cdot sec^{-1}$

325 x 50 μ

$l := 325 \cdot 10^{-6} \cdot m$ $\qquad$ $w := 50 \cdot 10^{-6} \cdot m$

$f1(l) = 1.966 \cdot 10^4 \cdot sec^{-1}$ $\qquad$ $f2(l, w) = 1.937 \cdot 10^4 \cdot sec^{-1}$

300 x 50 μ

$l := 300 \cdot 10^{-6} \cdot m$ $\qquad$ $w := 50 \cdot 10^{-6} \cdot m$

$f1(l) = 2.308 \cdot 10^4 \cdot sec^{-1}$ $\qquad$ $f2(l, w) = 2.274 \cdot 10^4 \cdot sec^{-1}$

275 x 50 μ

$l := 275 \cdot 10^{-6} \cdot m$ $\qquad$ $w := 50 \cdot 10^{-6} \cdot m$

$f1(l) = 2.747 \cdot 10^4 \cdot sec^{-1}$ $\qquad$ $f2(l, w) = 2.706 \cdot 10^4 \cdot sec^{-1}$

250 x 50 μ

$l := 250 \cdot 10^{-6} \cdot m$ $\qquad$ $w := 50 \cdot 10^{-6} \cdot m$

$f1(l) = 3.323 \cdot 10^4 \cdot sec^{-1}$ $\qquad$ $f2(l, w) = 3.274 \cdot 10^4 \cdot sec^{-1}$

225 x 50 μ

$l := 225 \cdot 10^{-6} \cdot m$ $\qquad$ $w := 50 \cdot 10^{-6} \cdot m$

$f1(l) = 4.103 \cdot 10^4 \cdot sec^{-1}$ $\qquad$ $f2(l, w) = 4.042 \cdot 10^4 \cdot sec^{-1}$

200 x 50 μ

$l := 200 \cdot 10^{-6} \cdot m$ $\qquad$ $w := 50 \cdot 10^{-6} \cdot m$

$f1(l) = 5.193 \cdot 10^4 \cdot sec^{-1}$ $\qquad$ $f2(l, w) = 5.116 \cdot 10^4 \cdot sec^{-1}$

175 x 50 μ

$l := 175 \cdot 10^{-6} \cdot m$ $w := 50 \cdot 10^{-6} \cdot m$

$f1(l) = 6.782 \cdot 10^{4} \cdot sec^{-1}$ $f2(l, w) = 6.682 \cdot 10^{4} \cdot sec^{-1}$

150 x 50 μ

$l := 150 \cdot 10^{-6} \cdot m$ $w := 50 \cdot 10^{-6} \cdot m$

$f1(l) = 9.231 \cdot 10^{4} \cdot sec^{-1}$ $f2(l, w) = 9.095 \cdot 10^{4} \cdot sec^{-1}$

125 x 50 μ

$l := 125 \cdot 10^{-6} \cdot m$ $w := 50 \cdot 10^{-6} \cdot m$

$f1(l) = 1.329 \cdot 10^{5} \cdot sec^{-1}$ $f2(l, w) = 1.31 \cdot 10^{5} \cdot sec^{-1}$

100 x 50 μ

$l := 100 \cdot 10^{-6} \cdot m$ $w := 50 \cdot 10^{-6} \cdot m$

$f1(l) = 2.077 \cdot 10^{5} \cdot sec^{-1}$ $f2(l, w) = 2.046 \cdot 10^{5} \cdot sec^{-1}$

75 x 50 μ

$l := 75 \cdot 10^{-6} \cdot m$ $w := 50 \cdot 10^{-6} \cdot m$

$f1(l) = 3.693 \cdot 10^{5} \cdot sec^{-1}$ $f2(l, w) = 3.638 \cdot 10^{5} \cdot sec^{-1}$

50 x 50 μ

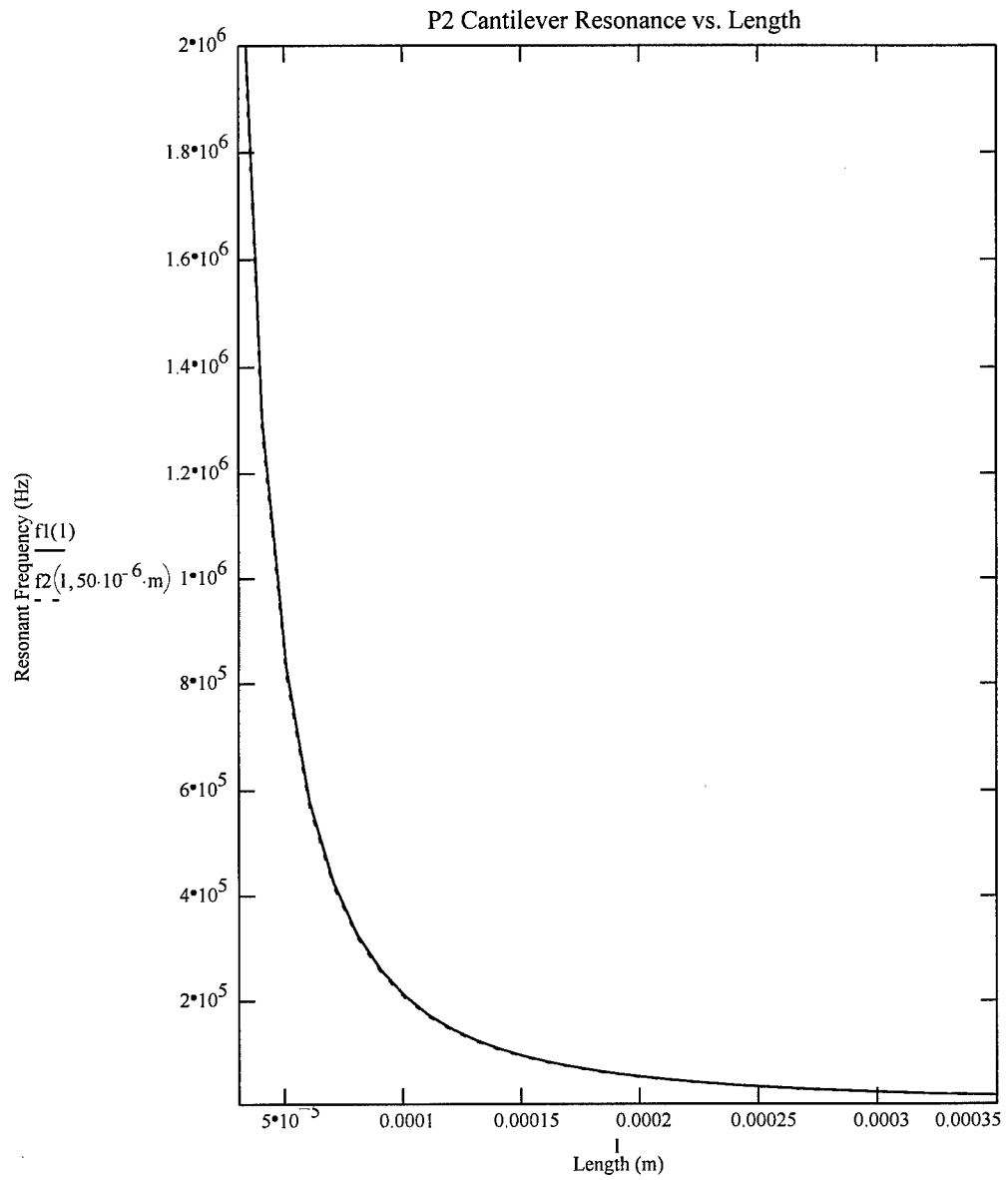$l := 50 \cdot 10^{-6} \cdot m$ $w := 50 \cdot 10^{-6} \cdot m$

$f1(l) = 8.308 \cdot 10^{5} \cdot sec^{-1}$ $f2(l, w) = 8.186 \cdot 10^{5} \cdot sec^{-1}$

set up range and granularity

$$r1 := 10 \cdot 10^{-6} \cdot m \qquad r2 := 350 \cdot 10^{-6} \cdot m \qquad n := 1 \qquad l := r1, r1 + \frac{r1}{n} \,..\, r2$$

P2 Cantilever Resonance vs. Length

l	$f1(l)$	$f2\left(l, 50\cdot 10^{-6}\cdot m\right)$
$1\cdot 10^{-5}\cdot m$	$2.077\cdot 10^{7}\cdot sec^{-1}$	$2.046\cdot 10^{7}\cdot sec^{-1}$
$2\cdot 10^{-5}\cdot m$	$5.193\cdot 10^{6}\cdot sec^{-1}$	$5.116\cdot 10^{6}\cdot sec^{-1}$
$3\cdot 10^{-5}\cdot m$	$2.308\cdot 10^{6}\cdot sec^{-1}$	$2.274\cdot 10^{6}\cdot sec^{-1}$
$4\cdot 10^{-5}\cdot m$	$1.298\cdot 10^{6}\cdot sec^{-1}$	$1.279\cdot 10^{6}\cdot sec^{-1}$
$5\cdot 10^{-5}\cdot m$	$8.308\cdot 10^{5}\cdot sec^{-1}$	$8.186\cdot 10^{5}\cdot sec^{-1}$
$6\cdot 10^{-5}\cdot m$	$5.77\cdot 10^{5}\cdot sec^{-1}$	$5.684\cdot 10^{5}\cdot sec^{-1}$
$7\cdot 10^{-5}\cdot m$	$4.239\cdot 10^{5}\cdot sec^{-1}$	$4.176\cdot 10^{5}\cdot sec^{-1}$
$8\cdot 10^{-5}\cdot m$	$3.245\cdot 10^{5}\cdot sec^{-1}$	$3.198\cdot 10^{5}\cdot sec^{-1}$
$9\cdot 10^{-5}\cdot m$	$2.564\cdot 10^{5}\cdot sec^{-1}$	$2.526\cdot 10^{5}\cdot sec^{-1}$
$1\cdot 10^{-4}\cdot m$	$2.077\cdot 10^{5}\cdot sec^{-1}$	$2.046\cdot 10^{5}\cdot sec^{-1}$
$1.1\cdot 10^{-4}\cdot m$	$1.717\cdot 10^{5}\cdot sec^{-1}$	$1.691\cdot 10^{5}\cdot sec^{-1}$
$1.2\cdot 10^{-4}\cdot m$	$1.442\cdot 10^{5}\cdot sec^{-1}$	$1.421\cdot 10^{5}\cdot sec^{-1}$
$1.3\cdot 10^{-4}\cdot m$	$1.229\cdot 10^{5}\cdot sec^{-1}$	$1.211\cdot 10^{5}\cdot sec^{-1}$
$1.4\cdot 10^{-4}\cdot m$	$1.06\cdot 10^{5}\cdot sec^{-1}$	$1.044\cdot 10^{5}\cdot sec^{-1}$
$1.5\cdot 10^{-4}\cdot m$	$9.231\cdot 10^{4}\cdot sec^{-1}$	$9.095\cdot 10^{4}\cdot sec^{-1}$
$1.6\cdot 10^{-4}\cdot m$	$8.114\cdot 10^{4}\cdot sec^{-1}$	$7.994\cdot 10^{4}\cdot sec^{-1}$
$1.7\cdot 10^{-4}\cdot m$	$7.187\cdot 10^{4}\cdot sec^{-1}$	$7.081\cdot 10^{4}\cdot sec^{-1}$
$1.8\cdot 10^{-4}\cdot m$	$6.411\cdot 10^{4}\cdot sec^{-1}$	$6.316\cdot 10^{4}\cdot sec^{-1}$
$1.9\cdot 10^{-4}\cdot m$	$5.754\cdot 10^{4}\cdot sec^{-1}$	$5.669\cdot 10^{4}\cdot sec^{-1}$
$2\cdot 10^{-4}\cdot m$	$5.193\cdot 10^{4}\cdot sec^{-1}$	$5.116\cdot 10^{4}\cdot sec^{-1}$
$2.1\cdot 10^{-4}\cdot m$	$4.71\cdot 10^{4}\cdot sec^{-1}$	$4.64\cdot 10^{4}\cdot sec^{-1}$
$2.2\cdot 10^{-4}\cdot m$	$4.291\cdot 10^{4}\cdot sec^{-1}$	$4.228\cdot 10^{4}\cdot sec^{-1}$
$2.3\cdot 10^{-4}\cdot m$	$3.926\cdot 10^{4}\cdot sec^{-1}$	$3.868\cdot 10^{4}\cdot sec^{-1}$
$2.4\cdot 10^{-4}\cdot m$	$3.606\cdot 10^{4}\cdot sec^{-1}$	$3.553\cdot 10^{4}\cdot sec^{-1}$
$2.5\cdot 10^{-4}\cdot m$	$3.323\cdot 10^{4}\cdot sec^{-1}$	$3.274\cdot 10^{4}\cdot sec^{-1}$
$2.6\cdot 10^{-4}\cdot m$	$3.073\cdot 10^{4}\cdot sec^{-1}$	$3.027\cdot 10^{4}\cdot sec^{-1}$
$2.7\cdot 10^{-4}\cdot m$	$2.849\cdot 10^{4}\cdot sec^{-1}$	$2.807\cdot 10^{4}\cdot sec^{-1}$
$2.8\cdot 10^{-4}\cdot m$	$2.649\cdot 10^{4}\cdot sec^{-1}$	$2.61\cdot 10^{4}\cdot sec^{-1}$
$2.9\cdot 10^{-4}\cdot m$	$2.47\cdot 10^{4}\cdot sec^{-1}$	$2.433\cdot 10^{4}\cdot sec^{-1}$
$3\cdot 10^{-4}\cdot m$	$2.308\cdot 10^{4}\cdot sec^{-1}$	$2.274\cdot 10^{4}\cdot sec^{-1}$
$3.1\cdot 10^{-4}\cdot m$	$2.161\cdot 10^{4}\cdot sec^{-1}$	$2.129\cdot 10^{4}\cdot sec^{-1}$
$3.2\cdot 10^{-4}\cdot m$	$2.028\cdot 10^{4}\cdot sec^{-1}$	$1.998\cdot 10^{4}\cdot sec^{-1}$
$3.3\cdot 10^{-4}\cdot m$	$1.907\cdot 10^{4}\cdot sec^{-1}$	$1.879\cdot 10^{4}\cdot sec^{-1}$
$3.4\cdot 10^{-4}\cdot m$	$1.797\cdot 10^{4}\cdot sec^{-1}$	$1.77\cdot 10^{4}\cdot sec^{-1}$
$3.5\cdot 10^{-4}\cdot m$	$1.696\cdot 10^{4}\cdot sec^{-1}$	$1.671\cdot 10^{4}\cdot sec^{-1}$

Poly2 Cantilevers with Gold layer (not implemented)

$E := 169 \cdot 10^9 \cdot Pa$ Young's Modulus

Function to calculate the % Error
T is the theoretical value
O is the observed value

$tp := 1.5 \cdot 10^{-6} \cdot m$ Thickness of Poly2

$\lambda := 1.875104$ Eigenvalue for simple beam $Error(T,O) := \left| \dfrac{T - O}{T} \right|$ $tg := 0.5 \cdot 10^{-6} \cdot m$

$\rho p := 2.3 \cdot 10^3 \cdot \dfrac{kg}{m^3}$ Density of Polysilicon $\rho g := 19.3 \cdot 10^3 \cdot \dfrac{kg}{m^3}$ Density of Gold

The two methods for calculating the resonant frequency:
f1 uses Equation 3-XX, and ignores the width of the beam.
f2 uses Equation 3-XX, and also takes into account the width of the beam
(however, this has no effect since w is a term in both k and M, and is therefore
factored out).

$f1(l) := \dfrac{\lambda^2 \cdot tp}{4 \cdot \pi \cdot l^2} \cdot \sqrt{\dfrac{E}{3 \cdot \rho p}}$

$f2(l,w) := \left| \begin{array}{l} k \leftarrow \dfrac{E \cdot w \cdot (tp)^3}{l^3} \\[2ex] M \leftarrow w \cdot l \cdot tp \cdot \rho p + w \cdot l \cdot tg \cdot \rho g \\[2ex] \dfrac{1}{2 \cdot \pi} \cdot \sqrt{\dfrac{k}{M}} \end{array} \right.$

225 x 50 μ   Half of the cantilevers label P12 200 have actual lengths (as drawn) of 225
microns

$l := 225 \cdot 10^{-6} \cdot m$ $w := 50 \cdot 10^{-6} \cdot m$

$f1(l) = 4.103 \cdot 10^4 \cdot sec^{-1}$ $f2(l,w) = 2.074 \cdot 10^4 \cdot sec^{-1}$

225 x 40 μ

$l := 225 \cdot 10^{-6} \cdot m$ $w := 40 \cdot 10^{-6} \cdot m$

$f1(l) = 4.103 \cdot 10^4 \cdot sec^{-1}$ $f2(l,w) = 2.074 \cdot 10^4 \cdot sec^{-1}$

225 x 30 μ

$l := 225 \cdot 10^{-6} \cdot m$ $w := 30 \cdot 10^{-6} \cdot m$

$f1(l) = 4.103 \cdot 10^4 \cdot sec^{-1}$ $f2(l,w) = 2.074 \cdot 10^4 \cdot sec^{-1}$

Note that the width has no effect on the calculated value of resonance, but does effect real
cantilevers

225 x 20 µ

$l := 225 \cdot 10^{-6} \cdot m$ $w := 40 \cdot 10^{-6} \cdot m$

$f2(l, w) = 2.074 \cdot 10^4 \cdot sec^{-1}$

225 x 10 µ

$l := 225 \cdot 10^{-6} \cdot m$ $w := 30 \cdot 10^{-6} \cdot m$

$f2(l, w) = 2.074 \cdot 10^4 \cdot sec^{-1}$

325 x 50 μ

$l := 325 \cdot 10^{-6} \cdot m$ $w := 50 \cdot 10^{-6} \cdot m$

$f2(l, w) = 9.943 \cdot 10^{3} \cdot sec^{-1}$

300 x 50 μ

$l := 300 \cdot 10^{-6} \cdot m$ $w := 50 \cdot 10^{-6} \cdot m$

$f2(l, w) = 1.167 \cdot 10^{4} \cdot sec^{-1}$

275 x 50 μ

$l := 275 \cdot 10^{-6} \cdot m$ $w := 50 \cdot 10^{-6} \cdot m$

$f2(l, w) = 1.389 \cdot 10^{4} \cdot sec^{-1}$

250 x 50 μ

$l := 250 \cdot 10^{-6} \cdot m$ $w := 50 \cdot 10^{-6} \cdot m$

$f2(l, w) = 1.68 \cdot 10^{4} \cdot sec^{-1}$

225 x 50 μ

$l := 225 \cdot 10^{-6} \cdot m$ $w := 50 \cdot 10^{-6} \cdot m$

$f2(l, w) = 2.074 \cdot 10^{4} \cdot sec^{-1}$

200 x 50 μ

$l := 200 \cdot 10^{-6} \cdot m$ $w := 50 \cdot 10^{-6} \cdot m$

$f2(l, w) = 2.625 \cdot 10^{4} \cdot sec^{-1}$

175 x 50 μ

$l := 175 \cdot 10^{-6} \cdot m$ $\qquad$ $w := 50 \cdot 10^{-6} \cdot m$

$\qquad\qquad\qquad\qquad$ $f2(l, w) = 3.429 \cdot 10^4 \cdot sec^{-1}$

150 x 50 μ

$l := 150 \cdot 10^{-6} \cdot m$ $\qquad$ $w := 50 \cdot 10^{-6} \cdot m$

$\qquad\qquad\qquad\qquad$ $f2(l, w) = 4.667 \cdot 10^4 \cdot sec^{-1}$

125 x 50 μ

$l := 125 \cdot 10^{-6} \cdot m$ $\qquad$ $w := 50 \cdot 10^{-6} \cdot m$

$\qquad\qquad\qquad\qquad$ $f2(l, w) = 6.721 \cdot 10^4 \cdot sec^{-1}$

100 x 50 μ

$l := 100 \cdot 10^{-6} \cdot m$ $\qquad$ $w := 50 \cdot 10^{-6} \cdot m$

$\qquad\qquad\qquad\qquad$ $f2(l, w) = 1.05 \cdot 10^5 \cdot sec^{-1}$

75 x 50 μ

$l := 75 \cdot 10^{-6} \cdot m$ $\qquad$ $w := 50 \cdot 10^{-6} \cdot m$

$\qquad\qquad\qquad\qquad$ $f2(l, w) = 1.867 \cdot 10^5 \cdot sec^{-1}$

50 x 50 μ

$l := 50 \cdot 10^{-6} \cdot m$ $\qquad$ $w := 50 \cdot 10^{-6} \cdot m$

$\qquad\qquad\qquad\qquad$ $f2(l, w) = 4.201 \cdot 10^5 \cdot sec^{-1}$

set up range and granularity

$$r1 := 10 \cdot 10^{-6} \cdot m \qquad r2 := 350 \cdot 10^{-6} \cdot m \qquad n := 1 \qquad l := r1, r1 + \frac{r1}{n} .. r2$$

P2G Cantilever Resonance vs. Length
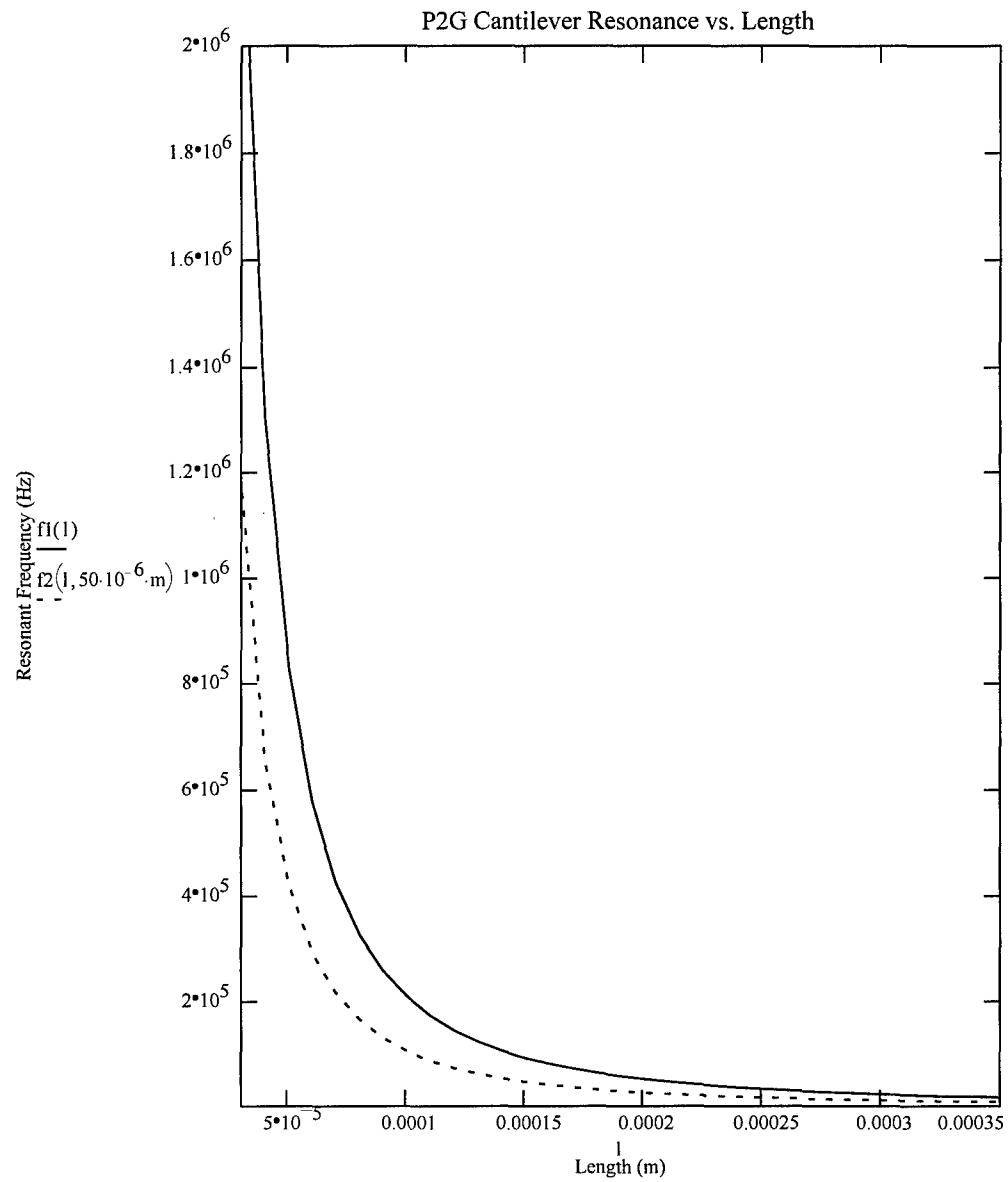
Note: The solid line is P2 only

l	f1(l)	$f2\left(l, 50\cdot10^{-6}\cdot m\right)$
$1\cdot10^{-5}\cdot m$	$2.077\cdot10^{7}\cdot sec^{-1}$	$1.05\cdot10^{7}\cdot sec^{-1}$
$2\cdot10^{-5}\cdot m$	$5.193\cdot10^{6}\cdot sec^{-1}$	$2.625\cdot10^{6}\cdot sec^{-1}$
$3\cdot10^{-5}\cdot m$	$2.308\cdot10^{6}\cdot sec^{-1}$	$1.167\cdot10^{6}\cdot sec^{-1}$
$4\cdot10^{-5}\cdot m$	$1.298\cdot10^{6}\cdot sec^{-1}$	$6.564\cdot10^{5}\cdot sec^{-1}$
$5\cdot10^{-5}\cdot m$	$8.308\cdot10^{5}\cdot sec^{-1}$	$4.201\cdot10^{5}\cdot sec^{-1}$
$6\cdot10^{-5}\cdot m$	$5.77\cdot10^{5}\cdot sec^{-1}$	$2.917\cdot10^{5}\cdot sec^{-1}$
$7\cdot10^{-5}\cdot m$	$4.239\cdot10^{5}\cdot sec^{-1}$	$2.143\cdot10^{5}\cdot sec^{-1}$
$8\cdot10^{-5}\cdot m$	$3.245\cdot10^{5}\cdot sec^{-1}$	$1.641\cdot10^{5}\cdot sec^{-1}$
$9\cdot10^{-5}\cdot m$	$2.564\cdot10^{5}\cdot sec^{-1}$	$1.297\cdot10^{5}\cdot sec^{-1}$
$1\cdot10^{-4}\cdot m$	$2.077\cdot10^{5}\cdot sec^{-1}$	$1.05\cdot10^{5}\cdot sec^{-1}$
$1.1\cdot10^{-4}\cdot m$	$1.717\cdot10^{5}\cdot sec^{-1}$	$8.679\cdot10^{4}\cdot sec^{-1}$
$1.2\cdot10^{-4}\cdot m$	$1.442\cdot10^{5}\cdot sec^{-1}$	$7.293\cdot10^{4}\cdot sec^{-1}$
$1.3\cdot10^{-4}\cdot m$	$1.229\cdot10^{5}\cdot sec^{-1}$	$6.214\cdot10^{4}\cdot sec^{-1}$
$1.4\cdot10^{-4}\cdot m$	$1.06\cdot10^{5}\cdot sec^{-1}$	$5.358\cdot10^{4}\cdot sec^{-1}$
$1.5\cdot10^{-4}\cdot m$	$9.231\cdot10^{4}\cdot sec^{-1}$	$4.667\cdot10^{4}\cdot sec^{-1}$
$1.6\cdot10^{-4}\cdot m$	$8.114\cdot10^{4}\cdot sec^{-1}$	$4.102\cdot10^{4}\cdot sec^{-1}$
$1.7\cdot10^{-4}\cdot m$	$7.187\cdot10^{4}\cdot sec^{-1}$	$3.634\cdot10^{4}\cdot sec^{-1}$
$1.8\cdot10^{-4}\cdot m$	$6.411\cdot10^{4}\cdot sec^{-1}$	$3.241\cdot10^{4}\cdot sec^{-1}$
$1.9\cdot10^{-4}\cdot m$	$5.754\cdot10^{4}\cdot sec^{-1}$	$2.909\cdot10^{4}\cdot sec^{-1}$
$2\cdot10^{-4}\cdot m$	$5.193\cdot10^{4}\cdot sec^{-1}$	$2.625\cdot10^{4}\cdot sec^{-1}$
$2.1\cdot10^{-4}\cdot m$	$4.71\cdot10^{4}\cdot sec^{-1}$	$2.381\cdot10^{4}\cdot sec^{-1}$
$2.2\cdot10^{-4}\cdot m$	$4.291\cdot10^{4}\cdot sec^{-1}$	$2.17\cdot10^{4}\cdot sec^{-1}$
$2.3\cdot10^{-4}\cdot m$	$3.926\cdot10^{4}\cdot sec^{-1}$	$1.985\cdot10^{4}\cdot sec^{-1}$
$2.4\cdot10^{-4}\cdot m$	$3.606\cdot10^{4}\cdot sec^{-1}$	$1.823\cdot10^{4}\cdot sec^{-1}$
$2.5\cdot10^{-4}\cdot m$	$3.323\cdot10^{4}\cdot sec^{-1}$	$1.68\cdot10^{4}\cdot sec^{-1}$
$2.6\cdot10^{-4}\cdot m$	$3.073\cdot10^{4}\cdot sec^{-1}$	$1.554\cdot10^{4}\cdot sec^{-1}$
$2.7\cdot10^{-4}\cdot m$	$2.849\cdot10^{4}\cdot sec^{-1}$	$1.441\cdot10^{4}\cdot sec^{-1}$
$2.8\cdot10^{-4}\cdot m$	$2.649\cdot10^{4}\cdot sec^{-1}$	$1.34\cdot10^{4}\cdot sec^{-1}$
$2.9\cdot10^{-4}\cdot m$	$2.47\cdot10^{4}\cdot sec^{-1}$	$1.249\cdot10^{4}\cdot sec^{-1}$
$3\cdot10^{-4}\cdot m$	$2.308\cdot10^{4}\cdot sec^{-1}$	$1.167\cdot10^{4}\cdot sec^{-1}$
$3.1\cdot10^{-4}\cdot m$	$2.161\cdot10^{4}\cdot sec^{-1}$	$1.093\cdot10^{4}\cdot sec^{-1}$
$3.2\cdot10^{-4}\cdot m$	$2.028\cdot10^{4}\cdot sec^{-1}$	$1.026\cdot10^{4}\cdot sec^{-1}$
$3.3\cdot10^{-4}\cdot m$	$1.907\cdot10^{4}\cdot sec^{-1}$	$9.644\cdot10^{3}\cdot sec^{-1}$
$3.4\cdot10^{-4}\cdot m$	$1.797\cdot10^{4}\cdot sec^{-1}$	$9.085\cdot10^{3}\cdot sec^{-1}$
$3.5\cdot10^{-4}\cdot m$	$1.696\cdot10^{4}\cdot sec^{-1}$	$8.573\cdot10^{3}\cdot sec^{-1}$

Comb - Poly 1

$w := 2.0 \cdot 10^{-6} \cdot m$ Width of supporting beams

$h := 1.9946 \cdot 10^{-6} \cdot m$ Thickness of Poly1 (Numbers given for MUMPS 12)

$E := 169 \cdot 10^{9} \cdot Pa$ Young's Modulus

$l := 150 \cdot 10^{-6} \cdot m$ Lenth of supporting beams

$\rho := 2.3 \cdot 10^{3} \cdot \dfrac{kg}{m^{3}}$ Density of Polysilicon

Calculate the Mass of the plate, beams, and trusses by breaking the areas into rectangles:

$MP := \left[2 \cdot \left[\left(171 \cdot 10^{-6} \cdot m \right) \cdot \left(12 \cdot 10^{-6} \cdot m \right) + \left(17 \cdot 10^{-6} \cdot m \right) \cdot \left(90 \cdot 10^{-6} \cdot m \right) \right] + 30 \cdot \left(40 \cdot 10^{-6} \cdot m \right) \cdot \left(3 \cdot 10^{-6} \cdot m \right) + \left(54 \cdot 10^{-6} \cdot m \right) \cdot \left(20 \cdot 10^{-6} \cdot m \right) \right]$

$MB := 8 \cdot \left(2 \cdot 10^{-6} \cdot m \right) \cdot \left(150 \cdot 10^{-6} \cdot m \right) \cdot h \cdot \rho$

$MT := 2 \cdot \left(15 \cdot 10^{-6} \cdot m \right) \cdot \left(78 \cdot 10^{-6} \cdot m \right) \cdot h \cdot \rho$

$M := MP + MB + MT$

$MT = 1.073 \cdot 10^{-11} \cdot kg$ $MB = 1.101 \cdot 10^{-11} \cdot kg$ $MP = 5.434 \cdot 10^{-11} \cdot kg$ $M = 7.608 \cdot 10^{-11} \cdot kg$

Calculate I and k

$I := \dfrac{h \cdot w^{3}}{12}$ $I = 0 \cdot m^{4}$ $k := \dfrac{24 \cdot E \cdot I}{l^{3}}$ $k = 1.598 \cdot kg \cdot sec^{-2}$

Alternate Method, taking into account non-ideal etching process

$a := 1.95 \cdot 10^{-6} \cdot m$ $b := 2.05 \cdot 10^{-6} \cdot m$ $I2 := \dfrac{h}{48} \cdot (a + b) \cdot \left(a^{2} + b^{2} \right)$ $I2 = 0 \cdot m^{4}$

$k2 := \dfrac{24 \cdot E \cdot I2}{l^{3}}$ $k2 = 1.599 \cdot kg \cdot sec^{-2}$

Calculate Mass and Frequency

$M := MP + \dfrac{1}{4} \cdot MT + \dfrac{12}{35} \cdot MB$ $M = 6.079 \cdot 10^{-11} \cdot kg$

$f := \dfrac{1}{2 \cdot \pi} \cdot \sqrt{\dfrac{k}{M}}$ $f = 2.58 \cdot 10^{4} \cdot sec^{-1}$

$f2 := \dfrac{1}{2 \cdot \pi} \cdot \sqrt{\dfrac{k2}{M}}$ $f2 = 2.581 \cdot 10^{4} \cdot sec^{-1}$

theoretical $:= f2$ observed $:= 19.4 \cdot KHz$

$error := \dfrac{|theoretical - observed|}{theoretical} \cdot 100$ $error = 24.84 \%$

Piston Mirror - PA4P1.0_Shrt

$tp1 := 1.9946 \cdot 10^{-6} \cdot m$ $Pw := 66 \cdot 10^{-6} \cdot m$ $Pl := 78 \cdot 10^{-6} \cdot m$

$E := 169 \cdot 10^{9} \cdot Pa$ $tp2 := 1.5441 \cdot 10^{-6} \cdot m$ $Cpd := 22 \cdot 10^{-6} \cdot m$ $Cgd := 20 \cdot 10^{-6} \cdot m$

$\sigma := 1.2 \cdot 10^{6} \cdot Pa$ $tox := 0.7508 \cdot 10^{-6} \cdot m$ $v := 0.22$ $n := 4$

$tg := 0.5200 \cdot 10^{-6} \cdot m$ $\rho p := 2.3 \cdot 10^{3} \cdot \dfrac{kg}{m^3}$ $\rho g := 19.3 \cdot 10^{3} \cdot \dfrac{kg}{m^3}$

$w := 1.0 \cdot 10^{-6} \cdot m$ $l := 86 \cdot 10^{-6} \cdot m$

$Aa := (Pw \cdot Pl) \cdot tp1$ Volume of actuator

Volume of Poly2/oxide mass

$Apm := \pi \cdot \left(\dfrac{Cpd}{2}\right)^2 \cdot (tp1 + tox)$

$Agm := \pi \cdot \left(\dfrac{Cgd}{2}\right)^2 \cdot tg$ Volume of gold mass

$Mp := (Aa + Apm) \cdot \rho p$ $Mp = 2.602 \cdot 10^{-11} \cdot kg$

$Mgm := Agm \cdot \rho g$ $Mgm = 3.153 \cdot 10^{-12} \cdot kg$

$M := Mp + Mgm$ $M = 2.917 \cdot 10^{-11} \cdot kg$

$v1 := 1 - v$ $v1 = 0.78$

$k := n \cdot \left(\dfrac{E \cdot w \cdot tp1^3}{l^3}\right)$ $k = 8.434 \cdot kg \cdot sec^{-2}$ $k2 := \dfrac{\sigma \cdot (v1) \cdot w \cdot tp1}{2 \cdot l}$ $k2 = 0.011 \cdot kg \cdot sec^{-2}$

$kt := k + k2$ $kt = 8.445 \cdot kg \cdot sec^{-2}$

$f := \dfrac{1}{2 \cdot \pi} \cdot \left(\sqrt{\dfrac{kt}{M}}\right)$ $f = 8.563 \cdot 10^{4} \cdot sec^{-1}$

Piston Mirror - PA4P1.25_Shrt

$tp1 := 1.9946 \cdot 10^{-6} \cdot m$ $Pw := 66 \cdot 10^{-6} \cdot m$ $Pl := 78 \cdot 10^{-6} \cdot m$

$E := 169 \cdot 10^{9} \cdot Pa$ $tp2 := 1.5441 \cdot 10^{-6} \cdot m$ $Cpd := 22 \cdot 10^{-6} \cdot m$ $Cgd := 20 \cdot 10^{-6} \cdot m$

$\sigma := 1.2 \cdot 10^{6} \cdot Pa$ $tox := 0.7508 \cdot 10^{-6} \cdot m$ $v := 0.22$ $n := 4$

$tg := 0.5200 \cdot 10^{-6} \cdot m$ $\rho p := 2.3 \cdot 10^{3} \cdot \dfrac{kg}{m^3}$ $\rho g := 19.3 \cdot 10^{3} \cdot \dfrac{kg}{m^3}$

$w := 1.25 \cdot 10^{-6} \cdot m$ $l := 86 \cdot 10^{-6} \cdot m$

$Aa := (Pw \cdot Pl) \cdot tp1$ Volume of actuator

Volume of Poly2/oxide mass

$Apm := \pi \cdot \left(\dfrac{Cpd}{2}\right)^2 \cdot (tp1 + tox)$

$Agm := \pi \cdot \left(\dfrac{Cgd}{2}\right)^2 \cdot tg$ Volume of gold mass

$Mp := (Aa + Apm) \cdot \rho p$ $Mp = 2.602 \cdot 10^{-11} \cdot kg$

$Mgm := Agm \cdot \rho g$ $Mgm = 3.153 \cdot 10^{-12} \cdot kg$

$M := Mp + Mgm$ $M = 2.917 \cdot 10^{-11} \cdot kg$

$v1 := 1 - v$ $v1 = 0.78$

$$k := n \cdot \left(\frac{E \cdot w \cdot tp1^3}{l^3} \right) \qquad k = 10.542 \bullet kg \bullet sec^{-2} \qquad k2 := \frac{\sigma \cdot (v1) \cdot w \cdot tp1}{2 \cdot l} \qquad k2 = 0.014 \bullet kg \bullet sec^{-2}$$

$$kt := k + k2 \qquad kt = 10.556 \bullet kg \bullet sec^{-2}$$

$$f := \frac{1}{2 \cdot \pi} \cdot \left(\sqrt{\frac{kt}{M}} \right) \qquad f = 9.574 \bullet 10^4 \bullet sec^{-1}$$

Piston Mirror - PA4P1.5_Shrt

$tp1 := 1.9946 \cdot 10^{-6} \cdot m \qquad Pw := 66 \cdot 10^{-6} \cdot m \qquad Pl := 78 \cdot 10^{-6} \cdot m$

$E := 169 \cdot 10^9 \cdot Pa \qquad tp2 := 1.5441 \cdot 10^{-6} \cdot m \qquad Cpd := 22 \cdot 10^{-6} \cdot m \qquad Cgd := 20 \cdot 10^{-6} \cdot m$

$\sigma := 1.2 \cdot 10^6 \cdot Pa \qquad tox := 0.7508 \cdot 10^{-6} \cdot m \qquad v := 0.22 \qquad n := 4$

$w := 1.5 \cdot 10^{-6} \cdot m \qquad tg := 0.5200 \cdot 10^{-6} \cdot m \qquad \rho p := 2.3 \cdot 10^3 \cdot \frac{kg}{m^3} \qquad \rho g := 19.3 \cdot 10^3 \cdot \frac{kg}{m^3}$

$l := 88 \cdot 10^{-6} \cdot m$

$Aa := (Pw \cdot Pl) \cdot tp1$ Volume of actuator

      Volume of Poly2/oxide mass

$Apm := \pi \cdot \left(\frac{Cpd}{2} \right)^2 \cdot (tp1 + tox)$

$Agm := \pi \cdot \left(\frac{Cgd}{2} \right)^2 \cdot tg$ Volume of gold mass

$Mp := (Aa + Apm) \cdot \rho p \qquad Mp = 2.602 \bullet 10^{-11} \bullet kg$

$Mgm := Agm \cdot \rho g \qquad Mgm = 3.153 \bullet 10^{-12} \bullet kg$

$M := Mp + Mgm \qquad M = 2.917 \bullet 10^{-11} \bullet kg$

$v1 := 1 - v \qquad v1 = 0.78$

$$k := n \cdot \left(\frac{E \cdot w \cdot tp1^3}{l^3} \right) \qquad k = 11.807 \bullet kg \bullet sec^{-2} \qquad k2 := \frac{\sigma \cdot (v1) \cdot w \cdot tp1}{2 \cdot l} \qquad k2 = 0.016 \bullet kg \bullet sec^{-2}$$

$$kt := k + k2 \qquad kt = 11.823 \bullet kg \bullet sec^{-2}$$

$$f := \frac{1}{2 \cdot \pi} \cdot \left(\sqrt{\frac{kt}{M}} \right) \qquad f = 1.013 \bullet 10^5 \bullet sec^{-1}$$

Piston Mirror - PA4P1.75_Shrt

$tp1 := 1.9946 \cdot 10^{-6} \cdot m \qquad Pw := 66 \cdot 10^{-6} \cdot m \qquad Pl := 78 \cdot 10^{-6} \cdot m$

$E := 169 \cdot 10^9 \cdot Pa \qquad tp2 := 1.5441 \cdot 10^{-6} \cdot m \qquad Cpd := 22 \cdot 10^{-6} \cdot m \qquad Cgd := 20 \cdot 10^{-6} \cdot m$

$\sigma := 1.2 \cdot 10^6 \cdot Pa \qquad tox := 0.7508 \cdot 10^{-6} \cdot m \qquad v := 0.22 \qquad n := 4$

$w := 1.75 \cdot 10^{-6} \cdot m \qquad tg := 0.5200 \cdot 10^{-6} \cdot m \qquad \rho p := 2.3 \cdot 10^3 \cdot \frac{kg}{m^3} \qquad \rho g := 19.3 \cdot 10^3 \cdot \frac{kg}{m^3}$

$l := 86 \cdot 10^{-6} \cdot m$

$Aa := (Pw \cdot Pl) \cdot tp1$ Volume of actuator

      Volume of Poly2/oxide mass

$Apm := \pi \cdot \left(\frac{Cpd}{2} \right)^2 \cdot (tp1 + tox)$

$Agm := \pi \cdot \left(\frac{Cgd}{2} \right)^2 \cdot tg$ Volume of gold mass

$$Mp := (Aa + Apm) \cdot \rho p \qquad Mp = 2.602 \cdot 10^{-11} \cdot kg$$

$$Mgm := Agm \cdot \rho g \qquad Mgm = 3.153 \cdot 10^{-12} \cdot kg$$

$$M := Mp + Mgm \qquad M = 2.917 \cdot 10^{-11} \cdot kg$$

$$v1 := 1 - v \qquad v1 = 0.78$$

$$k := n \cdot \left(\frac{E \cdot w \cdot tp1^3}{l^3} \right) \qquad k = 14.759 \cdot kg \cdot sec^{-2} \qquad k2 := \frac{\sigma \cdot (v1) \cdot w \cdot tp1}{2 \cdot l} \qquad k2 = 0.019 \cdot kg \cdot sec^{-2}$$

$$kt := k + k2 \qquad kt = 14.778 \cdot kg \cdot sec^{-2}$$

$$f := \frac{1}{2 \cdot \pi} \cdot \left(\sqrt{\frac{kt}{M}} \right) \qquad f = 1.133 \cdot 10^5 \cdot sec^{-1}$$

Piston Mirror - PA4P2.0_Shrt

$$tp1 := 1.9946 \cdot 10^{-6} \cdot m \qquad Pw := 66 \cdot 10^{-6} \cdot m \qquad Pl := 78 \cdot 10^{-6} \cdot m$$

$$E := 169 \cdot 10^9 \cdot Pa \qquad tp2 := 1.5441 \cdot 10^{-6} \cdot m \qquad Cpd := 22 \cdot 10^{-6} \cdot m \qquad Cgd := 20 \cdot 10^{-6} \cdot m$$

$$\sigma := 1.2 \cdot 10^6 \cdot Pa \qquad tox := 0.7508 \cdot 10^{-6} \cdot m \qquad v := 0.22 \qquad n := 4$$

$$tg := 0.5200 \cdot 10^{-6} \cdot m$$
$$w := 2.0 \cdot 10^{-6} \cdot m \qquad l := 86 \cdot 10^{-6} \cdot m \qquad \rho p := 2.3 \cdot 10^3 \cdot \frac{kg}{m^3} \qquad \rho g := 19.3 \cdot 10^3 \cdot \frac{kg}{m^3}$$

$$Aa := (Pw \cdot Pl) \cdot tp1$$

Volume of actuator

$$Apm := \pi \cdot \left(\frac{Cpd}{2} \right)^2 \cdot (tp1 + tox)$$

Volume of Poly2/oxide mass

$$Agm := \pi \cdot \left(\frac{Cgd}{2} \right)^2 \cdot tg$$

Volume of gold mass

$$Mp := (Aa + Apm) \cdot \rho p \qquad Mp = 2.602 \cdot 10^{-11} \cdot kg$$

$$Mgm := Agm \cdot \rho g \qquad Mgm = 3.153 \cdot 10^{-12} \cdot kg$$

$$M := Mp + Mgm \qquad M = 2.917 \cdot 10^{-11} \cdot kg$$

$$v1 := 1 - v \qquad v1 = 0.78$$

$$k := n \cdot \left(\frac{E \cdot w \cdot tp1^3}{l^3} \right) \qquad k = 16.867 \cdot kg \cdot sec^{-2} \qquad k2 := \frac{\sigma \cdot (v1) \cdot w \cdot tp1}{2 \cdot l} \qquad k2 = 0.022 \cdot kg \cdot sec^{-2}$$

$$kt := k + k2 \qquad kt = 16.889 \cdot kg \cdot sec^{-2}$$

$$f := \frac{1}{2 \cdot \pi} \cdot \left(\sqrt{\frac{kt}{M}} \right) \qquad f = 1.211 \cdot 10^5 \cdot sec^{-1}$$

Piston Mirror - PA4P1.0

$tp1 := 1.9946 \cdot 10^{-6} \cdot m$ $Pw := 58 \cdot 10^{-6} \cdot m$ $Pl := 70 \cdot 10^{-6} \cdot m$

$E := 169 \cdot 10^{9} \cdot Pa$ $tp2 := 1.5441 \cdot 10^{-6} \cdot m$ $Cpd := 22 \cdot 10^{-6} \cdot m$ $Cgd := 20 \cdot 10^{-6} \cdot m$

$\sigma := 1.2 \cdot 10^{6} \cdot Pa$ $tox := 0.7508 \cdot 10^{-6} \cdot m$ $v := 0.22$ $n := 4$

$w := 1.0 \cdot 10^{-6} \cdot m$ $tg := 0.5200 \cdot 10^{-6} \cdot m$ $\rho p := 2.3 \cdot 10^{3} \cdot \dfrac{kg}{m^{3}}$ $\rho g := 19.3 \cdot 10^{3} \cdot \dfrac{kg}{m^{3}}$

$l := 147 \cdot 10^{-6} \cdot m$

$Aa := (Pw \cdot Pl) \cdot tp1$ Volume of actuator

$Apm := \pi \cdot \left(\dfrac{Cpd}{2}\right)^{2} \cdot (tp1 + tox)$ Volume of Poly2/oxide mass

$Agm := \pi \cdot \left(\dfrac{Cgd}{2}\right)^{2} \cdot tg$ Volume of gold mass

$Mp := (Aa + Apm) \cdot \rho p$ $Mp = 2.103 \cdot 10^{-11} \cdot kg$

$Mgm := Agm \cdot \rho g$ $Mgm = 3.153 \cdot 10^{-12} \cdot kg$

$M := Mp + Mgm$ $M = 2.418 \cdot 10^{-11} \cdot kg$

$v1 := 1 - v$ $v1 = 0.78$

$k := n \cdot \left(\dfrac{E \cdot w \cdot tp1^{3}}{l^{3}}\right)$ $k = 1.689 \cdot kg \cdot sec^{-2}$ $k2 := \dfrac{\sigma \cdot (v1) \cdot w \cdot tp1}{2 \cdot l}$ $k2 = 0.006 \cdot kg \cdot sec^{-2}$

$kt := k + k2$ $kt = 1.695 \cdot kg \cdot sec^{-2}$

$f := \dfrac{1}{2 \cdot \pi} \cdot \left(\sqrt{\dfrac{kt}{M}}\right)$ $f = 4.214 \cdot 10^{4} \cdot sec^{-1}$

Piston Mirror - PA4P1.25

$tp1 := 1.9946 \cdot 10^{-6} \cdot m$ $Pw := 58 \cdot 10^{-6} \cdot m$ $Pl := 70 \cdot 10^{-6} \cdot m$

$E := 169 \cdot 10^{9} \cdot Pa$ $tp2 := 1.5441 \cdot 10^{-6} \cdot m$ $Cpd := 22 \cdot 10^{-6} \cdot m$ $Cgd := 20 \cdot 10^{-6} \cdot m$

$\sigma := 1.2 \cdot 10^{6} \cdot Pa$ $tox := 0.7508 \cdot 10^{-6} \cdot m$ $v := 0.22$ $n := 4$

$w := 1.25 \cdot 10^{-6} \cdot m$ $tg := 0.5200 \cdot 10^{-6} \cdot m$ $\rho p := 2.3 \cdot 10^{3} \cdot \dfrac{kg}{m^{3}}$ $\rho g := 19.3 \cdot 10^{3} \cdot \dfrac{kg}{m^{3}}$

$l := 147 \cdot 10^{-6} \cdot m$

$Aa := (Pw \cdot Pl) \cdot tp1$ Volume of actuator

$Apm := \pi \cdot \left(\dfrac{Cpd}{2}\right)^{2} \cdot (tp1 + tox)$ Volume of Poly2/oxide mass

$Agm := \pi \cdot \left(\dfrac{Cgd}{2}\right)^{2} \cdot tg$ Volume of gold mass

$Mp := (Aa + Apm) \cdot \rho p$ $Mp = 2.103 \cdot 10^{-11} \cdot kg$

$Mgm := Agm \cdot \rho g$ $Mgm = 3.153 \cdot 10^{-12} \cdot kg$

$M := Mp + Mgm$ $M = 2.418 \cdot 10^{-11} \cdot kg$

$v1 := 1 - v$ $v1 = 0.78$

$$k := n \cdot \left(\frac{E \cdot w \cdot tp1^3}{l^3} \right) \qquad k = 2.111 \cdot kg \cdot sec^{-2} \qquad k2 := \frac{\sigma \cdot (v1) \cdot w \cdot tp1}{2 \cdot l} \qquad k2 = 0.008 \cdot kg \cdot sec^{-2}$$

$$kt := k + k2 \qquad kt = 2.119 \cdot kg \cdot sec^{-2}$$

$$f := \frac{1}{2 \cdot \pi} \cdot \left(\sqrt{\frac{kt}{M}} \right) \qquad f = 4.711 \cdot 10^4 \cdot sec^{-1}$$

Piston Mirror - PA4P1.5

$tp1 := 1.9946 \cdot 10^{-6} \cdot m \qquad Pw := 58 \cdot 10^{-6} \cdot m \qquad Pl := 70 \cdot 10^{-6} \cdot m$

$E := 169 \cdot 10^9 \cdot Pa \qquad tp2 := 1.5441 \cdot 10^{-6} \cdot m \qquad Cpd := 22 \cdot 10^{-6} \cdot m \qquad Cgd := 20 \cdot 10^{-6} \cdot m$

$\sigma := 1.2 \cdot 10^6 \cdot Pa \qquad tox := 0.7508 \cdot 10^{-6} \cdot m \qquad v := 0.22 \qquad n := 4$

$w := 1.5 \cdot 10^{-6} \cdot m \qquad tg := 0.5200 \cdot 10^{-6} \cdot m \qquad \rho p := 2.3 \cdot 10^3 \cdot \frac{kg}{m^3} \qquad \rho g := 19.3 \cdot 10^3 \cdot \frac{kg}{m^3}$

$l := 147 \cdot 10^{-6} \cdot m$

$Aa := (Pw \cdot Pl) \cdot tp1$ Volume of actuator

$Apm := \pi \cdot \left(\frac{Cpd}{2} \right)^2 \cdot (tp1 + tox)$ Volume of Poly2/oxide mass

$Agm := \pi \cdot \left(\frac{Cgd}{2} \right)^2 \cdot tg$ Volume of gold mass

$Mp := (Aa + Apm) \cdot \rho p \qquad Mp = 2.103 \cdot 10^{-11} \cdot kg$

$Mgm := Agm \cdot \rho g \qquad Mgm = 3.153 \cdot 10^{-12} \cdot kg$

$M := Mp + Mgm \qquad M = 2.418 \cdot 10^{-11} \cdot kg$

$v1 := 1 - v \qquad v1 = 0.78$

$$k := n \cdot \left(\frac{E \cdot w \cdot tp1^3}{l^3} \right) \qquad k = 2.533 \cdot kg \cdot sec^{-2} \qquad k2 := \frac{\sigma \cdot (v1) \cdot w \cdot tp1}{2 \cdot l} \qquad k2 = 0.01 \cdot kg \cdot sec^{-2}$$

$$kt := k + k2 \qquad kt = 2.543 \cdot kg \cdot sec^{-2}$$

$$f := \frac{1}{2 \cdot \pi} \cdot \left(\sqrt{\frac{kt}{M}} \right) \qquad f = 5.161 \cdot 10^4 \cdot sec^{-1}$$

Piston Mirror - PA4P1.75

$tp1 := 1.9946 \cdot 10^{-6} \cdot m \qquad Pw := 58 \cdot 10^{-6} \cdot m \qquad Pl := 70 \cdot 10^{-6} \cdot m$

$E := 169 \cdot 10^9 \cdot Pa \qquad tp2 := 1.5441 \cdot 10^{-6} \cdot m \qquad Cpd := 22 \cdot 10^{-6} \cdot m \qquad Cgd := 20 \cdot 10^{-6} \cdot m$

$\sigma := 1.2 \cdot 10^6 \cdot Pa \qquad tox := 0.7508 \cdot 10^{-6} \cdot m \qquad v := 0.22 \qquad n := 4$

$w := 1.75 \cdot 10^{-6} \cdot m \qquad tg := 0.5200 \cdot 10^{-6} \cdot m \qquad \rho p := 2.3 \cdot 10^3 \cdot \frac{kg}{m^3} \qquad \rho g := 19.3 \cdot 10^3 \cdot \frac{kg}{m^3}$

$l := 147 \cdot 10^{-6} \cdot m$

$Aa := (Pw \cdot Pl) \cdot tp1$ Volume of actuator

$Apm := \pi \cdot \left(\frac{Cpd}{2} \right)^2 \cdot (tp1 + tox)$ Volume of Poly2/oxide mass

$Agm := \pi \cdot \left(\frac{Cgd}{2} \right)^2 \cdot tg$ Volume of gold mass

Piston Mirror - PA4P2.0

$$tp1 := 1.9946 \cdot 10^{-6} \cdot m \quad Pw := 58 \cdot 10^{-6} \cdot m \quad Pl := 70 \cdot 10^{-6} \cdot m$$

$$E := 169 \cdot 10^9 \cdot Pa \quad tp2 := 1.5441 \cdot 10^{-6} \cdot m \quad Cpd := 22 \cdot 10^{-6} \cdot m \quad Cgd := 20 \cdot 10^{-6} \cdot m$$

$$\sigma := 1.2 \cdot 10^6 \cdot Pa \quad tox := 0.7508 \cdot 10^{-6} \cdot m \quad v := 0.22 \quad n := 4$$

$$tg := 0.5200 \cdot 10^{-6} \cdot m \quad \rho p := 2.3 \cdot 10^3 \cdot \frac{kg}{m^3} \quad \rho g := 19.3 \cdot 10^3 \cdot \frac{kg}{m^3}$$

$$w := 2.0 \cdot 10^{-6} \cdot m \quad l := 147 \cdot 10^{-6} \cdot m$$

$$Aa := (Pw \cdot Pl) \cdot tp1$$

Volume of actuator

$$Apm := \pi \cdot \left(\frac{Cpd}{2} \right)^2 \cdot (tp1 + tox)$$

Volume of Poly2/oxide mass

$$Agm := \pi \cdot \left(\frac{Cgd}{2} \right)^2 \cdot tg$$

Volume of gold mass

$$Mp := (Aa + Apm) \cdot \rho p \quad Mp = 2.103 \cdot 10^{-11} \cdot kg$$

$$Mgm := Agm \cdot \rho g \qquad Mgm = 3.153 \cdot 10^{-12} \cdot kg$$

$$M := Mp + Mgm \qquad M = 2.418 \cdot 10^{-11} \cdot kg$$

$$v1 := 1 - v \qquad v1 = 0.78$$

$$k := n \cdot \left(\frac{E \cdot w \cdot tp1^3}{l^3} \right) \quad k = 3.377 \cdot kg \cdot sec^{-2} \qquad k2 := \frac{\sigma \cdot (v1) \cdot w \cdot tp1}{2 \cdot l} \qquad k2 = 0.013 \cdot kg \cdot sec^{-2}$$

$$kt := k + k2 \qquad kt = 3.39 \cdot kg \cdot sec^{-2}$$

$$f := \frac{1}{2 \cdot \pi} \cdot \left(\sqrt{\frac{kt}{M}} \right) \qquad f = 5.96 \cdot 10^4 \cdot sec^{-1}$$

Piston Mirror - PA2P1.0

$$tp1 := 1.9946 \cdot 10^{-6} \cdot m \quad Pw := 66 \cdot 10^{-6} \cdot m \quad Pl := 86 \cdot 10^{-6} \cdot m$$

$$E := 169 \cdot 10^9 \cdot Pa \quad tp2 := 1.5441 \cdot 10^{-6} \cdot m \quad Cpd := 22 \cdot 10^{-6} \cdot m \quad Cgd := 20 \cdot 10^{-6} \cdot m$$

$$\sigma := 1.2 \cdot 10^6 \cdot Pa \quad tox := 0.7508 \cdot 10^{-6} \cdot m \quad v := 0.22 \quad n := 2$$

$$tg := 0.5200 \cdot 10^{-6} \cdot m \quad \rho p := 2.3 \cdot 10^3 \cdot \frac{kg}{3} \quad \rho g := 19.3 \cdot 10^3 \cdot \frac{kg}{3}$$

$$w := 1.0 \cdot 10^{-6} \cdot m$$

$$w := 1.0 \cdot 10^{-6} \cdot m \qquad l := 88 \cdot 10^{-6} \cdot m \qquad \rho p \quad 2.3 \cdot 10 \cdot \frac{}{m^3} \qquad \rho g \quad 19.3 \cdot 10 \cdot \frac{}{m^3}$$

$Aa := (Pw \cdot Pl) \cdot tp1$

Volume of actuator

$Apm := \pi \cdot \left(\frac{Cpd}{2}\right)^2 \cdot (tp1 + tox)$

Volume of Poly2/oxide mass

$Agm := \pi \cdot \left(\frac{Cgd}{2}\right)^2 \cdot tg$

Volume of gold mass

$Mp := (Aa + Apm) \cdot \rho p \qquad Mp = 2.844 \cdot 10^{-11} \cdot kg$

$Mgm := Agm \cdot \rho g \qquad Mgm = 3.153 \cdot 10^{-12} \cdot kg$

$M := Mp + Mgm \qquad M = 3.159 \cdot 10^{-11} \cdot kg$

$v1 := 1 - v \qquad v1 = 0.78$

$k := n \cdot \left(\frac{E \cdot w \cdot tp1^3}{l^3}\right) \qquad k = 3.936 \cdot kg \cdot sec^{-2} \qquad k2 := \frac{\sigma \cdot (v1) \cdot w \cdot tp1}{2 \cdot l} \qquad k2 = 0.011 \cdot kg \cdot sec^{-2}$

$$kt := k + k2 \qquad kt = 3.946 \cdot kg \cdot sec^{-2}$$

$f := \frac{1}{2 \cdot \pi} \cdot \left(\sqrt{\frac{kt}{M}}\right) \qquad f = 5.625 \cdot 10^4 \cdot sec^{-1}$

Piston Mirror - PA2P1.25

$tp1 := 1.9946 \cdot 10^{-6} \cdot m \qquad Pw := 66 \cdot 10^{-6} \cdot m \qquad Pl := 86 \cdot 10^{-6} \cdot m$

$E := 169 \cdot 10^9 \cdot Pa \qquad tp2 := 1.5441 \cdot 10^{-6} \cdot m \qquad Cpd := 22 \cdot 10^{-6} \cdot m \qquad Cgd := 20 \cdot 10^{-6} \cdot m$

$\sigma := 1.2 \cdot 10^6 \cdot Pa \qquad tox := 0.7508 \cdot 10^{-6} \cdot m \qquad v := 0.22 \qquad n := 2$

$w := 1.25 \cdot 10^{-6} \cdot m \qquad tg := 0.5200 \cdot 10^{-6} \cdot m \qquad \rho p := 2.3 \cdot 10^3 \cdot \frac{kg}{m^3} \qquad \rho g := 19.3 \cdot 10^3 \cdot \frac{kg}{m^3}$

$l := 88 \cdot 10^{-6} \cdot m$

$Aa := (Pw \cdot Pl) \cdot tp1$

Volume of actuator

$Apm := \pi \cdot \left(\frac{Cpd}{2}\right)^2 \cdot (tp1 + tox)$

Volume of Poly2/oxide mass

$Agm := \pi \cdot \left(\frac{Cgd}{2}\right)^2 \cdot tg$

Volume of gold mass

$Mp := (Aa + Apm) \cdot \rho p \qquad Mp = 2.844 \cdot 10^{-11} \cdot kg$

$Mgm := Agm \cdot \rho g \qquad Mgm = 3.153 \cdot 10^{-12} \cdot kg$

$M := Mp + Mgm \qquad M = 3.159 \cdot 10^{-11} \cdot kg$

$v1 := 1 - v \qquad v1 = 0.78$

$k := n \cdot \left(\frac{E \cdot w \cdot tp1^3}{l^3}\right) \qquad k = 4.92 \cdot kg \cdot sec^{-2} \qquad k2 := \frac{\sigma \cdot (v1) \cdot w \cdot tp1}{2 \cdot l} \qquad k2 = 0.013 \cdot kg \cdot sec^{-2}$

$$kt := k + k2 \qquad kt = 4.933 \cdot kg \cdot sec^{-2}$$

$f := \frac{1}{2 \cdot \pi} \cdot \left(\sqrt{\frac{kt}{M}}\right) \qquad f = 6.289 \cdot 10^4 \cdot sec^{-1}$

Piston Mirror - PA2P1.5

$tp1 := 1.9946 \cdot 10^{-6} \cdot m$ $Pw := 66 \cdot 10^{-6} \cdot m$ $Pl := 86 \cdot 10^{-6} \cdot m$

$E := 169 \cdot 10^9 \cdot Pa$ $tp2 := 1.5441 \cdot 10^{-6} \cdot m$ $Cpd := 22 \cdot 10^{-6} \cdot m$ $Cgd := 20 \cdot 10^{-6} \cdot m$

$\sigma := 1.2 \cdot 10^6 \cdot Pa$ $tox := 0.7508 \cdot 10^{-6} \cdot m$ $v := 0.22$ $n := 2$

$w := 1.5 \cdot 10^{-6} \cdot m$ $tg := 0.5200 \cdot 10^{-6} \cdot m$ $\rho p := 2.3 \cdot 10^3 \cdot \dfrac{kg}{m^3}$ $\rho g := 19.3 \cdot 10^3 \cdot \dfrac{kg}{m^3}$

$l := 88 \cdot 10^{-6} \cdot m$

$Aa := (Pw \cdot Pl) \cdot tp1$ Volume of actuator

$Apm := \pi \cdot \left(\dfrac{Cpd}{2}\right)^2 \cdot (tp1 + tox)$ Volume of Poly2/oxide mass

$Agm := \pi \cdot \left(\dfrac{Cgd}{2}\right)^2 \cdot tg$ Volume of gold mass

$Mp := (Aa + Apm) \cdot \rho p$ $Mp = 2.844 \cdot 10^{-11} \cdot kg$

$Mgm := Agm \cdot \rho g$ $Mgm = 3.153 \cdot 10^{-12} \cdot kg$

$M := Mp + Mgm$ $M = 3.159 \cdot 10^{-11} \cdot kg$

$v1 := 1 - v$ $v1 = 0.78$

$k := n \cdot \left(\dfrac{E \cdot w \cdot tp1^3}{l^3}\right)$ $k = 5.904 \cdot kg \cdot sec^{-2}$ $k2 := \dfrac{\sigma \cdot (v1) \cdot w \cdot tp1}{2 \cdot l}$ $k2 = 0.016 \cdot kg \cdot sec^{-2}$

$kt := k + k2$ $kt = 5.92 \cdot kg \cdot sec^{-2}$

$f := \dfrac{1}{2 \cdot \pi} \cdot \left(\sqrt{\dfrac{kt}{M}}\right)$ $f = 6.889 \cdot 10^4 \cdot sec^{-1}$

Piston Mirror - PA2P1.75

$tp1 := 1.9946 \cdot 10^{-6} \cdot m$ $Pw := 66 \cdot 10^{-6} \cdot m$ $Pl := 86 \cdot 10^{-6} \cdot m$

$E := 169 \cdot 10^9 \cdot Pa$ $tp2 := 1.5441 \cdot 10^{-6} \cdot m$ $Cpd := 22 \cdot 10^{-6} \cdot m$ $Cgd := 20 \cdot 10^{-6} \cdot m$

$\sigma := 1.2 \cdot 10^6 \cdot Pa$ $tox := 0.7508 \cdot 10^{-6} \cdot m$ $v := 0.22$ $n := 2$

$w := 1.75 \cdot 10^{-6} \cdot m$ $tg := 0.5200 \cdot 10^{-6} \cdot m$ $\rho p := 2.3 \cdot 10^3 \cdot \dfrac{kg}{m^3}$ $\rho g := 19.3 \cdot 10^3 \cdot \dfrac{kg}{m^3}$

$l := 88 \cdot 10^{-6} \cdot m$

$Aa := (Pw \cdot Pl) \cdot tp1$ Volume of actuator

$Apm := \pi \cdot \left(\dfrac{Cpd}{2}\right)^2 \cdot (tp1 + tox)$ Volume of Poly2/oxide mass

$Agm := \pi \cdot \left(\dfrac{Cgd}{2}\right)^2 \cdot tg$ Volume of gold mass

$Mp := (Aa + Apm) \cdot \rho p$ $Mp = 2.844 \cdot 10^{-11} \cdot kg$

$Mgm := Agm \cdot \rho g$ $Mgm = 3.153 \cdot 10^{-12} \cdot kg$

$M := Mp + Mgm$ $M = 3.159 \cdot 10^{-11} \cdot kg$

$v1 := 1 - v$ $v1 = 0.78$

$\left(E \cdot w \cdot tp1^3\right)$

$$k := n \cdot \left(\frac{E \cdot w \cdot tp1^3}{l^3} \right) \qquad k = 6.888 \cdot kg \cdot sec^{-2} \qquad k2 := \frac{\sigma \cdot (v1) \cdot w \cdot tp1}{2 \cdot l} \qquad k2 = 0.019 \cdot kg \cdot sec^{-2}$$

$$kt := k + k2 \qquad kt = 6.906 \cdot kg \cdot sec^{-2}$$

$$f := \frac{1}{2 \cdot \pi} \cdot \left(\sqrt{\frac{kt}{M}} \right) \qquad f = 7.441 \cdot 10^4 \cdot sec^{-1}$$

Piston Mirror - PA2P2.0

$tp1 := 1.9946 \cdot 10^{-6} \cdot m \qquad Pw := 66 \cdot 10^{-6} \cdot m \qquad Pl := 86 \cdot 10^{-6} \cdot m$

$E := 169 \cdot 10^9 \cdot Pa \qquad tp2 := 1.5441 \cdot 10^{-6} \cdot m \qquad Cpd := 22 \cdot 10^{-6} \cdot m \qquad Cgd := 20 \cdot 10^{-6} \cdot m$

$\sigma := 1.2 \cdot 10^6 \cdot Pa \qquad tox := 0.7508 \cdot 10^{-6} \cdot m \qquad v := 0.22 \qquad n := 2$

$tg := 0.5200 \cdot 10^{-6} \cdot m$

$w := 2.0 \cdot 10^{-6} \cdot m \qquad \rho p := 2.3 \cdot 10^3 \cdot \frac{kg}{m^3} \qquad \rho g := 19.3 \cdot 10^3 \cdot \frac{kg}{m^3}$

$l := 88 \cdot 10^{-6} \cdot m$

$Aa := (Pw \cdot Pl) \cdot tp1$ Volume of actuator

$Apm := \pi \cdot \left(\frac{Cpd}{2} \right)^2 \cdot (tp1 + tox)$ Volume of Poly2/oxide mass

$Agm := \pi \cdot \left(\frac{Cgd}{2} \right)^2 \cdot tg$ Volume of gold mass

$Mp := (Aa + Apm) \cdot \rho p \qquad Mp = 2.844 \cdot 10^{-11} \cdot kg$

$Mgm := Agm \cdot \rho g \qquad Mgm = 3.153 \cdot 10^{-12} \cdot kg$

$M := Mp + Mgm \qquad M = 3.159 \cdot 10^{-11} \cdot kg$

$v1 := 1 - v \qquad v1 = 0.78$

$$k := n \cdot \left(\frac{E \cdot w \cdot tp1^3}{l^3} \right) \qquad k = 7.872 \cdot kg \cdot sec^{-2} \qquad k2 := \frac{\sigma \cdot (v1) \cdot w \cdot tp1}{2 \cdot l} \qquad k2 = 0.021 \cdot kg \cdot sec^{-2}$$

$$kt := k + k2 \qquad kt = 7.893 \cdot kg \cdot sec^{-2}$$

$$f := \frac{1}{2 \cdot \pi} \cdot \left(\sqrt{\frac{kt}{M}} \right) \qquad f = 7.955 \cdot 10^4 \cdot sec^{-1}$$

Bibliography

1 J. L. Stewart, E. Glaesser, and W. F. Caldwell, "An Electronic Analog of the Ear", Biophysics Laboratory, 6570th Aerospace Medical Research Laboratories, Aerospace Medical Division, Air Force Systems Command, Wright-Patterson Air Force Base, Ohio, June 1963 (Technical Documentary Report No. AMRL-TDR-63-60).

2 R. F. Lyon and C. Mead, "An Analog Electronic Cochlea," IEEE Trans. Acoust., Speech, and Signal Processing, vol. 36, pp. 1119- 1134, July 1988.

3 D. E. Sene, "Design, Fabrication, and Characterization of MicroOpto-Electro-Mechanical Systems", MS Thesis, AFIT/GE/ENG/95D-03, School of Engineering, Air Force Institute of Technology (AU), Wright-Patterson AFB, OH, Dec. 1995.

4 W. Liu, A. Andreou, and M. H. Goldstein, Jr. "Voiced-Speech Representation by an Analog Silicon Model of the Auditory Periphery," IEEE Trans. on Neural Networks, vol. 3, pp. 477-487, May 1992.

5 C. Mead, X. Arreguit, and J. Luzzaro, "Analog VLSI Model of Binaural Hearing," IEEE Trans. on Neural Networks, vol. 2, pp. 230-236, Mar. 1991.

6 D. A. Koester, R. Mahadevan, A. Shishkoff, and K. W. Markus, SmartMUMPs Design Handbook including MUMPs Introduction and Design Rules Revision 4.0, MEMS Technology Application Center, MCNC, Mar. 1996.

7 www.boystown.org World wide web site based on "Micromechanical Models of the Cochlea" by J. B. Allen and S. T. Neely in Physics Today, July 1992.

8 A. J. Hudspeth and Vladislav S. Markin, "The Ear's Gears: Mechanoelectrical Transduction by Hair Cells," Physics Today, vol. 47, pp. 22-28, Feb. 1994.

9 J. M. Colombi, "Cepstral and Auditory Model Features for Speaker Recognition," MS Thesis, AFIT/GE/ENG/92D-23, School of Engineering, Air Force Institute of Technology(AU), Wright-Patterson AFB, OH, Dec. 1992.

10 C. D. Geisler, "Coding of Acoustic Signals on the Auditory Nerve," <u>IEEE Engineering in Medicine and Biology</u>, vol. 6, pp. 22-28, June 1987.

11 M. H. Goldstein, Jr., "Auditory Periphery as Speech Signal Processor," <u>IEEE Engineering in Medicine and Biology</u>, vol. 13, pp. 186-196, Apr./May 1994.

12 L. E. Atlas, "Auditory Coding in Higher Centers of the CNS," <u>IEEE Engineering in Medicine and Biology,</u> vol. 6, pp. 29-32, June 1987.

13 L. Watts, D. A. Kerns, R. F. Lyon, and C. A. Mead, "Improved Implementation of the Silicon Cochlea," <u>IEEE J. of Solid-State Circuits</u>, vol. 27, pp. 692-700, May 1992.

14 J.-C. Bor and C.-Y. Wu, "Analog Electric Cochlea Design Using Multiplexing Switched-Capacitor Circuits," <u>IEEE Trans. on Neural Networks,</u> vol. 7, pp. 155-166, Jan. 1996.

15 O. M. Davies, "An Analysis of the Response of an Electronic Model of the Cochlea", MS Thesis, AFIT/GE/EE/65-7, School of Engineering, Air Force Institute of Technology(AU), Wright-Patterson AFB, OH, Aug. 1965.

16 M. R. Schroeder, "An Integrable Model for the Basilar Membrane," <u>J. of the Acoustical Society of America</u>, vol. 53, pp. 429-434, 1973.

17 G. Zweig, R. Lipes, and J. R. Pierce, "The Cochlea Compromise," <u>J. of the Acoustical Society of America</u>, vol. 59, pp. 975-982, Apr. 1976.

18 J. Sundberg, "The Acoustics of the Singing Voice," <u>Scientif. Amer.</u>, Mar. 1977.

19 J. B. Allen, "Cochlear Micromechanics - A physical model of transduction," <u>J. of the Acoustical Society of America,</u> vol. 68, pp. 1660-1670, Dec. 1980.

20 S. T. Neeley, "Mathematical Modeling of Cochlear Mechanics" <u>J. of the Acoustical Society of America</u>, vol. 78, pp. 345-352, July 1985.

21 E. Zwicker, "A Hardware Cochlear Nonlinear Preprocessing Model with Active Feedback," J. of the Acoustical Society of America, vol. 80, pp. 146-153, July 1986.

22 R. J. McAulay and Thomas F. Quatieri, "Speech Analysis/Synthesis Based on a Sinusoidal Representation," IEEE Trans. on Acoust., Speech, and Signal Processing, vol. 34, pp. 744-754, Aug. 1986.

23 S. T. Neely and D. O. Kim, "A Model for Active Elements in Cochlear Biomechanics," J. of the Acoustical Society of America, vol. 79, pp. 1472-1480, May 1986.

24 Li Deng and C. D. Geisler "A Composite Auditory Model for Processing Speech Sounds," J. of the Acoustical Society of America, vol. 82, pp. 2001-2012, Dec. 1987.

25 J. M. Kates, "A Time-Domain Digital Cochlear Model," IEEE Trans. on Signal Processing, vol. 39, pp. 2573-2592, Dec. 1991.

26 J. M. Kates, "Accurate Tuning Curves in a Cochlear Model," IEEE Trans. on Speech and Audio Processing, vol. 1, pp. 453-462, Oct. 1993.

27 H. Davis, "An Active Process in Cochlear Mechanics," Hear. Res., vol. 9, pp. 79-90, 1983.

28 N. Y. S. Kang, "Processing of Speech by Auditory Nervous System," J. of the Acoustical Society of America, vol. 68, pp. 830-835, Sept 1980.

29 J. J. Zwislocki, "Theory of the Acoustical Action of the Cochlea." J. of the Acoustical Society of America, vol. 82, pp. 778-784, 1950.

30 mems.engr.wisc.edu/images World wide web site of MEMS technology at the University of Wisconsin. Photos by Dr. Henry Guckel.

31 W. Benecke, L. Csepregi, A. Heuberger, K. Kühl, and H. Seidel, "A Frequency-Selective, Piezoresistive Silicon Vibration Sensor," IEEE 1985, CH2127-9/85/0000-0105.

32 S. Bouwstra, H. A. C. Tilmans, A. Selvakumar, and K. Najafi, "Base Driven Micromechanical Resonators," IEEE (1992) 0-7803-0456-X.

33 O. Brand, H. Boltes, and U. Baldenweg, "Thermally Excited Silicon Oxide Beam and Bridge Resonators in CMOS Technology," IEEE Trans. Electron Devices, vol. 40, pp. 1745-1753, Oct. 1993.

34 J.Y.-C. Chang, A. A. Abidi, and M. Gaitan, "Large Suspended Inductors on Silicon and Their Use in a 2-μm CMOS RF Amplifier," IEEE Electron Device Letters, vol. 14, pp. 246-248, May 1993.

35 W.-H. Chu, M. Mehregany, and R. L. Mullen, "Analysis of Tip Deflection and Force of a Bimetallic Cantilever Microactuator," J. of Micromechanical Microengineering, vol. 3, pp. 4-7, 1993.

36 B. Hök and K. Gustafsson, "Vibration Analysis of Micromechanical Elements," Sensors and Actuators, vol. 8, pp. 235-243, 1985.

37 M. F. Hribšek and R. W. Newcomb, "High-Q Selective Filters Using Mechanical Resonance of Silicon Beams," IEEE Trans. on Circuits and Systems, vol. 25, pp. 215-221, Apr. 1978.

38 L. Kiesewetter, J.-M. Zhang, D. Houdeau, and A. Steckenborn, "Determination of Young's Moduli of Micromachined Thin Films Using the Resonance Method," Sensors and Actuators, vol. 35, pp. 153-159, 1992.

39 S. S. Lee, R. P. Ried, and R. M. White, "Piezoelectric Cantilever Microphone and Microspeaker," Solid-State Sensor and Actuator Workshop, Hilton Head, South Carolina, pp. 33-37, June 1994.

40 C. Linder and N. F. De Rooij, "Investigations on Free-standing Polysilicon Beams in View of their Application as Transducers," Sensors and Actuators, A21-A23, pp. 1053-1059, 1990.

41 J. Marshall, M. Gaitan, M. Zaghloul, D. Novotny, Vi Tyree, J.-I. Pi, C. Piñà, and W. Hansford, "Realizing Suspended Structures on Chip Fabricated by CMOS Foundry Processes Through the MOSIS Service", U.S. Department of Commerce, Technology Administration, National Institute of Standards and Technology, NISTIR 5402, June 1994.

42 "MICROELECTROMECHANICAL SYSTEMS: A DOD Dual Use Technology Industrial Assessment, Final Report", DOD, Dec. 1995.

43 M. Parameswaran, H. P. Baltes, Lj. Ristic, and A. C. Dhaded, "A New Approach for the Fabrication of Micromechanical Structures," Sensor and Actuators, vol. 19, pp. 289-307, 1989.

44 B. C. Read, III, "Silicon Based Microactuators for Telerobotic Tactile Stimulation", MS Thesis, AFIT/GE/ENG/94D-25, School of Engineering, Air Force Institute of Technology(AU), Wright-Patterson AFB, OH, Dec. 1994.

45 H. Seidel and L. Csepregi, "Design Optimization for Cantilever-Type Accelerometers," Sensors and Actuators, vol. 6, pp. 81-92, 1984.

46 W. Zhang and H. Zhang, "Modeling and Analysis of Nonlinear Damping Mechanisms in Vibrating Systems," International J. of Mech. Sci., vol. 36, pp. 829-848, 1994.

47 J. Bernstein, M. Weinberg, E. McLauglin, J. Powers, and F. Tito, "Advanced Micromachined Condenser Hydrophone," Solid-State Sensor and Actuator Workshop, Hilton Head, South Carolina, June 1994.

48 W. Kühnel, "Silicon Condenser Microphone with Integrated Field-Effect Transistor," Sensors and Actuators, vol. 25-27, pp. 521-525, 1991.

49 W. Kühneland and G. Hess, "Micromachined Subminiature Condenser Microphones in Silicon," Sensors and Actuators, vol. 32, pp. 560-564, 1992.

50 R. P. Reid, E. S. Kim, D. M. Hong, and R. S. Muller, "Piezoelectric Microphone with On-Chip CMOS Circuits," J. of Micromechanical Systems, vol. 2, pp. 111-120, Sept. 1993.

51 R. Schellin and G. Hess, "A Silicon Subminiture Microphone Based on Piezoresistive Polysilicon Strain Gauges," Sensors and Actuators, vol. 32, pp. 555-559, 1992.

52 M. Gaitan, M. Parameswaran, R. B. Johnson, and R. Chung, "Commercial CMOS Foundry Thermal Display for Dynamic Thermal Scene Simulation," Proc. SPIE, Orlando Florida, Apr. 1993.

53 M. Parameswaran, R. Chung, M. Gaitan, R. B. Johnson, and M. Syrzcki, "Commercial CMOS Fabricated Integrated Dynamic Thermal Scene Simulator," IEEE IEDM 91-753, PP. 29.4.1-29.4.4, 1991.

54 M. Parameswaran, A. M. Robinson, D. L. Blackburn, M. Gaitan, and J. Geist, "Micromachined Thermal Radiation Emitter from a Commercial CMOS Process," IEEE Electron Device Letters, vol. 12, pp. 57-59, Feb. 1991.

55 B. C. Read, V. M. Bright , and J. H. Comtois, "Mechanical and Optical Characterization of Thermal Microactuators Fabricated in a CMOS Process," Micromachined Devices and Components, SPIE, vol. 2642, pp. 22-32, Austin, Texas, Oct. 1995.

56 R. J. Reay, E. H. Klaassen, and G. T. A. Kovacs, "Thermally and Electrically Isolated Single Crystal Silicon Structures in CMOS Technology," IEEE Electron Device Letters, vol. 15, pp. 399-401, Oct. 1994.

57 J. S. Suehle, R. E. Cavichi, M. Gaitan, and S. Semancik, "Tin Oxide Gas Sensor Fabricated Using CMOS Micro-Hotplates and In-Situ Processing," IEEE Electron Device Letters, vol. 14, pp. 118-120, Mar. 1993.

58 N. R. Swart and A. Nathan, "Coupled Electrothermal Modeling of Microheaters Using SPICE," IEEE Trans. on Electron Devices, vol. 41, pp. 920-925, June 1994.

59 R. J. Reay, Erno H. Klaassen, and G. T. A. Kovacs, "A Micromachined Low-Power Temperature-Regulated Bandgap Voltage Reference," IEEE International Solid-State Circuits Conference 1995, Integrated Sensors and Circuits, TA 9.7, p. 166.

60 M. W. Phipps, "Design and Development of Microswitches for MicroElectro-Mechanical Relay Matrices", MS Thesis, AFIT/GE/ENG/95J-02, School of Engineering, Air Force Institute of Technology(AU), Wright-Patterson AFB, OH, Jun. 1995.

61 J. H. Comtois, "Structures and Techniques for Implementing and Packaging Complex, Large Scale Micro-Electro-Mechanical Systems using Foundry Fabrication Processes", Ph.D. Thesis, AFIT/DS/ENG/96-04, School of Engineering, Air Force Institute of Technology(AU), Wright-Patterson AFB, OH, May 1996.

62 mems.mcnc.org/mumps.html World wide web site concerning MUMPs processing.

63 M. Gaitan, M. Parameswaran, M. Zaghloul, J. Marshall, D. Novotny, and J. Suehle, "Design Methodology for Micromechanical Systems at Commercial CMOS Foundries Through MOSIS," Proc. of the 35th Midwest Symposium on Circuits and Systems, Washington D.C., Aug. 1992.

64 J. C. Marshall, M. Parameswaran, M. E. Zaghloul, and M. Gaitan, "High-Level CAD Melds Micromachined Devices with Foundries," Circuits and Devices, vol. 8, pp. 10-15, Nov. 1992.

65 F. S. Tse, I. E. Morse, and R. T. Hinkle, Mechanical Vibrations, Theory and Applications. Allyn and Bacon, Inc, Boston, 1979.

66 J. H. Comtois., V. M. Bright, S. C. Gustafson, and M. A. Michalicek, "Implementation of Hexagonal Micromirror Arrays as Phase-Mostly Spatial Light Modulators," Proc. SPIE, vol. 2641, pp. 76-87, Oct. 1995.

67 R. M. Kuhns, "Design and Fabrication of a MicroMechanical Gyroscope", MS Thesis, AFIT/GE/ENG/95D-10, School of Engineering, Air Force Institute of Technology (AU), Wright-Patterson AFB, OH, Dec. 1995.

68 J. J. Yao and N. C. MacDonald, "A Micromachined, Single-Crystal Silicon, Tunable Resonator," J. of Micromechanics and Microengineering, Structures, Devices and Systems, vol. 5, pp. 257-264, Sep. 1995.

69 W. C.-K. Tang, "Electronic Comb Drive for Resonant Sensor and Actuator Applications," Ph.D. Thesis, University of California at Berkeley, Nov. 1990.

70 Conversations and e-mail with MCNC Engineers Vijay Dhuler and Ramaswamy Mahadevan, Summer 1996.

71 M. A. Michalicek, D. E. Sene, and V. M. Bright, "Advanced Modeling of Micromirror Devices," Proc. International Conference on Integrated Micro/Nanotechnology for Space Applications, NASA & Aerospace Corp. Publications, Oct. 1995.

72 Conversations and e-mail with J. Robert Reid, 5 Aug 1996. Procedures derived from the MUMPs design guide and through experimentation with many die runs.

Vita

Capt George C. Dalton II was born in Brooklyn, New York on December 24th, 1961. After graduating from Brooklyn Technical High School with a College Preparatory Electricity/Electronics Diploma in 1979, he attended the Polytechnic Institute of New York studying Electrical Engineering. In October, 1983 Capt Dalton entered active duty. After completing technical school, he was assigned as an Electronic Computer and Switching Systems Specialist at the 47 Communications Group, Cheyenne Mountain Complex, Colorado Springs, Colorado. During this time he was awarded an Associates of Applied Science (A.A.S.) degree in Electronic Systems Technology by the Community College of the Air Force (CCAF). In October 1986 he was reassigned to 6130th Tactical Control Flight, Osan Air Base, Republic of Korea. Returning to the U.S., Captain Dalton was assigned as an Instructor of electronics and computer maintenance with the 3390th Technical Training Group at Keesler AFB, Mississippi. While there he was awarded two more Associate's Degrees from CCAF, an A.A.S. in Electronic Engineering Technology and an A.A.S.

Vita

Capt George C. Dalton II ██████████████████████████
████████████ After graduating from Brooklyn Technical High School with a College Preparatory Electricity/Electronics Diploma in 1979, he attended the Polytechnic Institute of New York studying Electrical Engineering. In October, 1983 Capt Dalton entered active duty. After completing technical school, he was assigned as an Electronic Computer and Switching Systems Specialist at the 47 Communications Group, Cheyenne Mountain Complex, Colorado Springs, Colorado. During this time he was awarded an Associates of Applied Science (A.A.S.) degree in Electronic Systems Technology by the Community College of the Air Force (CCAF). In October 1986 he was reassigned to 6130th Tactical Control Flight, Osan Air Base, Republic of Korea. Returning to the U.S., Captain Dalton was assigned as an Instructor of electronics and computer maintenance with the 3390th Technical Training Group at Keesler AFB, Mississippi. While there he was awarded two more Associate's Degrees from CCAF, an A.A.S. in Electronic Engineering Technology and an A.A.S.

REPORT DOCUMENTATION PAGE

1. AGENCY USE ONLY (Leave blank)	2. REPORT DATE December 1996	3. REPORT TYPE AND DATES COVERED Master's Thesis

4. TITLE AND SUBTITLE
ARTIFICAL COCHLEA DESIGN USING MICRO-ELECTRO-MECHANICAL SYSTEMS

5. FUNDING NUMBERS

6. AUTHOR(S)
George C. Dalton II, Captain, USAF

7. PERFORMING ORGANIZATION NAME(S) AND ADDRESS(ES)
Air Force Institute of Technology
2750 P Street
WPAFB, OH 45433-7126

8. PERFORMING ORGANIZATION REPORT NUMBER
AFIT/GCS/ENG/96D-06

9. SPONSORING / MONITORING AGENCY NAME(S) AND ADDRESS(ES)
Phillips Laboratory (PL/VTEE)
ATTN: Capt Adrian Michalicek
3550 Aberdeen Ave. SE
Kirtland AFB, NM 87117-5776

10. SPONSORING / MONITORING AGENCY REPORT NUMBER

11. SUPPLEMENTARY NOTES

12a. DISTRIBUTION / AVAILABILITY STATEMENT

Approved for public release; distribution unlimited

12b. DISTRIBUTION CODE

13. ABSTRACT (Maximum 200 words)

The use of Micro-Electro-Mechanical Systems (MEMS) in the design of an artificial cochlea is investigated in depth. Interdigitated finger (comb), cantilever, bridge, and mirror resonators are presented as possible devices used to implement the artificial cochlea. These resonators are demonstrated to be extremely high Q devices, capable of being tuned with a simple DC bias. This suggests a change to existing cochlea models that claim highly complex AC feedback as being responsible for changes in the dampening of the basilar membrane. The new cochlea model presented here, using MEMS to approximate the tuning of the basilar membrane, may be closer to the workings of the actual cochlea, as we understand it today.

14. SUBJECT TERMS
Micro-Electro-Mechanical Systems (MEMS), artificial cochlea, MEMS cochlea, Interdigitated finger (comb), cantilever, bridge, mirror, resonators

15. NUMBER OF PAGES
208

16. PRICE CODE

17. SECURITY CLASSIFICATION OF REPORT	18. SECURITY CLASSIFICATION OF THIS PAGE	19. SECURITY CLASSIFICATION OF ABSTRACT	20. LIMITATION OF ABSTRACT
UNCLASSIFIED	UNCLASSIFIED	UNCLASSIFIED	UL

GENERAL INSTRUCTIONS FOR COMPLETING SF 298

The Report Documentation Page (RDP) is used in announcing and cataloging reports. It is important that this information be consistent with the rest of the report, particularly the cover and title page. Instructions for filling in each block of the form follow. It is important to *stay within the lines* to meet *optical scanning requirements*.

Block 1. Agency Use Only (*Leave blank*).

Block 2. Report Date. Full publication date including day, month, and year, if available (e.g. 1 Jan 88). Must cite at least the year.

Block 3. Type of Report and Dates Covered. State whether report is interim, final, etc. If applicable, enter inclusive report dates (e.g. 10 Jun 87 - 30 Jun 88).

Block 4. Title and Subtitle. A title is taken from the part of the report that provides the most meaningful and complete information. When a report is prepared in more than one volume, repeat the primary title, add volume number, and include subtitle for the specific volume. On classified documents enter the title classification in parentheses.

Block 5. Funding Numbers. To include contract and grant numbers; may include program element number(s), project number(s), task number(s), and work unit number(s). Use the following labels:

C	-	Contract	**PR**	- Project
G	-	Grant	**TA**	- Task
PE	-	Program Element	**WU**	- Work Unit Accession No.

Block 6. Author(s). Name(s) of person(s) responsible for writing the report, performing the research, or credited with the content of the report. If editor or compiler, this should follow the name(s).

Block 7. Performing Organization Name(s) and Address(es). Self-explanatory

Block 8. Performing Organization Report Number. Enter the unique alphanumeric report number(s) assigned by the organization performing the report.

Block 9. Sponsoring/Monitoring Agency Name(s) and Address(es). Self-explanatory.

Block 10. Sponsoring/Monitoring Agency Report Number. (*If known*)

Block 11. Supplementary Notes. Enter information not included elsewhere such as: Prepared in cooperation with...; Trans. of..., To be published in.... When a report is revised, include a statement whether the new report supersedes or supplements the older report.

Block 12a. Distribution/Availability Statement. Denotes public availability or limitations. Cite any availability to the public. Enter additional limitations or special markings in all capitals (e.g. NOFORN, REL, ITAR).

DOD	- See DoDD 5230.24, "Distribution Statements on Technical Documents."
DOE	- See authorities.
NASA	- See Handbook NHB 2200.2.
NTIS	- Leave blank.

Block 12b. Distribution Code.

DOD	- Leave blank.
DOE	- Enter DOE distribution categories from the Standard Distribution for Unclassified Scientific and Technical Reports.
NASA	- Leave blank.
NTIS	- Leave blank.

Block 13. Abstract. Include a brief (*Maximum 200 words*) factual summary of the most significant information contained in the report.

Block 14. Subject Terms. Keywords or phrases identifying major subjects in the report.

Block 15. Number of Pages. Enter the total number of pages.

Block 16. Price Code. Enter appropriate price code (*NTIS only*).

Blocks 17. - 19. Security Classifications. Self-explanatory. Enter U.S. Security Classification in accordance with U.S. Security Regulations (i.e., UNCLASSIFIED). If form contains classified information, stamp classification on the top and bottom of the page.

Block 20. Limitation of Abstract. This block must be completed to assign a limitation to the abstract. Enter either UL (unlimited) or SAR (same as report). An entry in this block is necessary if the abstract is to be limited. If blank, the abstract is assumed to be unlimited.